SMART WOUND DRESSINGS FOR ACCELERATED SCAR-FREE WOUND HEALING

by

Farinaz Jonidi Shariatzadeh

A thesis submitted to the Faculty of Graduate Studies of
The University of Manitoba
In partial fulfillment of the requirements for the degree of
Doctor of Philosophy

Biomedical Engineering
University of Manitoba
Winnipeg, Manitoba, Canada

ABSTRACT

SMART WOUND DRESSINGS for ACCELERATED SCAR-FREE WOUND HEALING

Farinaz Jonidi Shariatzadeh
University of Manitoba

Wound healing is a complex process comprising four main stages: hemostasis, inflammation, proliferation, and remodeling. Disruptions at any stage can lead to delayed healing, chronic wounds, or excessive scar formation. This project leverages nanotechnology to develop strategies that modulate different phases of wound healing, promoting tissue regeneration. Nanotechnology enables the manipulation of the wound healing trajectory through various chemical and physical cues to accelerate healing while minimizing scar formation. This study focuses on two key approaches: (1) infection prevention to reduce inflammation-related healing delays and (2) responsive delivery of an anti-scar drug within the critical window of scar formation.

For infection prevention, a theranostic biosensor was developed. The biosensor integrates a hemicyanine dye that undergoes a color change upon detecting bacterial lipase, allowing early and visible identification of bacterial presence. Additionally, it incorporates responsive nanoparticles that release antibacterial agents selectively in environments with elevated reactive oxygen species (ROS), ensuring targeted bacterial elimination.

For anti-scar drug delivery, solid lipid nanoparticles (SLNs) were engineered for targeted drug release during the early stages of scar formation. Since premature or delayed drug delivery can interfere with normal healing, a biomarker overexpressed specifically during scar formation was identified. SLNs were functionalized with a ligand targeting this marker. To prevent premature drug release, a cage-like protein coating was applied to the SLNs, enhancing stability until the optimal release window.

These strategies enabled early bacterial detection at low concentrations, selective bacterial elimination in ROS-rich environments, and precise delivery of anti-scar drugs to cells overexpressing connective tissue growth factor (CTGF), a biomarker specific to scar formation. By modulating different wound healing stages, this study aims to accelerate healing while minimizing scarring. However, further *in vivo* studies are essential to validate the clinical potential of these approaches.

.

For my parents the abstract in my language (Persian):

چکیده

پانسمان‌های هوشمند برای بهبود زخم سریع و بدون اسکار

فریناز جنیدی شریعت‌زاده

دانشگاه منیتوبا

فرآیند بهبود زخم شامل چهار مرحله اصلی است: هموستاز، التهاب، تکثیر و بازسازی. هرگونه اختلال در این مراحل می‌تواند مسیر بهبود زخم را منحرف کرده و منجر به ایجاد زخم‌های مزمن با تأخیر در بهبود یا تشکیل اسکارهای بیش از حد شود. این پروژه با بهره‌گیری از فناوری نانو، راهکارهایی را برای تأثیرگذاری بر مراحل مختلف بهبود زخم توسعه داده است تا فرآیند ترمیم به سمت بازسازی هدایت شود.

فناوری نانو این امکان را فراهم می‌کند که عوامل شیمیایی و فیزیکی مختلفی برای تسریع فرآیند بهبود زخم و جلوگیری از تشکیل اسکار دستکاری شوند. در این پروژه، از دو محرک برای ساخت بایوسنسورهای رنگی و درمانی (ترانُستیک) استفاده شد. این بایوسنسورها حاوی یک رنگ همی‌سیانین هستند که در حضور لیپاز باکتریایی تغییر رنگ می‌دهند و امکان تشخیص سریع و قابل مشاهده حضور باکتری را فراهم می‌کنند. بخش درمانی این بایوسنسورها شامل نانوذراتی است که به‌طور انتخابی در حضور گونه‌های فعال اکسیژن آزادسازی عوامل ضدباکتریایی را انجام می‌دهند. این آزادسازی هدفمند می‌تواند نفوذ سلول‌های ایمنی به محل زخم را کاهش داده و التهاب طولانی‌مدت را که یکی از عوامل اصلی تأخیر در بهبود و ایجاد اسکار است، کنترل کند.

علاوه بر این، نانوذرات جامد لیپیدی برای انتقال هدفمند داروهای ضد اسکار طراحی شدند. این سیستم انتقال دارو به‌گونه‌ای طراحی شد که دارو را در مراحل اولیه تشکیل اسکار آزاد کند؛ چرا که آزادسازی زودهنگام یا دیرهنگام می‌تواند فرآیند طبیعی بهبود را مختل کند. از آنجا که داروهای ضد اسکار اغلب اثرات مخربی دارند، زمان‌بندی در اثربخشی آن‌ها بسیار حیاتی است. برای این منظور یک نشانگر زیستی که به‌طور اختصاصی در مرحله تشکیل اسکار بیش‌بیان می‌شود، شناسایی شد و نانوذرات با لیگاندی برای هدف‌گیری این نشانگر بارگذاری شدند. به‌منظور جلوگیری از آزادسازی زودهنگام دارو، یک پروتئین قفس‌مانند استخراج و برای پوشش‌دهی نانوذرات استفاده شد تا پایداری آن‌ها تا زمان آزادسازی مورد نظر تضمین شود.

این پایان‌نامه نشان داد:

تشخیص موفق باکتری‌ها در غلظت‌های پایین؛

حذف هدفمند باکتری‌ها به‌طور اختصاصی در حضور گونه‌های فعال اکسیژن در غلظت های بالا و پایین باکتریایی مؤثر بود ؛

انتقال دقیق داروهای ضد اسکار به سلول‌هایی با بیان بالای فاکتور رشد بافت همبند که یک نشانگر زیستی خاص مرحله تشکیل اسکار است.

این راهکارها با هدف تأثیرگذاری بر مراحل مختلف بهبود زخم طراحی شدند تا فرآیند ترمیم را تسریع کرده واز تشکیل اسکار جلوگیری کنند. با این حال، آزمایش‌های بیشتر در مدل‌های *بالینی*قدم بعدی مهمی برای تأیید پتانسیل بالینی این روش‌ها خواهد بود.

DEDICATION

This thesis is dedicated to all women: to those who have fought so that I could stand here today, and to those who have struggled to ensure we have a rightful place in society, access to education, and the opportunity to pursue advanced knowledge. It is a tribute to the women throughout history who have devoted themselves to forging a path for future generations, enabling us to become who we are today. I dedicate this work to the women who have always shouldered multiple roles, balancing countless responsibilities while steadfastly striving toward their dreams.

This is for all women, with the hope that one day, everywhere, the ideals of "women, life, and freedom" will prevail.

زن

زندگی

آزادی

ACKNOWLEDGMENTS

I would like to express my deepest gratitude to my advisor, Dr. Song Liu, for his invaluable support and guidance throughout this research. His supervision and insightful advice have been instrumental in making this dissertation possible. From the day I joined his lab, he emphasized, "*I see you as a colleague, not a student*," a sentiment that meant so much to me. His unwavering support and trust over the years have not only shaped my academic journey but also fostered my personal growth.

Dr. Liu's mentorship provided me with incredible opportunities, including collaborating with major companies and startups, teaching, and supervising students. These experiences have greatly enriched my professional development, helping me clarify my future path and goals. This journey has been deeply rewarding, and I truly could not have completed it without his guidance. Words cannot fully express my appreciation, but I hope this dissertation reflects the gratitude I hold for his mentorship and support.

I am also sincerely grateful to my committee members, Dr. Sarvesh Logsetty and Dr. Franca Rodrigo, for their valuable input and suggestions, which strengthened this work.

This research would not have been accomplished without access to various labs across campuses, and I am thankful for our collaborators who welcomed me into their facilities, particularly Dr. Lin, Dr. Miller, Dr. Budisa, Dr. Bandera and Dr. Raouf. I am also deeply appreciative of the support and assistance provided by Dr. Yang Liu, Dr. Yathindranath, Dr. Heidari, and Mr. Balko throughout this journey.

I would like to extend my gratitude to the undergraduate students who contributed at different stages of the projects presented here, including Ms. Vyas, Mr. Boticki, and Mr. Olapade. My colleagues and friends in the Biomaterial Synthesis and Surface Engineering Lab,

deserve special thanks, particularly Ms. Sarah Currie, Dr. Changning Yu, Mrs. Mahamuda Sultana, and Mr. Quintin Litke.

Numerous collaborations have enriched my Ph.D. journey, and I am thankful for the professional network, connections, and friendships that have supported my growth. In particular, I am deeply grateful for the support of Dr. Maurice Huff, Mrs. Chelsea Laxuren, and Mr. Derby Whitfield, who have been outstanding sources of encouragement and assistance.

I gratefully acknowledge the financial support for this work from the Natural Sciences and Engineering Research Council of Canada (NSERC) Discovery Grant (Grant no. RGPIN/04922-2014), MITACS, UMGF, and GETS.

Finally, my heartfelt thanks go to my parents and my little sister. Their unwavering support and sacrifices have made this journey possible, and there are no words to express how grateful I am for their love and encouragement, which have helped me become the first one in my family to finish this path.

در نهایت، عمیق‌ترین سپاس خود را تقدیم والدین عزیزم و خواهر کوچکم می‌کنم. حمایت بی‌دریغ، فداکاری‌ها و عشق بی‌قید و شرط آن‌ها پایه و اساس این مسیر بوده است. هیچ کلمه‌ای نمی‌تواند قدردانی من را برای تشویق‌های همیشگی‌شان بیان کند؛ تشویق‌هایی که باعث شد بتوانم به عنوان اولین نفر در خانواده‌ام به این نقطه برسم.

DECLARATION OF ACADEMIC ACHIEVEMENTS

I, Farinaz Jonidi Shariatzadeh, hereby declare that this thesis is my original work, completed to fulfill the requirements for the PhD degree in the Department of Biomedical Engineering at the University of Manitoba. All experiments presented herein were conducted between September 2019 and December 2024 in compliance with the research policies and procedures of the University of Manitoba.

This dissertation comprises three published, peer-reviewed journal papers and one unpublished manuscript, in all of which I am the first author and primary contributor under the supervision of Dr. Song Liu. To the best of my knowledge, the content of this thesis does not infringe upon any copyright and has not been submitted or published previously for the award of any other academic degree or diploma.

The first-authored, peer-reviewed journal papers included in this thesis are as follows:

1. **Farinaz Jonidi Shariatzadeh**, Sarah Currie, Sarvesh Logsetty, Rae Spiwak, Song Liu, Enhancing wound healing and minimizing scarring: A comprehensive review of nanofiber technology in wound dressings, Progress in Materials Science, Volume 147,2025, https://doi.org/10.1016/j.pmatsci.2024.101350.
2. **Farinaz Jonidi Shariatzadeh**, Sarvesh Logsetty, and Song Liu, Ultrasensitive Nanofiber Biosensor: Rapid *In Situ* Chromatic Detection of Bacteria for Healthcare Innovation, ACS Applied Bio Materials, Volume 7 (4), 2024, DOI: 10.1021/acsabm.4c00038
3. **Farinaz Jonidi Shariatzadeh**, Vinith. Yathindranath, Yang Liu, Donald Miller, Francis Lin, Sarvesh Logsetty, Song Liu, Enhanced Targeted Drug Delivery for

Scar Prevention: Clathrin-Coated Solid Lipid Nanoparticles for Model Drug Encapsulation. Adv. Therap. Volume 7, 2024, https://doi.org/10.1002/adtp.202400185

Table of Contents

LIST OF TABLES

LIST OF FIGURES

1 Chapter 1: Introduction

1.1 Overview

As the body's largest organ, the skin has high regenerative capabilities. However, severe injuries make the wound healing process intricate and challenging. Various types of wounds, such as traumatic injuries, surgical incisions, and burns are widespread and carry significant implications for healthcare systems. In the United States alone, approximately 12 million traumatic wounds are treated annually in emergency rooms. Globally, around 250 million surgical incisions are performed each year, and 11 million severe burn cases require medical attention [1,2].

The healing processes of these wounds are diverse, often leading to scar formation. Burn scars, for example, can impact 30% to 95% of patients, depending on the wound depth and the total body surface area burned (TBSA). Scar formation can result in a range of complications, including functional impairments, psychological distress, and aesthetic concerns. The issue of scarring is a common concern among patients, even after routine surgical procedures, with many expressing a desire for improvements in the appearance of their scars [3].

Furthermore, scar formation imposes a substantial financial burden on healthcare systems. In the United States, over $20 billion is spent annually on treating and managing scars. The cost of treating scars is significantly higher than managing unscarred wounds, with expenses for burn-related scarring being 5.6 times greater. These costs encompass direct expenses, such as surgical interventions and pressure garment therapy, as well as indirect costs, such as lost productivity due to extended recovery periods [2].

Current scar management techniques, such as intralesional corticosteroid injections, pressure therapy, and laser therapy, provide some improvements but fail to restore skin to its pre-injury state. These methods are often accompanied by high recurrence rates and inconsistent

outcomes across individuals, underscoring the necessity for innovative solutions. Given the substantial financial, physical, and emotional burdens associated with scarring, the pressing need for effective scar prevention and management strategies is evident [4,5].

The problems around scar formation have led to a growing interest in advanced, engineered smart dressings and drug delivery systems, which hold significant promise for more effective scar prevention and treatment. These novel approaches could offer greater cost-effectiveness in the long term by reducing the need for repeated treatments and surgeries required to manage problematic scars, such as hypertrophic and keloid scars. The development and implementation of such advanced strategies are crucial for mitigating the significant impacts of scarring on patients and healthcare systems [6,7].

Recognizing that scars form due to collagen overexpression during the proliferative stage, driven by various factors such as wound size, depth, location, presence of infection, duration of the inflammatory stage, and individual differences, including sex, gender, and ethnicity [8,9], this project seeks to advance the development of technologies and smart wound dressings aimed at preventing scar formation through multiple pathways.

The strategies employed in this project focus on detecting and treating infections to minimize the inflammatory phase and reduce the presence of immune cells in the wound bed, which can delay healing and lead to scar formation [10–12]. Additionally, targeted delivery of anti-scar drugs to myofibroblasts aims to decrease collagen production during the critical scar formation period. In this chapter, we reviewed the relationship between infection and scar formation. Given that this project developed various smart wound dressings using electrospinning, each with different applications to reduce scar formation through distinct

pathways, the next chapter (Literature Review) explores the role of electrospun wound dressings in promoting accelerated, scar-free healing.

The following three chapters (Chapters 4, 5 and 6) will discuss each of the smart dressings or nanoparticles developed. Chapter 4, “Ultra-Sensitive Biosensor for Bacteria Detection” covers an infection-detecting wound dressing (biosensor). Chapter 5 “Antibacterial Biosensors for Early Detection and Elimination of Bacteria” includes theranostic wound dressing (biosensor) capable of both detecting and treating infections. Chapter 6, “Targeted Delivery of Anti-Scar Drug” focuses on responsive nanoparticles for the targeted delivery of anti-scar drugs. The ultimate goal of all the dressings is to facilitate accelerated wound healing without infection or scar formation, guiding the process toward regeneration.

1.2 Infection and Scar Formation

Different types of wounds, such as burns, surgical wounds, foot ulcers, and pressure ulcers, may vary in their pathological characteristics. Still all result in skin damage, compromising the body’s protective barrier and increasing vulnerability to external threats, including foreign microorganisms or even the skin’s microbiome [3]. Microbial infections in chronic wounds not only delay healing and cause scar formation but can also lead to more severe consequences, such as lower-limb amputation, reduced quality of life, and increased mortality rates [13].

It is important to note that the mere presence of foreign material or microorganisms does not necessarily lead to infection, as the body initiates an innate immune response as a key first step in wound healing. According to the International Wound Infection Institute, there are distinct stages in this process: contamination, colonization, critical colonization, and infection. Contamination occurs when microorganisms—originating from normal skin, the external

environment, or other parts of the body—are present in the wound but are not proliferating. The next stage, colonization, happens when the wound provides a conducive environment for microbial growth, though not enough to trigger an immune response. At this point, the microorganisms remain superficial and have not penetrated the deeper layers of the wound. As microorganisms begin to invade deeper tissue and cause damage, the wound reaches the stage of critical colonization, though physical symptoms may still not be apparent. When the immune system becomes fully engaged (microbial load around 10^5 CFU/g of tissue) and bacteria load exceeds 10^6 CFU/g accompanied by noticeable physical symptoms, the condition is classified as clinical infection when healing is impeded, and healthy tissues are also invaded by bacteria [14,15].

In other words, wound infection occurs when proliferating bacteria begin to invade the wound and damage the tissue, triggering a local or systemic host response. At this stage, medical interventions are necessary to help the host combat the infection. The body recognizes the presence of bacteria through pattern recognition receptors (PRRs), which detects conserved microbial components, known as pathogen-associated molecular patterns (PAMPs), or signals from damaged host cells, called damage-associated molecular patterns (DAMPs). This recognition initiates a series of biological processes, including the upregulation of chemokines that regulate immune and inflammatory responses, as well as the production of proinflammatory cytokines such as interleukins (IL-1, IL-6, IL-8, IL-12) and tumor necrosis factor-alpha (TNF-α). These cytokines act as chemoattractants, recruiting white blood cells, particularly polymorphonuclear leukocytes [16,17].

Neutrophils, a type of leukocyte, are the first responders, infiltrating the tissue within minutes of infection to clear bacteria and cellular debris. Macrophages also play a crucial role by

helping to eliminate bacteria and releasing growth factors and cytokines. If the innate immune defenses are bypassed, evaded, or overwhelmed, the adaptive immune system becomes involved. Failure to clear the invading microorganisms leads to microbial adhesion to host cells, rapid replication, and proliferation into soft tissues, causing localized inflammation and clinical infection. The presence of bacteria with a concentration higher than the critical infection threshold interferes with the healing process by prolonging the inflammatory phase [18,19].

The high concentration of immune cells at the wound site alters the healing trajectory, shifting the body into "survival mode." In response, the body overproduces collagen in an attempt to close the wound and prevent further microbial invasion, leading to scar formation [20]. Despite these efforts, some pathogens have developed mechanisms to breach host barriers, spread to deeper tissues, and potentially cause systemic infection.

Most infections at bacterial load higher than 10^6 CFU/g of tissue present visible symptoms such as inflammation (erythema, warmth, and swelling), pain, and purulence. However, in some cases, infections can develop without these signs. A delay in detecting infection allows bacteria time to form biofilms, which are exopolymer matrices composed of proteins, polysaccharides, and extracellular bacterial DNA. These biofilms adhere to various surfaces and cells, making it difficult for immune cells, such as neutrophils and macrophages, to penetrate and fight the bacteria. Within this biofilm niche, bacteria can reduce their metabolic activity, rendering them resistant to antibiotics. Once their metabolic activity increases again, they become more susceptible to antibiotics, but the dense structure of the biofilm slows down the penetration of therapeutic agents, reducing their effectiveness [16].

Biofilms also create additional advantages for bacteria. The high negative charge of the biofilm, due to the presence of acidic polysaccharides and DNA, can bind to positively charged

or neutralized antibiotics, further diminishing their efficacy. If multiple bacterial species are present within the biofilm, these protective features become even more vital. Although biofilms are microscopic, they cannot be observed with the naked eye as they form beneath the wound bed. Traditional diagnostic methods, such as wound sampling, are not only time-consuming but also less effective due to the strong attachment of biofilms to the wound matrix [16].

These factors significantly complicate the treatment of infections, leading to delayed healing or the development of chronic, non-healing wounds. Therefore, detecting bacteria before biofilm formation and the development of antibiotic resistance is critically important. It is estimated that antimicrobial resistance (AMR) contributed to 4.71 million deaths globally, with 1.14 million deaths directly attributable to bacterial AMR. In addition, wound infections affect a large number of people, with 6.5 million patients in the USA in 2009 alone and treatment costs exceeding $25 billion annually. Wound infections are also a major cause of antibiotic therapy and account for approximately 10% of hospital admissions in the USA. As a result, combating infection in its early stages is a crucial area of research [21,22].

Common therapies and practices for managing skin wound infections are centered around preventing bacterial growth, promoting healing, and reducing complications. These approaches can be divided into traditional treatments or advanced wound care techniques. The traditional treatments include Wound Cleaning and Debridement, Antibiotic Therapy (Topical Antibiotic and Systemic Antibiotics), using Antimicrobial Dressings and Antiseptic Solutions, Negative Pressure Wound Therapy (NPWT), and Hyperbaric Oxygen Therapy (HBOT). More advanced techniques involve using Nanotechnology, such as Antimicrobial Nanofibers and Nanoparticles, to combat infection [23].

1.3 Nanotechnology for Accelerated Wound Healing

Nanotechnology has become a versatile tool in the field of infection management, extending beyond its roles in prevention and treatment to play a critical part in detection. A range of nanotechnologies, including nanofibers and nanoparticles, serve multiple purposes, enabling both therapeutic and diagnostic applications. The increase in the utilisation of nanotechnology in the wound healing field is mainly due to nanomaterials' high surface area-to-volume ratio, which allows for enhanced signaling, increased interaction with biological agents, and an improved capacity for carrying antibacterial compounds [24].

Nanomaterials are commonly classified based on their composition, which includes four primary categories: carbon-based, inorganic, organic, and composite-based nanomaterials. Composite nanomaterials consist of a nanoscale phase combined with bulk materials, such as nanofibers, which are widely used for various biomedical applications [24].

In the context of infection detection, numerous biosensors utilize nanomaterials, including electrochemical and optical biosensors, though these often require complex designs and specialized detection and interpretation systems. This thesis, however, focuses specifically on nanomaterial-based colorimetric biosensors, which offer a simpler, more accessible means of identifying bacterial infections *in situ* or at the point of care. Colorimetric biosensors operate on a principle where the occurrence of a specific chemical reaction induces a color change, indicating the presence of a targeted pathogen or stimulus.

Effective bacterial detection via nanomaterials depends on several critical factors, including selectivity, sensitivity, reproducibility, and accuracy. In this regard, metallic nanoparticles have shown significant promise in infection detection; however, they typically require sampling and subsequent analysis to yield results, making them less suited for *in situ*

colorimetric detection [25]. The stated shortages have led to increased interest in paper-based nanobiosensors, which provide a more user-friendly and immediate visual detection method.

Nanofibers, in particular, are well-suited to these applications. By incorporating chromogenic probes, nanofibers can respond to external stimuli that change in the presence of bacteria—such as pH, temperature, enzymes, or toxins—resulting in a visible color shift that signals an infection. Nonetheless, one of the main limitations of colorimetric nanofiber-based biosensors is the potential for false positives. Addressing this issue, along with improving sensitivity, requires a thorough understanding of the interactions between the stimulus and the chromogenic probe to enhance the biosensor's reliability and accuracy [26].

In the therapeutic field, nanomaterials offer diverse approaches to infection treatment. An ideal nanocarrier for antibacterial applications must be biocompatible, non-immunogenic, and capable of controlled drug release. Various nanomaterials, such as nanoemulsions, polymeric nanoparticles, metallic nanoparticles, carbon-based nanoparticles, nanogels, and nanofibers, are used as delivery systems for antibacterial agents. Recently, interest has grown in responsive nanoparticles, which can selectively release drugs or antibacterial agents only in the presence of pathogenic bacteria, enhancing treatment precision and reducing side effects [27,28]. Despite their advantages, nanoparticles—particularly metallic ones—pose challenges due to uncertainties surrounding their behavior and degradation within the body. The safety concerns of nanoparticles have raised concerns about their long-term safety and accumulation in tissues, which is a crucial consideration for medical applications [29]. Therefore, there has been an increased focus on developing responsive degradable polymeric or lipid-based nanoparticles for use as nanocarriers for various antibacterial agents.

The aim of this chapter is to emphasize the relationship between infection and scar formation. Achieving scarless healing requires both the detection and prevention of infection, which are as crucial as the delivery of anti-scar therapies during the healing process. As discussed earlier, the presence of bacteria prolongs the inflammatory stage, creating a hypoxic and nutrient-deficient environment. The bacteria's presence leads to competition for resources between the patient's cells and bacteria, placing the body in a survival mode. Consequently, this not only delays wound healing but also increases the likelihood of scar formation [11,30]. Studies have demonstrated that the duration of the inflammatory stage, which is directly influenced by the presence of bacteria and infection, significantly impacts the amount of scar tissue formed at the end of the healing process. This effect arises from the activation of fibroblast cells during inflammation, which results in the overexpression of irregularly organized collagen [10].

With these factors in mind, this thesis aims to address various challenges in wound healing that can delay recovery and contribute to scar formation. The objective is to develop smart dressings and nanoparticles designed to accelerate healing by either detecting and preventing infection or enabling the targeted delivery of anti-scar drugs. The following chapter provides information on different nanofibrous wound dressings employed to promote accelerated and scarless healing. Chapter three discusses various hypothesis and objectives utilized in this thesis to develop the dressings and nanoparticles. The next three chapters, chapters 4 – 6, cover research papers to fulfill each objective.

2 Chapter 2: Literature Review

Enhancing Wound Healing and Minimizing Scarring: A Comprehensive Review of Nanofiber Technology in Wound Dressings

*Farinaz Jonidi Shariatzadeh, Sarah Currie, Sarvesh Logsetty, Rae Spiwak and Song Liu**

F.J. Shariatzadeh, Eng., Biomedical Engineering, Faculty of Engineering, University of Manitoba, Manitoba Winnipeg, Canada
S. Currie, Eng., Department of Biosystems Engineering, Faculty of Agriculture and Food Sciences, University of Manitoba, Winnipeg, Canada
R. Spiwak, Prof., Department of Surgery, Rady Faculty of Health Sciences, University of Manitoba, Winnipeg R3T 2N2, Canada
S. Logsetty, Prof., Departments of Surgery and Psychiatry, Rady Faculty of Health Sciences, University of Manitoba, Winnipeg R3T 2N2, Canada
S. Liu, Prof. Department of Biosystems Engineering, Faculty of Agriculture and Food Sciences, University of Manitoba, Winnipeg R3T 2N2, Canada. Song.liu@umanitoba.ca
* Corresponding Author

Revised from the review article published in Progress in Materials Science, Volume 147, 2025, 101350, ISSN 0079-6425, https://doi.org/10.1016/j.pmatsci.2024.101350. (https://www.sciencedirect.com/science/article/pii/S0079642524001191)

Contribution as the first author: **Farinaz Jonidi Shariatzadeh:** Writing – review & editing, Writing – original draft, Visualization, Methodology, Formal analysis, Conceptualization

Abstract:

Wound healing is a complex biological process that, when impaired, can lead to the formation of scars. Electrospun nanofibrous wound dressings have emerged as a promising option for promoting scar-free wound healing. This paper explores the complex role of physical, compositional, and chemical cues, each contributing to the remarkable healing potential of these wound dressings. The physical properties of these dressings, such as porosity and mechanical characteristics, can guide cellular behaviors and promote vascularization, fostering a conducive environment for reduced scarring. Furthermore, the integration of natural polymers that mimic the skin's extracellular matrix, known as compositional cues, adds another layer of complexity to these wound dressings. As chemical cues, therapeutic agents have demonstrated their potential to combat chronic wound scenarios leading to scar formation. However, achieving the desired therapeutic effect hinges on the nature of these agents and their controlled release. Therefore, the paper also delves into various loading techniques for tailoring the release profiles of these bioactive agents. Although electrospun nanofibrous wound dressings are promising as wound dressings, a viable commercial product remains elusive. This gap can be attributed to a lack of comprehensive *in vivo* studies, particularly in animal models that mimic human wound healing.

Keywords: Nanofibrous wound dressing, physical cues, compositional cues, chemical cues, drug loading, drug release, electrospinning, scar

2.1 Introduction

Despite significant advancements in skin tissue engineering, achieving a reproducible, cost-effective, non-invasive, clinically acceptable, and approved treatment for scarless wound healing remains elusive for severe wounds such as burns, chronic wounds, and diabetic ulcers. Scars, along with their associated sequelae, such as skin discoloration, reduced skin strength and itching, can have significant adverse effects on a patient's overall well-being, social life, and even financial situation [31–33]. Wound healing in severe and chronic wounds involves highly complex cascades of events and pathways. Accordingly, extensive research has explored a range of methods and materials to achieve scarless healing, with the aim of enhancing wound healing outcomes [34–36]. Several reviews have focused on biological pathways of scarless wound healing and engineered scaffolds for anti-scar wound healing [31,37–40] or post-healing methods to reduce the size of formed scars [41,42]. However, there is no systematic review on the role of nanofibrous wound dressings in scarless wound healing. This article aims to shed some light on the role of nanofibers in the scarless wound healing procedure.

The review provides an introductory overview of the wound healing process, including scar formation, and explores the potential of nanofibers to enhance wound healing outcomes. The benefits of nanofibers as a skin substitute or dressing are discussed, with emphasis on the physical, composition, and chemical cues that contribute to accelerated and scarless healing. Additionally, the review critically analyzes various mechanisms for loading therapeutic agents into nanofibers, with a focus on understanding how these methods influence the release kinetics of the drugs.

2.2 Skin Structure and Physiology

Skin, as the largest organ of the human body, comprises three distinct layers: the epidermis (superficial layer), dermis (intermediate layer), and the hypodermis, which is a subcutaneous layer enriched with adipose tissue. The skin's complex architecture contains specialized cells, rendering it a multilayered organ of paramount importance [43].

2.2.1 Epidermis

The epidermis, originating from the ectodermal layer during embryonic development, is characterized by a stratified architecture including five distinct layers: the stratum basale, stratum spinosum), stratum granulosum, stratum lucidum, and the outermost stratum corneum [44]. The thickness of these epidermal layers varies depending on anatomical location, with measurements ranging from 75 to 150 microns under typical conditions and escalating up to 0.6 mm in areas of increased mechanical stress, such as the palmar regions of the hands [43]. Notably, the epidermis remains an integral site housing essential appendages, including hair follicles, sweat glands (eccrine and apocrine), and sebaceous glands [45]. These appendages not only contribute to the overall physiological functions of the skin but also introduce variations in the epidermal landscape, reflecting its dynamic nature across different anatomical regions.

From a cellular perspective, the epidermis primarily consists of a stratified squamous epithelium characterized by densely packed cells undergoing continual mitotic activity. Notably, upon each quartile of cell division, a single cell remains within the epidermal layer for subsequent divisions, while the remaining three cells undergo differentiation into keratinocytes. These keratinocytes are responsible for synthesizing keratin, the predominant structural protein of the epidermis [46].

Molecularly, keratin exhibits a helical conformation, organizing into an intricate basket-like network. This network facilitates intracellular communication, linking nucleolar structures with the cytoplasm, thus contributing to the formation of the cellular cytoskeleton [45]. Functionally, keratinocytes play pivotal roles in tissue repair mechanisms, notably through the secretion of cytokines.

Cytokines, bioactive molecules, primarily act as chemical messengers, binding to specific receptors on target cells to modulate their physiological activities. Their versatile roles comprise inflammation, immunoregulation, cellular growth, and tissue repair. Noteworthy sources of these cytokines include not only epidermal cells but also various immune cells, such as leukocytes, mast cells, and vascular endothelial cells. Disturbances such as injury, infections, or ultraviolet radiation can significantly influence cytokine production, thereby allowing keratinocytes to orchestrate cellular responses for repair or regeneration. Prominent cytokines includes interleukins (IL-1, IL-2, IL-3, IL-6, IL-8), interferons (α, β, γ), tumor growth factors (α, β), and platelet activators. Additionally, during injury responses, keratinocytes secrete an array of bioactive molecules, including growth factors, chemokines, interferons, prostaglandins, and leukotrienes, further underscoring their pivotal role in wound healing [46].

Within the epidermal layer, a variety of specialized cells, distinct from keratinocytes, are integral constituents, including melanocytes, Merkel cells, and Langerhans cells, each endowed with specific functional roles [47]. Melanocytes, positioned within the basal layer of the epidermis, are responsible for cutaneous pigmentation through the synthesis and distribution of melanin. This pigment not only provides the characteristic hue of the skin but also serves protective roles against ultraviolet radiation [43,47]. Merkel cells, constituting a minor fraction, approximately less than 1%, of the total epidermal cellular population, are specialized

mechanoreceptor cells [43,47]. Langerhans cells, dendritic cells interspersed within the epidermal layers, play a key role in the skin's immunological defense mechanisms. Functioning as antigen-presenting cells, Langerhans cells facilitate immune surveillance, capturing antigens and subsequently presenting them to T lymphocytes, thereby orchestrating cutaneous immune responses and maintaining tissue homeostasis [43,47].

2.2.2 Basement Layer

The interface between the epidermal and dermal layers is established by a specialized basement membrane. This semi-permeable extracellular matrix structure governs the selective exchange of molecules between these two layers. This basement membrane not only provides structural support but also facilitates complex cellular interactions and signaling mechanisms essential for skin homeostasis [47]. Comprising a complex composition of macromolecules, the basement membrane is rich in proteins with specific functionalities. Noteworthy components of this matrix include fibronectin, which plays a critical role in cellular adhesion and migration processes, thereby ensuring structural integrity and cohesion between distinct layers of the skin. During the process of wound healing, fibronectin plays a dynamic role as a temporary matrix, orchestrating a series of cellular events essential for tissue regeneration and re-epithelialization. Specifically, fibronectin facilitates cellular migration by providing a substrate for cell attachment and spreading, thereby enabling the coordinated movement of cells toward the site of injury. Additionally, fibronectin mediates chemotactic responses, guiding cells to the wound bed and facilitating their integration into the repairing tissue architecture [43].

In addition to fibronectin, the presence of nonfibrillar collagen imparts tensile strength and structural integrity to this membrane. Laminin, a multifunctional glycoprotein, functions as a key adhesive molecule, mediating cellular interactions and contributing to the basement

membrane's overall stability. Furthermore, heparan sulfate proteoglycans, with their unique glycosaminoglycan chains, participate in modulating molecular transport and signaling events across the epidermal-dermal interface. These components synergistically coordinate the physiological interactions between the epidermis and dermis, thereby ensuring the skin's functional integrity and resilience [43].

2.2.3 Dermis

Beneath the basement layer lies the dermis, originating embryologically from the mesodermal germ layer. The dermal layer exhibits a thickness ranging from 2 to 4 mm, surpassing the dimensions of its overlying epidermal layer. The dermis exhibits a cellular composition distinct from the epidermis, predominantly populated by fibroblasts, albeit in reduced numbers relative to the epidermis cells [43]. The dermal matrix is characterized by a complex vascular network, facilitating nutrient exchange, waste removal, and thermoregulatory functions. Morphologically, the dermis is categorized into two discernible layers: the papillary dermis and the reticular dermis. The papillary dermis, located proximally below the epidermis, serves as an anchoring zone, ensuring structural cohesion between the epidermal and dermal layers. The second layer, the reticular dermis, deeper in location, forms a robust connective interface with the underlying hypodermal layer, providing structural support and facilitating mechanical resilience [43]. Fibroblasts represent a predominant cellular constituent within the dermal layer of the skin. Originating from mesenchymal progenitors, fibroblasts play a central role in maintaining dermal homeostasis and orchestrating extracellular matrix (ECM) synthesis and remodeling. These mesenchymal cells are pivotal in secreting structural proteins such as collagen, elastin, and fibronectin, thereby contributing to the dermis's structural integrity, tensile strength, and elasticity [47].

Moreover, upon injuries, fibroblasts within the dermal layer undergo activation, transitioning into an active synthetic phenotype known as myofibroblasts. This activated state prompts fibroblasts to synthesize and secrete an array of ECM components, such as collagen fibers and elastin. Such repairing processes are pivotal for preserving the structural and functional integrity of the skin, ensuring optimal tissue repair and regeneration post-injury [43].

Collagen, a structural protein, exhibits remarkable tensile strength owing to its intricate fibrous architecture. It originates as procollagen, a preliminary molecule that fibroblasts secrete into the ECM. After this secretion, procollagen is enzymatically cleaved by specific proteases that cleave collagen propeptide regions, enabling the collagen fibers to mature. These fibers then form into polymerized tropocollagen helices, notable for their covalent cross-links. This structure provides strength and elasticity to the skin's matrix. In terms of amino acid composition, collagen predominantly comprises glycine, proline, and hydroxyproline residues, which give the collagen unique structural and functional characteristics [43,45]. Within the dermal layer, collagen predominantly exists in two isoforms: collagen type I, constituting approximately 80% of the total collagen content, and collagen type III. Following dermal injury or trauma, the dynamic equilibrium between these collagen types undergoes modulation, triggering a transient elevation in collagen type III synthesis. This alteration in collagen composition serves as a repair mechanism, facilitating wound healing and tissue regeneration. However, as the tissue enters the remodeling phase, homeostatic mechanisms regulate collagen turnover, restoring the physiological balance between collagen type I and type III isoforms, thereby preserving the structural and functional integrity of the dermal matrix [43].

Elastin, synthesized and secreted by dermal fibroblasts, stands as a pivotal protein within ECM, providing skin tissue with its inherent elasticity and resilience. Structurally, elastin adopts

a coil-like conformation composed of amino acid residues such as alanine, valine, glycine, and proline. This elastomeric protein plays a critical role in mitigating mechanical stresses associated with routine cutaneous activities, such as movements like sitting and bending [43,45,47]. Additional elastic fibers in the dermal layer are oxytalan and elaunin.

Additionally, the dermal layer contains a diverse array of proteoglycans, macromolecules characterized by polysaccharide chains covalently linked to a protein core. Remarkably hydrophilic in nature, proteoglycans possess the capacity to trap water molecules, exhibiting a water-binding capacity extending up to 1,000 times their molecular volume, resulting in the formation of an aqueous gel-like matrix. Predominant glycosaminoglycans within this matrix consist of hyaluronic acid, chondroitin sulfate, dermatan sulfate, and heparan sulfate. These hydrated substances play a pivotal role in modulating tissue hydration, thereby facilitating metabolic processes and cellular functions such as migration, adhesion, and differentiation. Notably, these structural and functional proteins and molecules exhibit an increased concentration within the papillary dermal layer, underscoring their critical role in maintaining dermal integrity, resilience, and homeostasis [43]. Another crucial part of the dermal matrix is fibronectin, a multifunctional glycoprotein integral to various cellular processes and structural interactions within the skin's microenvironment.

Within the cellular landscape of the dermal layer, beyond the predominant fibroblasts, a diverse array of immune and connective tissue cells populate this matrix, such as mast cells, macrophages (wandering histiocytes), and lymphocytes. These cells contribute to the dermis' structural integrity and immunological surveillance. [45]. Mast cells, strategically positioned proximate to blood vessels at the epidermal-dermal junction, are high-affinity receptors for immunoglobulin E (IgE), and they play a critical role in allergic responses and immediate

hypersensitivity reactions [43,47]. Connective tissue macrophages, also referred to as wandering histiocytes, derive from circulating blood monocytes and predominantly inhabit the papillary dermis. Renowned for their phagocytic capabilities, these macrophages play pivotal roles in tissue homeostasis, immune surveillance, and the resolution of inflammation [43]. Furthermore, lymphocytes, instrumental in orchestrating immune responses within the skin, predominantly inhabit the dermal layer, constituting approximately 98% of the total skin lymphocytic population. Comprising both helper and suppressor T lymphocyte subsets, these cells actively participate in immune surveillance, neoplastic surveillance, and immunoregulatory functions. Notably, a substantial fraction of these dermal T cells localize proximally around postcapillary venules, facilitating their strategic positioning to respond promptly to immunological challenges and maintain cutaneous homeostasis [43,47].

2.2.4 Hypodermis

The hypodermis, the deepest layer under the dermal stratum, comprises a matrix of loose connective tissue that serves central roles in supporting, anchoring, and insulating the skin from underlying anatomical structures. This subcutaneous layer is characterized by a heterogeneous cellular composition, including adipocytes, fibroblasts, and macrophages, each contributing distinct functionalities to the hypodermal microenvironment [43,44]. Notably, the hypodermis provides an extensive vascular and nerve network, facilitating nutrient supply, waste removal, thermoregulatory processes, and sensory perception. A noteworthy feature of the hypodermis is its significant lipid reservoir, housing approximately half of the body's total adipose stores, thereby playing a pivotal role in energy metabolism and thermal regulation [43,45].

2.2.5 Skin Functionality

The diverse functionality of the skin is instrumental in preserving physiological homeostasis, including a myriad of roles including, but not limited to, barrier protection, immunological surveillance, sensory perception, thermoregulation, and metabolic and biochemical processes. The complexity of these functions highlights the criticality of maintaining skin integrity to safeguard internal homeostatic equilibrium [43,48]. Albeit its inherent resilience, the skin is susceptible to an array of damages that can compromise its structural and functional integrity. Various factors, including traumatic injuries (such as surgery and burns), systemic conditions (like ischemic-reperfusion injuries), or infections, can disrupt skin barrier function [43].

Such breaches in the skin barrier pose a significant risk, facilitating the entrance of pathogens and potential contaminants, thereby escalating the susceptibility to infections and complications. Consequently, understanding the details of the wound healing process becomes imperative, elucidating the sequential phases of hemostasis, inflammation, proliferation, and remodeling and their respective physiological. A comprehensive understanding of these healing stages is pivotal for evaluating potential impediments to complete wound healing and skin regeneration or the tendency to scar formation. The following section delves into a detailed exploration of the wound healing cascade, meticulously dissecting the complex interplay between cellular, molecular, and systemic factors that orchestrate both the restoration of tissue integrity and the subsequent process of scar maturation.

2.3 Skin Wound Healing and Scar Formation

One of the main responsibilities of the skin is to serve as a protective barrier against external threats, regulate temperature, and prevent water loss [49]. When the skin sustains

damage from external insults or is compromised due to immune system dysregulation, it can lead to the formation of wounds, which may manifest as either acute or chronic in nature [50]. The body addresses such cutaneous damage via the mechanism of wound healing. Nevertheless, deviations or interruptions in this sophisticated repairing process at any phase may result in scar formation rather than achieving complete skin regeneration. Wound healing can be categorized into four main stages: hemostasis, inflammation, proliferation, and remodeling. Each stage involves distinct pathways, cells, and biomolecules contributing to subsequent steps and overall healing, which may also overlap [51,52]- **Figure 2-1A**.

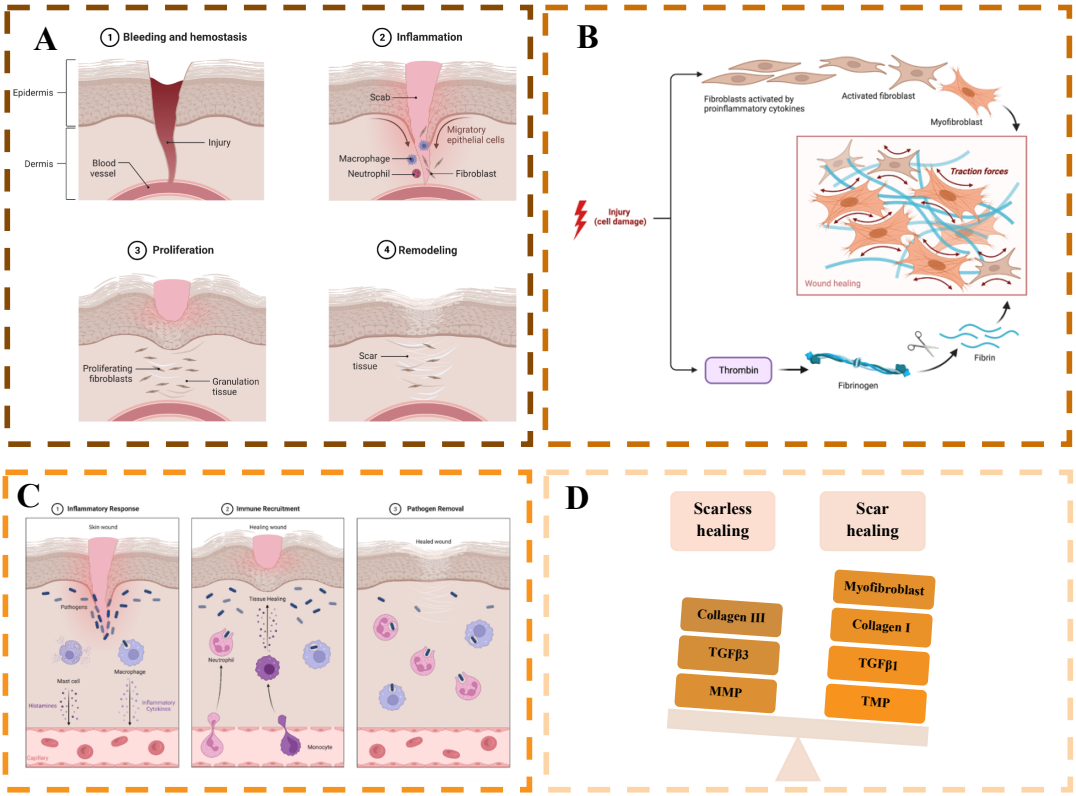

Figure 2-1 A) Overview of the sequential stages of wound healing:

Hemostasis, Inflammation, Proliferation, and Remodeling, along with their corresponding timeline. B) Impact of fibrin expression on the differentiation of fibroblasts into myofibroblasts. C) Role of the inflammatory stage in the healing process, emphasizing its function in eliminating pathogens from the wound. And D) Key distinctions between scar-based healing and scar-free healing, TIMP (tissue inhibitor of metalloproteinase).

2.3.1 Hemostasis

Hemostasis begins within seconds and continues for a few hours [53]. This process is a three-phase procedure beginning with vasoconstriction. Initially, vascular contraction is driven by endothelin from the injured endothelium, along with catecholamines, prostaglandins, and platelet-derived growth factor (PDGF), which influence muscle contraction but are insufficient for lasting bleeding control, **Figure 2-1 B**. The second phase (primary hemostasis phase) involves a coagulation cascade triggered by various biochemical mediators and marked by significant platelet activity in clot formation [54,55]. In healthy skin, the endothelial layer prevents thrombosis through secretions of heparin-like glycosaminoglycans. However, injury exposes thrombogenic layers, leading to platelet adhesion and activation. This activation alters platelet morphology and increases adhesion, with platelets releasing numerous substances that facilitate aggregation and adherence to components such as fibrinogen, fibronectin, von Willebrand factor (vWF), and collagen via the RGD sequences [54,56–58]. The platelet plug maturation occurs in the secondary hemostasis phase. The plug enriched with growth factors, including PDGF, transforming growth factor (TGF), epidermal growth factor (EGF), and insulin-like growth factor (IGF), is essential to both hemostasis and healing stages. These growth factors serve dual roles; while they are vital during the hemostatic phase, they also play pivotal roles in the following healing stages [54]. Their influence extends to cell types, such as fibroblasts, endothelial cells, smooth muscle cells, and monocytes. This phase features the activation of coagulant factors, transforming fibrinogen into a fibrin network that integrates with the platelet plug, forming a thrombus. This thrombus not only serves a hemostatic function but also acts as a scaffold for tissue repair and healing [54].

It is imperative to recognize potential consequences regarding scar formation during this hemostatic phase. The formation of an excessively dense initial clot or increased fibrin expression may inadvertently obstruct blood circulation, attenuating oxygen supply to the wound site and compromising the subsequent healing trajectory. Such impediments can cause the tissue to form scars. Furthermore, the disproportionate accumulation of fibrin during this phase exerts downstream effects on collagen synthesis in the subsequent stages, given the role of fibrin as a collagen precursor. This dysregulation accentuates the propensity for scar formation.

2.3.2 Inflammation

In the wound healing sequence, inflammation follows hemostasis, serving to counter infections and eliminate debris (**Figure 2-1C**). In the inflammation stage, which starts from day one and can last up to a week [53], different bioactive molecules are secreted, such as PDGF, TGF, interleukin (IL), and tumor necrosis factor (TNF), that are crucial in tissue development during later proliferation and remodeling stages [59,60]. This phase is marked by the recruitment of various immune cells, initiated by damage-associated molecular patterns (DAMPs) and other mediators and involves various cell types, including neutrophils, macrophages, mast cells, dendritic cells, and T-cells [54,61,62].

Neutrophils act as initial responders, protecting against external threats and facilitating tissue remodeling. Neutrophils possess antibacterial granules containing proteases. These proteases play a dual role: they combat bacteria and facilitate tissue remodeling. Specifically, proteases degrade the ECM and basement membrane, creating a passage for neutrophil migration from blood vessels into the injury site. Furthermore, proteases activate matrix metalloproteinases (MMPs), which are crucial for skin regeneration during wound healing. Dysregulation of MMP activity contributes significantly to scar formation [54,63–66]. As the wound healing progresses,

macrophages eventually replace neutrophils at the injury site. Effective neutrophil clearance, either through apoptosis, necrosis, or efferocytosis, is pivotal. Ineffective neutrophil clearance can elevate pro-inflammatory and cytotoxic molecules within the injured area, worsening the tissue damage. This clearance mechanism is paramount for initiating the resolution of the inflammatory phase. Prolonged neutrophil retention at the wound site can precipitate chronic inflammation, increasing the likelihood of scar formation. Macrophages, following neutrophils, contribute to both antimicrobial activities and the resolution of inflammation. The M1 macrophages eliminate bacteria via phagocytosis and promote MMP production, facilitating their mobility and aiding in skin regeneration. Moreover, M1 plays a role in the clearance of neutrophils and resolution of the inflammation stage. Upon fulfilling their primary role of neutrophil clearance, macrophages undergo a phenotypic shift to an anti-inflammatory state named M2. M2 macrophages contribute to angiogenesis and vascular genesis. Additionally, M2 macrophages communicate with fibroblasts, fostering their differentiation into myofibroblasts, thereby enhancing collagen synthesis and α-smooth muscle actin expression crucial for tissue integrity. However, once their roles in fibrosis and angiogenesis are executed, macrophages revert to a phagocytic state, eliminating the wound site of excessive cells and matrix components via phagocytosis and protease release, respectively. Disruptions in this phenotypic transition can influence scar formation due to increased collagen and ECM production. Notably, an imbalance in the population of pro-inflammatory macrophages, whether due to overabundance or scarcity, escalates the likelihood of scar tissue development. Furthermore, alterations or hindrances in macrophage interactions with cells like fibroblasts or T-cells can intensify scar formation, emphasizing the balance and coordination required for optimal wound healing [54,67].

Mast cells, involved in initial healing phases, release enzymes and histamine, aiding in re-epithelialization and wound contraction [68–72]. Some studies indicate that depleting mast cells during wound healing can result in hypertrophic scar formation. On the other hand, during scar formation, there's a marked increase in mast cell numbers, underscoring their complex role in tissue repair and scar formation, which requires more investigation [73,74].

Dendritic cells, primarily antigen-presenting cells, are vital for initiating T-cell responses and influencing the healing process [75]. T-cells, present in various subtypes, play a significant role in modulating re-epithelialization processes through cytokine and growth factor secretion. Upon injury, damaged keratinocytes respond by upregulating the expression of specific ligands that stimulate T-cell activation. Within the injury site, T-cells undergo morphological alterations, transitioning from a dendritic morphology to a rounded configuration. Then, they initiate the secretion of growth factors such as keratinocyte growth factor and IGF, which are pivotal for regulating keratinocyte proliferation. The absence or diminished presence of these T-cells can potentially hinder wound healing. The increased mechanical force that happens due to contraction during wound healing can cause abnormalities in the function of T-cells or surge their numbers, leading to scar formation [54].

Building upon our detailed exploration, it is crucial to acknowledge that diverse factors influencing this stage can exert deleterious effects on wound healing, potentially culminating in aberrant scar formation [76]. For example, excessive activation of immune cells (notably macrophages) can lead to the over-secretion of growth factors, resulting in an abundance of blood vessels and an excessive expression of collagen, all contributing to scar formation. Furthermore, during this stage, there is an increase in the production of reactive oxygen species (ROS), which contribute to tissue damage. Pro-inflammatory cytokines further impair the

healing process and elevate the likelihood of scar formation. Additionally, chronic inflammation can increase the activation of myofibroblasts, the primary culprits behind scar formation, through excessive collagen expression. Consequently, even a seemly inconsequential perturbation during this critical phase, manifesting as a protracted inflammatory response, substantially elevates the risk of pathological scar formation at the expense of complete skin regeneration.

2.3.3 Proliferation

The proliferation phase of wound healing includes a series of events, each vital for efficient tissue repair. In normal wound healing, the proliferation stage begins around day 4 (during mid-inflammation) and can extend up to three weeks [53]. This stage is characterized by simultaneous processes such as the development of granulation tissue, re-epithelialization, neovascularization, and immunomodulation [54]. In this section, we delve into these processes by examining the cells involved at each stage.

Granulation tissue serves as a temporary scaffold for cells involved in the healing process. This tissue is primarily constituted by activated fibroblasts, which lay down a temporary ECM. Subsequently, this matrix requires replacement with a more mature ECM during the remodeling phase. Granulation tissue formation necessitates vascularization to support essential processes like nutrient delivery, oxygenation, and cell migration. Revascularization begins with the activation of endothelial cells (ECs) in response to growth factors like VEGF and PDGF. These activated ECs contribute to ECM degradation within the granulation tissue, facilitating the formation of a new capillary network [77].

Fibroblasts are the main cells in the granulation tissue that are abundant in connective tissues across various organs, exhibiting diverse functions crucial to tissue repair and regeneration. These functions involve the production of ECM, expression of growth factors and

cytokines, as well as immunomodulatory activities. The dynamic population of fibroblasts at the injury site can be influenced by various cell interactions. For instance, transdifferentiation between endothelial cells and fibroblasts or the recruitment and differentiation of MSCs from the bone marrow into fibroblasts [78–80]. Based on their specific roles and functionalities, fibroblasts can manifest distinct phenotypes. Among the various fibroblast subtypes, myofibroblasts stand out prominently in the context of skin repair, characterized by the expression of α-SMA. These cells are particularly good at collagen synthesis and ECM deposition. However, their increased activity can lead to excessive scar tissue formation. Another pivotal subtype of fibroblasts, known as dermal papilla cells, plays a crucial role in hair follicle formation and maintenance, which is normally absent in adult skin repair [54]. Recent studies have unveiled plasticity within these fibroblast populations. Specifically, under specific signaling cues derived from epidermal stem cells, dermal papilla fibroblasts can differentiate into myofibroblasts and make an adipose layer instead of scar formation. By fostering adipocyte formation instead of scar tissue, clinicians might harness this intrinsic cellular plasticity to enhance wound healing outcomes [81].

The differentiation of fibroblast to myofibroblast mainly occurs during wound contraction and facilitates wound size reduction, optimizing subsequent re-epithelialization. During contraction, collagen fibrils align perpendicularly at wound edges in order to boost the wound's mechanical strength. This microenvironmental stiffness modulates fibroblast differentiation into myofibroblasts. The myofibroblast population typically peaks around day three post-injury, marked by surged collagen types I and III expression and α-SMA. This cellular pathway sets off a feedback loop driven by mechanical stresses on fibers, upregulating TGF-β1 expression, subsequent ECM synthesis, and further myofibroblast differentiation, potentially

resulting in scar formation [82,83]. In scarless healing, when enough ECM is produced, the myofibroblasts are eliminated from the injury site by apoptosis. Interestingly, MMPs also exhibit inhibitory effects on myofibroblast differentiation, though the underlying mechanisms remain incompletely elucidated. However, in scar-forming wounds, the persistent presence of myofibroblasts, coupled with insufficient apoptosis and reduced MMP levels, increases the chance of scarring [84,85].

A hallmark of this proliferative phase is the critical process of re-epithelialization, the restoration of the epidermal barrier predominantly mediated by keratinocytes. Beyond keratinocytes, the epidermis comprises various components such as immune cells, hair follicles, and different glands. Given the epidermis's vulnerability to injuries, it houses a substantial reservoir of stem cells. These stem cells are located in regions like the interfollicular epidermis, hair follicle junctions, bulge areas, and within the glands. Following damage, specific changes occur: sebaceous glands undergo turnover, hair follicles cease growth and enter a phase of degeneration, sweat glands become temporarily deactivated, and stem cells are recruited to differentiate into different cells [54].

Upon injury, keratinocytes undergo phenotypic changes. At the wound margins, they strategically loosen their intercellular adhesions and detach from the basal lamina, thereby facilitating wound closure through the formation of a migrating epithelial tongue [86]. This migration is a dynamic process influenced by various growth factors, cytokines, and proteins, including protein kinase C-α, members of the epidermal growth factor family, TGF-β, fibroblast growth factor family, inflammatory cytokines like IL-1, IL-6, and TNF-α [54].

Keratinocytes play multifaceted roles beyond their intercellular interactions. They engage in extensive communication with other cell types, including fibroblasts, immune cells, and

endothelial cells. For instance, keratinocyte secretions during the inflammation phase are crucial for activating macrophages and neutrophils. Furthermore, specific keratinocyte secretions, such as IL-1 and TNF-α, stimulate fibroblasts to produce factors essential for keratinocyte migration and proliferation. Additionally, during angiogenesis, growth factors like VEGF produced by keratinocytes increase vascular permeability, a prerequisite for the formation of new blood vessels. Notably, TGF-β, produced by fibroblasts, is crucial in reverting activated keratinocytes to their normal phenotype. Any disturbance in this complicated communication can lead to scar formation at the end of the healing process [54].

2.3.4 Remodeling

The final extended stage of wound healing, remodeling, involves fiber reorganization and maturation of the healed tissue. Although it is known as the end point of the healing process, it can take several months to several years. In this stage, residual dead cells undergo degradation, and the activity of immune and parenchymal cells becomes restricted. Additionally, collagen fibers undergo remodeling to enhance their mechanical properties and maximize the tensile strength of the repaired or regenerated skin. The existing collagen matrix, primarily composed of collagen type III, is broken down by MMPs and resynthesized and reorganized in an oriented manner, predominantly consisting of collagen type I. Furthermore, this stage involves a reduction in hyaluronic acid and fibronectin levels [19]. However, if any of these essential processes are disrupted, the balance of this stage will be disturbed, and the likelihood of scar formation will increase [87].

2.3.5 Scar Formation

As mentioned in each stage, depending on the severity and size of the wound, the healing process may be compromised. The disruptions lead to the formation of abnormal granulation

tissue, commonly recognized as a scar. Overall, it can be said that the primary culprits behind scar formation are the overexpression of collagen type I and TGF-β1, the over-differentiation of myofibroblasts, and insufficient breakdown of the ECM, as illustrated in **Figure 2-1D**. Given the significant impact that scars can have on various aspects of a patient's life, numerous techniques have been developed to prevent or minimize their formation. This subsequent section delves into common scar management strategies.

2.4 Scar Management

Considering the detrimental impact of scars on patients' quality of life, extensive efforts have been dedicated to developing various techniques for scar prevention and reduction. Scar management in chronic wounds and burn injuries is one of the ten priorities in The Skin Canada Priority Setting Initiative [88]. The current clinical methods for managing scar formation during wound healing can be categorized into two main approaches: preventative measures and post-formation treatments. Preventative measures include biochemical interventions, such as systemic administration or local application of bioagents like pharmaceutical agents [89,90], genes [89,90], stem cells [91], cytokines such as Interferons [42,92], and immune modulators, all aimed at promoting scar-free healing. On the other hand, post-formation treatments involve mechanical offloading and pressure therapy [90,93], laser radiation [42,94], radiotherapy [42,95], and surgical therapy [42,95], which are employed to reduce the size of existing scars, as illustrated in **Figure 2-2**. Nevertheless, both preventative and post-formation treatments available in clinical settings have limitations, including invasiveness, limited efficacy, reliance on advanced technologies, and high costs, which hinder their widespread application in wound healing. Therefore, extensive benchside research in the fields of biomaterials, tissue engineering, and regenerative medicine has been undertaken to address this pressing need [40,76,96].

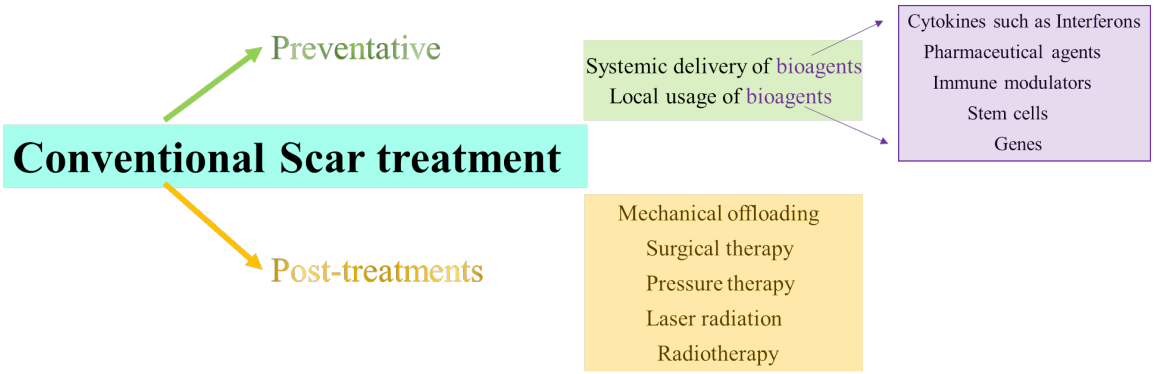

Figure 2-2 Conventional strategy for managing scars: Preventative and post-treatment.

2.5 Skin Tissue Engineering and Biomaterial Science

Tissue engineering is an emerging field that holds great promise in creating functional tissue to replace damaged or lost tissue and restore its normal function. Central to tissue engineering is the combination of biomaterials, cells, and signaling factors, particularly growth factors, to facilitate tissue regeneration. A diverse range of scaffolds, cells, and signaling factors (physical and chemical cues) can be employed in skin tissue engineering and the pursuit of scarless wound healing, **Figure 2-3**.

Biomaterials used in skin applications are precisely designed to interact with the surrounding tissue and cells, actively promoting regeneration by providing a stable yet degradable scaffold that guides cellular behavior. These biomaterials can be derived from natural or synthetic sources. They can also take on various forms, including hydrogels, nanofibrous films, and membranes, as well as nano and microparticles. Furthermore, these biomaterials can be tailored to possess specific features and properties to meet the unique requirements of skin tissue engineering. These characteristics may include specific structural arrangements, mechanical strength, rates of biodegradability, as well as physical properties like water absorption and gas permeation. By carefully designing and engineering these biomaterials,

researchers aim to optimize their performance in promoting scarless wound healing and achieving successful tissue regeneration.

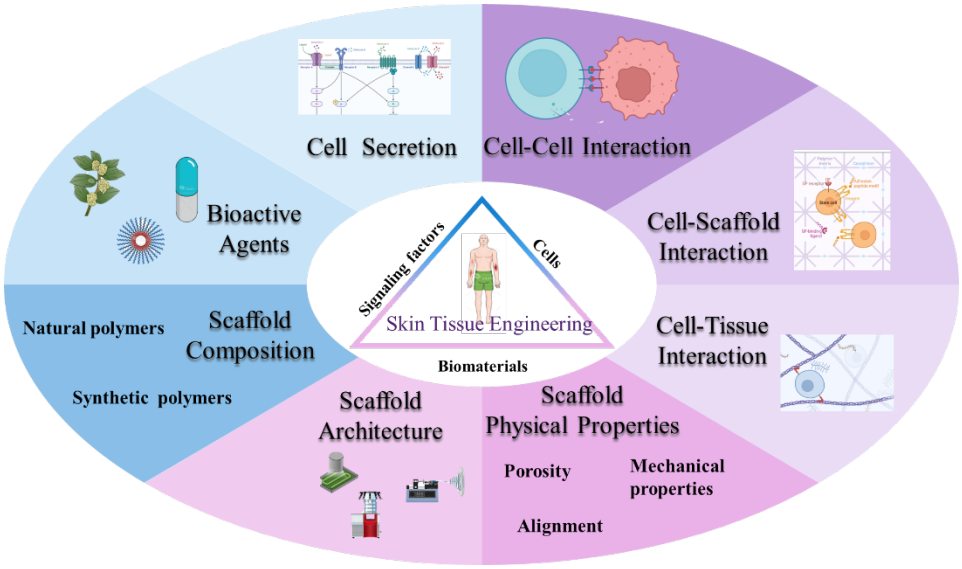

Figure 2-3 Skin Tissue Engineering Components.

A range of techniques exist for fabricating biomaterials designed explicitly for skin tissue engineering and promoting scarless wound healing, with each technique offering unique advantages depending on the desired properties of the final product. These fabrication techniques include but are not limited to 3D printing, freeze-drying, solvent-casting, self-assembly, and electrospinning. Among these techniques, electrospinning stands out prominently in skin tissue engineering and scar-free wound healing due to its exceptional attributes [97,98].

Electrospinning offers several notable advantages, making it highly suitable for tissue engineering applications. Firstly, it allows for easy fabrication and efficient mass production, making it practical for large-scale implementation. Moreover, electrospinning exhibits versatility in compatibility with various materials, providing a diverse range of options for biomaterial selection and therapeutic agents incorporation into nanofibrous scaffolds. The resulting

nanofiber-based structures possess a significantly increased surface area, allowing for enhanced cellular interactions and increased loading capacity for therapeutic agents. Additionally, the diameter of the electrospun nanofibers can be precisely controlled, offering opportunities for tailoring the scaffold properties to meet specific requirements. The porosity of the electrospun scaffold can also be modulated, ensuring optimal cell infiltration and nutrient exchange. Furthermore, the mechanical properties of the electrospun biomaterials can be fine-tuned to mimic those of natural skin tissue [99]- **Figure 2-4A**.

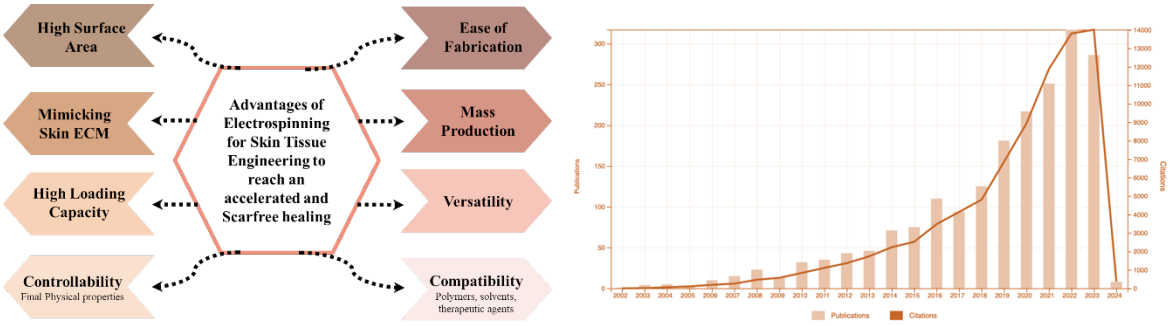

Figure 2-4 A) Advantages of Electrospinning for preparing scaffolds for wound healing and reaching Scar-free healing, B) B) Number of publications including electrospinning for wound dressing from 2002 to January 2024 showing increasing trends in the use of Electrospun membranes for wound healing application.

2.6 Electrospinning for Skin Tissue Engineering

When it comes to skin tissue engineering and achieving scarless wound healing, electrospun membranes demonstrate remarkable capabilities in mimicking the natural skin both in structure and composition. The biomimicry of electrospun nanofibrous membranes to the skin is based on the final fibrous structure of the membrane, as well as the nanostructure of fibers, which possess a high surface area and area-to-volume ratio. This biomimetic microenvironment facilitates optimal fibroblast, keratinocyte, and other cell interaction with the scaffold, providing a larger area for cell attachment. Furthermore, the diameter of electrospun nanofibers can be precisely controlled to replicate the size of skin extracellular matrix (ECM) protein fibers in the

range of 60-120 nm [100,101]. This replication of the ECM structure boosts critical cell-scaffold interactions, including adhesion, migration, and differentiation. Another advantage of electrospinning lies in its compatibility with various agents and solvents, enabling the functionalization of nanofibrous fibers with biomolecules that mimic the biochemistry of the natural ECM [102]. This compatibility allows for incorporating specific signaling factors and growth factors, further enhancing the regenerative potential of the electrospun membranes.

In addition to mimicking the structural and compositional aspects, electrospun nanofibrous membranes also possess properties that replicate those of natural skin. They maintain the necessary moisture for healing while effectively absorbing excess exudate. Furthermore, these membranes provide the desired porosity, allowing for crucial gas exchange required for wound healing while simultaneously preventing the invasion of pathogens [103].

Considering these remarkable attributes, electrospinning has emerged as a well-known technique in skin tissue engineering, facilitating the development of biomaterials with great promise for achieving scarless wound healing. **Figure 2-4B** shows the trend of research on electrospinning for skin application from 1900 to 2023. The following section will provide a brief description of the electrospinning principle.

2.6.1 Electrospinning Technique

The electrospinning procedure starts by applying a high voltage to a viscoelastic droplet containing polymers, solvents, and therapeutic agents. This voltage initiates the ejection of a charged solution from the needle of the electrospinning machine, known as the spinneret. The ejected solution then undergoes fiber formation, and the resulting fibers are collected on a designated collector, ultimately forming an electrospun mat suitable for use as a skin wound dressing-**Figure 2-5A**.

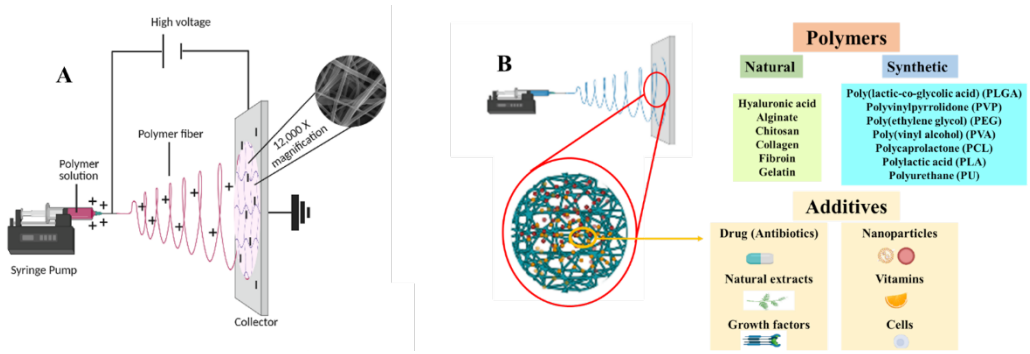

Figure 2-5) A) Electrospinning procedure and produced nanofibrous structure. Created with BioRender.com B) Different polymers and bioactive materials appropriate for electrospinning for wound healing application.

Several parameters can be adjusted throughout the electrospinning process to optimize the final membrane's properties. These parameters include the applied voltage, the distance between the tip and collector, the speed of collector rotation, the feeding rate of the solution, as well as the choice of solvents and polymers. Each of these factors can influence crucial characteristics such as the diameter of the fibers, the porosity of the membrane, and even the overall shape of the fibers.

By carefully manipulating these parameters, researchers and engineers can fine-tune the electrospinning process to achieve desired outcomes. Optimizing the fiber diameter, for instance, can impact the mechanical properties and surface area of the resulting membrane. Controlling the porosity can impact adequate cell infiltration and nutrient exchange. Furthermore, the choice of polymers can dictate the biocompatibility and degradation rate of the electrospun membrane, making it suitable for specific applications in skin tissue engineering and wound healing [104].

The electrospinning process offers compatibility with a wide range of synthetic and natural polymers, enabling the selection of suitable materials to create biocompatible wound dressings. An advantage of this technique is that any potentially toxic organic solvent used during electrospinning evaporates, ensuring that it does not contribute to cytotoxicity in the final

products [105]. Various polymers are commonly used in the preparation of electrospun wound dressings, including but not limited to polyurethane (PU) [106], polyvinylpyrrolidone (PVP) [107,108], polylactic acid (PLA), poly(lactic-co-glycolic acid) (PLGA) [109], polycaprolactone (PCL) [110,111], poly(vinyl alcohol) (PVA) [112]and poly(ethylene glycol) (PEG) [113] as synthetic polymers. Additionally, natural polymers such as collagen [114], hyaluronic acid [114], gelatin [115], chitosan [116], and alginate [117] are also commonly used. This diverse selection of polymers allows for tailoring wound dressings with specific properties and functionalities. The electrospun membranes can also serve as carriers for therapeutic components, further enhancing their effectiveness in wound healing. Therapeutic components may include biological, organic, or metallic substances, each serving different purposes, such as inactivating pathogenic microorganisms or promoting cell proliferation. Examples of loaded components in electrospun nanofibers for skin tissue engineering and wound healing include antibiotics and biocides [118], metallic nanoparticles (NPs) [28,119], natural extracts, growth factors, vitamins, and even cells– **Figure 2-5B** [120].

The choice of solvent depends on various factors, including the solubility of all materials, volatility, evaporation rate, boiling point, vapor pressure, toxicity, and, most importantly, compatibility of the solvent with therapeutic agents and other additives [121]. While most natural polymers and proteins are water-soluble, water is not an appropriate solvent for electrospinning due to its low conductivity and slow evaporation rate, requiring high temperatures. Hence, an additive or cosolvent is necessary to overcome these limitations. Various organic solvents can be employed as cosolvents for the electrospinning of water-soluble polymers, such as trifluoroacetic acid (TFA) [122], trifluoroethanol (TFE) [123], and hexafluoroisopropanol (HFIP) [124]. **Table**

2-1 provides an overview of common solvents suitable for various polymers, drawing from a variety of authoritative sources[100,125–133].

Table 2-1 Solubility of polymers in different solvents and compatibility of solvents as a cosolvent system for electrospinning.

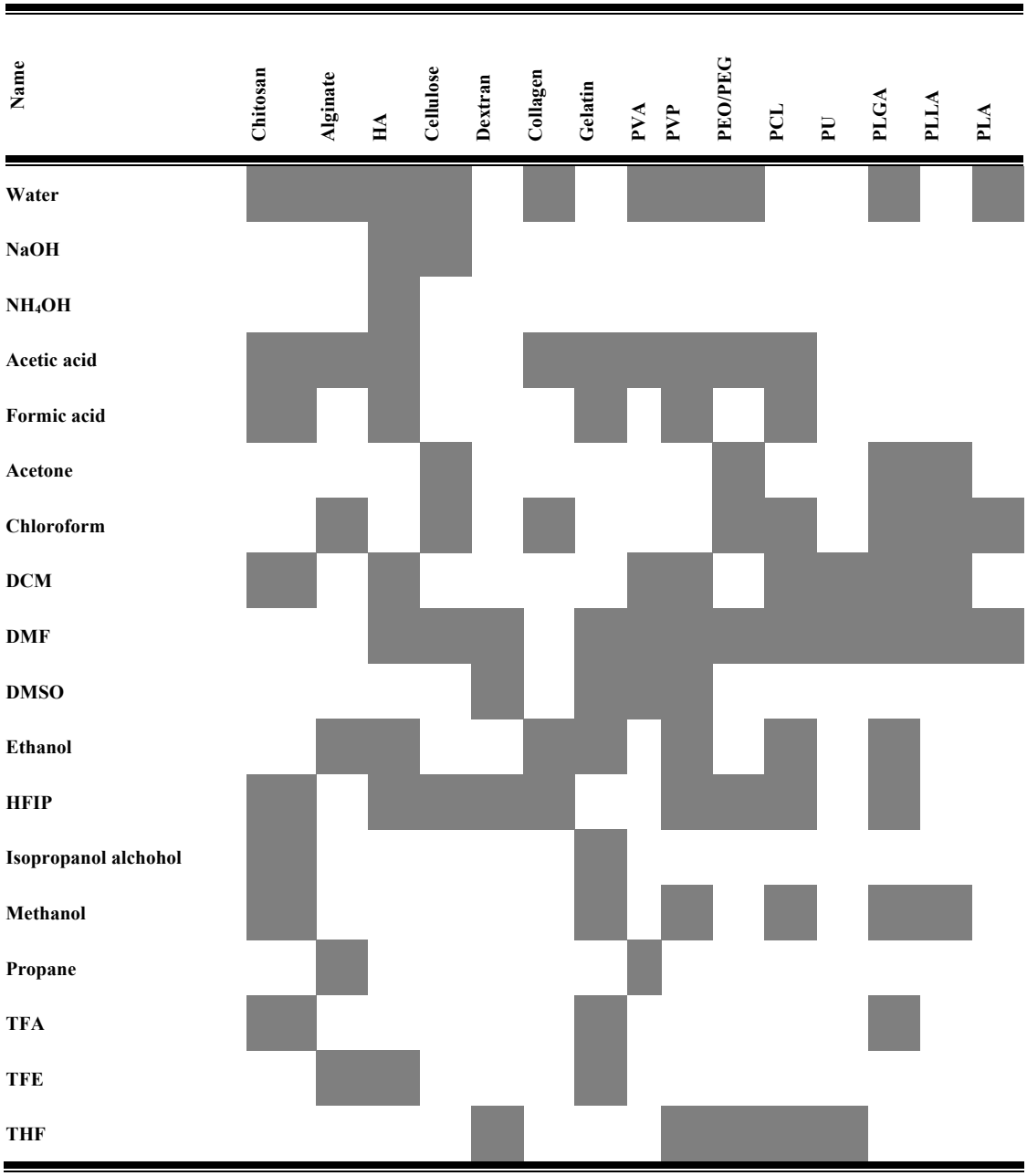

Incorporating therapeutic agents into the nanofibers also requires careful consideration of solvents to preserve their bioactivity. Depending on the sensitivity of the agents, they can be

directly dissolved in the solvent chosen for the polymer, or they may require a mild solvent to maintain their activity. Bioagents such as growth factors, proteins, cytokines, or cells are often sensitive to organic solvents, and their bioactivity may be compromised due to interactions with the solvent. Therefore, they should be loaded separately into the fibers through techniques like side-by-side electrospinning [128]. Various methods for loading bioactive and therapeutic agents are discussed in the final section of this paper. Other additives, such as chemical drugs and herbal extracts, can be directly dissolved in organic solvents or water, and the best cosolvent should be chosen based on the specific polymers used.

The following sections provide a comprehensive review of the methods and materials employed in developing nanofibrous wound dressings and skin substitutes, aiming to achieve accelerated scarless healing. Various innovative approaches and advancements in the field will be discussed, shedding light on the potential strategies for promoting efficient tissue regeneration and minimizing scarring.

2.6.2 Scar-free Wound Healing through Electrospun Nanofibers Wound Dressings

One significant avenue for studying scarless wound healing involves examining the healing process in the fetus. Fetal wound healing exhibits notable distinctions from adult wound healing, offering valuable insights for scar reduction. In the fetal ECM, hyaluronic acid and collagen type III exhibit notably higher concentrations in the early stages of healing when compared to the adult ECM. These components play a crucial role in stimulating cell migration and contribute significantly to scarless healing. Additionally, the presence of keratin-8 and -19 in the fetal ECM assists in downregulating the expression of transforming TGF-β. In adult wound healing, TGF-β overexpression and collagen type I overexpression in early stages is a key contributor to scar formation [134], as depicted in **Figure 2-6**. Achieving scarless healing in

adults necessitates a specific biological cascade: the downregulation of TGF-β expression, the controlled proliferation and differentiation of fibroblasts into myofibroblasts, and the initial upregulation of collagen type III deposition, which should subsequently be replaced by collagen type I in the later stages of healing by an increase in activity of MMPs.

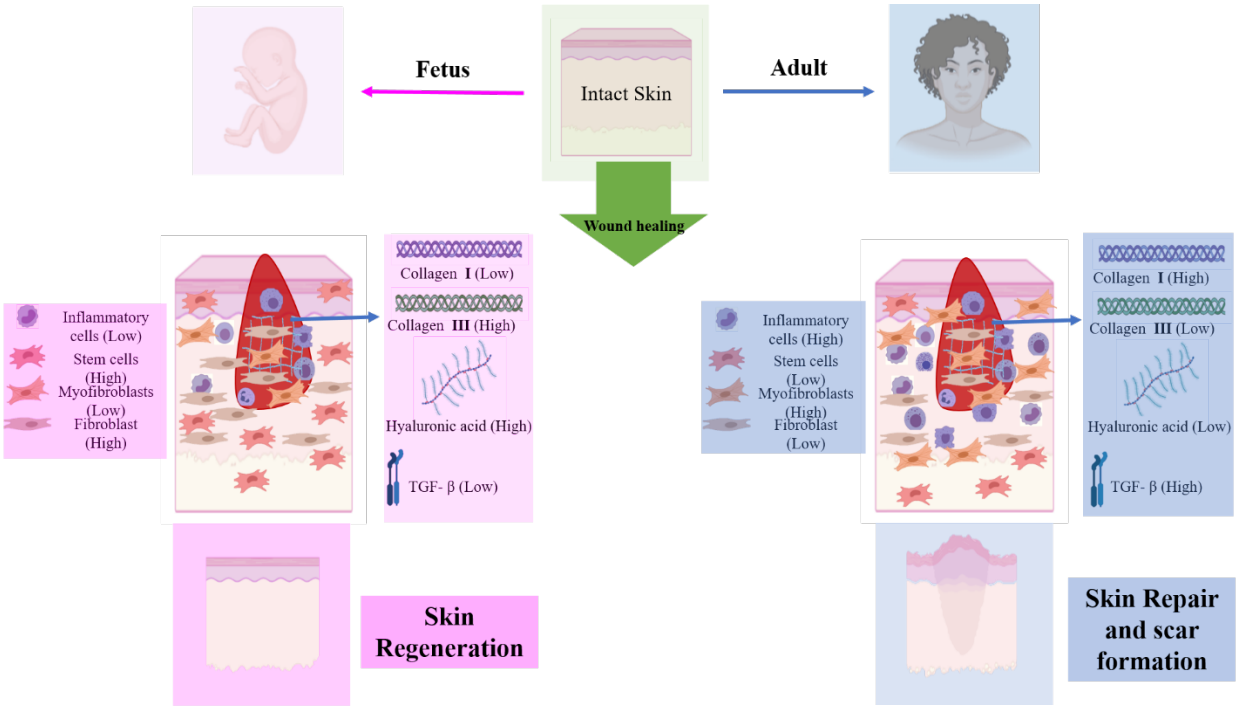

Figure 2-6 Differences in adult and fetus wound healing lead to skin repair (scar formation) and regeneration. Created with BioRender.com.

Numerous strategies focus on mimicking fetal wound healing processes in order to achieve scarless wound healing. This can be achieved by designing scaffolds replicating the fetal ECM's composition and physical properties, creating an artificial ECM. Alternatively, incorporating stem cells and bioactive molecules into the scaffold composition has shown promise in promoting scarless healing.

The ECM is an essential component of tissues, playing a crucial role in regulating cellular activities. Apart from providing structural support, the ECM serves as a non-cellular

omnipresent entity that influences and directs cellular behavior. **Figure 2-7** illustrates the multifaceted functions of the ECM [135]. One aspect of ECM's influence lies in the physical cues it provides to cells. These cues include factors such as topography, porosity, and ECM stiffness conveyed through the orientation of micro/nanoscale fibers within the ECM. These physical signals profoundly impact cellular behavior, influencing cell adhesion, migration, and differentiation processes. In addition to its physical characteristics, the ECM is enriched with various biomolecules that play a vital role in cellular regulation. These biomolecules, including cytokines, growth factors, enzymes, small bioactive molecules, vitamins, and acidic components, serve as biochemical cues [136]. They bind to cell receptors, initiating a cascade of cellular responses that affect cell-cell interactions, gene expression, pathway activation, and cell-biomolecule interactions.

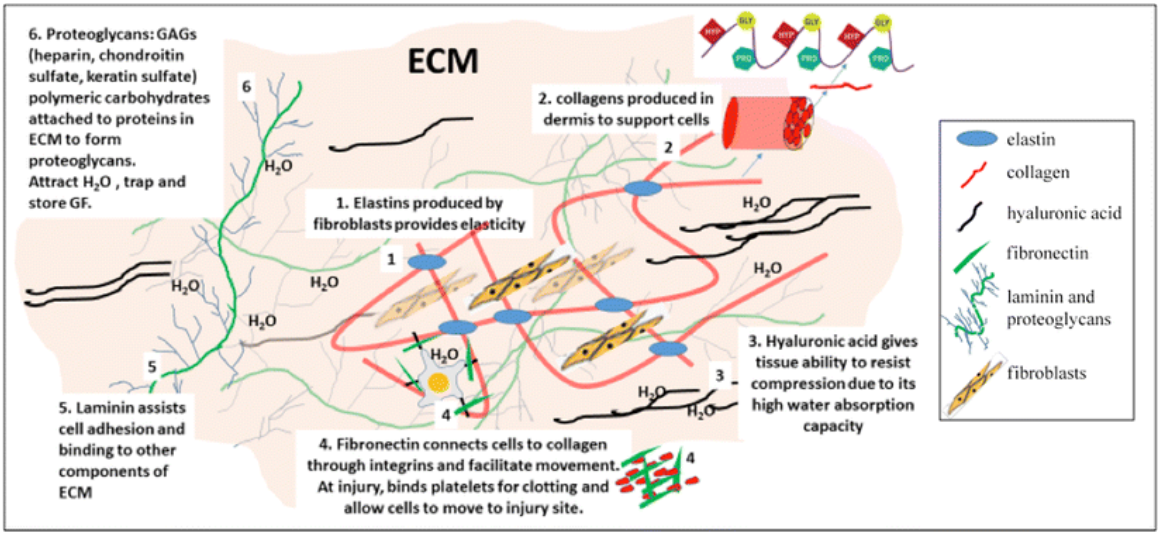

Figure 2-7 Structural and chemical roles of ECM in guiding cells in the skin. Reproduced with permission [137]. *Copyright © 2017, The Regenerative Engineering Society.*

The combination of physical and biochemical cues within the ECM creates a dynamic microenvironment that guides and controls cellular activities in natural tissues. By understanding and harnessing the influence of the ECM's physical and biochemical cues, researchers have the

opportunity to craft biomaterials and tissue engineering strategies that replicate and amplify these signals, thereby facilitating the regeneration of functional and healthy tissues.

In the context of evaluating the anti-scar ability of wound dressings, this review categorizes the approaches into three main groups based on their resemblance to the natural ECM. The first category, termed "physical cues," focuses on modifications or enhancements to the wound dressings' physical properties. These include thickness, porosity, and other physical characteristics. These alterations aim to mimic the natural ECM's physical cues and their influence on wound healing. By optimizing the physical properties of the wound dressings, researchers seek to create an environment that promotes scarless healing. The second category is related to the composition of wound dressings based on ECM components. The section is dedicated to wound dressings that not only mimic the ECM's chemical composition but also exhibit unique physical properties due to the presence of proteins or natural polymers. This category, labeled "compositional cues," includes wound dressings combining physical and chemical cues to boost their anti-scar properties. The last category, referred to as "chemical cues," involves the incorporation of biomolecules, bioactive agents, or small molecules into the nanofibrous wound dressings. These substances are selected to mimic the biochemical composition of the ECM. By integrating these biomolecules, wound dressings can provide specific biochemical cues that regulate cellular behavior and promote scarless wound healing.

By categorizing the approaches into physical, chemical, and compositional cues, researchers can better understand the different strategies employed in designing wound dressings that mimic the properties of the ECM. This classification aids in identifying and evaluating the efficacy of various wound dressing formulations in achieving scarless wound healing, as depicted in **Figure 2-8**.

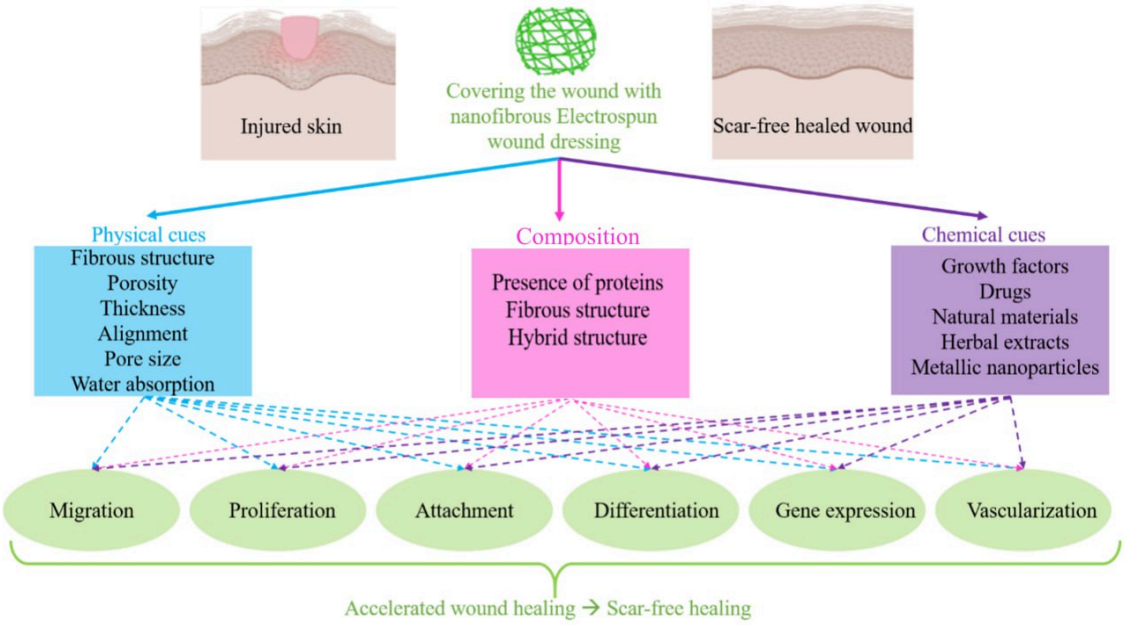

Figure 2-8 The role of a nanofibrous wound dressing in wound healing: Physical, Composition, and Chemical cues.

2.6.2.1 Physical Cues

While wound healing is a complex regulated process, certain physical features of artificial ECM (scaffold) have been recognized for their ability to enhance the healing capacity. The thickness [138], surface morphology[139], porosity [138], water absorption [140], mechanical properties [50], and three-dimensional structure [141] of wound dressings have all been identified as physical cues that can significantly impact the wound healing process by influencing cellular behavior at different stages of wound repair. These physical cues play a crucial role in mimicking the natural properties of the skin's ECM and are critical factors in fine-tuning wound dressings. In order to modify the structure and physical properties of scaffolds and biomaterials, identifying the ideal range of physical features that promote enhanced wound healing is a crucial initial step. This section delves into the optimal physical properties critical for designing effective wound dressings. We then explore various techniques and approaches

discussed in the reviewed literature to achieve these desired properties within a mimicking electrospun membrane. By critically evaluating these techniques, we aim to provide valuable insights and recommendations for developing electrospun wound dressings with the necessary physical attributes to facilitate scar-free wound healing.

The first property to evaluate is the thickness. The skin consists of two primary layers: the epidermis and the dermis, with additional layers of connective tissue and adipocytes providing support and functionality, as depicted in **Figure 2-9**.

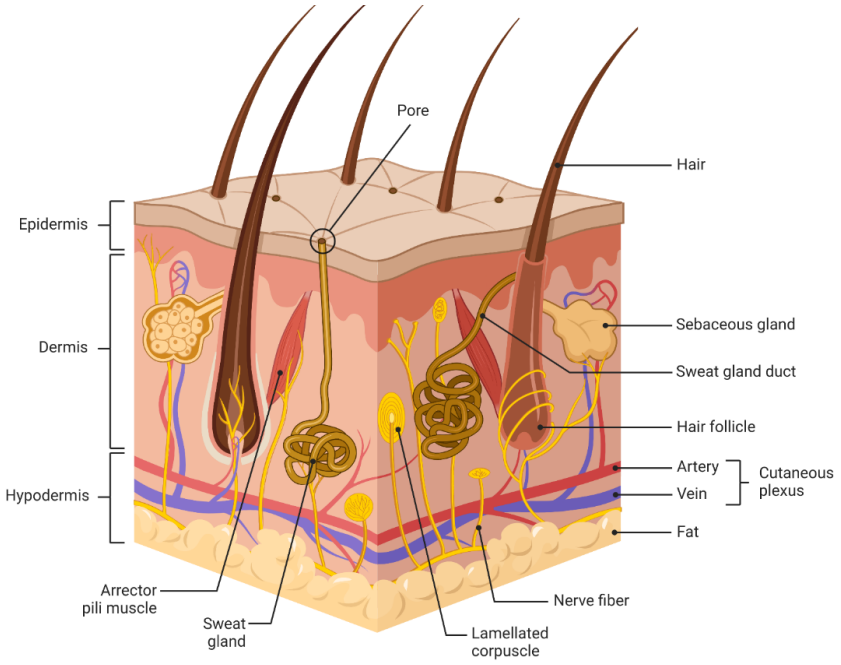

Figure 2-9 Skin layers: Epidermis and dermis supported with connective tissue and adipose tissue (fat) layers as the hypodermis, Created with BioRender.com

Each layer plays a distinct role in the natural healing process, and disrupting the coordinated function of these layers can hinder proper tissue regeneration, leading to the formation of unwanted fibrous tissue, known as scars. Therefore, an optimal wound dressing should possess a three-dimensional (3D) structure with an appropriate thickness capable of

providing the necessary support and promoting faster, scar-free healing at the injury site [142]. However, the optimal thickness of a wound dressing remains a subject of debate, influenced by the location and severity of the injury [143]. While thicker dermis/epidermis autografts (3-4 mm) have been shown to promote faster healing, their limited availability as donor tissue poses a challenge; therefore, the need for developing 3D and porous dressing in the range from 400 μm to 10 mm or more is increasing [144]. The next properties are pore size and porosity. A highly porous scaffold (with 3D porosity in the range of 60-90%) with micron-sized pores (50-500 microns) facilitates the infiltration of fibroblasts, adipocytes, and vascular cells, promoting tissue ingrowth and preventing neotissue necrosis, thereby supporting natural healing processes [145]. Another significant physical property affecting the healing process is air permeability or water vapor transmission rate (WVTR). In contrast to healthy skin, which exhibits a WVTR of 204 $g/m^2/day$, wounds like first-degree burns and granulating wounds can experience significant changes in WVTR, reaching values as high as 279 $g/m^2/day$ and 5138 $g/m^2/day$, respectively [146]. Therefore, to speed up healing, it's essential to consider the wound type when managing moisture levels. Effective wound dressings for rapid wound healing require a carefully managed WVTR that typically lies within a wide range of 840 and 2500 $g/m^2/day$ [147,148].

This section outlines potential approaches to achieving the ideal physical properties of electrospun membranes for scarless healing, accompanied by an overview of related research.

2.6.2.1.1 Thickness

Given the importance of mimicking the skin's layered structure for effective cellular behavior regulation, a thick, three-dimensional (3D) membrane is highly desirable. While conventional methods like extending electrospinning time or layering multiple wound dressings can increase thickness, they have limitations of lack of control over porosity. Here, innovative

techniques like gas-forming emerge as a promising strategy. This approach allows for the expansion of a two-dimensional membrane into a three-dimensional sponge, achieving desirable thickness and porosity simultaneously [149]. It's important to note that enhancing the thickness of nanofibrous wound dressings through new techniques often correlates with an increase in porosity and pore size. These two properties are intrinsically connected, as a thicker structure typically allows for more interconnected spaces within the fibrous matrix. Jiang et al. [121], engineered a sponge-like membrane via a gas-forming technique, employing $NaBH_4$ for its ability to emit non-toxic gas through controlled hydrolysis. When a poly(ε-caprolactone) electrospun nanofibrous membrane is immersed in an aqueous solution of $NaBH_4$ at 21 °C with mechanical agitation, it undergoes a transformation. Bubbling is initiated, and the membrane's initially dense, nanofibrous architecture is converted into a three-dimensional, porous structure resembling a sponge. The concentration of $NaBH_4$ and time of immersion can be altered to get various thicknesses. Once complete expansion is achieved, the 3D membranes are washed with deionized water and can be freeze-dried for further use. By employing this technique, it is possible to obtain a thick, porous, and three-dimensional membrane while retaining the nanoscale dimensions of the fibers [150].

When it comes to measuring the thickness of electrospun membranes, conventional techniques like micrometer screw gauges may present challenges and inaccuracies due to inadequate pressure regulation. There's a risk of impacting and compressing delicate nanofibers, which can alter the final measurements and perceived thickness [151]. However, microscopy imaging, particularly scanning electron microscopy (SEM) or other optical microscopies, can be utilized for this purpose. To measure the thickness using SEM, the membranes should be imaged from the side. This can be achieved by directly attaching the membranes to an SEM stub, thereby

exposing their sides to the detector. Alternatively, the membranes can be placed in a PDMS (polydimethylsiloxane) mold for stability. A mixture of PDMS monomer and curing agent (in a ratio of 10:1) should be poured onto the membrane and allowed to cure overnight at 50 °C [152]. Once cured, the molded membrane can be cross-sectioned and used for SEM imaging. Image processing software such as ImageJ can then be employed to measure the thickness accurately.

To reach scarless and accelerated healing, Zhang et al. [141] employed the bubble expansion technique to create a nanofibrous membrane using chitosan-PVA to accelerate hemostasis in deep wounds and promote scarless wound healing. Chitosan solution (80% acetic acid) and PVA solution (deionized water) were mixed in a 3:7 mass ratio and electrospun at 18 kV to fabricate the membrane. The final membranes were immersed in $NaBH_4$ solution for expansion. The fabrication process (0.1 M $NaBH_4$ 30 min) resulted in a thick and porous nanofibrous sponge measuring 10 mm in thickness and exhibiting a high bulk porosity of 90% (**Figure 2-10B)**. The thick and porous nature of the sponge not only facilitated enhanced cell infiltration but also increased the availability of interaction sites for cellular activities as presented in **Figure 2-10B**. The 3D sponges exhibited a stimulating effect on the growth of epithelial cells and fibroblast cells. Compared to culturing on 2D nanofibers less than 1mm thick, both cell types exhibited enhanced proliferation and expansion when cultured on the 3D mat substrate. This, in turn, resulted in an accelerated coagulation. Furthermore, the 3D nanofibrous sponges with increased thickness and porosity significantly boosted the rate of cellular penetration, playing a vital role in enhancing vascularization and reepithelization processes. The 3D structure and high porosity of the nanofibrous sponge contributed to accelerated healing and reduced scar formation in a mouse model with circular full-thickness wounds (10 mm in diameter). While all groups achieved complete wound closure within 21 days, the 3D

nanofibrous sponge exhibited significantly superior wound contraction compared to the control (gauze) and 2D nanofibrous membrane group. Specifically, the 3D nanofibrous sponge demonstrated a 60% reduction in wound size compared to the initial wound area within just 3 days, surpassing the 50% reduction of the 2D membrane and the 30% decrease of the control. Additionally, wounds treated with the 3D sponge group closed completely within the first week, highlighting its accelerated healing potential compared to the 2D group, which required two weeks for complete closure (**Figure 2-10B)**. The histology data analysis revealed that applying the 3D sponges in the wound treatment reduced the dermis and epidermis hypertrophy compared to the 2D membranes, indicating a lower incidence of adverse scar formation. The scarless healing process necessitates the initial overexpression of collagen type III, followed by a decrease in collagen type III expression to prevent scar formation. Since activated fibroblasts primarily express collagen, replacing these fibroblasts with adipocytes during healing reduces collagen expression and promotes scarless healing. Achieving this requires a functional dermis and the presence of adipocytes, which necessitates reconstructing the skin's adipose layer. The adipose layer facilitates adipocyte migration to the dermal layer. The presence of a porous structure with interconnected pores and optimal gap junctions can facilitate this transition, leading to minimized scar formation. The adipocytes staining of the healed wounds treated with the 2D nanofibrous membrane and 3D nanofibrous sponge showed that the number of adipocytes in the 3D samples was higher after 21 days. Additionally, the amount of collagen type III in the presence of the 3D sponge was 1.3 times higher than in the 2D samples during the first week but decreased to 0.3 times of the amount of collagen type III in the 2D samples by day 21 leading to less scar formation. These findings suggest that the 3D mat not only influenced cellular behavior

and tissue remodeling but also promoted a favorable wound healing environment that supported the regeneration of healthy tissue and minimized scar formation.

The influence of membrane thickness on scar-free healing extends beyond merely enhancing cell infiltration and penetration. Membranes with appropriate thicknesses have been shown to regulate gene expression and growth factor secretion, which are critical for scarless healing. Research indicates that the thickness of wound dressings, when closely mimicking the physiological dimensions of natural skin, can positively affect these factors, thus aiding in scarless healing. Given that wound healing is a complex process, no single factor can ensure reduced scar formation. Therefore, multiple properties of the membranes, such as thickness, pore size, and composition, must be considered, as they play interrelated roles in minimizing scars. The appropriate thickness of wound dressings depends on the wound's severity and size, as well as the skin's structure, which varies between animal models and humans. Consequently, defining a specific thickness range for achieving scarless healing in humans based on animal models remains challenging. The role of different thicknesses of nanofibrous membranes on the wound healing process has been evaluated by Xie et al. [153] . They developed gelatin-PCL nanofibrous membrane with different thicknesses (400, 800 and 1200 μm) by increasing the spinning time (**Figure 2-10C)**. The membranes were fabricated by dissolving gelatin-PCL in 2,2,2-Trifluroethanol and spinning at 12kV. The membrane with a thickness of 400 μm exhibited downregulation of TGF-β1 secretion 2 times more than a membrane with a thickness of 42 μm and 2.5 times more than the control without sample. The downregulation of TGF-β1is attributed to reduced fibroblast differentiation into myofibroblasts and decreased collagen expression. Myofibroblasts, known for their high TGF-β1 expression, are primarily responsible for scar formation. The gelatin-PCL membrane with the appropriate thickness (400 μm) helped maintain

fibroblasts in their original phenotype and prevented their differentiation into myofibroblasts. The preservation of the phenotype was attributed to a reduction in the expression of Tumor Necrosis Factor-stimulated gene-6 (TSG-6), a crucial regulator for the differentiation and inhibition of fibroblasts. The downregulation of TGF-β1 and the lower number of myofibroblasts resulted in accelerated and scarless healing, as evidenced by complete epithelial regeneration in an *in vivo* rat model (rat skin thickness of 1200 μm) as presented in **Figure 2-10C**. Interestingly, the study revealed that in a rat model with biopsy-punched wounds (5 mm in diameter), treatment with gelatin-PCL nanofibrous membrane at thicknesses of 400 μm and 800 μm significantly accelerated wound healing (95% and 88% wound closure) compared to both the control group (which received no membrane treatment) and wounds treated with the same type of gelatin-PCL nanofibrous membrane at a thickness of 1200 μm with 77% and 66% wound closure, respectively. Moreover, the collagen deposition was more than five-fold decreased in the sample with 800 μm thickness compared to the control with reduced collagen I/III ratio, which translated to minimized scar formation [124]. This finding emphasizes the importance of an optimum membrane thickness regarding skin thickness for cell filtration, adhesion, and proliferation, highlighting that a thick membrane may not always be the ideal choice for promoting scarless healing.

The significance of thickness and the presence of a 3D structured scaffold in tissue engineering, particularly skin tissue engineering, is widely recognized. However, electrospun membranes face limitations in achieving adequate thickness. Fortunately, several reviewed techniques have been developed to overcome this challenge, increasing the thickness of membranes to foster a conducive 3D microenvironment for cell growth. These techniques aim to preserve the nanostructure of the fibers, which is crucial for regulating cellular behavior and

achieving scar-free healing. Through the application of these techniques, electrospun membranes can be engineered to achieve an optimal combination of thickness and nanostructure, thereby promoting optimal cell response and facilitating healthy tissue regeneration, minimizing scar formation.

2.6.2.1.2 Porosity/Pore Size

Porosity facilitates cell infiltration, protein absorption, and cellular migration within a wound dressing [154,155]. However, electrospun membranes often lack sufficient porosity, hindering effective cell penetration and migration. Various techniques have been employed to enhance the porosity of nanofibrous membranes. One strategy involves increasing the fiber diameter to micron size, resulting in a more porous structure. However, this method sacrifices the biomimicking aspect as the interaction between cells and the larger fibers does not resemble the natural cell-ECM interaction. Another approach involves incorporating additives such as ionic salts to modify electrostatic repulsion, which may have cytotoxic effects. Sacrificial fibers or templates, such as hydrophilic PEO fibers or ice crystals, have also been used to address cytotoxicity concerns associated with additives. Nonetheless, achieving precise control over porosity remains challenging for these methods [149,150,156]. A more advanced technique for enhancing the porosity of nanofibrous membranes is the Aqueous Phase Fiber Reassembly Technology, which involves a series of steps, including electrospinning, mechanical cutting, freeze-drying, and heat treatment. In this method, the electrospun mats are cut into squares, homogenized in deionized water, freeze-dried, and then subjected to heat treatment to reinforce the scaffold while preserving the porous structure.

Various techniques are available to measure the porosity of electrospun membranes. For instance, the porosity can be calculated based on the bulk density and volume of the materials using the following equation [141].

$Porosity = \frac{(V - V_0)}{V} \times 100$ *and* $V = L \times W \times T$ $V_0 = \frac{m_0}{\rho_0}$ *Equation 2-1*

Where L is length, W is width, T is thickness and, m_0 is the mass of the bulk materials and ρ_0 is the density of the bulk materials.

To reach accelerated healing with minimized scar formation, Yu et al. [157] employed the Aqueous Phase Fiber Reassembly Technology to prepare a biomimetic wound dressing using a PCL-PEG-PCL triblock copolymer. The polymers were dissolved in a 3:1 DCM/DMF cosolvent system before electrospinning at 15 kV. After spinning, the membranes were homogenized to get shorter fibers, freeze-dried, and finally treated at 53 ˚C to get reinforced membranes. Notably, this technique resulted in an increase in both pore size (from 575 nm to 2911.9 nm) and porosity (from 87.6% to 92.6%), while the fiber diameter remained in the nanoscale range (160 nm), **Figure 2-10A**. The highly porous nanofibrous membrane promoted cell migration, increased cell proliferation, and facilitated oriented collagen deposition. Consequently, in a mouse full-thickness wound model (10 mm in diameter), normal tissue regeneration was observed within two weeks with full wound closure while for control and 2D membranes only 80% closure was achieved. This regeneration replaced abnormal granulation tissue with a healthy epithelial layer featuring uniform and dense collagen fibers. The wound area was reduced to a tenth of the size compared to the control group, which underscores the method's ability to achieve accelerated healing (**Figure 2-10A)**.

While porosity and pore size in electrospun membranes may not receive as much attention as these properties in hydrogels, they indeed play a critical role in the wound healing

process. Cellular behavior and intercellular communication can be effectively regulated by modifying the porosity, particularly the interconnected porosity, of the electrospun membranes. By optimizing these properties to promote desired cell infiltration and migration, an optimal environment can be created to support scar-free healing.

2.6.2.1.3 Water Vapor Transition Rate (WVTR) and Wettability

The water vapor transmission rate (WVTR) is critical in wound healing, as excessive or inadequate moisture can lead to complications. Researchers have explored various techniques to achieve an optimal WVTR in wound dressings. Several membrane features, including the chemistry of components, wettability, pore sizes, and porosity of nanofibrous membranes, contribute to WVTR. One method to alter the WVTR involves blending various polymers, each with distinct hydrophobic and hydrophilic properties. This strategy aims to adjust the dressing's affinity to water. The goal is to create a membrane that absorbs exudates and facilitates gas exchange. Another strategy to control the WVTR of electrospun membranes involves modifying their physical properties. These properties, including fiber diameter, pore size, and overall membrane porosity, are interconnected. For instance, the addition of surfactants can alter fiber diameters, which in turn affects the packing density of the fibers within the membrane. This ultimately influences the size and distribution of pores, thereby governing the movement of water/vapor molecules through the membrane[158,159]. Furthermore, fine-tuning electrospinning parameters, such as voltage, feeding rate, and the distance between the needle and collector, can influence these key membrane properties and consequently affect WVTR.

The WVTR can be measured by a simple test based on ASTM E96M-16 Uniformly cut samples are weighed and then placed over open glass bottles (e.g., Penicillin bottles) filled with a known volume of solution. The pre-measured weight of each bottle is recorded. These sealed

bottles, with the samples attached, are stored in a chamber maintained at 37°C and 75% humidity. An open bottle is used as a control. If necessary, the samples can be clamped to the dish mouth, which defines the area of the specimen exposed to the vapor pressure in the solution. The solution level and bottle weight are monitored time. This data is used to calculate the WVTR using a specified formula.

$$WVTR(gh^{-1}m^2) = \Delta W/T/A. \quad \textit{Equation 2-2}$$

Where ΔW is mass changes, T is the time of mass changes (desired intervals) (h), and A is the sample area.

Regarding the role of WVTR on wound healing, especially in Atopic dermatitis (eczema), Krysiak et al. [160] investigated the changing of WVTR by combining hydrophobic and hydrophilic polymers and altering the porosity of the membranes. Different membranes with varying compositions and porosities were fabricated, namely polystyrene (PS), Nylon6-PA6, and a composite membrane of PS and PA6 (spun simultaneously through separate nozzles). PS and PA6 were dissolved in separate solutions: PS in DMF and PA6 in a 1:1 (v/v) formic acid: acetic acid mixture. The resulting solutions were then electrospun at 12-14 kV to fabricate the membranes. To adjust the porosity of the fabricated membranes for eczema treatment, different oils were applied after electrospinning, and the structure of the fibers and oil spreading were assessed to identify the most effective patch. The study revealed that porosity had a more substantial impact on WVTR than the nanofibers' chemistry. The PS, PA6, and PS-PA6 composite membranes exhibited similar WVTR values of approximately 3×10^3 g/m^2/day. However, the introduction of oil reduced the WVTR to 1.5×10^3 g/m^2/day for both PA6 and PS-PA6 membranes. The presence of oil filled the pores of these samples, decreasing their porosity and enhancing moisture retention. Notably, oil did not significantly affect the WVTR of the hydrophobic PS sample since this membrane had larger pores, and oils remained on the fibers

instead of filling the pores. In the skin moisture test, the skin was covered with 25 μL of borage oil, and then the nanofibrous membranes were used, covered with a commercially available skin foil. PS, PA6, PS-PA6 composite, and two sandwich models with either PS or PA6 as the first layer (1. Skin-Oil-PS-PA6-foil, 2. Skin-Oil-PA6-PS-foil) were tested. Significantly, both the PS-PA6 composite membrane and the sandwich membranes demonstrated the ability to rehydrate dry skin within 6 hours, which can lead to accelerated wound healing. This study highlights the significance of optimizing membrane porosity and composition to regulate WVTR and maintain adequate wound hydration, which is crucial for successful tissue regeneration.

Lin et al. [161] employed a similar strategy of blending materials with varying hydrophilicity to achieve the desired WVTR in their wound dressings. They fine-tuned the WVTR by adjusting the ratios of natural proteins, namely fibroin and sericin. Their objective was to maintain a WVTR within the optimal range of 840 to 2500 g/m²/day. This range is critical because a lower WVTR can result in the accumulation of exudate at the injury site, increasing the risk of infection, whereas a higher WVTR can cause excessive fluid loss and lead to the dressing adhering to the wound, potentially resulting in secondary injury. Fibroin, a protein with low hydrophilicity consisting mainly of non-polar amino acids, was mixed with sericin, a highly hydrophilic protein rich in polar amino acids. This mixture was prepared in varying ratios of fibroin to sericin (10:0, 9:1, 8:2, and 7:3) using formic acid as the solvent. The addition of sericin to the membranes increased their hydrophilicity due to the presence of functional groups such as hydroxyl and carboxylic acid, **Figure 2-10D**. This led to an increased water affinity and higher exudate absorption capacity, essential for wound healing. Furthermore, the presence of sericin reduced the diameter of the fibers, resulting in an increased specific surface area and WVTR, **Figure 2-10D**. The membranes with higher sericin content exhibited higher WVTR as follows

1101.76 g/m^2/day, 1237.35 g/m^2/day, and 1257.32 g/m^2/day for the 9:1, 8:2, and 7:3 ratios, respectively compared to 1070.55 g/m^2/day for pure fibroin membrane. Additionally, the incorporation of sericin improved the mechanical properties of the membranes, such as elongation at break and breaking stress. The membranes, composed of a mixture of fibroin and sericin, showed high cytocompatibility with fibroblasts and an increased proliferation rate (**Figure 2-10D**). The addition of sericin enhanced fibroblast adhesion thanks to the boosted hydrophilicity of the membranes. The final membranes demonstrated desirable hydrophilicity and mechanical properties suitable for wound dressing applications. However, further *in vivo* tests are required to evaluate the performance of the dressing in achieving accelerated healing.

Beyond leveraging blends of hydrophobic and hydrophilic polymers to modulate the WVTR, employing various polymers to construct layer-by-layer membranes can fine-tune the membrane's overall hydrophilicity. This technique not only influences WVTR but also regulates cell and pathogen adherence. For example, it can deter bacterial colonization on the dressing while promoting cell attachment, thereby enhancing the probability of accelerated healing through surface asymmetry in hydrophilicity. These dressings typically consist of a hydrophobic outer layer and a hydrophilic inner layer, mimicking the skin's epidermis and dermis structure. The hydrophobic outer layer acts as a protective barrier, preventing bacteria attachment and debris entry into the wound. Meanwhile, the hydrophilic inner layer creates a favorable cell attachment and growth environment. In order to measure the hydrophilicity of electrospun membranes, contact angle tests can be conducted. One commonly used method is the sessile-drop method, where a droplet of approximately 5 μL is placed on the membrane, and images are taken from the side at different time intervals (typically 0 and 60 seconds) using a microscope equipped with a camera. Image processing software such as ImageJ can analyze the micrographs

and determine the contact angle. The contact angle obtained from this analysis provides information about the surface's hydrophilicity or hydrophobicity. Techniques such as the Wilhelmy plate method can be utilized for more advanced analysis of dynamic contact angles. This method involves measuring the advancing and receding motion of a plate as it is immersed or retracted from a fluid. The dynamic contact angle can be determined by analyzing the motion and corresponding forces [151].

The design of a dual-layer wound dressing featuring a hydrophobic exterior and a hydrophilic interior to replicate the skin's natural structure and protect the wound from external contaminants necessitates the use of superhydrophobic membranes (contact angle greater than 150˚) for the outer layer [162]. Superhydrophobic surfaces, inspired by natural examples such as plant leaves and insect wings, have found widespread applications in various fields, including antibacterial coatings and drug delivery systems [162]. However, fabricating a superhydrophobic layer through electrospinning poses significant challenges. Traditional hydrophobic polymers like PCL or PU do not provide sufficient hydrophobicity to achieve the desired superhydrophobic properties. This limitation necessitates exploring alternative strategies or materials to create the desired superhydrophobic surface for the outer layer of the dressing. Coating the membrane with oils or modifying it with fluorine components can also adversely affect membrane permeability or introduce toxicity concerns, respectively [163]. To address these limitations, Yu et al. [163] drew inspiration from the natural world, specifically from the superhydrophobic characteristics found in plant leaves and insect wings. They developed a superhydrophobic outer layer for the wound dressing by electrospinning PCL dissolved in a 3:7 v/v formic acid: acetic acid mixture onto a nylon mesh with micron-sized pores (40 and 80 μm) at 20 kV, creating a unique texture resembling natural superhydrophobic materials The

hydrophobic outer layer membranes were named PCL40 (electrospun on nylon mesh with a pore size of 40 μm), PCL80 (electrospun on nylon mesh with a pore size of 80 μm), and PCL (electrospun on aluminum foil without nylon mesh). All three PCL samples exhibited a consistent average fiber diameter of 270 nm. The inner layer of the dressing was based on hydrophilic gelatin and pioglitazone crosslinked with genipin for enhanced stability and functionality (**Figure 2-10E)**. Both PCL40 and PCL80 exhibited improved anti-adhesion properties against *E. coli, S. aureus,* and *P. aeruginosa*, demonstrating one order of magnitude greater reduction in bacterial attachment compared to PCL membrane. The asymmetric membrane with PCL40 was chosen as the optimum sample with WVTR of 1556 g/m^2/day and the outer and inner layers contact angles of 145˚ and 40˚, respectively. The unique features of this wound dressing allowed for the complete closure of full-thickness wounds (6 mm in diameter) in a diabetic (type2) mouse model within 10 days, a significant improvement over Tegaderm, which required more than 14 days. Additionally, it promoted the complete regeneration of both the epidermis and dermis layers, characterized by dense and oriented collagen fibers, **Figure 2-10E** [163]. Similar results were observed in a diabetic (type 1) rat model with 8 mm diameter full-thickness wounds. Interestingly, in this model, the control group (gauze) experienced infections that resulted in a 20% increase in wound size due to inflammation on day 5. In contrast, the PCL40-Gel-Pio samples showed a 60% decrease in wound size within 5 days, achieving full closure in 21 days, whereas the control group only reached 80% closure. The regenerated skin treated with the PCL40-Gel-Pio membrane exhibited dense collagen formation, hair follicles, and vascularization. Vascularization peaked on day 5 with the PCL40-Gel-Pio treatment and decreased by day 14, coinciding with the peak expression of MMP-9. These phenomena indicate accelerated regeneration with minimized scar formation. It is

important to note that the desired amount of moisture can vary depending on the type of wound being treated. For instance, wounds associated with conditions like eczema may require higher moisture levels than surgical wounds. Moreover, it is important to recognize that WVTR is not determined by a single factor but rather influenced by a complex interplay of various variables. The chemistry of the components used in the wound dressing, the orientation and diameter of the fibers, and the porosity of the final membrane all contribute to achieving the optimal WVTR. A thorough understanding of these variables and their interplay allows for the targeted design of wound dressings with precisely controlled WVTR.

2.6.2.1.4 Alignment

Cell response to the morphology and alignment of their substrate is a critical aspect of wound healing. These physical features of a dressing can influence cellular behavior and the production of ECM components, such as collagen. Kim et al. [164] investigated the role of nanotopography on cell behavior and fate during wound healing via 3D printing technology. They showed that the density and orientation of nanopatterns were two key features that can be modified to change the quality of skin healing through changes in cell migration, division, and the rate of ECM production.

Various techniques can be employed to achieve aligned, cross-aligned, or other orientations of fibers in electrospinning. These techniques include using collectors made of different metals or adjusting the speed of the collector by using different collector configurations such as rotational drum collector, rotational disc collector, and rotational wire collector. Additionally, fiber alignment can be achieved by utilizing two oppositely placed metallic needles, creating a two-pole air gap, or using magnetic field-assisted methods [165]. These diverse approaches allow researchers to control the orientation and alignment of fibers during

electrospinning, allowing for the customization of fibrous materials to suit specific applications. The quantification of fiber alignment is commonly conducted using 2D image analysis of SEM micrographs. Powerful image analysis software, such as Directionality and OrientationJ plugins for ImageJ, allows for meticulous quantification of fiber orientation. These tools generate color-coded visualizations that not only depict fiber orientation but also validate the accuracy of the analysis. Additionally, the software can produce orientation distribution graphs, providing a quantitative assessment of fiber alignment characteristics [151,165].

Regarding the impact of the shape or pattern of nanofibers on wound healing, Sun's group [166] investigated the role of basket-weave pattern nanofibers in regulating cell behavior. In natural skin, collagen fibers exhibit a fine basket-weave structure (50-500 nm). Designing a scaffold that mimics this natural skin pattern can guide cells toward a normal wound-healing process. Sun's research group suggested that the pattern of fibers can potentially shorten the inflammatory stage by influencing pro-inflammatory cytokines and reducing the chance of scar formation due to prolonged inflammation. They fabricated crossed and aligned collagen type I/PCL electrospun nanofibers using a specially designed collector with two copper strips to achieve the basket-weave pattern, **Figure 2-10F**. Membranes were produced through electrospinning PCL-collagen dissolved in HFIP, using a voltage setting of 14 kV. *In vivo,* results of diabetic rats with full-thickness wounds (diameter of 18 mm) demonstrated that the crossed (perpendicular fibers) and aligned (parallel fibers) patterns stimulated the transition of classically activated macrophages (M1) to alternatively activated macrophages (M2). M2 macrophages are responsible for cell division, collagen synthesis, and post-inflammatory remodeling, whereas M1 macrophages secrete pro-inflammatory cytokines. The transition from M1 to M2 macrophages is crucial for resolving the high inflammatory response and reducing the

inflammatory stage. The immunohistochemical analysis revealed that the expression of Arginase 1, a marker for M2 macrophages, was increased in the presence of aligned and crossed membranes. Conversely, the expression of NOS2, a marker for M1 macrophages, was undetectable, indicating the resolution of inflammation, **Figure 2-10E.** The changes in cell morphology induced by the crossed or aligned fibers were identified as the main reason for macrophage polarization and phenotype changes. Overall, the aligned (parallel fibers) and crossed (perpendicular fibers) patterns contributed to accelerated healing by cutting down the inflammation period, boosting cell migration, and limiting the differentiation of fibroblasts into myofibroblasts, which could be translated into less scar formation. However, the precise biological mechanisms and pathways underlying these effects are still unclear.

While the significance of fiber alignment in mimicking the ECM structure is well-recognized, its specific impact on achieving scar-free healing has not been extensively studied compared to its role in the differentiation of stem cells. Further research is needed to explore the influence of fiber alignment on scar tissue formation and identify the optimal fiber alignment strategies that can promote scar-free healing.

2.6.2.1.5 Mechanical Properties

The mechanical properties of nanofibrous membranes play a crucial role in cellular behavior, including stem cell differentiation and ECM secretion by mature somatic cells through mechanotransduction. Various strategies can be employed to tailor the mechanical properties of nanofibrous membranes. One approach involves the creation of reinforced composites. Here, natural or synthetic polymers are combined with additives like NPs to significantly enhance mechanical properties. The alignment of fibers within the membrane also impacts its mechanical characteristics [167]. Researchers have explored a variety of techniques to achieve precise

control over the mechanical properties of electrospun nanofibrous membranes, such as manipulating fiber diameter and membrane thickness, employing post-treatment methods, and utilizing crosslinking strategies [168].

The influence of mechanical properties on wound healing can be classified at two different levels: macroscopic (bulk) and microscopic/nanoscopic (local). At the macroscopic level, the bulk mechanical characteristics play a pivotal role. These properties can impact the closure rate of the wound and are influenced by the wound's environmental (physiology) factors, including contraction forces, fluid flow, and extrinsic loads [169]. It is suggested that for optimal healing, the dressing should exhibit bulk tensile strengths similar to that of natural skin, which possesses viscoelastic properties with a tensile strength range of 20-30 MPa, Young's modulus (E) between 0.005 and 150 MPa, and elongation at break values of 35-115% [170,171]. An ideal wound dressing should, therefore, mimic these mechanical characteristics to accommodate the healing process effectively, allowing for stretching and recovery to its original form as the wound heals. This mimicry in elasticity with natural skin can prevent subcutaneous shear damage that might otherwise delay healing [169]. The challenge with synthetic polymers lies in their high tensile strength coupled with low elongation at break, whereas natural polymers often exhibit the opposite characteristics. Therefore, finding a mixture of different polymers and additives to reach these properties has been widely explored [172,173]. The significance of bulk mechanical properties in wound dressings for healing is well-acknowledged. The bulk mechanical behavior of these dressings is inherently linked to their structural composition. For example, E for most single-layer dressings is observed to be less than 1 MPa, whereas for multi-layered dressings, this value can range between 1 to 35 MPa. Examples of fiber-based single-layered dressings include Kaltostat, consisting of alginate fibers with an E of 0.24 MPa; Aquacel

Ag/Extra, made from sodium carboxymethyl cellulose fibers with E values of 0.28 and 0.65 MPa; and Exufiber, comprising nonwoven PVA with an E of 0.95 MPa. Multi-layered dressings such as Carbonet, incorporating cellulose fibers and activated charcoal within polyethylene nets with an E of 6.38 MPa; and Carboflex, consisting of alginate fibers and a hydrocolloid with activated charcoal and a water-resistant top layer, exhibiting an E of 0.49 MPa, demonstrate a broader range of mechanical properties [174]. Given that the mechanical properties of natural skin vary significantly depending on the specific area, with Young's modulus ranging from 0.005 to 150 MPa and elongation at break from 35% to 115%, it is challenging to define a single "ideal" mechanical property for wound dressings. Therefore, wound dressings must be carefully designed to match the application, considering the area, type, size, and severity of the wound. This tailored approach ensures that the dressing mimics the natural microenvironment, promoting cell regeneration, accelerating healing, and minimizing scar formation during healing.

At the microscopic/nanoscopic (local) level, the interactions between cells and their underlying substrates are determined by the mechanical characteristics of these substrates. Cells exhibit a sensitivity to the stiffness of their environment, which significantly affects their adhesion, migration, proliferation, spreading, and differentiation processes [175]. The mechanical features at these scales can influence the healing trajectory through various mechanisms. For instance, the stiffness of nanofibers at the local level can modulate immune cell phenotypes, potentially extending or shortening the inflammatory phase dominated by proinflammatory macrophages. Additionally, the transition of fibroblasts into myofibroblasts, which is the main reason for scar formation, is closely tied to the local stiffness of the substrate (higher than 20 kPa facilitates the differentiation) [176–179]. The local tissue stiffness is defined as the elastic modulus, showing the resistance to deformation, and can be measured by atomic

force microscopy (AFM). Upon encountering a substrate, cells sense the substrate's mechanical properties via a process known as mechanotransduction. The integrin family of transmembrane receptors plays a pivotal role in this process by providing adhesion sites through their binding to substrate (eg. ligands). This binding facilitates the formation of a multiprotein complex known as focal adhesions, which serve as conduits for the transmission of chemical and mechanical cues into the cell, thereby influencing cellular behavior through connections to the cell's cytoskeleton [175,177]. These focal adhesions enable cells to exert pulling or pushing forces against the substrate, aiding in their migration. The substrate's ability to resist these forces and undergo deformation is critical for effective cell migration. Notably, the size of the focal adhesion complex is significantly influenced by substrate stiffness [177]. In the context of nanofibrous structures, mechanotransduction added complexity as cells can exert forces on fibers from multiple directions, with elasticity varying based on the force direction [175]. It is important to note that the deposition of ECM by cells leads to substantial alterations in local mechanical properties [175].

The evaluation of the mechanical properties of nanofibrous membranes involves two standard protocols: single-fiber mechanical tests (for microscopic/nanoscopic-local mechanical properties) and membrane mechanical tests (macroscopic-bulk mechanical properties). However, conducting single-fiber mechanical tests can be challenging, requiring isolating fine fibers and using high-resolution instruments. For instance, AFM is used to find different mechanical features of single fibers through different setups, such as tensile testing for E, three-point bending for bending modulus, and nanoindentation for elasticity measurements of single fibers. Usually, nano-tensile equipment is used in conjunction with other characterization techniques

like Transmission Electron Microscopy (TEM) or SEM for local mechanical testing of single fibers [175,180].

Membrane mechanical tests offer a more practical approach to evaluating the bulk mechanical properties of nanofibrous membranes. The mechanical tests include indentation, tensile, and bending tests. The most common mechanical test is conducted with Uniaxial tensile testing equipment, adhering to the ASTM D882–18 standard [168]. In this test, a rectangular membrane sample is subjected to tension, facilitating the evaluation of its macroscopic mechanical properties. This protocol is often preferred for evaluating the mechanical properties of nanofibrous membranes intended for wound dressing applications. The choice of the appropriate mechanical test depends on the specific application.

While significant progress has been made in understanding the correlation between mechanical properties and wound healing, the precise influence of these properties on achieving scar-free regeneration warrants further investigation. Nonetheless, existing research has primarily focused on enhancing the mechanical characteristics of wound dressings to optimize cellular responses. In a study by Dodero et al. [181], chitosan-based wound dressings were investigated to determine how physical and chemical crosslinking methods influence their mechanical properties. Chitosan, a natural polymer known for its biocompatibility, biodegradability, and antibacterial properties, has been extensively used as a main component in wound dressings. However, its stability in aqueous solutions and mechanical properties fall short of the requirements for wound dressing applications. To address this, additives, crosslinkers, or other synthetic polymers are incorporated to enhance the mechanical properties. The study employed electrospinning to fabricate chitosan membranes from a 5% acetic acid solution containing equal parts (by weight) of chitosan and PEO at 17.5 kV. Subsequently, the

membranes underwent immersion in either a 10% w/v Na_2HPO_4 aqueous solution or 2.5% v/v ethylene glycol diglycidyl ether (EGDE) aqueous solution at 60°C to achieve physical or chemical crosslinking, respectively. Mechanical properties, including E, tensile strength (σ_b) and elongation at break, were evaluated using uniaxial tensile testing. Rectangular samples (40×10 mm) were subjected to a tensile load at a crosshead speed of 25 mm/min using a 0.1 N pre-load cell on an Instron machine. Physical crosslinking via phosphate ionic bonds significantly enhanced the mechanical properties of the nanofibrous scaffold, doubling both E and σ_b compared to the chemically crosslinked counterpart. The physically crosslinked scaffold exhibited E and σ_b values of E 250 and 11 MPa, respectively, while the chemically crosslinked scaffold demonstrated values of 120 MPa and 6 MPa.). This structural reinforcement resulted from a more uniformly aligned fiber network, as evidenced by morphological analysis. Consequently, the physically crosslinked scaffold demonstrated superior cell adhesion and proliferation for both fibroblasts and keratinocytes *in vitro*. Conversely, chemically crosslinked samples exhibited increased structural defects and compromised cellular viability, particularly for keratinocytes, due to the release of cytotoxic byproducts. These findings underscore the importance of crosslinking strategy in optimizing the biocompatibility and efficacy of nanofibrous wound dressings.

The mechanical properties of wound dressings play a crucial role in supporting the healing process, as wounds undergo various mechanical loads during contraction. Further exploration is needed to understand the impact of mechanical properties on scar-free healing and to create wound dressings that match the mechanical properties of skin. A promising research path is comparing the mechanical properties of skin during healing in fetuses and adults. This

investigation should evaluate properties such as tensile strength, elasticity, viscoelasticity, and deformation behavior of the skin at different stages of healing in both fetal and adult models.

As discussed in this section, the physical properties of wound dressings are key factors in guiding the healing process and achieving scar-free healing. These physical cues can guide cell behavior by mimicking the natural cellular microenvironment. **Table 2-2** presents the reviewed physical cues, techniques for modulating these properties and methods for their measurement. Additionally, **Table 2-3** provides a comprehensive summary of all the reviewed papers, highlighting their key findings and contributions in the field of wound healing.

Table 2-2 Physical Properties of Engineered Wound Dressings and Methods for Modulating and Measuring These Properties

Property	Modification Techniques	Measurement techniques
Porosity-pore size	Increasing fiber diameter Adding additives such as salts Using sacrificing templates Using the Aqueous phase fiber reassembly technique	SEM imaging and image analyzing Solvent diffusion Bulk Density
Thickness	Increasing the time of spinning Preparing layers dressings Using gas forming technique	SEM imaging and image analyzing Other optical measurements
Water vapor transition rate (WVTR)	Blending different polymers Changing pore size Adding surfactants Changing fiber size	Based on ASTM E96
Wettability	Blending different polymers Surface coating	Contact angle test
Fiber alignment	Using collectors with different metals Changing the speed of the rotating Using two opposed needles Using two pole air gaps Using magnetic field	SEM imaging and image analyzing
Mechanical properties	Changing polymer composition Crosslinking Using composites and reinforcing materials	Uniaxial tensile test

In addition to physical properties, the substrate's chemical composition significantly affects cell behavior**.** Variations in the chemical composition of scaffolds are directly associated with physical characteristics, including porosity and fiber diameter, which cells can detect as physical signals. Therefore, it is relevant to examine the connected effects of physical and

compositional cues on cellular responses. The following section reviews the role of "compositional cues" in promoting wound healing by controlling the chemical properties of the selected polymers in the wound dressing material.

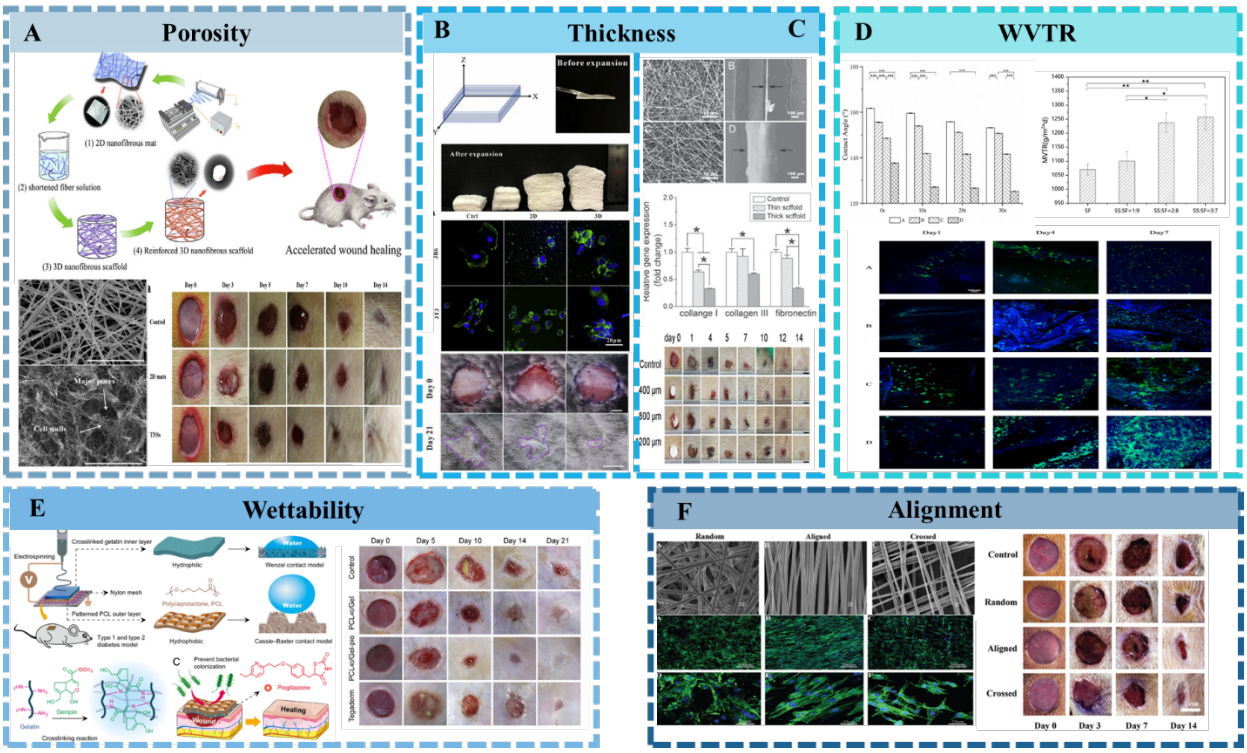

Figure 2-10 Physical cues

This figure illustrates the impact of various physical parameters in engineered wound dressings on wound healing. A) Porosity: The influence of porosity on wound healing was investigated using a porous electrospun membrane fabricated through an Aqueous phase fiber reassembly technique. The porous dressing demonstrated accelerated wound closure and reduced scar formation in an in vivo model, Reprint, with permission from [157] Copyright 2019 Elsevier. B) Thickness: The effect of wound dressing thickness on wound healing was explored using a thick membrane fabricated via gas foaming. The thick 3D membrane exhibited enhanced cell attachment, leading to faster wound closure and nearly scar-free healing in an animal model; Reprint with permission from [141] Copyright 2019 Elsevier. C) Thickness (alternative approach): The impact of varying membrane thickness on wound healing was examined by adjusting the spinning time. Interestingly, the thickest membrane did not result in scar-free healing, while membranes with a thickness of approximately 400 µm displayed reduced collagen expression and faster wound closure in an in vivo model, Reprint with permission from [153] Copyright 2019 IOPScience. D) Water Vapor Transition Rate (WVTR): The WVTR was manipulated by altering the polymer ratio in the wound dressing. Adding hydrophilic sericin to fibroin resulted in a higher WVTR and enhanced fibroblast adhesion, promoting an accelerated healing process. Reprint with permission from [161] Copyright 2021 Taylor & Francis. E) Wettability: The influence of wound dressing wettability on wound healing was achieved using a gradient wettability design. This design involved using a hydrophobic polymer as the outer layer and incorporating a micron-sized pattern with an inner layer of gelatin. This unique design protected against pathogens while mimicking the natural extracellular matrix (ECM), leading to accelerated healing with reduced scar formation in an in vivo model. Reprint with permission from [163] Copyright 2020 American Chemical Society. F) Fiber Alignment: The effect of fiber alignment in wound dressings on wound healing was achieved using a designed collector. The resulting cross-aligned fibers mimicked the natural structure of the skin ECM, influencing the behavior of macrophages and facilitating faster healing in an in vivo model. Reprint with permission from [166] Copyright 2018 Royal Society of Chemistry.

Table 2-3 Physical, Physio-chemical and chemical cues for affecting cells' behavior and healing pathways through nanofibrous wound dressings

Cues	Type	Method	Polymer	Result	Reference
Physical cues	3D structure	Gas injection	Chitosan	Fast coagulation Scarless healing	[141]
	Increasing Thickness (3D)	Multilayer electrospinning	Gelatin and PCL	Downregulation in the expression of collagen type I and TGF-β	[153]
	Porosity	aqueous phase fiber reassembly technology	PCL-PEG-PCL Block copolymer	Porous structure, high water absorption, scarless wound healing	[157]
	Nanopattern	UV-assisted capillary molding technique	Neonatal rat dermis	More migration in a vertical pattern	[164]
	Basketweave pattern	Designing collector	Collagen and PCL	Decreasing the inflammation and increasing migration rate and e re-epithelization	[166]
Compositional cues	Composition of scaffold-Natural polymer-biomimicking	Electrospinning	Gelatin and PCL	Gelatin: smaller wound area PCL: No significant change	[182]
	Fibrillar conformation- Natural polymer-biomimicking	rotary jet	Fibronectin	Regeneration of epiderm, derm, and adipose layer	[183]
	Biodegradable scaffold- Natural polymer-biomimicking	Electrospinning	Silk fibroin	Decreasing the expression of TGF-Beta1 and pro-inflammatory cytokine (IL-1 Alfa)- scarless healing	[184]
	Composition of scaffold-Natural polymer-biomimicking	Electrospinning	Marine collagen	Accelerated wound healing	[185]
	Composition of scaffold-Natural polymer-biomimicking	Electrospinning	Bovine collagen	Accelerated wound healing	[186]
	Hybrid scaffold- Natural polymer-biomimicking	Electrospinning	Collagen and hyaluronic acid	Changes in MMPs and TIMPs- scarless healing	[187]
	Hybrid scaffold- Natural polymer-biomimicking	Crosslinking with GA	Collagen and chitosan	Increasing the healing rate	[188]
Chemical cue: BGrowth Factors	Growth factor: EGF	Surface modification	PCL-PEG-PCL copolymwe	Increasing keratinocyte proliferation rate- Accelerated wound closure	[113]
	Growth factor: EGF bFGF	EGF: surface modification bFGF: blending in the core	PCL-PEG-PCL copolymwe	Increasing keratinocyte and fibroblast proliferation and migration- Accelerated wound closure	[110]
	Growth factor: EGF Natural material: Aloe vera	Blending	PLGA	Accelerated wound closure and new epithelization	[109]
	Growth factor: VEGF PDGF bFGF EGF	MultiJet electrospinning HA:Blending-bFGF Secondary carrier (Gelatin)-VEGF Collagen: Blending-EGF Secondary carrier (Gelatin)-PDGF	Collagen and hyaluronic acid	A high rate of vascularization-accelerated scar-free wound healing	[114]

	Growth factor: VGF PDGF-BB	VGF: blending PDFD-BB: secondary carrier-PLGA	Chitosan-PEO	Increasing the proliferation and angiogenesis rate – Scarless healing	[116]
Chemical cues: Drug	Ibuprofen (IBU)	pH-sensitive	PLLA	Downregulating TGF-Beta1- accelerated scar-free wound healing	[189]
	IBU	Blending	PLA	Accelerated wound healing	[190]
	Dimethyloxalylglycine (DMOG)-	Secondary carrier: silica NPs	PLA	Increasing the vascularization-accelerated wound healing	[155]
	Polyhexamethylene biguanide (PHMB)	Multi-jet	CA-PEU	High water absorption-antibacterial-accelerated wound healing	[191]
	Kyn	Blending	PVA-PLGA	Downregulating TGF-Beta1 and collagen expression-Scar-free healing	[192]
Chemical cue: Natural materials	*Calendula officinalis*	Blending	hyperbranched polyglycerol	Anti-inflammation and increasing the epithelization-Accelerated wound healing	[193]
	Spirulina	Blending	PCL	Capture ROS-Accelerated and scar-free wound healing	[194]
	Curcumin	Blending	Gum tragacanth-PCL	Early epithelization-Accelerated and scar-free wound healing	[195]
	Curcumin and chrysin	Blending	PCL-PEG-PCL copolymer	MMP-2 and TIMP downregulation- scarless wound healing	[196]
	Lithospermi radix	Blending	Gelatin-chitosan	Accelerated wound healing	[197]
	Alfalfa	Blending	PCL	High re-epithelization rate-Scar-free wound healing	[198]
Chemical cue: Nanoparticle	Silver NPs	Blending	Different polymers: Synthetic and natural	Antibacterial-accelerated wound healing	-

2.6.2.2 Compositional Cues

Cellular behavior is significantly influenced by interactions with ECM, which are shaped not only by its chemical composition but also by its physical characteristics. The physical properties of ECM cannot be considered completely independently from chemical composition, since they are often dictated by that composition. For instance, different types of collagens can alter substrate stiffness, which is sensed by cells through focal adhesion mechanisms. This sensing initiates a series of events that govern key cellular activities like migration, proliferation, and differentiation. Thus, significant interplay between the chemical and physical properties of the ECM orchestrates cellular guidance during healing. This understanding informs the design of engineered scaffolds, prompting researchers to explore various polymers to mimic the ECM's natural architecture. The ultimate goal is to improve healing outcomes and minimize scarring by recreating the skin's ECM microenvironment or emulating fetal wound healing conditions. While the ECM was once viewed merely as a structural support for tissue growth and cellular foundation until the 1990s, it is now recognized as a critical regulator of diverse cellular behaviors, including adhesion, migration, proliferation, and differentiation[199]. This exceptional capacity of the ECM to guide cells has brought it to the forefront of tissue engineering and regenerative medicine.

Key components of the skin's natural ECM, such as collagen families (I-VII, XI), fibrin, fibronectin, vitronectin, elastin, hyaluronan, chondroitin sulfate, decorin, versican, and tenascin [200], play crucial roles in cell signaling during various stages of wound healing. The interaction of cells with these components can lead to the secretion of biomolecules, changes in structure, or even modifications in protein sequences. This section reviews the most common natural polymers used to mimic the ECM composition through electrospinning.

2.6.2.2.1 Collagen

Collagen is an ideal candidate for ECM mimicry due to its critical role in providing suitable microenvironments for fibroblast growth. Its arginine-glycine-aspartic acid (RGD) sequences promote cell binding, support cell adhesion, and facilitate re-epithelialization[201]. The mechanical properties of collagen bundles, such as stiffness, also impact cellular behavior. For instance, changes in collagen maturation (crosslinking and organization) across various healing stages can alter ECM stiffness, influencing fibroblast proliferation and differentiation and consequently affecting healing dynamics and the extent of scar tissue formation [200]. Given collagen's multifaceted role in the healing process, it stands out as a preferred natural polymer for developing wound dressings to achieve accelerated healing and minimized scar formation.

Collagen can be derived from various sources, including fish, porcine, and bovine. However, animal-based collagen sources, particularly porcine and bovine, have drawbacks such as the risk of disease transmission, potential microbial contamination, and allergenicity [201–203]. Marine collagen presents an attractive alternative due to its lower risk of disease transmission and absence of religious concerns compared to standard bovine or porcine collagen sources. In this regard, Zhou et al. [185] successfully electrospun purified marine collagen into a wound dressing. The dressing's efficacy in supporting keratinocyte adhesion, proliferation, and subsequent wound healing was evaluated both *in vitro* and *in vivo. In vivo* studies employed a full-thickness wound model in rats to assess wound closure rates. The tilapia collagen was dissolved in HFP at a concentration of 8 wt% and electrospun under a voltage range of 16-18 kV. The collagen nanofibrous membrane, with an average fiber diameter of 310 nm and a pore size of 2.75 μm, facilitated keratinocyte adhesion within 24 hours and exhibited 114% proliferation after five days *in vitro***, Figure 2-11A**. The nanostructure and high surface area of the collagen

nanofibers greatly influenced keratinocyte behavior. Additionally, the hydrophilic nature of the collagen, with a contact angle of 26º, boosted the water absorption capacity of the wound dressing, promoting cell growth. During the regeneration process of healthy skin, keratinocytes differentiate into four layers: basal, spinous, granular, and cornified layers within the epidermis. Genes related to keratinocyte differentiation were examined as an indication of regeneration of the four different epidermal skin layers: basal, spinous, granular and cornified. Collagen nanofibers upregulated the expression of involucrin, filaggrin, and TGase1 genes, increasing keratinocyte differentiation rates. This contributed to fast and early re-epithelization with a reduced inflammatory response over two weeks, as evidenced by faster wound closure in an *in vivo* rat model (wound with a diameter of 1.8 cm), where the wound area was reduced to half the size of the control (wound without dressing) in the collagen-treated group in one week, **Figure 2-11A**. Although the precise reason for this phenomenon remains unknown, the presence of amino acids such as RGD sequence that aid in maintaining cell phenotype is a potential contributing factor. These findings demonstrate that marine collagen can be a viable alternative to mammalian collagen, as it shares a similar composition to mammalian collagen type I [204] and exhibits high bioactivity for wound healing applications [185]. Recombinant human collagen is another promising alternative to porcine and bovine collagens. Deng et al. [205] employed recombinant human collagen peptides (RHC) in chitosan/PEO nanofibers with *in situ* crosslinking with EDC (RHC:Chitoan: PEO 4:4:1). The wound dressing exhibited faster wound closure in a rat second-degree burn model with a diameter of 1.8 cm (over 57.5±7.1 % wound closure after 11 days, compared to 41.8±5.4% for the Tegaderm control), alongside boosted angiogenesis.

To achieve rapid re-epithelialization, Pal et al. [206] conducted a study using PCL-chitosan nanofibers coated with collagen type I. The bilayer wound dressing was fabricated by

electrospinning a mixture of PCL and chitosan solution in chloroform: methanol (3:1) and 90% acetic acid, respectively, as the first layer. The membranes were then immersed in collagen solution extracted from fish, followed by freeze-drying and crosslinking with EDC/NHS. Subsequently, an additional layer of fibers was electrospun onto the collagen-coated membranes to create a bilayer wound dressing (**Figure 2-11B**). This composite dressing exhibited significant wound contraction in a rat model of third-degree burn injury with the size of 2.5 cm×2.5 cm, achieving 96.99±0.5% closure after 20 days. This performance markedly surpasses that of the control Tegaderm dressing, which showed only 57.6±1.2% wound closure, with the bilayer dressing also resulting in less scar formation, **Figure 2-11B**. The faster re-epithelialization was attributed to enhanced cellular adhesion resulting from the interactions between cells and the collagen coating, notably binding to the collagen RGD sites. Despite the promise of emerging collagen sources in electrospun nanofibrous membranes for accelerated wound healing, traditional sources such as bovine and porcine collagen remain the most prevalent in wound healing research.

Su Rho et al. [186] addressed challenges associated with utilizing collagen for electrospinning. Membranes were prepared by spinning 8 wt% calf's collagen type I in HFIP at 0.02 mL/min and 15-20 kV, crosslinked with glutaraldehyde vapor. The initial *in vitro* results for human keratinocyte cells revealed a very low adhesion rate for the crosslinked collagen membranes, potentially due to collagen denaturation during electrospinning or crosslinking. To restore the bioactivity, they coated the nanofibrous collagen membranes with ECM proteins: collagen type I (50 μg/ml), fibronectin (1 μg/ml), or laminin (10 μg/ml). Cell adhesion improved with collagen type I and laminin treatments, but fibronectin did not have a significant effect. These results indicated that keratinocyte adhesion on the scaffolds is highly dependent on

integrating ligands. The collagen wound dressings tested *in vivo* with full-thickness wounds on rats (size of 1 cm×1 cm) demonstrated a faster healing rate within one week with fewer inflammatory cells, possibly due to enhanced bioactivity of the dressing via the presence of the coated ECM proteins.

Like many natural polymers, collagen exhibits insufficient mechanical properties. This lack in mechanical stability not only hampers the handling of pure collagen wound dressings but also impedes their ability to withstand external and internal forces during the healing process, thereby failing to provide adequate support for the wound [207]. The Young's moduli of collagen-based scaffold have been reported to be in the range of 40-50 kPa [208]. These values are significantly lower than Young's modulus of commercially available wound dressings, which generally ranges between 10-15 MPa [186]. Various approaches have been explored to enhance the mechanical properties of collagen-based wound dressings. These include crosslinking (using agents such as glutaraldehyde, EDC-NHS, and genipin), reinforcement with nanoparticles, blending with other synthetic or natural polymers [209], or employing collagen as a coating [206,210,211]. For instance, the E of collagen type I crosslinked with glutaraldehyde can reach around 10 MPa [186]. Coating collagen type I on a PCL-chitosan and PCL-gelatin matrix resulted in an E value of 3.98 ± 1.04 MPa, and 30.8 MPa ,[210] respectively. Consequently, careful consideration of the wound's type, severity, and location is essential in determining the most suitable technique.

Overall, collagen, the most abundant protein in the natural ECM, holds immense promise as the primary component for developing an anti-scar wound dressing. However, the potential of wound dressings can be further enhanced by creating hybrid scaffolds using other ECM proteins. Such hybrid scaffolds can potentially improve wound dressing performance by stimulating cell

behavior during wound healing and enhancing the physical properties of the wound dressing, including its mechanical properties. Finding the optimal concentration for preparing the hybrid scaffold is crucial, as this key factor significantly impacts the fabrication of nanofibrous collagen-based wound dressings. In the next section, we review combinations of collagen with different natural polymers as wound dressings.

2.6.2.2.2 Hybrids of Collagen with Other Natural Polymers

Combining collagen with other natural polymers can harness synergistic effects for wound healing. Researchers have incorporated the skin's natural ECM components, such as hyaluronic acid and tropoelastin, with collagen to mimic the natural supporting matrix of healthy skin. Additionally, the utilization of other natural polymers like chitosan has been investigated to leverage their unique properties for wound healing.

Hyaluronic acid is a glycosaminoglycan present in the ECM of human skin which is a high-molecular-weight polymer composed of disaccharide repeats of D-glucuronic acid and N-acetyl-D-glucosamine. Due to its polyanionic and hydrophilic properties, it can provide structure and viscosity to the ECM, playing a passive role in the biological processes of connective tissues [212]. The primary function of hyaluronic acid is to maintain skin hydration and osmotic balance. Two cell-associated receptors, CD44 and RHAMM (Receptor for HA-Mediated Motility), mediate the biological effects of HA. CD44 is distributed in tissues and is involved in different cellular activities such as leukocyte activation, cell adhesion and migration, and hyaluronic acid internalization. RHAMM is a key regulator of cell movements and is associated with cell migration after injury. The role of hyaluronic acid in wound healing is complex. Research has shown that in fetal scarless healing, the expression of hyaluronic acid and its receptor CD44 is significantly increased (**Figure 2-6**). Conversely, in fibrotic healing, increased

expression of CD44 is also reported compared to normal adult skin [213,214]. A comparison between normal fibroblasts and fibroblasts from hypertrophic scars revealed that while CD44 expression was significantly higher in hypertrophic fibroblasts, only 25% of cells expressing CD44 also expressed hyaluronic acid. Interestingly, when normal fibroblasts were incubated with hyaluronic acid, a time-dependent decline in CD44 expression was observed, a trend not seen in hypertrophic fibroblasts. Studies indicate that CD44 and hyaluronic acid expression in adult wounds are not correlated, and hyaluronic acid-cell surface binding differs between normal fibroblasts and hypertrophic fibroblasts. In hypertrophic fibroblasts, receptor-mediated attachment of hyaluronic acid to cell surfaces, followed by hyaluronic acid endocytosis, leads to HA degradation, explaining the reduced hyaluronic acid levels in wound areas. However, CD44 does not downregulate hyaluronic acid content in normal skin and fetal wound healing [212,213,215].

The molecular weight and concentration of HA are critical in wound healing. Native hyaluronic acid (>500 kDa) helps control inflammation, increase collagen type III expression in the initial stage of healing, and boosts TGF-β3 expression. In contrast, fragmented hyaluronic acid (<400 kDa) increases inflammation, collagen type I expression, and myofibroblast differentiation. Smaller hyaluronic acid fragments (<1 kDa) accelerate healing and prevent myofibroblast differentiation. In regard to concentration, high hyaluronic acid concentrations might interfere with integrin-mediated collagen adhesion due to a negative charge of hyaluronic acid [187,200,216]. Therefore, based on reviewed research, different fibroblast phenotypes exhibit distinct behaviors. While high expressions of CD44 and hyaluronic acid in fetal wound healing cannot be generalized to adult healing, careful consideration of hyaluronic acid size and concentration is crucial for effective wound healing strategies. Combining hyaluronic acid with

collagen could be beneficial for accelerated healing if both the size and concentration of HA are appropriately optimized. For instance, Hsu et al. [187] evaluated a combination of collagen with different concentrations of hyaluronic acid as a potential wound dressing. Hybrid collagen-hyaluronic acid nanofibers were fabricated by electrospinning collagen (8wt%) with varying concentrations of HA dissolved in a mixture of HFIP: FA at an applied voltage of 23kV. The biomimicking membranes, featuring nanofibers with an average diameter of 200 nm, stand as a successful example of replicating the skin's natural ECM. This achievement encompasses not only chemical composition but extends to the nano-scale environment, patterning, and fibers' diameter, closely mirroring the intricate structure of the natural ECM. It is worth highlighting that the concentration of hyaluronic acid profoundly impacts cellular behavior during the wound healing process. Thus, Hsu et al. aimed to identify the best concentration of HA to achieve scar-free wound healing. Among samples with different concentrations of HA (0.5, 1, 1.5, and 2 mg/mL), the sample containing 1.5 mg/mL HA demonstrated the lowest expression of CD44, tissue inhibitors of metalloproteinases (TIMPs)/MMPs that could lead to scarless healing by mimicking the microenvironment of naturally healthy skin [187].

Tropoelastin, the precursor to elastin, has been combined with collagen to create an ECM-mimicking dressing that provides substantial support for wound healing [217]. Elastin, a vital component of healthy skin, is often absent or low in healing and scarred tissue. Providing its precursor through a wound dressing enhances its expression and promotes scar-free wound healing. Keller et al. [217] fabricated a nanofibrous wound dressing composed of a 9:1 blend of human dermal collagen and recombinant human tropoelastin. The electrospinning process was conducted using HFIP as the solvent at a voltage range of 24-27 kV. This dressing promoted accelerated wound closure in a diabetic murine full-thickness wound model (wound diameter of

8 mm) compared to a commercial Oasis dressing. Additionally, the dressing exhibited a closer resemblance to native skin and showcased the emergence of follicular neogenesis after 28 days of remodeling – a phenomenon absent in the control group. These findings highlight the potential of ECM-mimicking dressings, enriched with tropoelastin and collagen, to significantly accelerate wound healing [217].

Collagen-chitosan combinations are also promising. Chen et al. [188] fabricated a chitosan-collagen wound dressing via electrospinning. A polymer solution comprising chitosan, collagen and PEO was prepared using a mixture of acetic acid and deionized water as the solvent system. The solution was subsequently electrospun at a voltage range of 20-34kV. Chitosan, a positively charged polymer, facilitates faster hemostasis and possesses antibacterial properties, thus accelerating healing by reducing the time required for hemostasis and minimizing the risk of infection. In *vivo* studies (rat model with 2cm×2cm full-thickness wounds) showed the crosslinked collagen-chitosan wound dressing's potential for accelerating wound healing, reducing wound size to less than 5% after 21 days [188]. Moreover, chitosan can induce a biphasic cellular response that promotes wound healing, as evidenced by upregulated TGF- β 1 expression during early wound healing stages and down-regulated TGF-β1 expression in late stages [206][218]. This effect of chitosan on TGF-β1 levels is particularly beneficial for improved wound healing since high expression of TGF-β1 in the early stages promotes wound contraction, while extended high expression in later healing stages can contribute to scarring [219]. Apart from collagen, gelatin, the denatured version of collagen, also holds potential for wound application, and its use is explored in the following section.

2.6.2.2.3 Gelatin

Gelatin, a denatured form of collagen, has garnered significant interest in tissue engineering due to its lower antigenicity and reasonable cost compared to collagen. Gelatin features essential components like the RGD sequence, glycine, proline, and hydroxyproline, which are crucial in influencing cell behavior and promoting faster healing. Dubsky et al. [182] demonstrated gelatin's potential to accelerate wound closure, compared to a synthetic polymer PCL. Gelatin and PCL membranes were fabricated via electrospinning. Gelatin membranes were prepared using an acetic acid solution, while PCL membranes were produced using a THF/DMF solvent system. Although both membranes supported cell adhesion, gelatin effectively mimicked the natural ECM of the skin, leading to promising impacts on wound healing such as higher cell proliferation, ultimately decreasing wound area (by 80% in a rat model with 8 mm diameter full-thickness wound). These findings highlight the promising potential of gelatin-based wound dressings in tissue engineering applications. Another natural polymer abundantly found in the ECM is fibronectin, which shows promise for accelerated wound healing. It is discussed in detail in the following section.

2.6.2.2.4 Fibronectin

Fibronectin is a crucial fiber-forming protein in the ECM of the skin, playing a significant role in natural scar-free healing. This versatile protein influences wound healing in both soluble and insoluble states in plasma and ECM. In acute wounds, soluble fibronectin transitions to an insoluble form upon interacting with cells and binding to integrin receptors, particularly on fibroblasts. This interaction recruits more fibroblasts to the wound bed and enhances their migration, which is crucial for the healing process [200]. Fibronectin's multiple domains allow it to interact with many cells, biomolecules, and proteins, facilitating the

deposition of mature and stable ECM during wound healing. In the case of using fibronectin for a wound dressing application, Chantre et al. [183] developed a rotary jet with high extensional and shear strain to fabricate fibronectin's fibrillar conformation, resembling a basket-weave pattern to preserve its activity, **Figure 2-11C**. Fibronectin nanofibers with a mean diameter of 427 ± 138 nm, mimicking the natural diameter range of 5-1000 nm for cell-derived native fibronectin fiber [220], were employed in a murine full-thickness wound model. When topically applied and secured with Tegaderm, these nanofibers accelerated the healing rate within 11 days and reached full wound closure in two weeks, while for the control group, 16 days were required for full wound closure., **Figure 2-11C**. Staining results revealed that after 20 days, the fibronectin-treated wound exhibited a similar architecture to natural skin, particularly regarding the thickness of the layers. This was attributed to the faster wound contraction, allowing enough time for the layers' maturation, in addition to fibronectin's positive effect on ECM remodeling. Moreover, fibronectin's key role in recruiting cells further influenced the healing process, as migrated adipocytes restored the adipose layer, provided support to the epidermis and dermis layers, and ultimately reduced scar tissue formation. These findings underscore the potential of fibronectin-based wound dressings in promoting accelerated wound healing and scarless tissue regeneration. **Table 2-3** presents a comprehensive summary of all the reviewed papers and their respective outcomes concerning the wound healing procedure.

Biomimicking the structure and composition of the natural ECM is a promising strategy to accelerate the wound healing rate and mitigate the risk of scar formation. A dynamic and complex interaction between ECM, cells, and secreted biomolecules in healthy tissue maintains tissue homeostasis and facilitates tissue regeneration. However, as previously highlighted, this delicate balance is disrupted in severe and chronic wounds. In such situations, delivering

biomolecules, agents, or therapeutic substances to the injured site can help guide cells to respond as they would under normal conditions. Since electrospun wound dressings exhibit remarkable capabilities for loading therapeutic agents into their nanofibrous structures, the following section delves into a thorough exploration of diverse biological, chemical, or natural substances embedded within nanofibrous wound dressings. These substances, referred to as chemical cues, are investigated for their role in amplifying the dressings' healing potential.

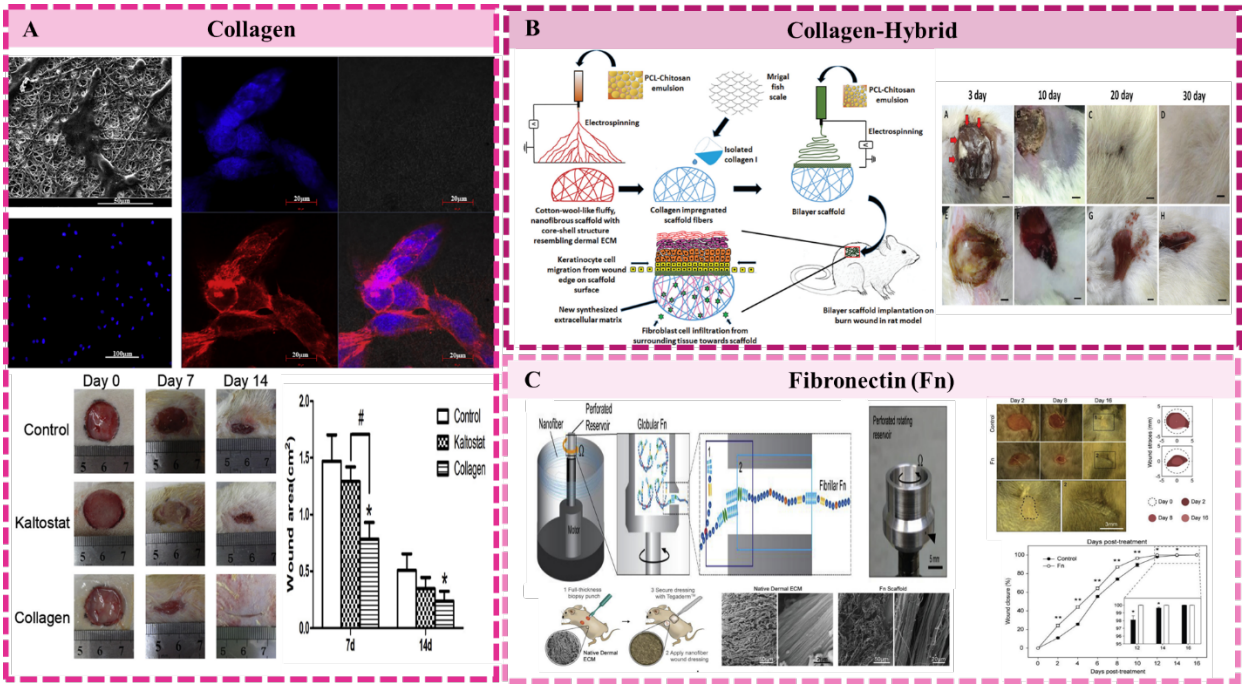

Figure 2-11 Compositional cues

This figure illustrates the influence of various natural polymers in engineered wound dressings on wound healing. A) Collagen: A wound dressing based on marine collagen enhanced the adhesion of human keratinocytes (HaCaTs), a crucial factor for scar-free wound healing. SEM, fluorescent, and confocal images show cells on the membranes. In a rat model, this wound dressing led to complete wound closure within two weeks, resulting in less scar formation than a commercial wound dressing (Kaltostat), Reprint with permission from [185] Copyright 2016 Elsevier. B) Collagen Hybrid with Other Natural Polymers: A multilayered wound dressing was created by electrospinning an emulsion of PCL-Chitosan, coating it with collagen, and adding another layer to mimic skin structure. This approach achieved accelerated and scar-free healing, as evidenced by faster wound closure (top) in a rat burn model compared to Integra wound dressing (bottom), Reprint with permission from [221] Copyright 2017 Royal Society of Chemistry. C) Fibronectin: A fibrous wound dressing was produced using rotary jet spinning, closely resembling the architecture of the native dermal ECM. This dressing accelerated wound healing within two weeks while minimizing scar formation. Reprint with permission from [183] Copyright 2018 Elsevier.

2.6.2.3 Chemical Cues

During the 1950s and 1960s, the primary aim of biomaterials was to provide adequate support to injured tissues or to substitute their functions. However, with the progression of tissue engineering and regenerative medicine into the late 1980s, the emphasis began to shift towards guiding cellular processes to initiate the repair and regeneration of damaged tissues. This transition marked a significant evolution in the field, moving from a focus on passive support and replacement to actively facilitating the body's natural healing mechanisms through advanced biomaterials and engineering techniques [222]. Meeting this requirement hinges on effectively transmitting signals to cells and providing them with directives for optimal performance. These signals are conveyed either through the scaffold's physical properties and composition or are directly administered to cells using chemical agents. Biochemical agents, referred to as chemical cues, encompass a range of substances, including proteins and peptides (such as enzymes, antibodies, and growth factors), nucleic acids (such as DNA, RNA, and aptamers), small molecules (such as pharmaceuticals drugs/inhibitors, vitamins and hormones), natural extracts and derivatives (such as plant extracts, essential oils, animal-derived compounds and microbial metabolites) and nanomaterials and particles (such as liposomes, dendrimers, quantum dots and metal and metal oxide nanoparticles). By harnessing these diverse chemical cues, researchers aim to guide cells effectively and unlock their potential for tissue restoration and regeneration.

A comprehensive understanding of the tissue's intricate cellular communication networks is essential for the rational selection and delivery of chemical cues to elicit desired cellular responses. The cellular microenvironment within the tissue is a complex ecosystem where cell-cell interactions, cell-ECM interactions, and various signaling pathways regulate crucial biological processes. Within the body, essential communication between cells and the ECM is

facilitated by proteins known as cytokines and growth factors. This section reviews the effect of various chemical cues loaded into nanofibrous wound dressings. First, growth factors are reviewed as the primary chemical cue for promoting wound healing. Then, four other chemical cues are reviewed for their role in mitigating factors that contribute to delayed healing, including prolonged inflammation, the presence of infections, abnormalities in gene expression, and inadequate angiogenesis. Addressing these critical disruptions in the normal wound healing process by incorporating active bioagents in nanofibrous dressing can lead to enhanced healing outcomes and reduced scar formation.

In order to evaluate the improved healing outcome in the presence of different chemical cues released from the nanofibrous, *in vivo* evaluations are required. In *in vivo* wound healing assays, the type of the wound, as well as the animal model, are of paramount importance. Most *in vivo* models in this field have full-thickness or burn wounds in rodents (mice and rats) with impaired (diabetic) or normal healing; however, the size of the wound varies in different studies. Despite physiological differences in skin between rodents and humans, rodent models are invaluable for studying human wound-healing mechanisms, thanks to the substantial genetic similarities in wound healing shared between the two. Rodents are also favored for their ease of handling and genetic modifiability, facilitating the study of specific outcomes or disease models [223,224]. However, the presence of the *panniculus carnosus* layer in rodent skin, which is absent in most human skin, leading to rapid wound contraction in these models. To mitigate this, some researchers employ methods such as surrounding the wound with a silicone ring to prevent contraction. Notably, rat models have outcomes more closely aligned with human wound healing processes. This is partly because mouse skin has a thinner epidermis with a lower keratinocyte population, and it undergoes more rapid healing, whereas healing in rat models can be extended

[223,224]. Given the size difference between these two species, it is crucial to adjust the wound size proportionally to ensure relevant and translatable results. This section is dedicated to elucidating the impact of diverse chemical cues on wound healing dynamics within murine and rodent models. The primary goal is to identify optimal combinations of these cues that promote expedited healing while attenuating scar formation. It is imperative to acknowledge the inherent limitations of these models in accurately recapitulating human scar formation. Consequently, extrapolating the influence of tested chemical cues on scar minimization within the context of nanofibrous wound dressing requires cautious interpretation.

2.6.2.3.1 Growth Factors

Natural healing processes rely on a balance of the secretion of various biomolecules, governing cell interactions and tissue regeneration within the injured area. However, internal and external factors can disrupt this balance, leading to overexpression or suppression of certain growth factors during the healing process, ultimately causing healing disruption. To address this issue, one approach involves manipulating biological mediators, specifically growth factors, to effectively communicate with cells and prompt them to act in a manner that facilitates skin regeneration. Delivery of growth factors to the wound site, either individually or in combination with other bioactive agents, can be effectively achieved using electrospun nanofibrous dressings. Key growth factors involved in wound healing are TGF-β, EGF, basic Fibroblast Growth Factor (bFGF), vascular endothelial growth factor (VEGF), and PDGF.

Growth factors can be incorporated directly into nanofibers to facilitate sustained and fast release. However, their bioactivity may be compromised when incorporated into polymer solutions containing organic solvents for electrospinning. An *in vitro* release study could be conducted to assess the bioactivity of growth factors incorporated within the wound dressing.

The wound dressing could be immersed in simulated wound fluid, and the released growth factors could be quantified and assessed for their ability to induce cell proliferation compared to the original, untreated free growth factors. If the cellular responses of the released growth factor from wound dressing are close to the free growth factor, it can be concluded that the bioactivity of the growth factors is preserved throughout the fabrication process [109]. One way to overcome the problem of diminished bioactivity caused by the organic solvent is employing core-shell structures, wherein the polymer substrate is dissolved in an organic solvent to form the shell, while the growth factor is dissolved in an aqueous solution of hydrophilic polymers such as PVA and PEG to form the core. A core-shell nozzle keeps the growth factor isolated from the organic solvent, preserving its bioactivity [110]. Additionally, physical adsorption by immersing the nanofibrous wound dressing in growth factor solution serves as another method to prevent the deactivation of growth factors [113]. It is important to note that due to the absence of chemical binding or encapsulation within the nanofibers, this technique often results in an initial burst release of the growth factors. This rapid release can occur in the initial hours following application, which may not be ideal for prolonged therapeutic effects.

For delayed-release applications, encapsulating the growth factors within NPs before their loading into the nanofibers can mitigate deactivation and facilitate controlled release [114]. Immobilizing growth factors on nanofibers presents another alternative strategy for delaying their release. This method not only preserves the bioactivity of growth factors during the fabrication process by avoiding direct contact with organic solvents but also maintains their bioactivity at the wound site [113]. The early stages of wound healing (such as the inflammation stage), characterized by its abundance of enzymes and high proteolytic activity, can lead to the rapid degradation of certain growth factors, such as EGF [225]. Conventional delivery methods,

including direct injection or sustained release from nanofibrous dressings, might not be effective in such conditions. Conjugating growth factors directly to nanofibers for their sustained release extends their availability to cells, which could significantly improve the healing outcomes and therapeutic potential of the wound dressing [113].

The method of incorporating the selected growth factors should be chosen with consideration of their desired release timeline. For instance, in cases where the delivery of two growth factors is required with different timelines, the strategies of direct loading and conjugation can be combined. This has been done for the delivery of bFGF and EGF through a nanofibrous membrane by loading bFGF directly into the core consisting of PVA while the shell consists of PCL-PEG-NH_2 block copolymer/PCL. This design led to a rapid 30 % release of bFGF within 12 hrs due to diffusion, whereas EGF conjugated onto the nanofibers through carbodiimide chemistry had a delayed release of less than 20% in one week [110]. Another technique for achieving delayed release is the incorporation of growth factors into nanoparticles. With this technique, the dressing can be engineered to deliver the desired growth factors at a specific time during wound healing. For instance, this technique has been used to achieve rapid vascularization in the initial stage of healing, followed by the maturation of vessels in later stages. The rapid vascularization and epithelization require specific fast release of growth factors such as PDGF and EGF in the initial days, while vascular maturation is governed by other growth factors such as bFGF and VEGF in later days. To satisfy these demands, a hyaluronic acid-collagen nanofibrous wound dressing was fabricated by directly loading PDGF and EGF into the nanofibers for fast release through diffusion (50% for PDGFand 30% for EGF on the first day). The other two growth factors requiring late release were loaded into gelatin NPs and

then loaded into nanofibers. This allowed delayed release of them depending on the rate of NPs degradation (less than 10% on the first day) [114].

Upon verifying the bioactivity of growth factors loaded into the nanofibrous wound dressing, *in vitro* cellular assays can evaluate their role in the expression of various biomarkers associated with accelerated and scarless healing. The main cell types used for these assays are fibroblasts and keratinocytes [113]. Additionally, for dressings designed for rapid vascularization, endothelial cells such as human umbilical vein endothelial cells (HUVECs) are also employed [114]. Beyond cytotoxicity and proliferation assessments, more specific data can be obtained from special *in vitro* cellular tests. Given that one of the advantages of nanofibrous wound dressings is their ability to emulate the structure of natural skin, assays focused on cell adhesion and migration are commonly employed to substantiate this claim [109]. Typically, in such assays, the negative control comprises cells cultured without any treatment to serve as a baseline for comparison, while the positive control is usually a commercially established wound dressing known for its efficacy, providing a benchmark for the performance of the nanofibrous dressing. Examining *in vitro* cell phenotypes of the cells, especially keratinocytes and fibroblasts, are of significant importance when it comes to assessing accelerated and scarless healing [113]. For instance, the maintenance of keratinocytes in their native morphology is crucial for skin regeneration, whereas alterations in the phenotype of keratinocytes can trigger a series of events leading to the overproliferation of fibroblasts and their subsequent differentiation into myofibroblasts during healing processes. Hence, the assessment of keratinocyte phenotypes is critical and can be conducted through the analysis of specific markers such as keratin 1 and loricrin expression [113].

Following *in vitro* assessments, the subsequent phase involves *in vivo* evaluation of nanofibrous wound dressings loaded with growth factors to investigate their efficacy in the wound healing process. One of the common wound models for evaluating the performance of these dressings is full-thickness wounds (excisional wounds). In this model, the wound is created by the complete removal of skin layers—epidermis, dermis, and subcutaneous fat—without suturing the wound edges. This allows for the comprehensive study of all healing phases, including hemostasis, inflammation, granulation tissue formation, epithelialization, and angiogenesis. Typically, the progression of wound closure is monitored through serial photography, documenting changes in wound size and rate of closure over time. The percentage of wound closure, also known as healing rate, is calculated based on the following equation.

$$Wound\ Closure\ \% = \frac{(A_0 - A_x)}{A_0} \times 100 \qquad \textit{Equation 2-3}$$

Where A_0 is the wound area at time 0, and A_x is the wound area at the desired time point.

Additionally, biopsies of the healed tissues are subjected to histological and immunohistological analyses to assess various parameters, such as the expression levels of growth factors, cytokines, collagen deposition, and the prevalence of different cellular populations within the healing tissue. To introduce a context of delayed or impaired healing, diabetic animal models are often utilized. This approach facilitates the examination of the wound dressing's effectiveness in environments characterized by compromised healing capabilities, providing insights into the potential therapeutic benefits of the dressing in challenging clinical scenarios [223,224].

In diabetic mouse models, full-thickness wounds (approximately 8 mm in diameter) can take up to 2 weeks to achieve 80% or greater closure without any wound dressing. Applying nanofibrous wound dressings loaded with growth factors can significantly expedite this healing

process. The extent of acceleration depends on factors such as the specific growth factor used, the method of incorporation into the nanofibers, the polymer substrate composition of the dressing, and the incorporation of additional substances.

Notably, the use of a combination of two growth factors, each with distinct release kinetics, has been observed to result in the most rapid and effective healing outcomes [110]. Nanofibrous dressings were fabricated using a core-shell technique, with b-FGF in a PVA core and PCL-PEG-NH_2 block copolymer/PCL in the shell. The second growth factor, EGF, was immobilized on the surface of the nanofibers through amine-carboxylic acid binding. This design facilitated the rapid release of b-FGF (30% within 12 hours) while maintaining a constant presence of EGF on the nanofibers' surface. Wounds treated with this dual growth factor-loaded dressing experienced 35% closure within just 4 days, marking a 25% improvement over the untreated control group. After one week, wounds treated by the wound dressing with both growth factors achieved nearly complete healing (95%), in stark contrast to 50% closure in the control group. It is noteworthy that dressings loaded solely with b-FGF or EGF did not achieve full closure within a week, reaching 80% and 70% closure, respectively. The phenotypic expression levels of keratinocyte-specific genes (keratin 14, 5, 10, and 1) in the healed tissue indicated that all genes were expressed in wounds treated with the nanofibrous dressing loaded with b-FGF and immobilized with EGF. This expression pattern suggests that keratinocytes maintain their phenotype, contributing to natural healing processes. The presence of keratin 5 and 14, associated with the basal layer regeneration, alongside keratin 1 and 10, related to the granular layer regeneration, confirmed the complete regeneration of the epithelial layer structure. In contrast, dressings loaded solely with b-FGF facilitated only basal layer repair, whereas samples with only EGF loading did not fully develop even the basal layer. Histological

evaluations revealed collagen and keratin deposition in the healed tissues. Incorporating b-FGF into the nanofibers at a concentration of 0.98 μg per sample required less growth factor compared to other delivery methods which require between 2 to 100 μg, while the clinically optimal amount is 1 $\mu g/cm^2$ [226]. Conjugating EGF to the fibers appeared to reduce its deactivation rate, thereby preserving keratinocyte phenotypes [110]. These findings underscore that the accelerated tissue regeneration observed was achievable only through the synergistic application of both growth factors, highlighting the efficacy of combining b-FGF and EGF in nanofibrous wound dressings for enhanced healing outcomes.

Incorporating Aloe vera (AV), a natural component, with growth factors represents an alternative approach to expedite healing in this *in vivo* model [109]. While the healing rate with the AV and growth factor combination did not surpass that of the dual growth factor strategy, it achieved a closure rate (60%) exceeding that of the untreated control group (25%) in a week. The nanofibrous dressing was fabricated through emulsion electrospinning, blending EGF and AV with PVA in the aqueous phase and PLGA in HFIP as the organic phase. The bioactivity of the EGF in the electrospun samples was confirmed through fibroblast assays, indicating the preservation of EGF's bioactivity post-fabrication. Known for its anti-inflammatory and antibacterial properties, AV was effective against *Staphylococcus aureus* and *Staphylococcus epidermidis*. This antibacterial activity is attributed to AV's components, such as α-bisabolol, lupeol, cinnamic acid, salicylic acid, and uric acid, which interfere with bacterial enzymatic processes. The synergistic effect of AV and EGF resulted in a 15% increase in wound closure within four days compared to the control or samples treated solely with free EGF. By the end of one week, wounds treated with the EGF and AV combination exhibited 60% closure, complete re-epithelialization albeit with irregular thickness, and full resolution of chronic inflammation.

Although this combination did not achieve as rapid and complete wound closure as the dual growth factor approach, it significantly (*p-value*<0.05) outperformed the control and EGF-only treatments, with less than 50% closure by the end of one week. These findings highlight the importance of combining growth factors with other bioactive materials to enhance healing outcomes [109].

The least effective performance in terms of accelerating healing in this *in vivo* model was observed with nanofibrous wound dressings made of a mixture of PCL and PCL-PEG-NH_2 block copolymer, to which EGF was conjugated [113]. As noted earlier, the conjugation of EGF can preserve the keratinocyte phenotype, as evidenced by the *in vitro* expression of Keratin 1 and loricrin. Although the conjugated EGF was not released to interact with cells, it was still directly engaged with EGF receptors in keratinocytes. The immobilization of EGF on the nanofibers resulted in a 45% closure rate within one week and 95% closure by the end of two weeks. While this did not yield significantly accelerated healing compared to the untreated control in two weeks with an 80% closure rate (*p-value* >0.05), the study highlighted the significant role of EGF in the initial stages of the healing process since there was a 30% increase in the healing rate compared to the control in the first week. Moreover, the findings underscore the advantage of covalent conjugation of EGF over physical loading of EGF, which showed a 20% and 60% closure rate in one and two weeks, respectively [113] Notably, the closure rate in the control group (80%) surpassed that of the group treated with physically loaded EGF (60%). The study does not provide an explanation for this outcome, indicating the necessity for further investigation to elucidate the mechanisms underlying the delayed healing observed in the physically loaded EGF-treated group

Considering that the reviewed studies on diabetic mice with full-thickness wounds predominantly employed synthetic polymers, a comparative analysis reveals that the combined application of two growth factors is more effective than the combination of a growth factor with a natural component, and both approaches are more efficacious than using a single growth factor for achieving faster wound closure. Furthermore, it is crucial to highlight that the design of nanofibrous wound dressings, particularly in terms of the growth factor release kinetics, plays a significant role in facilitating accelerated healing, emphasizing the importance of strategic formulation and functionalization in the development of wound healing dressings.

Another *in vivo* model for assessing accelerated healing in full-thickness wounds with growth factor-loaded nanofibrous wound dressing is the rat model. In this model, the size of the wound significantly influences the healing rate; for example, a larger wound with a diameter of 15 mm may require up to 6 weeks to achieve complete closure without any treatment, whereas a smaller wound of 5 mm diameter could heal fully within a month. Rat models are particularly favored for studying angiogenesis during wound healing, especially when examining the efficacy of nanofibrous wound dressings loaded with endothelial-related growth factors. Chronic wounds often exhibit prolonged healing due to impaired interactions with surrounding tissues, low cellular migration, and inadequate angiogenesis. Thus, promoting vascularization at the wound site is imperative, as it facilitates the supply of oxygen and nutrients while also creating conduits for the delivery of critical soluble biomolecules and cells. The angiogenesis process can be significantly expedited by employing nanofibrous wound dressings as vehicles for the targeted delivery of various endothelial growth factors. Such strategies can be evaluated within rat models to determine their efficacy in promoting enhanced wound healing.

In a study employing a rat model with a small 5 mm full-thickness wound, a chitosan-based nanofibrous dressing containing VEGF and PDGF-loaded PLGA NPs was used [116]. VEGF exhibited a rapid release profile, with 63% released within the first hour and a complete release within a day due to diffusion. Conversely, PDGF encapsulated in PLGA NPs demonstrated a controlled release, with 28% released in two hours and 40% over a week, attributed to a combination of diffusion and NP degradation. The bioactivity of the loaded growth factors was assessed using fibroblast cultures, confirming 100% bioactivity. Notably, the proliferation rate in the presence of growth factors loaded nanofiber exceeded that of the free and pure growth factor. This demonstrates the enhanced biological properties of the dressing, likely due to the higher surface area provided by nanofibers compared to tissue culture plastic. The increased surface area allows cells more space to grow before reaching confluency, thereby prolonging the proliferation phase.. *In vivo* results revealed a 40% reduction in wound size within the first week for dressings containing growth factors, compared to a 20% reduction for the control group with no dressing. The treated wound with growth factor-loaded dressings exhibited more granulation tissue, regenerated epidermis, and new capillary formation. By the second week, the growth factor-loaded dressing had achieved an 80% wound closure, with a decrease in granulation tissue, indicating a progression from the inflammatory phase. This was attributed to the synergistic effects of the growth factors and the anti-inflammatory properties of chitosan. Additionally, collagen deposition and myofibroblast presence were significantly higher in treated wounds compared to controls during these weeks. By the fourth week, complete wound closure was observed in the growth factor-treated samples, with reduced collagen and myofibroblast levels and evidence of hair regrowth and minimal scarring, while the control group reached only 90% closure with a visual scar and no hair regrowth. These results emphasize

the significant effects of combining two growth factors—VEGF and PDGF—on promoting accelerated wound healing within four weeks and reducing scar formation. VEGF plays a crucial role in early-stage blood vessel formation, while PDGF contributes to epithelialization and collagen synthesis, demonstrating a synergistic approach to enhancing the wound healing process [116].

In the context of larger wounds, which more closely mimic human wound scenarios, a diabetic rat model featuring a 15 mm diameter full-thickness wound was employed to assess the impact of various growth factor combinations and HA-collagen substrates on the healing process [114]. The healing in the presence of HA-collagen nanofibrous wound dressings loaded with bFGF, EGF, VEGF, and PDGF resulted in significantly expedited healing within 4 weeks, while the control in the same wound needed more than 6 weeks. Moreover, the rate of wound closure was notably quicker than that closure rate observed in smaller, 5 mm wounds in non-diabetic rats, which took up to 5 weeks to heal, despite the fact that the treated wound was three times larger and exhibited impaired healing capabilities. This represented a notable improvement, being 2 weeks faster than the untreated control group. The observed acceleration in wound healing was attributed to the engineered design of the wound dressing, which includes a strategic release timeline for the growth factors and a composition that closely emulates the natural ECM. The nanofibrous membrane was designed to initiate a burst release of EGF and bFGF during the early phases of wound healing, aiming to expedite epithelialization and vascularization. Subsequently, a delayed release mechanism was implemented for PDGF and VEGF, which were encapsulated in gelatin NPs to facilitate the maturation of newly formed vascular structures (**Figure 2-13A**). The bioactivity of the membranes were assessed using HUVECs since electrospinning solvents like acetic acid and DMF may risk compromising the growth factor

bioactivity. These evaluations not only confirmed the preserved bioactivity of the growth factors within the samples but also revealed that the incorporation of HA and collagen into the membranes further enhanced cellular proliferation rates by twofolds, underscoring the synergistic benefits of combining bioactive molecules with supportive ECM components in wound healing applications. The *in vivo* outcomes revealed that by the first week, nanofibers laden with all four growth factors achieved 26% closure, whereas the control group, without any treatment, exhibited no significant closure rate of less than 10%. Histological analyses at this stage indicated the formation of new epidermal layers and the regeneration of the papillary basement membrane in samples containing all four growth factors, signifying the beginning of epidermal and dermal junction regeneration. Additionally, there was an increase in Ki-67 gene expression, a marker for myofibroblast proliferation, within the first week. By the fourth week, the samples incorporating all four growth factors had completely healed, characterized by a decreased expression of Ki-67, high neovascularization, and the regeneration of all four epidermal layers. During the healing process, a notable shift in collagen expression was observed; collagen type III exhibited high expression levels in the initial healing phase but decreased by the fourth week, whereas collagen type I showed low initial expression with a subsequent increase, indicating a transition from collagen type III to collagen type I fibers, similar to the natural healing process in adults. In contrast, nanofibers incorporating two free growth factors achieve only 80% wound closure after four weeks, significantly lagging behind the complete closure observed in nanofibrous membranes containing four growth factors within the same timeframe. While nanofibers with two growth factors eventually attained full closure at six weeks, outperforming the control group, which still had not fully healed, these findings

emphasize the potential advantages of a more comprehensive growth factor profile in accelerating wound healing [114].

The findings obtained from rat models align with results from mice models, underscoring the efficacy of combining multiple growth factors in enhancing healing speed and promoting skin regeneration over mere repair. A comparative review of all studied papers underscores the significance of tailoring the release profiles of various growth factors to optimize their bioavailability at different healing stages, which in turn can significantly impact the overall healing outcomes. Moreover, the results suggest that the use of natural polymers as substrates may enhance the effectiveness of growth factors, further accelerating the healing process. **Figure 2-12** offers a comprehensive overview of the growth factors that can accelerate wound healing.

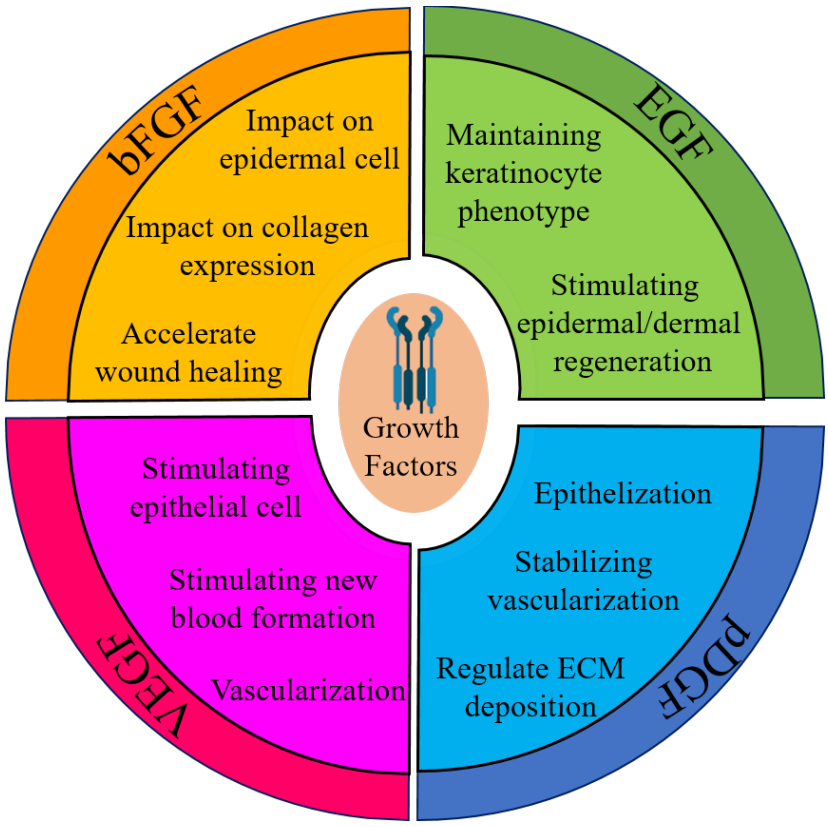

Figure 2-12 Loaded growth factor in nanofibrous wound dressing for reaching accelerated and scar-free healing and their roles in wound healing.

In addition to growth factors, a range of bioactive agents can serve as chemical cues to accelerate the wound-healing process through anti-inflammatory, angiogenic, and anti-scar capabilities. Selecting the appropriate chemical cue necessitates a comprehensive evaluation of the wound's unique microenvironment and condition. In the subsequent section, we explore the diverse factors causing delayed healing and elucidate potential chemical cues to mitigate these issues.

2.6.2.3.2 Agents for Controlling Inflammation

The inflammatory stage is a pivotal phase within the wound healing process that can affect the trajectory of healing toward regeneration or repair. During this stage, the elimination of cellular, extracellular, and pathogenic debris from the wound bed typically occurs from day one up to a week in the healing process. Nonetheless, any form of interference can prolong this inflammatory stage, intensifying the presence of neutrophils and ROS at the wound site, which can cause the development of scars [227]. Beyond its role in pathogen defense, this phase is characterized by the secretion of growth factors and cytokines, including TGF, PDGF, TNF, IL-1α, IL-1β, IL-6, and IL-8. These bioactive agents exert significant influence over immune cells and fibroblasts, orchestrating the formation of a temporary connective tissue scaffold based on collagen type III. In the later stages, this temporary ECM is replaced by mature collagen type I fibers. However, the severe wound scenario is marked by a delayed transition from the inflammatory stage to subsequent phases. This delay results in an excessive accumulation of ECM, mainly comprised of collagen type I, impeding the progress of tissue renewal and resulting in scar formation [228,229].

Considerable efforts have been directed towards mitigating inflammation in wound management through diverse methodologies and materials. The forefront of this endeavor

spotlights delivery systems distinguished by sustained bioactive agent release profiles [230]. Within different delivery systems, electrospun nanofibrous membranes have emerged as a promising option for encapsulating and controlling the release of therapeutic agents to manage inflammation [182,183]. Therapeutic agents aimed at mitigating the prolonged inflammatory phase can be selected from a broad spectrum of bioactive substances, including pharmaceuticals and natural extracts and derivatives materials such as herbal/plant extracts.

In the group of pharmaceuticals, various non-steroidal anti-inflammatory drugs (NSAIDs) are utilized in wound healing, including ibuprofen (IBU) [231], diclofenac [232], dexamethasone [233], phenylbutazone [233], and piroxicam [234]. Their mechanism of action in controlling inflammation involves modulating Prostaglandin E2 (PGE2)-lipids in the injury sites, which is produced from arachidonic acid by cyclooxygenases (COX) and prostaglandin E synthases (PGES). PGE2 serves both as an inflammatory mediator and a fibroblast modulator. The release of PGE2 following toxic stimuli can induce local edema and hyperalgesia. NSAIDs, including selective COX-2 inhibitors, effectively manage inflammation and pain by suppressing PGE2 synthesis [235,236]. Despite their cost-effectiveness, availability, and common use for pain management, the impact of NSAIDs on wound healing remains a subject of debate. In the short term, in addition to anti-inflammatory effects, PGE2 has been shown to decrease fibroblast proliferation, inhibit collagen synthesis, and increase the expression of MMPs, which all translate to less scar formation. However, in the long term, anti-inflammatory agents, such as COX-2 inhibitors, could negatively affect fibroblasts and keratinocyte phenotypes and proliferation and impair wound healing processes [236]. Consequently, the dosage and route of administration of these drugs are of paramount importance.

In addition to NSAIDs, naturally derived compounds offer potential for modulating the inflammatory response. In earlier eras, wound management predominantly hinged upon regionally procured elements, commonly encompassing herbal, animal, and naturally sourced products [237]. Despite the remarkable steps achieved in wound care practices, natural extracts and derivatives continue to find relevance within this domain. To optimize the efficacy of these natural components, they have been incorporated into carrier systems, with electrospun nanofibers demonstrating exceptional effectiveness. The electrospinning technique, which is used to fabricate these nanofibers, is particularly advantageous due to its broad solvent compatibility, allowing for versatile and effective integration of various natural components. The natural anti-inflammatory agents typically control the inflammation via one of two primary mechanisms. The first mechanism involves their interaction with excessive ROS. Many natural anti-inflammatory substances exhibit antioxidant capabilities, primarily attributed to the presence of polyphenolic groups within their molecular structure. These compounds can donate electrons to ROS, thereby preventing the progression of ROS-induced damage by converting the excessive ROS into more stable molecules and mitigating toxicity associated with elevated ROS levels. Alternatively, natural anti-inflammatory agents can exert direct effects on inflammatory cells, particularly macrophages, facilitating a swift transition from the pro-inflammatory M1 phenotype to the anti-inflammatory M2 phenotype, thereby shortening the inflammation phase [238].

Natural-based products are often considered preferable to pharmaceutical drugs due to fewer side effects, yet their usages have some challenges. Key obstacles are associated with the extraction and purification processes. Despite advancements in these areas, a significant limitation persists the low yield of active compounds from natural sources. Moreover, the use of

toxic solvents such as DCM, methanol, or hexane in the extraction process poses a risk of residual solvent contamination, which could lead to cytotoxic effects. In addition to extraction challenges, the solubility of these natural substances may restrict their routes of administration and bioavailability at the wound site [238].

Despite the challenges associated with both drug-based and natural-based anti-inflammatory components, numerous studies have focused on their incorporation into nanofibrous wound dressings. In evaluating the efficacy of these bioactive dressings for wound healing, several properties are considered crucial, including antioxidant capabilities, release kinetics, cytocompatibility, and, most importantly, the ability to achieve *in vivo* wound closure. The evaluation of antioxidant capabilities and cytocompatibility of materials is often performed using *in vitro* cell culture and gene expression studies. To assess antioxidant properties, cells are initially cultured with agents like hydrogen peroxide, which elevates ROS levels. Subsequently, the nanofibrous dressing, loaded with an anti-inflammatory agent, is introduced to the cell culture. Thereafter, the activity of enzymes such as Superoxide Dismutase (SOD) and Catalase, which play crucial roles in protecting cells from oxidative damage, is then measured. Furthermore, the expression of genes related to these antioxidant enzymes, including Catalase, CuZnSOD, ecSOD, and MnSOD, is analyzed to determine the material's antioxidant and anti-inflammatory effects. For example, in one study, PCL nanofibers loaded with *Spirulina* extract were utilized to assess both the enzymatic activities and gene expression levels of fibroblasts exposed to the dressing and hydrogen peroxide [194]. The *Spirulina* extract, containing Phycocyanin, is known for its antioxidant/anti-inflammatory properties. Phycocyanin plays a crucial role in activating antioxidant enzymes, neutralizing free radicals, and triggering anti-inflammatory pathways such as NF-κB, TLR, and PI3K/Akt/mTOR [239]. The enzyme activity

assays conducted on cells exposed to hydrogen peroxide, both with and without *Spirulina*-loaded samples, demonstrated that *Spirulina* directly mitigates ROS by 70% and enhances cell viability. Consequently, the expression levels of enzymes associated with scavenging ROS such as catalase, CuZnSOD and MnSOD) were observed to increase in the presence of *Spirulina*, indicating ROS elimination had started. Notably, the expression of catalase in the presence of *Spirulina*-loaded nanofibers was nearly three times higher than that observed with free *Spirulina*. For the other two enzymes, the increase in expression was similar between the free and loaded. These findings suggest that *Spirulina* incorporated within nanofibers retains its bioactivity comparable to that of free *Spirulina*. However, the long-term effects of *Spirulina* release (more than a day) were not evaluated in this study.

The release kinetics of anti-inflammatory components from nanofibers are influenced by various factors, including the method of incorporation and the concentration of the loaded component. Besides impacting the release kinetics, the optimum concentration of the anti-inflammatory agent is crucial for achieving an effective anti-inflammatory response. Insufficient levels might fail to offer therapeutic benefits, whereas excessive concentrations carry the risk of toxicity. For example, in a study where IBU was loaded into Poly(L-lactide) acid (PLLA) nanofibrous dressings at varying concentrations (10%, 20%, and 30%), it was observed that the proliferation rate of keratinocytes depended on the IBU concentration. The dressing containing 20% IBU demonstrated the most significant proliferation enhancement, with increases of 60%, 30%, and 70% compared to dressings with 30% IBU, 10% IBU, and plain PLA, respectively, in two weeks. Conversely, fibroblast proliferation exhibited a different response pattern, showing similar rates across the PLA, 10% IBU, and 30% IBU samples, with only the 20% IBU samples showing a 10% increase in proliferation [190].

Beyond assessing the impact of the concentration of loaded anti-inflammatory agents on cells *in vitro*, their effect on the healing process can also be directly evaluated using *in vivo* models [196]. Similar to studies involving growth factors, the predominant wound model used is full-thickness wounds, though the size of these wounds can range from 1 to 3 cm in diameter, allowing for a broad investigation of healing dynamics across varying wound severities.

To comprehensively assess *in vivo* responses, investigations beyond histological and immunohistochemical analyses are required, including the quantification of specific proteins such as TGF-βs, MMPs, TIMPs, and collagens. For scarless healing, high expression of collagen type III is expected in the initial stages, with low levels of collagen type I, which should increase in the later stages as it contributes to the strength of the regenerated skin. Furthermore, the expression of TGF-β1 and TGF-β2 should be downregulated due to their association with scar formation, whereas TGF-β3, known for its anti-scarring properties, should be upregulated. MMPs, which serve as ECM-degrading enzymes, should be overexpressed to facilitate ECM replacement and the breakdown of excess collagen type I, with their activity being modulated by TIMPs. A high MMPs/TIMPs ratio indicates remodeling rather than scar formation. Given that the inflammatory stage significantly influences the production of many of these proteins, particularly TGF-βs secreted by macrophages, neutrophils, and lymphocytes, introducing anti-inflammatory agents can alter protein expression, potentially leading to improved healing outcomes and reduced scarring [240].

The impact of anti-inflammatory agents incorporated into nanofibrous wound dressings on the expression of certain proteins and their contribution to scar-free healing has been explored in *in vivo* rat models. Specifically, two studies were conducted, one employing natural agents (curcumin and chrysin) [196] and the other utilizing IBU [189]. Although direct comparison is

challenging due to differences in wound sizes across studies, analyzing these cases provides valuable insights into their effectiveness in promoting accelerated healing and reducing scar formation. In one study, IBU was incorporated into a pH-responsive PLLA nanofibrous dressing and applied to full-thickness wounds measuring 2 cm in diameter [189]. In another study, curcumin and chrysin were loaded into PCL-PEG-PCL triblock copolymer nanofibers and applied to full-thickness wounds of 2x2 cm^2 in a rat [196]. Although the IBU study encompassed a wound area three times larger, the pH-responsive IBU-loaded PLLA and curcumin-loaded PCL-PEG-PCL triblock copolymer samples exhibited comparable wound closure rates, with both approaching complete healing (over 90%) by the end of the second week. Non-responsive IBU-loaded samples, designed for sustained release, exhibited closure rates similar to those of the chrysin-loaded samples, ranging between 80-85%. Interestingly, the combined use of curcumin and chrysin did not significantly enhance the closure rate, achieving 87% closure. Despite varying closure rates achieved by each bioagent, all resulted in accelerated healing compared to the control groups, with the smaller wound size exhibiting a 70% closure, whereas the larger wound in control achieved 40% closure within two weeks. These findings suggest that IBU may offer a more efficient acceleration of the healing process. However, trends in protein and gene expression differed markedly from the closure rates. Both naturally loaded dressings and IBU-loaded responsive dressings contributed to elevated MMP expression, with the IBU-loaded responsive dressing exhibiting a threefold increase compared to the control. Curcumin-loaded dressings doubled MMP expression; chrysin increased it by 2.2 times, and the mixed curcumin-chrysin dressing increased it by three times. Conversely, the expression of TIMP was almost halved in the presence of the IBU-loaded responsive sample, whereas all naturally loaded samples resulted in a 1.5 to 2-fold increase in TIMP expression. However, the expression levels

of these proteins alone do not definitively indicate whether healing quality is enhanced or diminished. To assess the potential of these bioagents in preventing scar formation, the MMP to TIMP ratio is crucial. For IBU-loaded responsive samples, this ratio had a sixfold increase compared to the control. In natural-loaded samples, the increase varied depending on the composition, with an eightfold rise for the curcumin-chrysin mix, fourfold for chrysin alone, and fivefold for curcumin alone. This suggests that healing was progressing towards a scar-free pathway for both types of dressings, although IBU's role in wound closure was notably more effective. Interestingly, despite the lack of a synergistic effect in the closure rate for the curcumin-chrysin mix, this combination exhibited a significantly higher MMP/TIMP ratio. This indicates that scarless healing does not always coincide with accelerated healing and rapid closure, and in some cases, accelerated wound closure might compromise the minimization of scarring. For the IBU-loaded samples, further protein analysis revealed that collagen deposition (both type I and III) was substantially reduced in the responsive samples—fourfold lower for type I and twofold lower for type III. The type I/III ratio of the IBU-loaded responsive samples was half that of the control, indicating a stronger tendency towards scarless healing. Additionally, TGF-β1 and TGF-β3 expression mirrored this trend, with a fourfold decrease in the IBU-loaded responsive samples compared to the control. Histological analysis also confirmed reduced scar formation in wounds treated with IBU-loaded responsive dressings, evidenced by the minimal presence of α-SMA, a key biomarker for scar formation [189].

The healing process can be further enhanced by employing cell-laden anti-inflammatory nanofibrous dressings. While incorporating cells directly during the electrospinning process presents challenges for cell viability due to high voltage and the presence of toxic solvents, post-seeding of cells onto nanofibrous dressings after their fabrication can circumvent these issues.

Various cell types, including fibroblasts, keratinocytes, and mesenchymal stem cells, can be seeded onto these dressings post-manufacture, offering a promising approach for wound healing applications [241]. Cell-seeding on anti-inflammatory nanofibrous wound dressings has been explored in both mice [190] and rat models using dressings of different compositions. A full-thickness wound model in mice, measuring 2x2 cm^2, was treated with a two-layer IBU-loaded PLA dressing [190]. The upper layer was seeded with keratinocytes, while the lower layer was seeded with fibroblasts to replicate the skin's natural structure, **Figure 2-13B**. These cell-seeded samples were compared to IBU-loaded PLA dressings without cells and a standard bandage control comprising Tegaderm, gauze, and an adhesive layer. The cell-seeded dressings were prepared by adding cells at a density of 20,000 cells/cm^2 and cultured for 14 days with media changes every three days. A common issue in the mouse model is wound contraction, which often occurs instead of epithelialization during healing. In this study, wound contraction was quantified using the same formula previously applied for measuring wound closure. Consequently, merely observing a decrease in contraction rates might not adequately indicate regeneration. Histological analyses are essential to determine whether the observed wound closure is indeed a result of regenerative healing. Such analyses can reveal the presence and extent of epidermal regeneration, differentiating between simple contraction and the more desirable outcome of rapid tissue regeneration. Interestingly, both acellular and cellular IBU-loaded samples reduced the contraction rate from 75% to 57% and 70%, respectively, with no significant difference between the two over two weeks, **Figure 2-13B**. Histological analysis revealed that cellular samples exhibited the highest angiogenesis, with 34 vessels/cm^2, compared to 22 vessels/cm^2 in acellular samples and 29 vessels/cm^2 in the control group. The regenerated epidermal thickness was 35 μm in cellular samples, 28 μm in acellular samples, and 24 μm in the

control group, with no significant difference between the control and acellular samples. The dermal layer thickness was 801 μm, 774 μm, and 923 μm for cellular, acellular, and control groups, respectively. The increased epidermal thickness in cellular samples suggests the contributory role of seeded keratinocytes and fibroblasts in epidermal regeneration [190]. Although the nude mouse model, without contraction prevention through a splint or silicon ring, may not perfectly replicate human healing, it demonstrated that cell incorporation could enhance healing quality and promote complete epidermal regeneration. Another study using a diabetic rat model with full-thickness wounds of 10 mm diameter provided more realistic data for samples seeded with mesenchymal stem cells, further underscoring the potential benefits of cell-seeding in wound dressings for improved healing outcomes [242]. These dressings, comprising PCL and Gum Tragacanth (GT) fibers loaded with curcumin, highlight the potential advantages of cell seeding for enhanced healing outcomes. GT, a natural polysaccharide containing minerals and proteins, directly contributes to hemostasis through its mineral content, including calcium, magnesium, and potassium, and can accelerate healing. In this research, the dressings were seeded with mesenchymal stem cells at a density of 4000 cells/cm² for three days before application to the wounds. The healing progress in wounds covered with cellular and acellular samples was then compared to that of untreated controls (open wounds). After two weeks, wounds treated with cellular dressings achieved complete closure (100%), while acellular dressings facilitated 95% closure, both surpassing the control group's 80% closure rate. Notably, this study used only a 3% curcumin loading, yet the closure rates were comparable to those observed in a similar study with 15% curcumin loading in healthy rats [196], underscoring the significant synergic impact of cell seeding and anti-inflammatory agent (curcumin) on accelerated healing, even in diabetic rats with compromised healing capabilities. Histological

analysis revealed that within the initial five days, only the wounds treated with cellular samples exhibited epithelialization, collagen deposition, and granulation tissue formation, along with angiogenesis, whereas acellular samples did not lead to complete epithelialization. By the end of the two weeks, both cellular and acellular samples had achieved full epithelialization with minimal inflammatory cells present. However, the distinction between cellular and acellular healing was pronounced; excessive collagen deposition in acellular samples resulted in scar formation, characterized by a sparse vascular network and absence of skin appendages. In contrast, cellular samples facilitated complete regeneration with a well-defined vascular network and the regeneration of sweat glands and hair follicles [242]. This study underscores the synergistic effect of curcumin in promoting the transition from the inflammatory to the proliferative stage of healing, with mesenchymal stem cells significantly accelerating the healing process, thus illustrating the combined potential of bioactive agents and cell seeding in wound dressings for achieving accelerated and scarless healing in diabetic models.

The reviewed papers in this section collectively highlight the crucial role of rapid transitioning from the inflammation stage to the proliferation phase in achieving accelerated wound healing. Various strategies, including the incorporation of NSAIDs or natural bioactive compounds into wound dressings, demonstrated similar rates of wound closure. However, the capacity to prevent scar formation and promote regeneration significantly depends on the composition of dressing and additives loaded in the dressing. For example, responsive dressings that release IBU upon inflammatory triggers or dressings seeded with therapeutic cells have shown the potential to facilitate complete tissue regeneration. Delayed healing, often resulting from prolonged inflammation, can be attributed to factors such as excessive production of ROS or an abundance of inflammatory cells, often worsened by the presence of infection.

Furthermore, infections present in the later stages of healing, such as proliferation, can create a competitive environment for oxygen and nutrients essential for cellular processes, thereby impeding recovery. Thus, controlling infection emerges as a pivotal aspect of enhancing healing outcomes. The following section explores the utilization of electrospun nanofibrous wound dressings as a carrier to manage infections, thereby supporting wound healing and improved therapeutic results.

2.6.2.3.3 Agents for Combating Wound Infection

Bacteria are constantly present on the skin's surface, with the intact skin acting as a robust physical barrier that shields the body from microbial invasion. The skin’s acidic pH, secreted fatty acids, and antibacterial biomolecules effectively prevent infections in healthy skin. However, when the skin is compromised due to injury, this protective barrier is breached, creating a conduit for bacteria to infiltrate the wound site [243]. Additionally, the accumulation of dead tissues and debris in wounds provides an ideal environment for bacteria to attach and grow, thereby increasing the bacterial load to initiate infections, which significantly complicates the healing process [19]. Infections can manifest at any stage of wound healing, from the initial inflammation phase, where they can prolong inflammatory responses and delay healing, to later stages, such as proliferation, where bacteria compete with healing cells for vital resources like oxygen and nutrients. Additionally, the body's response to bacterial presence, including the increased production of ROS in the process of bacterial elimination, can further damage tissues and impede healing [243]. An especially concerning aspect of wound infections is the common recourse to broad-spectrum antibiotics for treatment, which carries the significant risk of promoting antibiotic resistance [244]. Antibiotic-resistant bacterial strains complicate infection

management and pose severe health risks, particularly when infections advance into the bloodstream, leading to systemic infections that are challenging to treat.

Given the detrimental impact of infections on wound healing, antibacterial wound dressings have gained attention for the effective prevention and management of infection. In this field, electrospun membranes can either be carriers for antibacterial agents or have inherent antibacterial properties. In this section, antibacterial nanofibrous wound dressings are categorized into two main groups, differentiated by their composition and the nature of their antibacterial agents. The first group is nanofibrous dressings loaded with organic antibacterial agents. These organic agents can include a wide range of substances, such as natural extracts from plants and synthetic organic compounds. The second group is nanofibrous dressings loaded with inorganic antibacterial agents. This group is characterized by the presence of metallic nanoparticles, such as silver, copper, or zinc, and other inorganic compounds like metal oxides. The antibacterial mechanism of these inorganic agents typically involves the release of metal ions, which lead to disrupting bacterial cell membranes, inhibiting essential bacterial enzymes, interfering with bacterial DNA and protein synthesis, or inducing oxidative stress through the generation of ROS, ultimately leading to bacterial cell death.

In the first group, a diverse array of agents can be incorporated to enhance antimicrobial efficacy. Among these, herbal extracts are particularly noteworthy due to their abundance of bioactive components such as vitamins and polyphenols, which play a significant role in wound healing and infection management. Notable herbal extracts with recognized antibacterial properties include *Centella asiatica, Portulaca oleracea, Houttuynia cordata, Achyranthes aspera, Datura metel, Malva sylvestris*, and *Calendula officinalis*. The antibacterial effectiveness of these extracts is derived from their bioactive metabolites, which disrupt bacterial membranes,

interfere with cellular functions, and block essential metabolic pathways [245]. Beyond herbal extracts, essential oils from botanical sources are renowned for their potent antimicrobial activities. These oils interact with bacterial cell membranes and walls, increasing membrane permeability and leading to the leakage of cellular contents and causing disruption of pH balance. Moreover, they can inhibit critical cellular processes like ATP production, DNA transcription, and protein synthesis. The disruption of nutrient transport across bacterial membranes by essential oils further increases bacterial susceptibility [246]. In addition to natural antibacterials, synthetic agents like Polyhexamethylene biguanide (PHMB) offer a broad-spectrum defense against various microorganisms, including bacteria and fungi. PHMB's antimicrobial action is primarily attributed to its interaction with microbial cell membranes, where it binds to phospholipids, leading to membrane disruption, leakage of cellular contents, and subsequent cell death. The rapid mode of action of PHMB, coupled with its low risk of inducing microbial resistance, renders it an effective option for managing infections in wound care.

The primary objective of antibacterial nanofibrous wound dressings is to achieve efficient and sustained delivery of antibacterial agents directly to the wound site. This targeted approach not only prevents the degradation of these agents, Unlike other administration routes like oral ingestion, the more targeted delivery approach via nanofibrous wound dressing bears advantages such as reduced dosage compared to systemic administration and decreased frequency of application. For example, studies have shown that incorporating PHMB into polyester urethane (PEU) nanofibers results in a rapid release of 58% of the agent within just 5 minutes. However, the addition of cellulose acetate (CA) to the nanofibers can moderate this burst release due to the formation of hydrogen bonds between PHMB and CA. The rate of release is influenced by the

ratio of PEU to CA and the specific fabrication technique employed. When dressings were prepared using a 4:1 ratio of PEU to CA with a co-spinning (dual-jet) method, the initial release rate within the first 5 minutes dropped to 20%. Reducing the PEU to CA ratio to 2:1 increased the initial release to 45%. In single-jet (blending) samples, both ratios resulted in less than 40% release within the initial 5-minute period. After one day, PEU samples exhibited a 90% release, followed by a 70% release for both the 2:1 co-spinning and blending ratios, while the 4:1 ratio sample for both co-spinning and blending showed a 60% release, **Figure 2-13C**. These findings suggest that a higher concentration of CA can effectively delay the release of antibacterial agents, which is often the desired outcome for maintaining prolonged antimicrobial activity. Designing antibacterial nanofibrous wound dressings necessitates careful consideration of both the release kinetics and the composition of the antibacterial agents to ensure optimal performance. The desired release profile should align with the healing trajectory of the wound, providing sustained antimicrobial protection without overwhelming the wound site with excessive concentrations of the agent, which could potentially impair tissue regeneration or lead to cytotoxicity.

In addition to *in vitro* release testing, which involves placing the nanofiber sample in a release medium (PBS or water) at 37°C with agitation, *ex-vivo* release tests offer a more representative assessment of the release kinetics in a biological context. In an *ex vivo* setup, a Franz diffusion cell equipped with animal skin, such as that from a mouse, is used to simulate the release of antibacterial agents through the skin layers. Given that skin is thicker and more complex than a dialysis bag, the release rate in this setup tends to be slower than that observed in *in vitro* conditions. For instance, the release behavior of Ajwain essential oil encapsulated within the core of nanofibers—with a core composition of gelatin and PVA and a shell of Ajwain,

arabinose, AV and PVP—was evaluated both *in vitro* and *ex vivo* [247]. *In vitro* testing showed a 13% release in the first hour, culminating in an 86% release after two days. While the *ex vivo* release exhibited a linear pattern, reaching 83% over three days. The *ex vivo* model more accurately recapitulates *in vivo* conditions, suggesting that these antibacterial nanofibrous dressings can effectively manage infection for up to three days, highlighting their potential for clinical translation.

In the second group, metallic NPs, particularly silver (Ag) NPs, stand out for their ability to effectively address the challenge of infections, especially those caused by multi-resistant and biofilm-forming bacteria [248]. Silver NPs are recognized for their broad-spectrum antimicrobial properties, making them a valuable addition to wound care strategies. The antibacterial efficacy of Ag NPs is significantly influenced by the rate at which silver ions (Ag^+) are released. Typically, Ag NPs are insoluble in aqueous solutions, and their release from nanofibrous structures often begins with the desorption of Ag NPs from the surface of the nanofibers, followed by the diffusion of Ag^+ ions into the wound environment [249]. Ag^+ ions are formed through the oxidation of Ag NPs by dissolved oxygen in the aqueous solution environment [250]. This release mechanism is crucial because the antimicrobial action of silver is primarily attributed to these ions. The release behavior of Ag^+ from Ag NPs loaded in a nanofibrous dressing has been studied by collagen nanofibrous wound dressing incorporated with Ag NPs [249]. With this design, there was no initial burst release, which is often expected with nanoparticle-incorporated systems. This phenomenon was attributed to the electrostatic interactions between the Ag NPs and the collagen matrix, which may stabilize the nanoparticles and moderate their release. Consequently, the release profile of Ag^+ ions from such dressings tends to follow zero-order kinetics, meaning the release rate is constant and independent of the

concentration of Ag NPs remaining in the dressing. This controlled release is facilitated by the influx of water into the collagen matrix, which gradually, oxidized the Ag NPs, and releases Ag^+ ions over time. A complete release of Ag^+ ions from collagen-based nanofibrous dressings was achieved within a day, indicating that such dressings are capable of delivering the required antibacterial agents promptly and efficiently to the wound site [249]. This timely release of Ag+ is crucial for providing immediate antimicrobial protection to the wound, preventing infection, and supporting the healing process without the risk of prolonged exposure to high concentrations of Ag^+, which could potentially lead to cytotoxicity or silver resistance.

Evaluating the antimicrobial efficacy of antimicrobial nanofibrous dressings is a critical step in determining their suitability for clinical applications. Assessment toward both gram-positive and gram-negative bacteria is typical, as these two groups of microorganisms have different cell wall structures and can exhibit varied responses to antibacterial agents. *In vitro* antibacterial tests such as Zone of Inhibition (ZOI) and AATCC Quantitative Test 100 provide a controlled environment to measure the antibacterial effectiveness of these wound dressings. ZOI is a qualitative method widely used to evaluate the antimicrobial activity of a substance. The test involves culturing bacteria on an agar plate and then placing the antibacterial nanofibrous wound dressing sample on the agar surface for 24 hr with an initial inoculum concentration of 1×10^8 colony-forming unit (CFU)/mL. After incubation, the area around the sample is observed for a clear zone, known as the zone of inhibition, which indicates the absence of bacterial growth. The diameter of this zone provides a measure of the antimicrobial efficacy of the dressing; larger zones imply greater antibacterial activity. The ZOI test is a valuable method for demonstrating the successful release of active antibacterial agents loaded within nanofibrous dressings. For instance, in an experimental setup, PCL nanofibrous dressings were coated with varying

concentrations (10, 20 and 30%) of Achyranthes aspera (AS) and Datura metel (DM) leaf extracts. These coatings were tested against a spectrum of Gram-positive bacteria (including *Corynebacterium diphtheriae, Enterococcus species, Staphylococcus epidermidis, Lactobacillus acidophilus, Bacillus subtilis*) and Gram-negative bacteria (such as *Escherichia coli, Shigella sp., Vibrio parahaemolyticus, Pseudomonas sp., Pseudomonas otitidis, Klebsiella pneumoniae, Vibrio sp*.). The findings revealed that the highest concentration of extracts used for coating (30%), which exhibited entrapment efficiencies of 72% for AS and 81% for DM, produced the largest ZOI. Specifically, DM coatings resulted in ZOI ranging from 10-30 mm, while AS coatings showed a ZOI of 8-10 mm. Notably, the ZOI for PCL coated with 30% DM was comparable to that of the extract alone and the standard antibiotic methicillin. However, for AS, the standard antibiotic methicillin demonstrated the largest ZOI (15-30 mm), followed by the extract alone (10-20 mm). Interestingly, the ZOI of the 30% extract-coated samples exceeded that of Ag NPs loaded in collagen nanofibers (88% entrapment) within the first 24 hours, where the release of Ag ions resulted in a ZOI of 2.7 mm for *S. aureus* and 2.1 mm for *P. aeruginosa*. However, after three days, the ZOI expanded to 3.2 mm and 2.3 mm, respectively, suggesting that the sustained release of Ag ions is effective in reducing bacterial presence over an extended period [249]. This comparative analysis underscores the significance of optimizing the concentration of antibacterial agents in nanofibrous dressings to achieve the most effective antimicrobial action.

AATCC Quantitative Test Method 100 offers a quantitative approach to assess the antibacterial effectiveness of textiles, including nanofibrous wound dressings. The method involves inoculating the test material with a known concentration of bacteria and then incubating it under specified conditions. After incubation, the number of surviving bacteria is quantified,

usually by plating serial dilutions on agar plates and counting the resulting colonies. The reduction in bacterial count relative to a control sample is calculated based on the following equation, providing a quantitative measure of the material's antibacterial activity.

$$Bacteria\ Reduction = (\frac{N_0 - N_f}{N_0}) \times 100 \quad \textit{Equation 2-4}$$

where N_0 is the number of bacteria immediately after adding the sample (N_0 depends on the numbers of bacteria in antibacterial samples (A) and control samples (B); if A and B are different, the larger number will be chosen, if A and B do not have a significant difference the average of A and B will be used as N_0 ($=\frac{A+B}{2}$), and N_f is the number of bacteria after adding the antibacterial sample for desired contact period. This technique has been used for different antibacterial nanofibrous wound dressings. For instance, PHMB-loaded PEU-CA nanofibrous dressings demonstrated a significant reduction in *E. coli* populations by initial inoculum concentration of 1×10^7 CFU/mL, achieving a 96-99% reduction (1.4-2.0 log reduction) across various samples after 5 hr incubation. These samples included two different ratios of PEU to CA (2:1 and 4:1) and were produced using two distinct fabrication methods: blending and co-spinning. Notably, the antibacterial effectiveness of PHMB remained consistent regardless of the polymer concentration or fabrication technique employed, highlighting the robust antimicrobial properties of PHMB. Similarly, wound dressings loaded with Ajwain essential oil exhibited a 100% reduction (estimated maximum observable log reduction of ~5.1 based on the reported procedure of antibacterial quantification) in bacterial populations for both *S. aureus* and *P. aeruginosa* after 24 hrs. with an initial inoculum concentration of 1–1.5 × 10^8 CFU/ml, underscoring the potent antibacterial capabilities of natural essential oils [247]. In another study, a gelatin-oxide starch membrane incorporating Henna extract at varying concentrations (10%, 20%, and 30%) was subjected to both ZOI and bacterial reduction tests against *S. aureus* and *E.*

coli [251]. The results indicated that an increase in Henna concentration directly correlated with enhanced antibacterial activity. Specifically, *E. coli* exhibited ZOI measurements of 2.45 mm, 3.54 mm, and 4.45 mm for the 10%, 20%, and 30% concentrations, respectively. *S. aureus* showed ZOI measurements of 1.53 mm, 2.40 mm, and 3.34 mm for the same respective concentrations. Furthermore, the 30% Henna-loaded samples achieved a 92% reduction (1.1 log reduction) in *S. aureus* and a 95% reduction (1.3 log reduction) in *E. coli* after 2h hr of contact [251]. A comparative analysis of different antibacterial nanofibrous wound dressings reveals that natural-based antibacterial agents offer promising results comparable to those of synthetic agents. Both categories can effectively eliminate bacterial contaminants. This diversity in effective antibacterial agents provides valuable options for the development of advanced wound care products tailored to specific clinical needs and bacterial challenges.

In vivo models, including mice and rat models with either full-thickness or burn wounds, serve as critical platforms for evaluating the antibacterial efficacy of nanofibrous wound dressings. These models can involve wounds either inoculated with bacteria from the outset or normal wounds without deliberate bacterial introduction. For instance, in a study employing a rat model with full-thickness wounds of 1.5 cm in diameter, the wounds were inoculated with 1000 µL of 1-1.5x10^8 CFU/mL *S. aureus* and incubated overnight. Subsequently, the wounds were treated with either standard gauze or Ajwain-loaded nanofibrous dressings [247]. After four days of treatment, the Ajwain-loaded dressings demonstrated a significant bacterial reduction, achieving a 3-log reduction in bacterial count. Remarkably, by the end of two weeks, no detectable bacteria were present on the wounds treated with the Ajwain dressings, indicating an 8-log reduction, whereas the control wounds remained infected with no significant log reduction. The effective control of infection by the Ajwain-loaded dressings facilitated accelerated wound

healing. Within one week, wounds treated with these dressings exhibited a 71% closure rate, in stark contrast to the 25% closure observed in the control infected wounds. By the end of the second week, the Ajwain-treated wounds achieved nearly complete closure (99%), while the control wounds had only reached 64% closure. Notably, within the first week, re-epithelialization had commenced in the Ajwain-treated wounds, accompanied by a reduction in inflammatory cell presence and the formation of granulation tissue with a thick epidermal layer. By the end of the second week, the Ajwain-treated wounds exhibited complete re-epithelialization, regeneration of hair follicles, absence of inflammatory cells, and maturation of blood vessels. In contrast, the control wounds exhibited a high presence of inflammatory cells and incomplete re-epithelialization [247]. These findings suggested that, despite *ex-vivo* release studies indicating release durations of up to only three days, the Ajwain-loaded nanofibrous dressings were capable of eliminating bacterial presence within two weeks and significantly promoting skin regeneration.

In addition to utilizing infected *in vivo* models, normal wound models without bacterial inoculation have also been employed to evaluate antibacterial dressings. However, these models might not fully assess the antibacterial efficacy of the dressing. For example, rat models with varying wound sizes and types have been utilized. A particular study used a rat model with a full-thickness wound of 10 mm in diameter to assess the healing efficiency of DM and AS coated on PCL nanofibers [252]. The control groups included wounds treated with gentamicin and untreated wounds. Within the initial five days, wounds treated with DM and AS-coated samples exhibited a closure rate twice that of both untreated and gentamicin-treated wounds, achieving 40% closure. By day nine, the control groups had reached 60% closure, while the DM and AS-coated samples achieved 95% closure, displaying well-vascularized granulation tissue and a

thick epidermal layer with diminished inflammatory cells, in contrast to the control group's disorganized and thinner epidermal structure [252]. No signs of infection were observed in the AS and DM-treated samples, indicating that their antibacterial properties are comparable to gentamicin. However, the absence of an appropriate *in vivo* design with an infected wound makes it difficult to draw definitive conclusions about the effectiveness of AS and DM-loaded samples in controlling infection. Despite this limitation, the results suggest that these samples enhance the healing process in non-infected wounds similarly to growth factor-loaded and anti-inflammatory agent-loaded samples. Furthermore, the role of silver ions released from collagen nanofibrous dressings was investigated using a rat model with a full-thickness wound of 2 cm in diameter [249]. Wounds were treated with silver nanoparticle (Ag NP)-loaded collagen dressings, while the control group received standard gauze treatment. Interestingly, the Ag-loaded samples facilitated faster hemostasis by interacting with proteins and precipitating soluble proteins, thus promoting quicker wound closure. Histological analysis revealed that wounds treated with Ag-collagen dressings had twice the collagen deposition and a thicker keratin layer, along with more mature re-epithelialization compared to the control group, which lacked re-epithelialization. However, this study did not assess closure rates or infected wounds, limiting definitive conclusions about the role of silver in wound healing [249].

Another *in vivo* model utilized for assessing the antibacterial properties of nanofibrous dressings involves second-degree burn wounds, in which skin layer damage is comparable to that of full-thickness wounds. These burn wounds can be experimentally generated using two primary methods: exposure to water steam or application of hot metallic rods heated to approximately 85°C. In a particular study, a 2x2 cm^2 burn wound was created on a rat using steam to evaluate the efficacy of PHMB loaded into PEU-CA nanofibrous dressings compared to

untreated wounds [253]. After one week of applying the PHMB-loaded dressings, the untreated wounds displayed no signs of hair regeneration and were characterized by edema, scabbing, and a gray appearance. Conversely, wounds treated with PHMB-loaded dressings exhibited none of these symptoms, showing minor hair regeneration. By the end of two weeks, the PHMB-treated wounds demonstrated complete re-epithelialization, thickened epidermis, new capillary formation, granulation tissue, sweat glands, and hair follicle regeneration, contrasting sharply with the high levels of inflammation and disrupted re-epithelialization seen in the control group, **Figure 2-13C** [253]. This observation suggests that the utilization of synthetic antibacterial agents in wound care strategies can significantly improve the healing process. Not only do these agents contribute to better wound quality by preventing infection and mitigating inflammation, but they also promote more rapid tissue regeneration, leading to quicker recovery times and potentially reducing the risk of complications associated with wound healing. In another model using mice, burn wounds with a diameter of 0.5 cm created with a heated rod were treated with dressings loaded with 30% Henna incorporated into a gelatin-oxidized starch matrix [251]. The control wounds, covered with gauze, showed severe inflammatory responses within the first four days, characterized by thick inflammatory tissue (approximately 399 μm thick) and minimal signs of re-epithelialization or collagen deposition, leading to only 11% wound closure. In contrast, the Henna-loaded dressings facilitated new blood vessel formation, hair follicle regeneration, sweat gland growth, and re-epithelialization with organized collagen structure and a significantly reduced inflammatory zone (13 μm), achieving 25% closure within the same timeframe. While the study did not report the complete closure timeline, the early signs of hair follicle and sweat gland regeneration suggest that Henna can significantly accelerate the healing process and steer it towards more regenerative outcomes.

The comprehensive analysis of the literature highlights the significant role of both synthetic and natural antibacterial agents in wound management when incorporated into nanofibrous dressings. These agents are instrumental in preventing infections, which is crucial for the healing process, particularly in burn wounds that are highly susceptible to bacterial colonization. Beyond infection control, these dressings contribute to improved healing outcomes by enhancing tissue quality and expediting the regeneration process. This multifaceted approach to wound care, leveraging the antibacterial and regenerative properties of nanofibrous dressings, marks a promising advancement in the treatment of burn injuries.

Beyond the realm of infection control and wound healing facilitation through growth factors or natural compounds, chemical cues also offer a direct avenue for gene manipulation. This innovative approach, which involves altering gene expression to influence wound healing processes at a molecular level, is the focus of the subsequent section. This method represents a frontier in wound care, potentially enabling more precise control over the healing trajectory by targeting specific genetic pathways involved in tissue repair and regeneration.

2.6.2.3.4 Agents for Modulating Gene Expression

Gene-modulating chemical cues delivered by nanofibers can take a pivotal role in accelerating the healing process and minimizing scar formation. While gene therapy, encompassing the use of DNAs, siRNAs, and aptamers for direct gene expression manipulation, is a broad field with nanofibers emerging as promising carriers, this section focuses only on chemical cues, excluding growth factors that can directly alter gene and protein expressions associated with delayed healing and scar formation. Key proteins implicated in wound healing and scar formation, including TGF-βs, MMPs, α-SMA, and SMAD proteins, serve as primary targets for modulation through loaded chemical cues in electrospun wound dressings [254].

Moreover, the impact of chemical cues on gene expression extends beyond protein regulation, encompassing influences on other biomolecules, such as hormones, and direct modulation of cellular activities.

Targeting hormonal pathways, such as those involving the estrogen receptor-α (ER-α), estrogen receptor-β (ER-β), can significantly enhance wound healing by promoting matrix deposition, accelerating epithelialization, and mitigating inflammation [255]. Alfalfa leaves, traditionally used in Chinese medicine for wound healing, both topically and orally [256] are rich in bioactive compounds like chlorophylls and phytoestrogens (such as apigenin, luteolin, coumestrol, quercetin, medicarpin, daidzein, and genistein) [257]. This herbal medicine, known for its phytoestrogens' ability to bind to the ER-α and ER-β pathways, exemplifies modulating gene expressions in wound healing through hormonal pathways. The impact of alfalfa leaves on wound healing has been investigated by loading it into PCL nanofibers. Given that the healing efficacy of alfalfa leaves is attributed to its bioactive components, particularly genistein—a phytoestrogen and structural analog of estrogen, the preservation of these bioactive elements during the fabrication process is essential. Liquid Chromatography-Mass Spectrometry (LC-MS) analysis was conducted to evaluate the bioactivity of the electrospun samples, revealing that 75% of alfalfa's bioactive properties were retained post-electrospinning. This substantial preservation of bioactive components is pivotal, ensuring the nanofibrous dressings retain their therapeutic potential effectively. *In vitro* studies involving the culture of fibroblasts and keratinocytes on the alfalfa-loaded PCL nanofibrous dressings revealed a twofold increase in cell coverage compared to those with PCL alone. This increased cell coverage is instrumental in facilitating re-epithelialization [198].

Another target is the epithelial cells, which can undergo Epithelial-Mesenchymal Transition (EMT), a process where epithelial cells rearrange their cytoskeleton, lose cell-cell junctions and polarity, alter ECM interactions, and acquire behaviors like mesenchymal cells such as increased motility. EMT facilitates wound healing by improving re-epithelialization, driven by changes in gene expression that downregulate epithelial junction components and upregulate genes promoting cytoskeletal and adhesion alterations [258]. *Lithospermi radix* (LR), an herbal medicine, is known for its ability to facilitate EMT [259]. LR contains various components, including quinones and shikonin, which not only directly influence the healing process by modulating gene expression but also provide anti-inflammatory and antibacterial properties. Specifically, shikonin has been found to activate the EMT-related genes Zeb 1 and Zeb 2 while also regulating the expression of TGF-β, modulating collagen secretion, and influencing cell apoptosis [260]. The LR, as a chemical cue, was incorporated into gelatin nanofibers to create a bilayer chitosan-gelatin wound dressing [197]. To fabricate this bilayer structure, a solution containing gelatin and LR was electrospun directly onto a freeze-dried chitosan sponge. The *in vitro* release profile of LR from this bilayer dressing revealed an initial rapid release of approximately 40% of the LR within the first hour, followed by a sustained release that continued for up to one day.

The modulation of gene expression for wound healing, particularly for achieving accelerated and scarless healing, involves a complex interplay of various proteins and genes rather than the isolated effect on a single target. This complexity is underscored by the fact that effective wound healing strategies, such as reducing scar formation, often require a multifaceted approach [254]. For example, an increase in MMPs expression, which is generally limited in adult wound healing, needs to be accompanied by the suppression of α-SMA and collagen

synthesis to mitigate scar formation [261,262]. This interconnected relationship between protein expressions for optimized healing has been demonstrated with a PVA nanofibrous wound dressing loaded with Kynurenic Acid (KyA) [230]. KyA, a metabolite derived from the catabolism of tryptophan, exhibits a range of properties, including anti-inflammatory, anti-proliferative, antioxidant, and neuroprotective [261,264]. KyA's role in wound healing is particularly notable for its ability to upregulate MMPs in dermal fibroblasts, thereby facilitating scar reduction. However, KyA's influence extends beyond MMPs; it also contributes to the downregulation of collagen type I and α-SMA expression and the reduction in fibroblast proliferation [263]. The release dynamics of KyA from the PVA nanofibers, which were coated with PLGA, showed an initial release of 14% within the first 4 hours, extending to 85% over 4 days. This sustained release mechanism led to a notable 10% decrease in the proliferation rate of fibroblasts while promoting a 10% increase in keratinocyte proliferation. Gene expression analyses revealed the anti-scarring capabilities of the KyA-loaded nanofibrous wound dressing. Specifically, MMP-1 expression was doubled, indicating enhanced matrix remodeling capabilities, while expressions of α-SMA and collagen type I were decreased by 30% and 40%, respectively, compared to the control group. These results are indicative of KyA's potential to mitigate fibrotic responses and promote a more regenerative healing process.

The effectiveness of various chemical cues in modulating gene expression and impacting wound healing has been assessed through *in vivo* models, including studies on mice and rats. These assessments include evaluations of wound closure rates and histological analyses. For instance, in a mouse model with full-thickness wounds of 6 mm diameter, PCL nanofibrous dressings loaded with alfalfa achieved a 90% closure rate in two weeks, outperforming control (70%) and certain commercial dressings named hydrocolloid (50%) and matching the efficacy of

collagen dermal templates (90%) [198] and other nanofibrous dressings loaded with growth factors or anti-inflammatory agents (80-90%). Moreover, alfalfa-loaded nanofibrous dressings not only facilitated complete re-epithelialization with minimal gap between epithelial layers (0-1000 μm) compared to control (500-2500 μm) but also supported the regeneration of hair follicles, as assessed by the presence of cytokeratin 14. This effectiveness extended to *ex vivo* human skin models, where alfalfa-loaded samples achieved complete re-epithelialization within a week with the lowest gap (0-800 μm), outperforming controls (1000-2000 μm) [198].

While naturally derived chemical cues incorporated into nanofibers have shown promise *in vitro*, their *in vivo* performance does not consistently surpass that of growth factors or anti-inflammatory agents. For example, in a rat model with full-thickness wounds measuring 1.5x1.5 cm^2, a scaffold loaded with LR in a gelatin-chitosan bilayer facilitated an 87% closure rate within two weeks. Although this rate exceeds that of control samples covered with gauze (74%) and a commercial dressing known as Comfeel (76%) [197], it falls short of the closure rates achieved with Ibuprofen (IBU)-loaded responsive PLA nanofibrous dressings (90%), curcumin-loaded PCL nanofibrous dressings (92%), and growth factor-loaded HA-gelatin nanofibrous dressings (90%), even for larger wounds (three times larger). This suggests that gene modulation via naturally derived bioagents like LR alone may not be sufficient to accelerate healing effectively.

The comparison between alfalfa and LR in accelerating healing underscores that the specific bioactive components and the pathways through which gene modulation occurs can dramatically influence healing outcomes. Alfalfa, with its estrogenic bioactive components, can rival the efficacy of growth factors and anti-inflammatory agents, whereas LR, with shikonin as its bioactive component, does not demonstrate superiority.

In addition to assessing the wound closure rate for accelerated healing, the impact of chemical cues on gene modulation can be directly evaluated to predict scar formation. For instance, a KyA-loaded PVA nanofibrous dressing was tested in an *in vivo* rat model with splinted full-thickness wounds measuring 10 mm in diameter to examine the expression of scar-related genes. When treated with KyA-loaded dressings three days post-injury, a significant upregulation in MMP expression (fivefold increase) was observed after two weeks, alongside a fourfold decrease in both collagen type I and α-SMA expressions. Furthermore, the presence of myofibroblasts in the wound area was reduced threefold, and the count of immune cells was four times lower than that in control samples. Additionally, pro-collagen deposition in wounds treated with KyA-loaded dressings was lower than control, **Figure 2-13D** [192]. These results collectively underscore KyA's potential as an effective anti-scarring agent. KyA's potential in clinical applications has been recognized through a product known as FS2, which has been evaluated in human trials and shown a favorable safety profile. However, despite these promising findings regarding KyA's role in modulating scar formation and gene expression, the specific effects of KyA-loaded dressings on the overall speed of wound healing and closure have yet to be fully reported [265].

The wound healing process is intricate, requiring the careful selection of appropriate bioagents for incorporation into nanofibers. The compatibility of bioagents with the polymer matrix and solvent system, along with their synergistic interactions, are as critical as considerations of the wound’s location, dimensions, and severity. In addition to identifying chemical cues with the potential to expedite healing or reduce scar formation through various mechanisms, one promising approach is to provide signals that promote efficient angiogenesis. This strategy enhances the delivery of various growth factors and other bioagents, thereby

optimizing the overall healing process. The following section delves into angiogenesis factors as a final category of chemical cues for enhancing wound healing. Recognizing the breadth of this subject, a comprehensive review is beyond the scope of this paper. However, a concise overview of nanofiber-based delivery of angiogenesis factors, coupled with a discussion of established methodologies for assessing angiogenic responses, is presented.

2.6.2.3.5 Agents for Angiogenesis

Angiogenesis, which is the formation of new capillaries from existing blood vessels, plays a critical role in wound healing and skin regeneration by facilitating the transportation of essential elements like oxygen, nutrients, waste materials, signaling factors, and progenitor cells within the ECM. Given that most cells are located within 100–200 μm of the nearest capillary, diffusion is the primary means by which these elements are exchanged [266]. Consequently, successful tissue regeneration strategies necessitate a well-vascularized network to prevent tissue necrosis [267]. Angiogenesis occurs in a series of steps: (1) degradation of the vascular basement membrane, (2) proliferation and alignment of endothelial cells leading to lumen formation, (3) sprouting and migration through the ECM, (4) vessel maturation, and (5) stabilization [268,269]. This process is regulated by various biomolecules, including VEGF, FGF, PDGF, TGF- β1, Hepatocyte Growth Factor (HGF), nitric oxide synthase, and MMPs. Angiogenesis challenges in wound healing are particularly evident in severe injuries where newly formed capillaries exhibit impaired maturation, leading to vessel leakage, compromised cytokine receptor function, delayed cellular infiltration, and impeded re-epithelialization [270,271]. This lack of mature angiogenesis extends the healing duration, prompting numerous studies to focus on delivering angiogenic factors. Electrospun membranes, in particular, have shown promise not only as carriers for these factors but also as independent promoters of angiogenesis through their intrinsic physical

properties, such as optimal pore size (around 300 μm), porosity, and fiber alignment. Various polymers, including PCL, PLA, collagen, and gelatin, have been widely used in the fabrication of nanofibrous wound dressings to support angiogenesis [268,269]. However, the compact and dense nature of electrospun membranes can impede vessel network formation. This limitation can be addressed by increasing porosity through methods discussed in the physical cues section.

Various bioagents can be utilized for the delivery of angiogenic chemical cues in electrospun membranes. While the delivery of growth factors has been discussed in a previous section, other pro-angiogenic agents like the drugs tazarotene[272] and astragaloside IV [273], as well as biological agents like hormones [274] and heparin[275], can also be incorporated. Additionally, cell and gene delivery represent another avenue for enhancing angiogenesis [268,269]. Given the wide range of this field, this section briefly touches upon appropriate *in vitro* tests to evaluate the angiogenic potential of chemical cues for wound healing. Moreover, two *in vivo* models, diabetic rats, and mice, are reviewed to compare their healing in the presence of angiogenic nanofibrous dressing.

Evaluating the angiogenic potential of nanofibrous wound dressings *in vitro* can be effectively conducted by HUVECs and fibroblasts. The attachment and proliferation of these cells in the presence of the dressing can be assessed by culturing them on the membranes, followed by fixation and imaging, typically with SEM. Additionally, migration assays can be performed by creating a monolayer of cells in a culture dish, introducing a disruption with a pipette tip, placing the membrane over the gap, and then taking digital images to monitor the time taken for cells to bridge the gap. The interaction of HUVEC with PLA nanofibers containing Dimethyloxalylglycine (DMOG)-loaded silica NPs has been investigated to assess their attachment and migration capabilities [155]. DMOG, recognized for its pro-angiogenic

properties, can simulate a hypoxic environment conducive to healing acceleration. However, excessive dosages of DMOG carry risks such as tumor formation and increasing erythropoiesis, highlighting the need for careful optimization of the drug concentration for cellular delivery and a controlled release mechanism to prevent overwhelming cell exposure to high drug concentrations at once. Incorporating DMOG at varied concentrations (5%, 10%, and 15%) within silica NPs and embedding these in the PLA nanofibrous matrix resulted in an extended initial release period of 48 hours, with a sustained release observed up to 360 hours. HUVEC cells cultured on these DMOG-containing samples demonstrated enhanced adhesion rates in comparison to PLA alone, exhibiting cell spreading and elongation along the fibers. Notably, samples with 10% and 15% DMOG concentrations showed the most significant increase in cell adhesion and proliferation, with a 1.2-fold increase relative to PLA. Similarly, migration assays revealed an approximate 10% increase in cell migration for samples containing 10% and 15% DMOG [155]. These findings underscore the critical impact of angiogenic agent concentration on the behavior of HUVEC cells, emphasizing the importance of optimizing DMOG dosage within nanofibrous dressings to harness its angiogenic potential while mitigating associated risks.

Two key assays are employed for assessing angiogenesis: the tube formation assay and the Chorioallantoic Membrane (CAM) assay. Tube Formation Assay evaluates the capacity of endothelial cells to form capillary-like structures on a gel substrate like Matrigel, which simulates the complex ECM environment. The sample is placed in a Boyden chamber, and upon incubation, endothelial cells start to organize into network-like structures reminiscent of *in vivo* capillaries. The degree of tube formation is quantified by analyzing the total length of the tubes, branch numbers, and junction points, either manually or with image analysis software. The impact of DMOG-loaded PLA nanofibers on tube formation by endothelial cells has been

investigated, revealing that the presence of varying concentrations of DMOG facilitates the self-assembly of capillary-like structures characterized by enhanced tube lengths and increased nodal points. Notably, samples containing 10% DMOG concentration exhibited the most significant improvement, showing a 2.5-fold increase in tube length and a doubling in the number of nodes compared to the PLA control. This suggests that the incorporation of DMOG within PLA nanofibers effectively promotes angiogenesis, with a 10% concentration of DMOG optimizing the formation of tubular structures, indicative of enhanced angiogenic potential [155].

CAM Assay utilizes the highly vascularized chorioallantoic membrane of developing chicken embryos. After incubating fertilized eggs to a specific developmental stage, a window is created in the eggshell to expose the CAM, where the samples are directly applied. The window is then sealed with parafilm, and after further incubation, the CAM is examined under a microscope to observe angiogenic responses, including new blood vessel formation and branching. Quantification involves counting new vessels, measuring vessel growth, or employing advanced imaging for detailed analysis [276]. CAM assay has been employed to assess the efficacy of an oxygen-releasing nanofibrous wound dressing, which incorporates PCL and Sodium Percarbonate (SPC) [277]. Oxygen is a critical factor in angiogenesis, and its deficiency is often a limiting factor in the angiogenic capability of tissues. SPC serves as an oxygen source by releasing hydrogen peroxide, which subsequently decomposes to yield oxygen. The comparative analysis of the CAM assay results for PCL alone and PCL-SPC nanofibrous dressings demonstrated a significant enhancement in angiogenesis attributed to the oxygen released from the SPC-containing dressings. Specifically, the rate of angiogenesis in the presence of the PCL-SPC dressing was increased threefold, and the number of blood vessels observed in the PCL-SPC sample was approximately 30 [277]. This indicates that integrating an oxygen-

releasing component like SPC into nanofibrous dressings can substantially augment the angiogenic response, thereby potentially improving the healing process.

Besides these assays, the protein and gene expression levels of cells cultured *in vitro* can also be analyzed to gauge the nanofibrous wound dressings' angiogenic capability. Key markers such as VEGF and Hypoxia-Inducible Factor-1α (HIF-1α) are often measured to understand the underlying mechanisms driving angiogenesis induced by the dressings. The evaluation of HIF-1α expression in response to DMOG-loaded PLA wound dressings revealed during the first three days, there was no significant difference in HIF-1α expression between the 5% DMOG sample and plain PLA. However, the 10% and 15% DMOG samples induced a twofold increase in HIF-1α expression. Notably, after one week, all DMOG-containing samples exhibited a similar level of HIF-1α expression, which was double that of the PLA control [155]. This pattern suggests that the angiogenic influence of DMOG is both concentration and time-dependent. In contrast, the expression of HIF-1α in the presence of PCL and SPC showed a threefold increase compared to the control, but this was evident as early as one day after treatment [277]. This rapid increase in HIF-1α expression highlights the crucial role of oxygen availability in angiogenesis. The presence of oxygen released from the PCL-SPC dressing seems to significantly and immediately influence the angiogenic process, as indicated by the rapid upregulation of HIF-1α. These findings collectively demonstrate that the effectiveness of both DMOG and SPC in promoting angiogenesis is closely linked to their respective mechanisms of action and timing, with oxygen presence being a critical factor in early angiogenic responses.

The angiogenic properties of wound dressings can also be comprehensively assessed using *in vivo* animal models, with both mice and rat models being viable options. However, rat models are often favored due to their larger size. For a thorough assessment of the healing

efficacy and the angiogenic potential of the wound dressings *in vivo*, several key evaluations can be conducted, such as healing rate/wound closure, protein expression for specific proteins involved in the wound healing and angiogenesis process such as collagen type I and III. Moreover, histological examination of the healed tissue can reveal the extent of vessel formation, collagen deposition, and the development of granulation tissue. Immunohistochemistry can be used to visualize specific cell types or proteins within the healed tissue. A common target is CD31, a marker of endothelial cells, which can highlight the formation of new blood vessels within the healing tissue [276].

In a diabetic mouse model with full-thickness wounds of 8 mm diameter, the angiogenic potential of 20% DMOG-loaded Silica NPs embedded in aligned PLA nanofibers was evaluated [155]. The wounds treated with DMOG-loaded samples demonstrated accelerated healing, achieving 82% closure within the first week, compared to 76% for PLA samples and 70% for controls, as shown in **Figure 2-13E**. Histological analysis revealed that the expression of CD31 and the rate of angiogenesis were significantly enhanced in DMOG-loaded samples-treated mice, approximately twofold greater than that observed in control and PLA groups. However, by the second week, the expression levels in all groups decreased to half of their initial values, though DMOG-loaded samples-treated mice maintained a twofold increase over controls. This underscores DMOG's role in early-stage angiogenesis during wound healing.

Immunohistochemistry results suggested reduced scar formation in wounds treated with the DMOG-loaded nanofibrous membrane, characterized by an initial surge in collagen type III expression during the first week, followed by a subsequent decline and concomitant increase in collagen type I expression in the second week. [155]. These findings highlight that enhancing angiogenesis during wound healing not only accelerates the healing but also decreases the

likelihood of scar formation. However, the concentration of the angiogenic agent and its delivery mechanism should be carefully considered when designing the final wound dressing.

Angiogenesis was also assessed in a diabetic rat model with full-thickness wounds measuring 2x2 cm^2 [277]. In this study, a silicone splint was utilized to inhibit contraction, resulting in no significant difference in closure rates among all samples, including controls, PCL, and PCL-SPC, which all reached 70-80% closure within four weeks. However, histological analysis revealed that only wounds treated with PCL-SPC exhibited complete epithelialization along with a homogenous network of vessels and consistent dermal and epidermal layers [277]. This suggests that oxygen release can enhance angiogenesis and improve healing quality, steering it towards regeneration rather than repair, although the specific impact of oxygen on the rate and speed of healing remains to be conclusively determined.

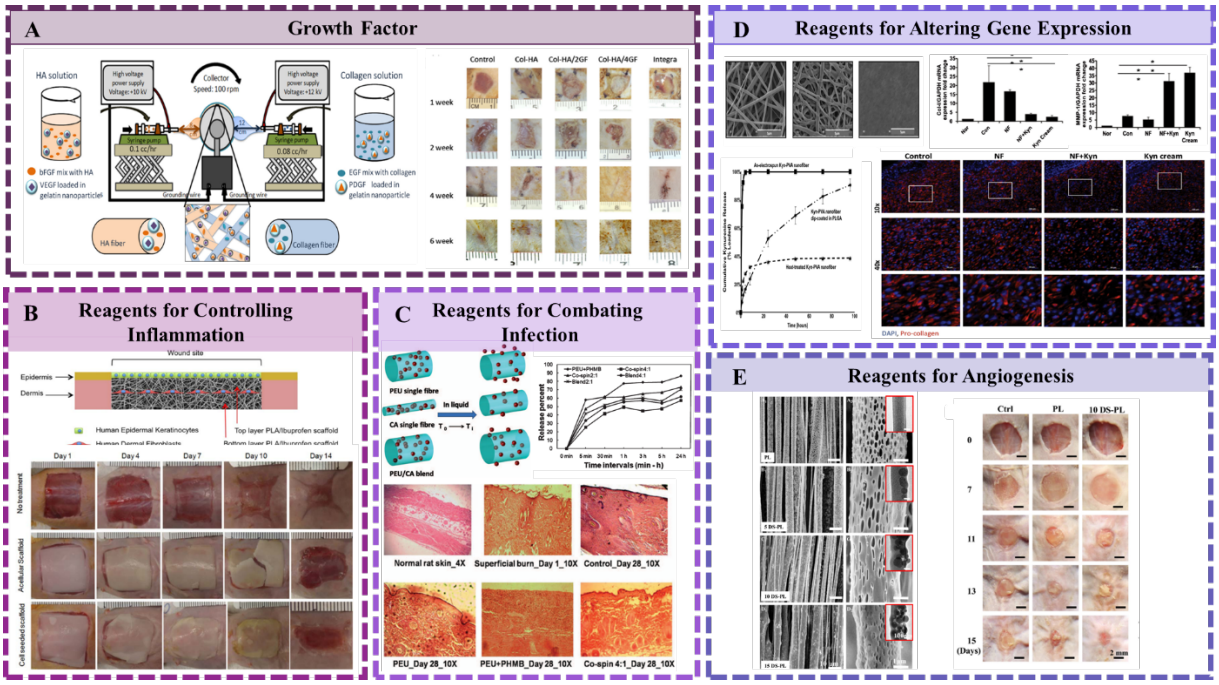

Figure 2-13 Chemical cues

This figure illustrates the influence of various bioactive agents and small molecules in engineered wound dressings on wound healing, targeting different chronic wound scenarios to minimize the risk of scar formation. A) Delivering Growth Factors: A wound dressing was fabricated using the multi-jet technique, incorporating hyaluronic acid and collagen. Two growth factors were used for each solution, one directly loaded into the fibers and the other loaded into gelatin particles within the fibers. While the bare GF exhibited burst release, the NPs-loaded GF showed sustained release. The synergistic effect of these growth factors accelerated wound healing with reduced scar formation in a rat model in 6 weeks. Reprint with permission from [114] Copyright 2014 Elsevier. B) Agents for Inflammation: A PLA-based wound dressing containing ibuprofen was developed to minimize the inflammatory response and expedite healing. Two types of cells were loaded into the wound dressings, and cell-seeded membranes further accelerated the healing process. Reprint with permission from [190], Copyright 2015 Wiley. C) Agents for Infection: A wound dressing based on cellulose acetate and PEU was designed for the sustained release of polyhexamethylene biguanide (PHMB) as an antibacterial agent. Blending cellulose acetate and PEU facilitated sustained release. In a burn model, the co-spun wound dressing promoted skin regeneration, while the control and PEU alone resulted in scar formation. Reprint with permission from [253], Copyright 2012 Wiley. D) Agents for Altering Gene Expression: A PVA-based wound dressing was created to deliver an anti-scar drug that regulates MMP and TGF expression. To achieve sustained drug release and prevent initial burst release, the nanofibers were coated with PLGA, extending the release duration from 10 to 120 hours. Sustained drug release reduced collagen and increased MMP expression, resulting in scarless healing. Reprint with permission from [192], Copyright 2016 Wiley. E) Agents for Angiogenesis: An aligned wound dressing containing an angiogenesis drug loaded in silica particles was engineered to enhance vascularization at the injury site, accelerating the healing rate. This wound dressing expedited healing and reduced scar formation within 15 days. Reprint with permission from [155]. Copyright 2018 Elsevier.

Table 2-4 presents the compatibility of various chemical cues with different solvents.

Table 2-4 Different Chemical cues and their solvents for reaching accelerated scar-free healing via loading in nanofibers.

Name of the chemical cue	Compatible solvent	Category for scar-free healing
bFGF	Water, PBS or other aqueous buffers, NaOH, DMF (less than 25 v/v %)	Growth factors
EGF	Water, PBS or other aqueous buffers, HFIP (emulsion), Acetic acid	
VEGF	Water, PBS or other aqueous buffers, NaOH, DMF (less than 25 v/v %)	
PDGF	Water, PBS or other aqueous buffers, Acetic acid	
Ibuprofen	DCM, DMF, Chloroform	Reducing inflammatory response
Calendula officinalis	DMF, Methanol	
Spirulina	THF, DMF	
Gum tragacanth	Acetic acid	
Curcumin	Acetic acid	
Chrysin	Acetone, Chloroform, Methanol, DMSO	
Honey	water	
Polyhexamethylene biguanide (PHMB)	THF, DMF	Infection control
Gentamicin	Water, Acetic acid	
Silver nitrate	Acetic acid, HFIP	
Kynurenic acid	NaOH, water	Gene alteration
Emodin	Ethanol	
Lithospermi radix	Formic acid	
Alfa-alfa	HFIP	
Vitamin D	DCM	
Dimethyl oxalylglycine (DMGO)	DCM	Angiogenesis

Table **2-3** provides a comprehensive summary of all the reviewed papers for physical, compositional, and chemical cues, offering insights into the outcomes concerning the wound healing process. Given the introduction of diverse chemical cues, the subsequent focus lies on exploring efficient loading methodologies, as these significantly impact the efficacy of these agents**. Figure 2-14** provides a comprehensive visual representation of various chronic wound scenarios, and the therapeutic agents loaded into nanofibrous wound dressings to address each scenario. The ensuing section delves into the intricacies of incorporating bioactive agents into nanofibers, with a particular emphasis on optimizing release kinetics. Through this in-depth analysis, we aim to elucidate effective strategies for the controlled and efficient release of these agents from nanofibrous wound dressings.

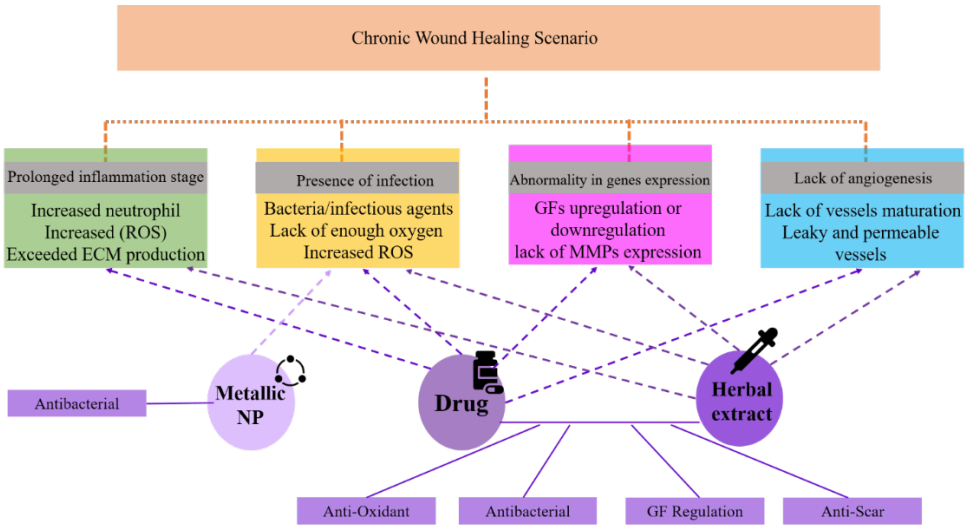

Figure 2-14 Different chronic wound scenarios and agents for overcoming each for accelerated and scarless healing.

2.6.3 Loading Therapeutic/Bioactive Agents into Membranes

The proper loading and release of the aforementioned chemical cues are as vital as the nature of the cues themselves in preventing scar formation. Common methods for incorporating various agents into nanofibers encompass blending, surface modification, crosslinking post-electrospinning, core-shell encapsulation, or the utilization of secondary carriers, emulsion, as well as various electrospinning techniques like side-by-side, coaxial, and multi-jet electrospinning. [120,278–281] **Figure 2-15**.

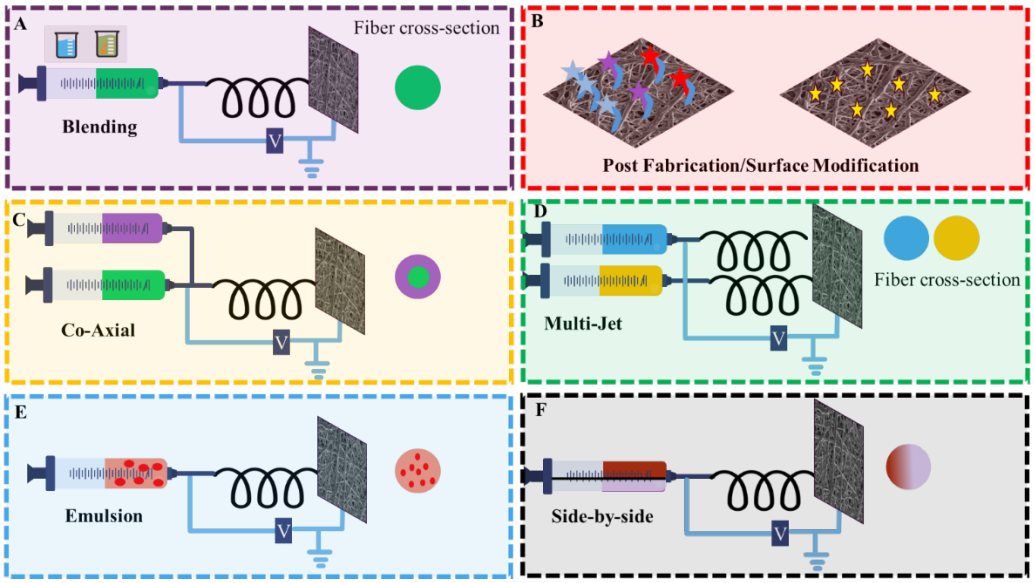

Figure 2-15 Different techniques of loading bioactive agents into nanofibers:

A) Simple Blending: This method involves blending bioactive agents with the polymer solution before electrospinning. However, it requires pre-steps to prepare the blended solution. B) Post Fabrication: In this technique, the fabricated wound dressing undergoes additional steps to immobilize active bioagents on its surface or is immersed in different solutions to load bioactive agents into the membrane. C) Co-Axial Electrospinning: Co-axial electrospinning uses two solutions for the core and shell, resulting in fibers with a core surrounded by the shell. D) Multi-Jet Electrospinning: Different solutions are simultaneously used in this technique, and the final membrane consists of mixed individual fibers from each solution. E) Emulsion: Emulsion involves mixing two-phase solutions, and the final fibers contain droplets of the second phase. F) Side-by-Side Electrospinning: In this technique, two different polymer solutions are fed through separate capillaries, which do not come into contact until they reach the nozzle. Each solution can have a unique feeding rate, but both are connected to the same voltage. At the nozzle, a single Taylor cone, incorporating both polymers, is formed, and the jet consists of a heterogeneous mixture of the polymers.

This section provides a comprehensive review of the various techniques, along with a discussion of their respective advantages and disadvantages.

2.6.3.1 Blending Electrospinning

The most straightforward approach to incorporating an agent into nanofibers is through blending. In this method, the desired agent is dissolved or dispersed in a final electrospinning solution [278]. However, finding a suitable common solvent that works with polymers and agents, possesses electrospinnable properties, and is compatible with the bioactive agent can be a challenge [281]. Another drawback of blend electrospinning arises from the potential for compromised bioactivity of the loaded bioactive agents due to exposure to harsh electrospinning solvents (such as organic solvents or acids). For example, Ji et al. [282] investigated the impact

of organic solvent in the blending electrospinning on the bioactivity of electrospun proteins. The membrane was fabricated by electrospinning mixture of bovine serum albumin (BSA) or alkaline phosphatase (ALP) and PCL in trifluoroethanol (TFE). Initial attempts to electrospin a mixture of 12% PCL and 0.2% BSA failed due to lack of spinnability, but successful electrospinning was achieved with the addition of 10% PEG. The resulting membrane exhibited a 92% protein loading efficiency, with a 10% burst release in the first 4 hours and a sustained release up to 70% over 5 weeks. Post-release, significant fiber erosion and cavity formation were observed. Protein activity of samples post-fabrication assessed via ALP, was reduced to 49.3%, and circular dichroism analysis indicated structural changes with a 22% decrease in α-helix content, a 25% increase in β-sheets, and a 3% decrease in random coil content, suggesting conformational alterations due to the interaction with organic solvent. Interestingly, membranes with protein in a core separate from the PCL shell showed lower activity (13%), which improved to 76% with PEG addition, highlighting PEG's role in stabilizing proteins by preventing adsorption to the organic polymer phase during electrospinning. These findings underscore the detrimental effect of organic solvents on the bioactivity of proteins and growth factors, indicating that blending electrospinning may compromise the effectiveness of bioactive agents in electrospun scaffolds.[161]. Additionally, blending lacks control over the agent's release, possibly leading to burst release due to fiber degradation or simple diffusion [280,283]. Consequently, blending is not considered a reliable loading and targeted delivery method. Nevertheless, due to its ease of fabrication, blending remains one of the conventional methods for loading bioactive agents into nanofibers. In this method, altering the concentration or composition of polymers can influence drug release, loading capacity, and release profile [278]. While blending may not offer the highest efficiency compared to more advanced techniques, it is suitable for loading antibacterial

and antibiotic agents [281]. This is particularly valuable for preparing wound dressings to protect wounds from infectious agents and accelerate healing. Examples of antibiotics that have been incorporated into synthetic or natural polymers through blend electrospinning include tetracycline, cefoxitin, chlorhexidine, quaternary ammonium salts, silver, titanium dioxide NPs, chitosan, and honey. These polymers include PVA, PLA, PLGA, PCL, collagen, chitosan, or cellulose acetate. These combinations create antibacterial wound dressings designed to inhibit infection [284–293]. Another application of blending involves utilizing burst release for hemostatic agents. Since a rapid burst release profile is desirable for the delivery of hemostatic agents for rapid cessation of bleeding, blending is a suitable technique to facilitate rapid hemostasis, which is a key component of optimal wound healing [281]. For incorporating other agents, more advanced electrospinning methods such as co-axial, side-by-side, and multi-jet electrospinning can be employed to overcome the main challenge associated with blending (finding an appropriate common solvent). Furthermore, instead of directly loading agents into the fibers, they can be immobilized onto the wound dressing afterward through post-fabrication modifications, which are reviewed in the following sections.

2.6.3.2 Post Electrospinning surface modification

Surface modification involves attaching the bioactive agent or drug onto the surface of nanofibers through physical interaction or chemical reactions. This technique offers a significant advantage in preventing the initial burst release or rapid release of agents from nanofibers. However, it's essential to consider limitations in loading capacity and the strength of bonds between agents and surfaces in chemical reactions, particularly when endocytosis is required for drug uptake [278]. Utilizing responsive materials sensitive to local stimuli appears promising to overcome the availability and mobility limitations, especially for surface immobilizing of growth

factors through chemical grafting [294]. Despite the chemical grafting that can denature the bioactive agents, physical immobilization on nanofibers' surfaces is a drug-friendly method that doesn't require harsh conditions. Common methods for physical immobilization include simple physical adsorption, NPs assembly, and layer-by-layer assembly [295]. Physical adsorption is a post-fabrication method primarily reliant on interactions like hydrogen bonding, electrostatic attraction, van der Waals forces, and hydrophobic interactions. In contrast, NPs assembly is a simultaneous technique where bioagents are dissolved in a separate solution with an opposite charge to the electrospinning solution [295]. During electrospinning, this solution containing bioactive agents is electrosprayed onto the surface of electrospun nanofibers [296]. Another post-fabrication approach for physically modifying the surface of nanofibers is layer-by-layer assembly, creating a coating with varying thicknesses. Its ease of fabrication, compatibility with various bioactive materials, and suitability for different geometries make it highly appealing. However, since the technique of layer-by-layer assembly relies on charge interactions of polyanions or polycations with the nanofibers' surface, the technique by nature is limited to application for charged bioactive agents.

Chemically bonding bioactive agents to the nanofiber surface has been developed to exert control over the release rate. Introducing functional groups like amines, carboxyls, and hydroxyls on the nanofiber's surface makes it possible to attach a bioactive agent via a covalent bond. Despite its effectiveness in achieving durable attachment of bioactive agents, this method can compromise the functionality of incorporated bioactive agents. This drawback arises from the potential alteration of their active sites, hindering their interaction with cells [295]. Gautam et al. [210] presented a study involving the chemical surface modification of PCL/gelatin electrospun membranes using collagen type I for wound dressing. Nanofibers, with varying PCL to gelatin

ratios, were immersed in a solution of 1-ethyl-3-(3-dimethylaminopropyl) carbodiimide (EDAC) to activate the carboxyl groups. Subsequently, the activated nanofibrous membrane was incubated with collagen type I solutions of varying concentrations for 24 hours. This approach facilitated the formation of amide bonds between the activated carboxyl groups and the amine groups of collagen, chemically bonding collagen type I onto the PCL/gelatin nanofibrous membrane. Collagen type I modification not only enhanced the proliferation rate of fibroblasts on the scaffolds compared to unmodified controls but also supported the preservation of their phenotype. These results suggest the potential of this approach for developing advanced nanofibrous wound dressings that promote favorable cellular interactions and accelerate wound healing processes.

In another study by Krithica et al. [211], aminolized PCL nanofibers were fabricated to facilitate the immobilization of collagen type I. To achieve this, first PCL solution in DMF:chloroform was electrospun at 30 kV. Then electrospun PCL fibers with average diameter of 270 nm were cut, washed, and then immersed in 1,6-hexanediamine/2-propane for aminolysis. Subsequently, the modified fibers were placed in a glutaraldehyde solution to establish crosslinking sites for collagen attachment. Finally, the nanofibers were treated with a collagen solution for immobilization. The outcomes of this study revealed that surface modification of PCL nanofibers with collagen type I significantly enhanced the proliferation and fractional infiltration of NIH 3T3 fibroblasts compared to unmodified controls. This improved cellular response suggests promising potential for these collagen-modified PCL nanofibers as wound dressing materials.

Choi et al. [110] conducted a study to assess the practicality of delivering two growth factors, bFGF and EGF, using a combination of coaxial electrospinning and chemical surface

modification. The growth factor bFGF was encapsulated within the nanofibers in the aqueous PVA core with PCL-PEG-NH_2 block copolymer in methanol: chloroform as. EGF was then surface-immobilized via a reaction with the surface-exposed amine groups of copolymer PCL-PEG-NH_2 linker. The findings revealed distinct release patterns: bFGF exhibited a rapid burst release due to diffusion from the nanofiber core on the first day, while EGF demonstrated minimal (<2%) release over one week due to covalent immobilization on the fiber surface (release of EGF depends on degradation of the PCL-PEG fibers). This outcome underscores the fundamental distinctions among various loading techniques. The selection of an appropriate method for incorporating bioactive agents into nanofibrous membranes is crucial. This choice is influenced by several factors, including the bioactivity of the agent and the need for controlled release at different stages of wound healing. To achieve high loading capacities and sustained release profiles, alternative loading methods like co-axial electrospinning, multi-jet electrospinning, and emulsion can be employed. These techniques will be reviewed in the following section.

2.6.3.3 Co-axial electrospinning

Control over the drug release rate can be achieved through co-axial electrospinning. Depending on the desired release rate, this technique involves loading the drug or bioactive agent into either the shell or core solution. Loading the drug into the shell solution is advisable for a burst release, whereas mixing the drug with a core solution is recommended for sustained and prolonged release. The release rate achieved with this method is closely tied to the properties of the core and shell polymers. Altering the polymer composition, hydrophilicity, and hydrophobicity of the core and shell components enables a wide range of release rates [279,280]. Unlike blending, the primary advantage of this method is that the core and shell solutions are

electrospun simultaneously but can have different solvents. Thus, the challenge of identifying a common solvent for drugs and polymers is resolved [278]. For example, Wei et al. [297] fabricated a core-shell nanofibrous membrane consisting of a PCL core and a chitosan/collagen shell. The core solution was prepared using a mixture of acetic acid and HIFP, while the shell solution utilized methylene dichloride. This core-shell design offers distinct advantages. The PCL core ensures robust mechanical strength, critical for maintaining the structural integrity of the dressing. In contrast, the chitosan/collagen shell enhances biocompatibility. Importantly, two different bioactive agents were strategically loaded into the membrane to target specific stages of wound healing. Silver NPs loaded into the shell solution for their broad-spectrum antibacterial activity, exhibit a burst release during the initial stages to combat infection. Conversely, vitamin A palmitate, loaded within the core, exhibits a slower release profile over three days, primarily influencing cellular activity during the proliferation phase. This targeted release strategy along with positive cell viability and antibacterial test results suggest significant promise for this core-shell membrane as a potential clinical wound dressing.

In addition to co-axial electrospinning, other electrospinning methods, such as multi-jet or side-by-side electrospinning, offer promising solutions to the limitations of the conventional blending electrospinning method. The fundamental concept behind these methods is similar to co-axial electrospinning, involving using different electrospinning solutions. However, in side-by-side or multi-jet electrospinning, two or multiple nozzles are employed instead of a single nozzle, resulting in a hybrid membrane composed of various nanofibers [281]. Another loading method, emulsion, has been introduced as a simple alternative to co-axial electrospinning, which eliminates the need for a specialized nozzle system.

2.6.3.4 Emulsion Electrospinning

In the emulsion method, instead of electrospinning two distinct solutions, an emulsion of an aqueous phase and an organic phase is prepared, which is then electrospun to create core-shell nanofibers. The emulsion can be water-in-oil or oil-in-water, depending on whether it is desired to encapsulate a hydrophobic or hydrophilic agent. For incorporation of hydrophilic bioactive agents for wound healing applications, typically, the aqueous phase contains the drug or bioactive agent, and the oil phase contains the polymer. This results in the formation of a water-in-oil emulsion, eliminating the issues associated with variations in the electrospinning parameters of two separate solutions. While this method simplifies the fabrication process compared to co-axial electrospinning, it still shares a weakness with the blending technique, which is the potential for reduced bioavailability of bioactive agents or drugs, especially proteins and growth factors, due to the presence of an organic solvent. Although the bioactive agents in the aqueous droplets of the emulsion are protected from contact with the organic phase, the preparation method of emulsification, such as ultrasonication, can increase the interaction of the bioactive agent with the organic solvent. For example, Yang et al. encapsulated lysozyme (as a model protein) into the core of Poly(D,L-lactide) (PDLLA) core-shell nanofibers using emulsion electrospinning with lysozyme in the aqueous phase and PDLLA in the organic phase. A 16% loss of specific activity of lysozyme was reported after the emulsification process, which was attributed to the ultra-sonication procedure, which exposes the protein to the organic solvent, matrix polymer and dispersion forces resulting in the denaturation of the protein [298]. Notably, there was no additional activity loss after the electrospinning process, indicating that the exposure to high voltage and shear forces during electrospinning did not have a significant impact on the activity of the loaded enzyme. Despite this drawback, the emulsion method has

been utilized to develop skin wound dressings incorporating growth factors [278]. For instance, Wang et al. [299] leveraged the emulsion electrospinning technique to fabricate an electrospun wound dressing. They electrospun an emulsion where PCL and HA were dissolved in the oil phase, while EGF and bovine serum albumin (BSA) were dissolved in the aqueous phase. In this design, the hydrophilicity of HA promoted the subsequent release of EGF from the nanofibers. The dual release of EGF and HA had a synergistic effect, resulting in enhanced cell infiltration and increased expression of collagen and TGF. Furthermore, the incorporation of HA and EGF resulted in the upregulation of collagen type III and TGF-β1 expression. The relative expression level of collagen type III tripled in the nanofibers containing EGF and HA after 5 days of culture, which contributed to an accelerated wound closure rate in a full-thickness wound model in a rat (wound area 18 mm×18mm).

Due to their extensive surface area, nanofibers are well-suited for incorporating bioactive agents or drugs. As discussed earlier, several factors influence the choice of the most suitable technique for loading biomolecules into nanofibers. The advantages and disadvantages of all the introduced methods are summarized in **Table 2-5.** While electrospinning is the most common method for producing nanofibers used in skin wound dressings and skin substitutes, alternative techniques like self-assembly, drawing, mold templating, and phase separation can also be employed in nanofiber fabrication.

Table 2-5 Advantages and Disadvantages of Loading Methods for Therapeutic/Bioactive Agents into Membranes

Techniques	Advantages	Disadvantages
Blending	**Ease of Fabrication:** Blending is straightforward and relatively easy to implement. **Incorporation of Multiple Agents:** Suitable for incorporating various agents like antibiotics, hemostatic agents, and other bioactive substances. **Flexibility:** Altering polymer concentrations or compositions can influence drug release, loading capacity, and sustainability.	**Lack of Control:** Blending lacks precision in controlling the agent's release, potentially leading to burst release. **Challenges with Cosolvent:** Finding a suitable cosolvent compatible with both polymers and bioactive agents can be challenging. **Limited Targeted Delivery:** Not considered reliable for targeted delivery due to inconsistent release patterns.
Surface Modification	**Controlled Release:** Offers control over the release rate, preventing initial burst release. **Versatility:** Various methods like physical adsorption, NPs assembly, layer-by-layer assembly, and dip-coating can be employed based on requirements. **Preservation of Bioactivity:** Ensures bioactivity preservation during the attachment process.	**Limited Loading Capacity:** May have restrictions on the amount of agent that can be loaded onto the surface. **Potential Bond Weakness:** The strength of bonds between agents and surfaces can be a concern. **Modification Impact: Chemical attachment** methods can alter active sites of molecules, affecting functionality in cell interactions.
Co-axial	**Controlled Release:** Enables precise control over drug release rate. **Preservation of Bioactivity:** The bioactivity of the drug or bioactive agent remains intact during the process. **Multiple Release Rates:** Allows for varied release rates based on polymer properties.	**Complexity:** Experimental design can be intricate, limiting broader application. **Specialized Equipment:** Requires specific equipment and expertise. **Potential Limitations in Polymer/solvent Selection**: The choice of polymers and solvents can impact the efficiency of the technique.
Emulsion	**Simplified Fabrication:** Simplifies the process by preparing a combined mixture, avoiding the challenges of separate solutions. **Versatility:** Can incorporate both low and high molecular weight agents. **Dual Release:** Facilitates the release of multiple agents with synergistic effects.	**Risk to Bioactive Agents:** Potential damage to sensitive bioactive agents, especially proteins and growth factors. **Presence of Organic Solvent:** The organic solvent can pose risks to certain bioactive agents. **Complexity in Formulation:** Requires careful formulation to ensure stability and effectiveness.

2.7 Conclusions

Accelerating wound healing can significantly reduce morbidity and mortality rates among patients with severe wounds, such as burns or diabetic ulcers. A prominent challenge in addressing these severe wounds is the limited regenerative capacity of the skin. In certain cases, hindered healing processes result in scar formation, which imposes a financial burden and leads to aesthetic and health-related concerns. Utilizing biomaterials to protect the injured area and stimulate rapid skin regeneration is paramount in such critical situations. Nanofibers's unique properties, including nanotopography for cell signaling, high surface area for biomolecule adsorption, and mimicry of the ECM, make them promising candidates for advanced wound

dressings. Nanofibrous wound dressings offer distinct advantages over other alternatives like hydrogels. Notably, in addition to their architectural similarity to natural skin, which provides crucial physical cues, nanofibrous wound dressings possess optimal absorption rates and breathability. This prevents issues like wound dehydration or fluid accumulation at the wound site. Furthermore, their ease of handling, fabrication, and the ability to finely adjust their properties make electrospun wound dressings increasingly popular for various wound healing applications. Fabricating an effective wound dressing requires a delicate balance of material choice, structure, physical attributes, and biological cues. In this paper, we have delved into a range of physical and chemical cues that have been investigated by researchers with the ultimate goal of expediting wound healing while mitigating scarring. Although the wound healing process is complex, factors such as the physical properties of the wound dressing—such as porosity, alignment, and pore size—along with the controlled release of therapeutic agents like growth factors, drugs, and herbal extracts, can play pivotal roles in expediting wound healing and reducing the likelihood of scarring. One of the primary causes of scarring is excessive wound contraction, primarily driven by the dominance of myofibroblasts over fibroblasts. The fibrous structure of a wound dressing, coupled with its mechanical properties, can positively impact fibroblast proliferation. Additionally, when nanofiber diameters reach 300 nm or less, they not only boost fibroblast proliferation and migration but also guide them to spread along the fibers. This leads to increased focal adhesion of cells and, subsequently, higher proliferation rates and prevents over-differentiation to myofibroblast that causes excessive wound contraction and scar formation. Furthermore, the micron-scale pore size of nanofibrous wound dressings plays a crucial role in facilitating fibroblast migration, proliferation, and infiltration. This attribute also promotes improved vascularization and nutrient exchange, resulting in accelerated healing and

reduced risk of scarring. Futhermore, fiber alignment plays a crucial role in influencing cell morphology. By mimicking the distinctlayers and alignments of natural skin, aligned nanofibers can promote a more favorable healing environment. This factor needs careful consideration during wound dressing design.

Beyond their well-established physical features, nanofibrous wound dressings can be further enhanced by incorporating bioactive agents to promote accelerated and potentially scarless wound healing. Growth factors such as TGF, VGF, and EGF have demonstrated significant efficacy in regulating collagen and MMP expression, as well as promoting vascularization. Furthermore, a diverse range of additional bioactive agents, including antibiotics, anti-inflammatory drugs, herbal extracts, and metallic NPs, can modulate the wound healing cascade by controlling inflammation, preventing infection, and influencing gene expression and angiogenesis. The controlled release of these bioactive agents from the nanofibers offers a powerful tool to orchestrate cellular behavior and ultimately guide the wound towards faster healing with minimal scarring.

2.8 Future Insights

This comprehensive review has elucidated the critical role played by the physical properties of electrospun membrane dressings in optimizing various aspects of wound healing, encompassing both skin regeneration and the potential for scarless wound healings. Additionally, various electrospinning processes for controlling the release profiles of chemical cues were discussed, aiming to achieve scar-free healing. However, electrospinning technology continues to advance, leading to the fabrication of increasingly diverse morphologies and complex structures with immense potential for minimizing scar formation during skin wound healing. One such promising new development is the multifluid approach, which creates multi-chamber

nanostructures particularly beneficial for engineered drug delivery systems. Employing a multiple-channel spinneret facilitates the replication of intricate structures that can inspire innovative biomimicry approaches, further advancing the development of nanomaterials and nanodevices [300]. These advancements pave the way for smaller, more orderly, and more intricate structures with varied morphologies, including single hollow, sheath-separate-core, and multi-channel hollow nanofibers [300]. These complex structures allow for precise tailoring of components, compositions, and spatial distributions within the nanofibers, thereby enabling them to exhibit multiple functionalities.

It is hypothesized that electrospun heterogeneous nanofibers with multi-chamber structures can be loaded with multiple active ingredients, each with its own ideal release profile, thus enhancing synergistic therapy [230,301]. Ongoing advancements in multifluid electrospinning processes have led to the creation of intricate nanostructures such as core-shell, Janus, tri-section Janus, and trilayer core-shell nanofibers, along with a combination of these structures [302–304]. Janus fibers, characterized by two or more independent parts parallel to each other on a micro or nano scale, offer unique advantages [305]. These fibers have been explored for various applications, such as oral and colon-targeted drug delivery [306,307]. However, their potential in skin tissue engineering remains largely unexplored and warrants further investigation.

Furthermore, in the field of complex structures, the integration of electrospinning and electrospraying—both techniques utilizing electrohydrodynamic atomization—presents an exciting possibility for creating beads-on-a-string structures [308]. These hybrids can be fabricated through a single-step electrospinning procedure or by combining electrospinning and electrospraying. In the latter method, electrosprayed particles are suspended in an

electrospinnable polymeric solution, which is then processed to form the desired beads-on-a-string solid structures [308]. This hybrid approach holds promise for advanced drug delivery systems by enabling the incorporation of diverse chemical cues with tailored release profiles [309,310]. Beyond its established applications in drug delivery, the potential of this new paradigm in electrospinning for skin regeneration and scar minimization warrants further investigation. The unique combination of surface morphology, mechanical properties, and controlled release profiles of various chemical cues offered by these complex structures could significantly enhance skin regeneration outcomes by promoting optimal cell adhesion, proliferation, and differentiation.

A pivotal aspect of advancing electrospun membrane technologies for scarless wound healing lies in the utilization of appropriate animal (*in vivo*) models. Despite the potential of these membranes, their clinical transition is hindered by a lack of comprehensive *in vivo* studies. This gap in research is primarily due to the reliance on rodent models, which, while beneficial for initial evaluations, do not adequately replicate human wound healing mechanisms. Rodents have a different skin structure and healing process, often leading to faster healing and less scarring compared to humans, which can distort the assessment of the effectiveness of electrospun membranes in scarless healing. To bridge this gap, future research should focus on employing more representative animal models. The porcine model is one such alternative, as porcine skin closely resembles human skin in terms of its structure, thickness, and healing process. However, the use of porcine models is often limited by higher costs and ethical considerations. Therefore, developing cost-effective and ethically sustainable porcine models could be a significant step forward in this research domain. Another promising direction is the exploration of other large animal models that may present a closer approximation to human skin

characteristics and wound healing patterns. These could include models like sheep or non-human primates, each offering unique insights into the wound healing process and the efficacy of electrospun membranes. Moreover, there's a need for more longitudinal studies that track the healing process over extended periods. These studies should focus not just on the rate of wound closure but also on the quality of the regenerated skin, particularly in terms of its structural and functional similarities to natural skin. Parameters such as the formation of scar tissue, re-establishment of normal skin appendages, and restoration of skin pigmentation and texture should be evaluated. Advancements in imaging and molecular analysis technologies can also play a crucial role in these studies, providing deeper insights into the biological processes at play during the healing process. These technologies can help in tracking cellular behaviors, angiogenesis, and the integration of the electrospun membrane with the native tissue at a microscopic level. Finally, there is a growing need for the standardization of protocols and benchmarks in the testing of electrospun membranes using animal models. Establishing these standards will ensure consistency and comparability in research outcomes, aiding in the more efficient translation of promising findings into clinical applications.

Building on the advancements in electrospun nanofibrous wound dressings for accelerated scarless healing, a promising future pathway is the development of patient-specific wound dressings. This personalized approach aligns with the growing trend towards tailored medical treatments, which can significantly enhance the efficacy and outcomes of wound care. For patient-specific electrospun wound dressings, two approaches might be used. First, using pre-fabricated nanofibrous membranes cultured with the patient's cells and the second, using *in situ* electrospinning. The first approach leverages pre-fabricated electrospun nanofibrous membranes as scaffolds for personalized wound dressing. These scaffolds are seeded with

autologous cells harvested from the patient and cultured for a defined incubation period. This strategy offers several advantages. First, it minimizes the risk of immune rejection by utilizing the patient's own cells. Second, the seeded cells can actively participate in wound healing by promoting the deposition of ECM components, thereby mimicking the natural tissue regeneration cascade. This close mimicry of the native environment can significantly enhance the regeneration of skin tissue. The second approach is the *in situ* electrospinning of nanofibers directly onto the wound site. This technique allows for the creation of a wound dressing that perfectly conforms to the shape and size of the wound, providing optimal coverage and protection. *In situ* electrospinning can be particularly beneficial in surgical settings and for treating irregularly shaped or hard-to-reach wounds. For military applications, where immediate and effective wound care is crucial, portable *in situ* electrospinning devices are developed to provide immediate frontline care, significantly improving the healing process in combat-related injuries [311]. While the developed portable electrospinning machine offers a promising platform for point-of-care wound treatment, further advancements are necessary to unlock its full potential. Expanding its functionality to accommodate a broader range of biocompatible natural polymers would significantly enhance its versatility. Additionally, rigorous *in vivo* studies are required to evaluate the efficacy of the resulting dressings in promoting accelerated wound healing with minimal scarring. The integration of computational modeling and advanced imaging techniques can be instrumental in achieving this goal. In silico models can predict the behavior and therapeutic efficacy of electrospun fibers within diverse wound microenvironments. These models can be tailored to incorporate patient-specific variables such as wound size, depth, location, age, skin type, and underlying health conditions, enabling the design of truly personalized wound dressings. Furthermore, high-resolution imaging techniques can be

employed for pre-operative wound assessment, guiding the customization process and ensuring optimal coverage. These same techniques can be used post-application to monitor the healing process in real time, providing valuable data for further refinement of the dressings and treatment protocols. When it comes to translation to clinical application and reaching accelerated and scarless healing in real life, one of the main limitations of electrospun wound dressings is their inherent 2D structure. While these dressings can provide a barrier and facilitate cell growth, they often fall short of adequately mimicking the complexity of native skin, especially in terms of regenerating intricate skin appendages such as hair follicles and sweat glands. The goal of achieving complete skin regeneration includes not just the epidermal layer but also the essential appendages. The absence of such features in wound healing is not just a cosmetic issue; it has significant implications for the functionality and overall health of the skin. For example, the lack of sweat glands compromises thermoregulatory functions, while missing hair follicles affect sensory perception and protection. To address these challenges and facilitate clinical translation, innovative approaches in electrospun wound dressing design are required, such as fabricating asymmetric layered nanofibrous wound dressings or utilizing hybrid wound dressings combining electrospun membranes and hydrogels. For the first approach, asymmetric multilayered nanofibrous dressings are designed with each layer engineered to mimic a specific layer of the skin. This can be achieved by varying properties such as fiber diameters and porosity across different layers. Another promising pathway is the development of hybrid dressings that integrate nanofibrous membranes with hydrogels to mimic the epidermis and nanofibrous membrane the dermis structure of the skin [312–315]. Such dressings can leverage the mechanical support and controlled release capabilities of nanofibers, combined with the moisture-retaining and giving thickness and 3D structure of hydrogels [316]. These multi-

layered, hybrid dressings aim to address the diverse requirements of skin regeneration more comprehensively. For instance, incorporating different types of cells into each layer can aid in replicating various aspects of skin: fibroblasts in the hydrogel layer, which is in contact with the wound, and keratinocytes in the nanofibrous layer. The differences in the pore size of these layers prevent the migration of cells out of the layer and, hence, facilitate accelerated healing [317]. Therefore, this approach can create a more skin-like structure, promoting comprehensive regeneration and leading to less scar formation. The nanofibrous component provides structural integrity, supports cell adhesion, and facilitates the controlled delivery of bioactive agents. While the hydrogel layer offers a physiologically relevant matrix that promotes hydration, nutrient diffusion, and cellular interactions necessary for appendage formation. By integrating the distinct advantages of both nanofibrous membranes and hydrogels, these advanced wound dressings have the potential to revolutionize skin regeneration. They hold the promise of enabling the full regenerative potential of the skin, including the reformation of its appendages, thus achieving a more holistic approach to wound healing and skin tissue engineering, leading to scarless healing. Future research should focus on optimizing these hybrid structures for practical use, ensuring their biocompatibility, effectiveness in appendage regeneration, and scalability for clinical applications.

Looking ahead, the evolution of electrospun wound dressings for accelerating healing and achieving scarless skin regeneration exceeds the realm of bioactive membranes, venturing into the integration of advanced technologies such as biosensors and responsive materials. Biosensor-based electrospun dressings could be equipped with sensors capable of monitoring various environmental factors within the wound microenvironment, such as bacterial presence, oxygen levels, reactive oxygen species, temperature fluctuations, and pH changes. These factors are

critical in the wound healing process, and their imbalance can lead to delayed healing or scar formation. Integrating sensors into wound dressings could revolutionize treatment by enabling the real-time tracking of wound conditions [106,108,318]. This innovation would offer clinicians immediate, data-driven insights to inform their treatment strategies. This technology could be particularly beneficial in managing chronic or complex wounds, where constant monitoring is essential for effective treatment. Beyond detection, the next generation of nanofibrous wound dressings could be engineered to be smart and capable of responding to changes in the wound environment. These dressings could be designed to release bioactive agents in response to specific stimuli detected by the sensors. For example, upon detecting an increase in bacterial load or a change in pH indicative of infection, the dressing could release antimicrobial agents [76]. Similarly, in response to low oxygen levels, it could release substances that promote angiogenesis. This responsive approach ensures that the therapeutic agents are released precisely when needed, optimizing the healing process and reducing the risk of complications such as excessive scarring. Another exciting avenue is the development of stimulant wound dressings that utilize physical forces like magnetic, electric, or mechanical stimuli to promote scar-free wound healing. For instance, electrically stimulated dressings could improve tissue regeneration by mimicking the body's natural electrical signals involved in wound healing. Similarly, mechanical stimulation could be used to influence cell behavior and tissue formation, aiding in scarless healing. These advanced dressings, combining sensor technologies, smart responsiveness, and physical stimuli, represent a significant leap forward in wound care. They hold the promise of not only accelerating the healing process but also actively preventing scar formation, thereby improving the quality of life for patients.

In conclusion, the future of electrospun wound dressings represents a convergence of multiple disciplines, notably materials science, bioengineering, and medicine. This integrative approach is poised to drive significant innovations in the field. As research progresses, these advanced wound care technologies are increasingly becoming a tangible reality, offering promising new options for enhanced patient care in complex wound management scenarios.

2.9 Acknowledgment

The authors appreciate and acknowledge the financial support from the Natural Sciences and Engineering Research Council of Canada (NSERC) Discovery Grant (RGPIN-2019-06094) and UofM GETS program funding.

2.10 CRediT Authorship Contribution Statement

Farinaz Jonidi Shariatzadeh: Writing – review & editing, Writing – original draft, Visualization, Methodology, Formal analysis, Conceptualization. **Sarah Currie:** Writing – review & editing, Methodology. **Sarvesh Logsetty:** Writing – review & editing, Validation, Conceptualization. **Rae Spiwak:** Writing – review & editing, Methodology. **Song Liu:** Writing – review & editing, Validation, Supervision, Methodology, Funding acquisition, Conceptualization.

2.11 Declaration of Competing Interest

The authors declare that they have no known competing financial interests or personal relationships that could have appeared to influence the work reported in this paper

.

3 Chapter 3: Hypothesis and Objectives

.

3.1 Rationale and Hypothesis

The primary aim of this thesis was to develop different biomaterials for altering different scenarios of wound healing with the potential to reach accelerated and scarless healing. Scar formation is a common outcome of wound healing and arises from various internal and external factors. A key contributor to excessive scar formation is prolonged inflammation. During extended inflammation, inflammatory cells and cytokines stimulate fibroblasts, promoting the secretion of collagen in parallel arrangements rather than the basket-weave configuration characteristic of healthy tissue. This process also alters the collagen type I to type III ratio and inhibits the expression of matrix metalloproteinases (MMPs), further contributing to scar formation.

It is crucial to mitigate prolonged inflammation to shift wound healing from a scarring trajectory toward regeneration. One significant factor perpetuating inflammation is bacterial presence. Bacterial infection prolongs the inflammatory phase, disrupting the collagen organization necessary for proper healing. Therefore, early detection of bacteria and prevention of infections are vital for reducing immune cell activity and curbing inflammation.

However, common sustained delivery systems for antibiotics in wound care have several significant drawbacks. They often result in low bioavailability and limited penetration of antibiotics to the site of infection, reducing their overall effectiveness. Additionally, these systems can lead to the accumulation of antibiotics in healthy tissues, increasing the risk of systemic toxicity and adverse side effects. Another critical issue is the exposure of bacteria to sub-lethal doses of antibiotics due to sustained release, which promotes the development of antimicrobial resistance. To overcome these limitations, the development of stimuli-responsive

carrier systems is essential. These systems can dynamically respond to the bacterial microenvironment or specific physical stimuli, ensuring targeted drug delivery, enhancing therapeutic efficacy, and minimizing side effects while simultaneously offering a novel approach to combat antimicrobial resistance.

In addition to managing inflammation, promoting scarless healing may be achieved by using anti-scar drugs. These agents often enhance MMP activity, which is essential for the degradation of temporary extracellular matrix scaffolds during wound remodeling. However, the timing and targeted delivery of such drugs are critical to ensure their efficacy without disrupting other aspects of healing.

This chapter delves into hypotheses to address the identified challenges and outlines the objectives that guide the exploration of strategies to accelerate wound healing and reduce scarring.

3.1.1.1 Bacteria Detection at Low Concentration

As previously discussed, one of the primary factors contributing to prolonged inflammation during wound healing is the presence of bacteria. If bacteria are detected in the wound area at low concentrations—before infection develops and triggers an immune response—the recruitment of inflammatory cytokines and cells can be minimized. Immune cells typically combat bacteria at low concentrations without disrupting normal wound healing. However, when bacterial concentrations exceed critical thresholds, the healing process can be impaired. Current standard diagnostic techniques, however, are limited in their ability to detect bacteria at low concentrations when the natural healing trajectory can still be maintained. They are typically employed only after physical symptoms of infection have manifested, and bacterial

detection through culturing or sampling often requires several days. This delay underscores the need for a real-time biosensor capable of detecting bacteria at low concentrations.

To address this challenge, our group has developed a hemi-cyanine dye that is cleaved by bacterial lipase. This enzymatic cleavage induces intramolecular charge transfer, resulting in a visible color change.

In this thesis, we aimed to detect bacteria at low concentrations—before the significant recruitment of inflammatory cells—in order to prevent prolonged inflammation and improve wound healing outcomes.

The dye is incorporated into a nanofibrous membrane biosensor to enhance its sensitivity. This membrane, with its high surface area, promotes increased interactions between the bacteria and the lipase enzyme. Furthermore, we hypothesize that the sensitivity of the biosensor can be further improved by aligning the nanofibrous membrane and incorporating a bacterial inducer, as depicted in **Figure 3-1**. Specifically, we proposed that aligned fibers facilitate bacterial localization while the addition of Tween 80—a known inducer of bacterial lipase activity—amplifies lipase response without requiring higher bacterial concentrations. This combined strategy aims to enable the biosensor to detect bacterial concentrations as low as 10^5 CFU/g, providing a powerful tool for early bacterial detection and inflammation control in wound management.

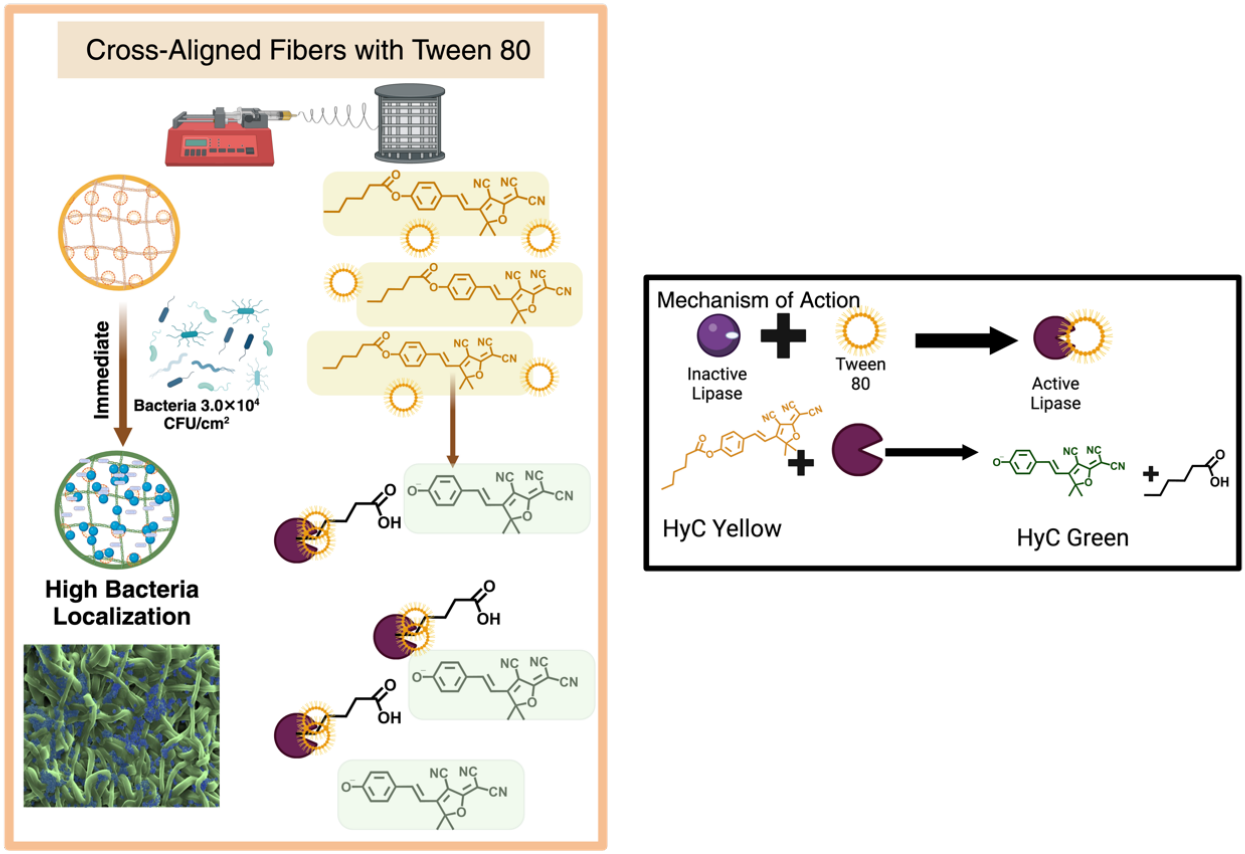

Figure 3-1 The first Hypothesis: Detecting bacteria at a low concentration before infection occurs by a sensitive biosensor with an aligned nanofibrous structure and a lipase inducer.

3.1.1.2 Targeted Delivery of Antibiotics

In addition to early detection of bacteria to prevent infection and prolonged inflammation, eliminating bacteria from the wound environment is essential for promoting healing. However, this must be achieved without increasing the risk of bacterial resistance to antibiotics. Bacterial presence in wounds is a primary reason for the overlap between the inflammatory and proliferative stages of healing, which disrupts the regeneration process. The persistence of immune cells at the injury site, along with elevated levels of pro-inflammatory and inflammatory cytokines, adversely affects fibroblast function and collagen production, hindering proper tissue regeneration.

Localized delivery of antibiotics offers a promising approach to eliminating bacteria while reducing immune cell activity and inflammatory cytokines. However, sustained release of antibiotics can promote bacterial resistance, a significant concern in wound management. In contrast, responsive delivery of biocides not only allows for targeted action but ensures that biocides are released only in the presence of bacteria, thereby minimizing unnecessary exposure to healthy tissues. Responsive delivery also helps to reduce the risk of bacterial resistance by avoiding constant or excessive biocide presence. Additionally, responsive delivery enhances the efficacy of treatment by concentrating the biocide at the site of infection, improving its effectiveness while preserving the natural wound healing process. By limiting biocide release to critical conditions it minimizes cytotoxicity and other side effects on non-target cells, making it a safer and more efficient approach to managing infections. Stimuli-responsive systems, triggered by factors such as pH changes, temperature variations, toxins, or bacterial enzymes, provide a targeted method for drug release. Among these stimuli, the increased levels of reactive oxygen species (ROS) generated by immune cells in response to bacterial presence serve as a reliable indicator of infection.

We hypothesized that a nanoparticle-based drug delivery system responsive to ROS could effectively release antibiotics to combat bacteria at the wound site only if the ROS agent is present. By incorporating these nanoparticles into the color-changing biosensor, we proposed the development of a theranostic biosensor—a dual-function system capable of both detecting bacteria and delivering treatment, as depicted in **Figure 3-2**. This integrated approach aims to prevent infection progression, thereby reducing inflammation and promoting a regenerative healing pathway. Ultimately, such a system would accelerate wound repair while minimizing scar formation.

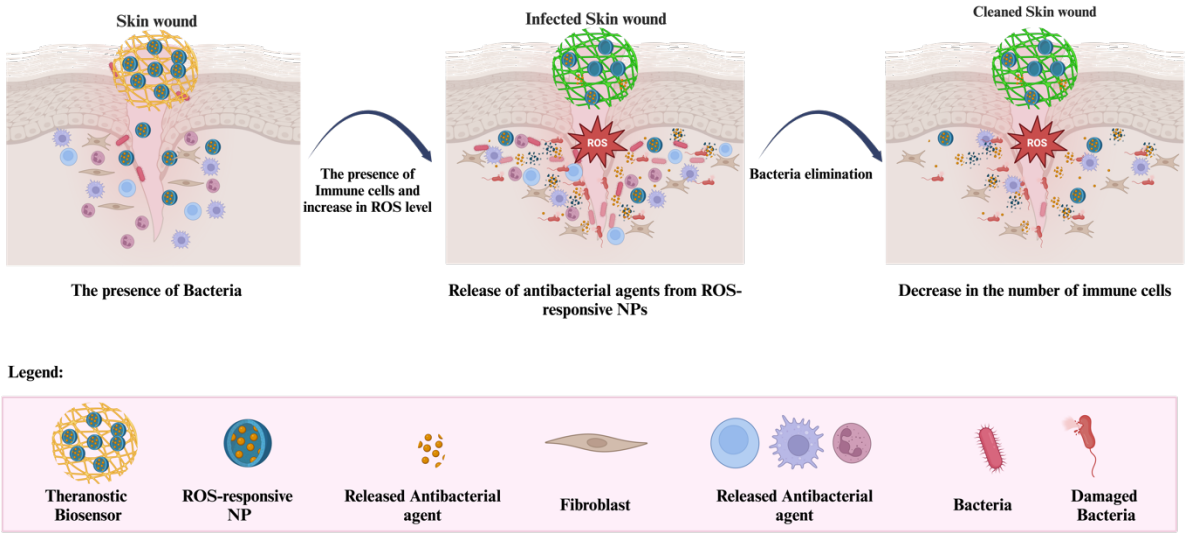

Figure 3-2 The second Hypothesis: Targeted delivery of antibiotics with ROS-responsive NPs to eliminate bacteria and shorten the inflammation stage.

3.1.1.3 Targeted Delivery of Anti-Scar Drug

In addition to managing the inflammatory stage, the proliferation phase of wound healing can be strategically manipulated to achieve accelerated healing with a reduced likelihood of scar formation. Anti-scar drugs are commonly used to degrade temporary collagen scaffolds, facilitating their replacement with basket-weave-structured collagen fibers. These drugs often enhance the activity of MMPs, which degrade the temporary ECM. However, the precise delivery of these drugs to the correct location and at the optimal time remains a significant challenge.

Daily application of anti-scar drugs during the proliferation phase typically requires frequent dressing changes, which not only increases the risk of infection but also causes additional injury to the wound site. To address this issue, incorporating the drug into wound dressings has been proposed. However, the sustained release of these drugs during the initial (inflammatory) or later (remodeling) phases of healing can have adverse effects, such as

prolonging the wound healing process or making the wound chronic. Thus, designing a targeted delivery system capable of releasing the drug at the appropriate time is of critical importance.

Targeting the specific window of scar formation requires identifying a biomarker that is highly expressed during this phase but not in others. Connective tissue growth factor (CTGF) is one such biomarker, as its levels increase during the scar formation stage when fibroblasts transition to myofibroblasts. We hypothesized that loading an anti-scar drug into lipid-based nanoparticles decorated with insulin-like growth factor (IGF) can enable targeted delivery to cells with higher expression of CTGF, as depicted in **Figure 3-3**. Using CTGF as a ligand to facilitate endocytosis, the nanoparticles can release the drug precisely at the stage of scar formation. This targeted approach has the potential to minimize scar formation, optimize tissue regeneration, and achieve accelerated wound healing.

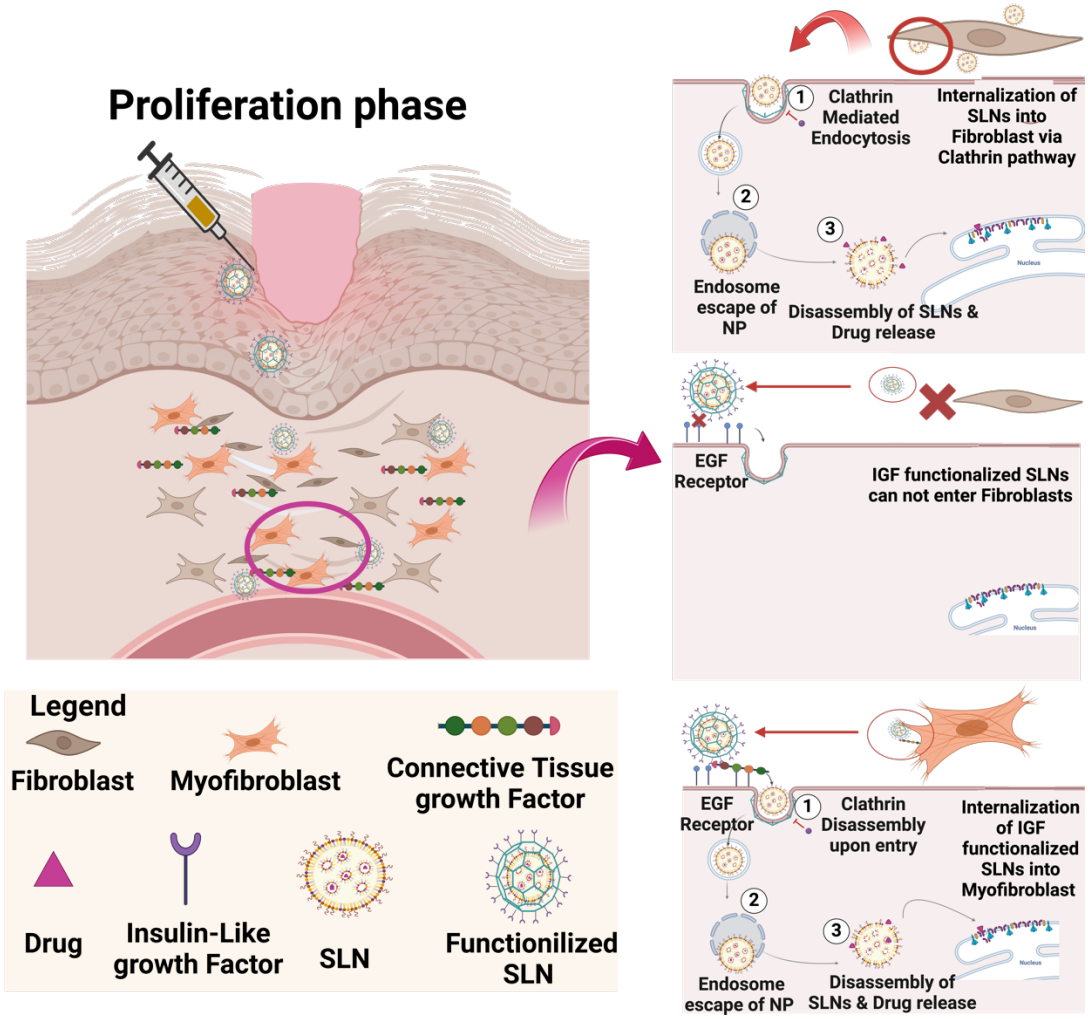

Figure 3-3 The third Hypothesis: Targeted delivery of anti-scar drug in the scar formation stage.

3.2 Objectives

Various approaches have been employed in this thesis to validate the proposed hypotheses. The primary goal was to manipulate different stages of the healing process to achieve accelerated healing and regeneration potentially. The objectives were categorized into three main areas to address accelerated healing using various strategies. The first objective focused on developing a biosensor capable of detecting bacteria at low concentrations to prevent infections. The second involved creating a responsive drug delivery system for the controlled release of biocidal agents. Lastly, the third objective aimed at designing targeted delivery systems for anti-scar drugs. The following sections provide a detailed discussion of each objective, along with the corresponding sub-objectives within each category.

3.2.1 Fabricating a Biosensor for Bacteria Detection at Lower Concentrations

The first objective was to fabricate aligned nanofibers to enhance the sensitivity of biosensors for detecting bacteria at lower concentrations. Aligned fibers are hypothesized to improve bacterial localization and their interaction with the fibers and incorporated dyes, thereby enhancing detection capabilities. While the effect of fiber alignment on various human cell types, such as stem cells, muscle cells, and fibroblasts, has been extensively studied, its influence on bacterial localization remains unexplored. Achieving fiber alignment via electrospinning requires modifications to the collector system of the electrospinning equipment.

The second objective aimed to increase bacterial lipase activity without altering the bacterial population in the wound. For this objective, an inducer was incorporated into the fibers to increase the lipase activity. Although the effects of various inducers, including ions and carbon or nitrogen sources, on lipase activity have been widely studied, these inducers are typically added in solution to liquid media. In this study, the challenge was to incorporate the

inducer into the fibers in solid form and evaluate its effect on lipase activity within the wound environment. This approach ensures that lipase activity is enhanced locally, contributing to the improved performance of the biosensor.

3.2.2 Fabricating Antibacterial Biosensors to Kill Bacteria without Causing Resistance

Two primary objectives were defined to develop a theranostic biosensor capable of both detecting bacteria and preventing infection.

The first objective focused on ensuring that the biosensor does not produce false-positive results in the absence of bacteria in the wound or media. Therefore, various additives were tested and incorporated into the nanofiber structure to eliminate false-positive signals, improving the reliability and specificity of the biosensor.

The second objective addressed the prevention of infection by designing a system for targeted antibacterial delivery. The design involved synthesizing a polymer responsive to ROS that can undergo a structural transformation from hydrophilic to hydrophobic. This transformation enables the polymer to form self-assembled nanoparticles loaded with antibacterial agents. In the presence of ROS, the structural change triggers the disassembly of the nanoparticles, releasing the antibacterial agents precisely where and when needed.

The subsequent step for this objective was to incorporate these ROS-responsive nanoparticles into nanofibrous wound dressings, resulting in a theranostic dressing. This advanced dressing combines diagnostic and therapeutic functionalities, enabling bacteria detection and infection prevention within a single platform.

3.2.3 Fabricating Targeted Delivery Systems for Scar Formation Window

To directly manipulate the proliferation stage of wound healing using an anti-scar drug, the primary objective was to fabricate lipid-based NPs with high drug-loading efficiency and an appropriate size to ensure effective penetration through the skin.

The next key objective was to develop a targeted delivery system by functionalizing the nanoparticles with a unique biomarker that exhibits a high affinity for CTGF. This approach was designed to enable selective delivery of the anti-scar drug to cells expressing CTGF, thereby maximizing therapeutic efficacy while minimizing off-target effects.

The final objective was to test the targeting ability of fabricated NPs using a cellular model with known CTGF expression. Breast cancer MCF7 cells were selected for this purpose, as they express CTGF. The CTGF expression of these cells was validated using an antibody assay to confirm their suitability for evaluating the targeted delivery system. The validity test with MCF7 was done since differentiating fibroblasts to myofibroblasts and keeping their phenotypes required more expertise and experiments. However, it is part of future works for this thesis.

The following chapters address each of these objectives in detail, outlining the experiments conducted to achieve the final goals and discussing the results obtained at each phase.

4 Chapter 4: Ultra-Sensitive Biosensor for Bacteria Detection

Ultra-Sensitive Nanofiber Biosensor: Rapid in situ Chromatic Detection of Bacteria for Healthcare Innovation

Farinaz Jonidi Shariatzadeh[1], Sarvesh Logsetty[2] and Song Liu[1,3]*

1) Biomedical Engineering, Faculty of Engineering, University of Manitoba, Winnipeg, Manitoba, Canada, R3T 2N2
2) Departments of Surgery and Psychiatry, Rady Faculty of Health Sciences, University of Manitoba, Winnipeg, Manitoba, Canada, R3E 3P5
3) Department of Biosystems Engineering, Faculty of Agricultural and Food Sciences, University of Manitoba, R3T 2N2 song.liu@umanitoba.ca; +1) 204-474-9616).

Revised from the research article published in ACS Applied Bio Materials 2024 7 (4), 2378-2388, DOI: 10.1021/acsabm.4c00038
(https://pubs-acs-org /doi/full/10.1021/acsabm.4c00038)

Contribution as the first author: **Farinaz Jonidi Shariatzadeh:** Writing – review & editing, Writing – original draft, Visualization, Validation, Methodology, Data Curation, Formal analysis, Conceptualization.

ABSTRACT:

Rapid detection of bacterial presence in skin wounds is crucial to prevent the transition from acute to chronic wounds and the onset of systemic infections. Current methods for detecting infections, particularly at low concentrations (<1.0E+5.0 CFU/cm^2), often require complex technologies and direct sampling, which can be invasive and time-consuming. Addressing this gap, we introduce a colorimetric nanofibrous biosensor enabling real-time, *in situ* monitoring of bacterial concentrations in wounds. This biosensor employs a colorimetric hemicyanine dye (HCy) probe, which changes color in response to bacterial lipase, a common secretion in infected wounds. To enhance the biosensor's sensitivity, we incorporated two key material science strategies: aligning the nanofibers to promote efficient bacterial attachment and localization and integrating Tween 80, a surfactant, within the nanofiber matrix. This combination of physical and chemical cues results in a notable increase in lipase activity. The cross-aligned core-shell nanofibers, embedded with Tween 80 and HCy, demonstrate an immediate and distinct color change when exposed to as low as 3.0E+4.0 CFU/cm^2 of common pathogens such as *P. aeruginosa* and MRSA. Significantly, the presence of Tween 80 amplifies the colorimetric response, making visual detection more straightforward and four times more pronounced. Our nanobiosensor design facilitates the detection of low-concentration bacterial infections *in situ* without the need to remove wound dressings. This advancement marks a significant step forward in real-time wound monitoring, offering a practical tool for the early detection of clinical bacterial infections.

Keywords: Colorimetric probe, color-changing sensor, real-time infection detection, nanofibers, bacterial lipase, Tween80.

Table of Contents artwork here

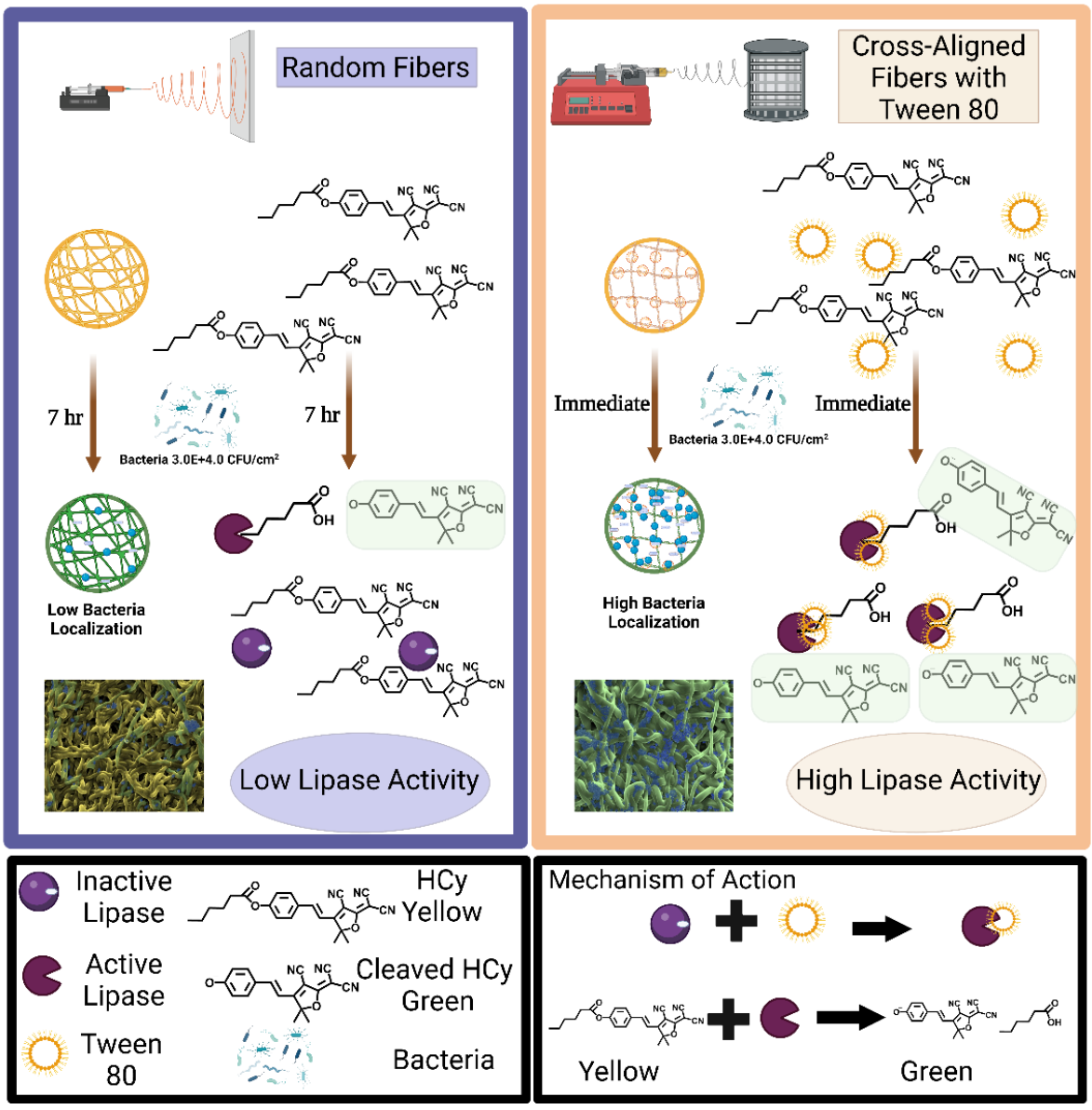

4.1 Introduction

Wound infection is one of the major causes of non-healing wounds and a significant contributor to the associated healthcare costs [319]. Standard infection detection techniques such as swabbing/plating and polymerase chain reaction often fail to provide timely results, require highly trained personnel, and are expensive [319,320]. Moreover, the lack of a sensitive bedside bacteria detection technique at the early stages of colonization necessitates drastic antibiotic usage in later stages, increasing bacterial resistance and compromising patients' health by causing a chronic wound or scar formation [321–323]. Consequently, in order to overcome the mentioned drawbacks, developing *in situ* colorimetric biosensors that can detect the presence of bacteria before reaching the critical colonization stage has been in the spotlight [324]. The *in situ* colorimetric biosensor advantages include their low cost, ease of handling, easy storage, easy readout, and real-time observability with the naked eye, which does not necessitate dressing removal, wound sampling, or sample preparation [325–327]. The detection principle for *in situ* chromatic biosensors relies on utilizing dyestuffs that can change their structure after exposure to a stimulant.

Bacterial infections are associated with physical and biochemical biomarkers, such as alkali pH, low oxygen level, and the presence of extracellular bacterial enzymes. The incorporated dyestuffs with different functional groups undergo structural changes in the presence of these biomarkers, leading to a visual signal [326,328]. For instance, various natural dyes can be used as *in situ* colorimetric biosensors based on pH. The pH of natural skin ranges from 4.0 to 6.0. When the skin is injured, the wound exudate increases the pH to 7.0-7.4. If infection occurs, the pH increases to 8.0 and higher due to byproducts of bacteria such as ammonia [328,329]. Therefore, incorporating dyes that change their color at different pH have

been used for bacteria detection. Although pH changes in the case of bacterial infection, it also changes significantly during wound healing stages (acidic in hemostasis and inflammation stages and alkaline in the proliferation stage) [330–332]. Consequently, the pH alone cannot be a reliable indicator. Alternatively, bacterial toxins and extracellular enzymes such as lipase can be used as more reliable indicators for *in situ* infection detection [333–336].

Incorporating an *in situ* colorimetric biosensor is aimed at delivering an economically viable biosensing solution that provides easily interpretable results and the ability to signal the presence of infection in wounds rapidly. In this context, the use of electrochemical or fluorescence-based biosensors is hindered by their limited accessibility and complex readout procedures. Furthermore, despite their advantages, biosensors based on DNA or aptamer technologies often fall short in terms of cost-effectiveness. To overcome these shortcomings, our team has developed a colorimetric nanofibrous membrane, which transitions from yellow to green upon exposure to lipase secreted by bacteria [106]. The chromogenic probe, a hemicyanine (HCy) dye, features an ester bond susceptible to cleavage by lipase. This cleavage facilitates more efficient intramolecular charge transfer (ICT), resulting in noticeable color changes. The HCy chromogenic probe, chosen for its sensitivity to lipase activity, does not exhibit selectivity towards specific bacteria strains. Instead, it is susceptible to cleavage by lipase secreted from a wide array of pathogenic bacteria, encompassing both gram-positive and gram-negative bacteria. Given the crucial role of lipase secretion in bacteria-host interaction, influencing pathogenicity and infection progression, the HCy probe emerges as a suitable tool for detecting infections in skin wounds [334–337]. The non-specific responsiveness of the probe to lipase from various bacterial sources enhances its utility as a versatile indicator of bacterial presence and underscores its potential significance in monitoring and diagnosing infections in wound settings.

The dye was incorporated within nanofibers composed of water-swellable polyurethane (PU), a medical-grade polymer with FDA approval for wound dressing applications. The use of PU in the membrane not only preserves the structural integrity of the biosensor but also shields it from degradation in the presence of water or human fluids. Simultaneously, the PU material permits water penetration, facilitating interaction between lipase and the dye. To enhance the sensitivity of the biosensor, a core-shell structure was adopted, wherein the HCy dye was loaded into the shell. This design significantly increased the likelihood of interaction between the dye and lipase compared to a single PU configuration [106,108]. After being doped with polyvinyl pyrrolidone (PVP) in the shell, the membrane can detect bacteria within 2 hr. of exposure (2.5E+05 CFU/ cm^2 *P. aeruginosa* and 1.0E+06 CFU/cm^2 MRSA) [108]. Given that bacterial concentrations ranging from 1.0E+4.0 and 1.0E+5.0 CFU/cm^2 represent the critical colonization threshold in skin wounds, beyond which tissue damage and infection can occur[338,339], this study was focused on enhancing the detection limit to identify bacteria at these critical concentrations. We hypothesized that physical (nanofibers cross-alignment) and chemical (additives) cues could boost the sensitivity of the biosensors. The provided cues can amplify the analytic signal (the quantity and activity of bacterial lipase) while the bacterial number remains steady.

Nanofiber alignment's impact on various cellular behaviors (fibroblasts, neural cells, and stem cells), including migration, adhesion, and differentiation, has been extensively studied [340,341]. However, its effect on the attachment and activity of bacterial cells is still not fully understood, highlighting the need for additional research in this area. One specific study by Wang [342] explored the impact of polystyrene (PS) coating with parallel alignment on glass Petri dishes for *P. aeruginosa*. Wang's findings revealed that bacterial attachment, biofilm

formation, and biofilm detachment are significantly influenced by the surface's topology. Different diameters and spacings of aligned PS nanofibers affected bacterial attachment in varying ways. Notably, an aligned structure with a diameter of 375 nm and spacing of 0.7 μm increased bacterial attachment by nearly 6.5 times compared to an uncoated surface. While Wang's research underscores the importance of surface topography in bacterial attachment, it primarily focuses on parallel alignment as a coating. Our paper aims to explore the hypothesis that cross-aligned nanofibers might offer better localization of bacterial cells in nanofibrous membranes, potentially enhancing the interaction between bacteria and the chromogenic probe. The electrospun membranes were prepared by a modified electrospinning machine to achieve cross-aligned nanofibers. Besides the physical cue, we incorporated a chemical cue in the nanofibers to increase lipase activity. Increasing the lipase activity in liquid culture (in broth) has been done massively by adding surfactants, carbon, nitrogen sources, as well as divalent metallic ions [343]. However, adding these additives in a solid state has not been fully explored yet. To improve the sensitivity of the biosensor through material science, we chose to add a surfactant (Tween 80) as a solid chemical cue in our biosensor. Tween 80 has been reported to help unmask the activation domain by providing an interfacial surface. It has been shown that surfactants such as Tween 80 increase the water-lipid interfacial area and lead to a higher lipase activation rate [344]. Better localization of bacteria (due to nanofiber alignment) and more active lipase (due to the presence of Tween 80) could contribute to a higher chance of dye hydrolysis in a lower concentration of bacteria, hence boosting sensitivity. The nanofibers' alignment was observed under a conventional SEM, and a boosted detection sensitivity was demonstrated in a bacterial test using two prevalent wound pathogens, *P. aeruginosa* and MRSA, as well as a colorimetric lipase assay. The tween 80 incorporated HCy membrane with aligned nanofibers

could immediately detect bacteria around 2.77 E+04 - 3.17 E+04 CFU/$cm^{2,}$ which is lower than the critical colonization concentration. Noteworthily, the sensitivity of the newly developed biosensor shows a 10-100 fold improvement in the limit of detection compared to our previous design [108].

4.2 Experimental section

4.2.1 Fabrication of Nanobiosensors

Six membranes based on core-shell PU: PU/PVP/HCy nanofibers were prepared with co-axial spinneret apparatus (all material information and electrospinning machine design are provided in the supporting document). For core solution, 6 w/v% PU was dissolved in DMF: THF 1:1 solution overnight at 45 ˚C, and for shell solutions, 7 w/v % PU, 3.5 w/v % PVP, and 1.01 w/v % HCy were dissolved in DMF: THF overnight at 45 ˚C. The Tween 80 solution was mixed thoroughly with the shell solutions for the surfactant samples. Randomly oriented electrospun nanofibers and cross-aligned electrospun nanofibers membranes were prepared based on PU, PVP, and HCy without Tween 80 to evaluate the role of alignment on the properties of the membrane. Moreover, four membranes with different concentrations of Tween 80 in the shell composition were fabricated to evaluate the role of Tween 80 on different properties, especially lipase activity and sensitivity of the membranes, **Table S8-1** and **S8-2.**

4.2.2 Chemical Characterization of Nanobiosensors

Prepared membranes were used for chemical characterization with attenuated total reflectance-Fourier transform infrared (ATR-FTIR, Thermo Scientific, Nicolet is10) to demonstrate the presence of Tween 80 in the structure.

4.2.3 Morphological Characterization of Nanobiosensors

Morphology and alignment of the electrospun nanofibers were characterized using scanning electron microscopy (SEM, FEI Quanta FEG 650). Information about sample preparation and image analysis is provided in the supporting document (**Chapter 8**).

4.2.4 Limit of Bacteria Detection via Nanobiosensors

Bacteria suspensions were prepared (supporting document- **Chapter 8**), and bacteria lawns on TSA with different concentrations of bacteria were used to find the threshold of color change regarding the concentration of bacteria (limit of detection). Sample preparation and detection procedures are explained in the supporting document (**Chapter 8**).

4.2.5 Colorimetric Behavior of Nanobiosensors in The Presence of Bacteria

In addition to taking digital images, the color of biosensors was evaluated with a spectrophotometer (GretagMacbeth ColorEye 2180UV) with L: C 2:1 for the CMC formula to calculate ΔE and Δh (difference in hue) of samples (equations and information about CMC system is provided in the supporting document- **Chapter 8**). In addition to the quantitative data for the color change, a color pallet was prepared for each bacterium and each membrane at the threshold concentrations and high concentrations that can be used as a reference for the color-changing behavior of the biosensors. It should be noted that the data was compared to its own control on an agar plate for each sample.

4.2.6 Assay of Lipase Activity

An assay of lipase activity was conducted as follows. The bacteria plates were prepared as described in the supporting document, and after 5 hr. of incubation at 37 ˚C, samples were placed on the plates. The initial concentration of each plate was calculated based on a biopsied agar plug upon placing the samples, and the final concentration of each plate was calculated

based on the biopsied agar plug after 5 hr. of incubation at 37 ˚C. Detailed steps are explained in the supporting document (**Chapter 8**).

4.2.7 Interaction of bacteria and Nanobiosensors (Effect of Alignments on Bacteria Localization)

The high concentration plate of MRSA (5.2 E+08 CFU/cm^2) was used to evaluate the interaction of bacteria and biosensors. Biosensors with 1×1 (cm×cm) dimensions were placed on agar and incubated for 1 hr. at 32 ˚C. Then biosensors were collected and fixed for SEM imaging (details in supporting document-**Chapter 8**).

4.2.8 Colorimetric Behavior of Nanobiosensors in an *ex-vivo* Burn Model

To evaluate the behavior of Nanobiosensors in a more realistic situation, we used the porcine burn model developed in our group's previous studies, details provided in supporting document [106]. MRSA and *P. aeruginosa* were used to prepare infected wound models since these two bacteria are predominant in the skin and burn infections. The models were prepared by spreading 20 µL of bacteria solutions (10E+6.0 CFU/mL) on the burnt skin. After 2 hr. of incubation at 37 ˚C, 1×1 (cm×cm) samples were placed on wounds, and the color-changing behavior of biosensors was monitored. A burnt skin without bacteria was used as a control for each sample, and ΔE was calculated as described before.

4.2.9 Statistical Analysis

All data presented in this study are in mean format ± standard deviation, and the number of replications is present as an n-value. To compare the data, we used the one-way analysis of variance (ANOVA) while considering a significant difference at $p < 0.05$.

4.3 Result and discussion

4.3.1 Chemical Characterization of Nanobiosensors

This study aimed to increase the sensitivity of bacterial detection by chemical means, incorporating Tween 80 in the shell composition and physical means, controlling nanofiber alignment. Various nanofibrous membranes were fabricated with a core-shell nanofiber structure. All membranes had PU as their core and PU: PVP with a 2:1 ratio as their shell. Randomly oriented electrospun nanofibers based on PU and PVP were fabricated as controls to evaluate the role of alignment. Moreover, membranes with different concentrations of Tween 80 from 0% to 4% (w/v) were prepared to investigate the role of the surfactant in boosting sensitivity. The chemical composition of the membranes was characterized by ATR-FTIR. The chemical structures of components and the main peaks of each membrane are presented in **Figure S8-1**, with a detailed discussion of the assignment of these peaks provided in the supporting document. The analytical data suggest that Tween 80 has been successfully incorporated into the shell of nanofibers, with no evidence of chemical interaction with the other constituent polymers or the dye.

4.3.2 Morphological Characterization of Nanobiosensors

SEM images of the nanofibrous membranes were taken with different magnifications to evaluate the diameter and alignment of the nanofibers. **Figure S8-2** presents the SEM images of the samples (R, W, T0.1, T0.5, T2, and T4) with two magnifications (1,000× and 10,000×). The nanofiber diameter distribution of each sample is presented in **Figure S8-3.** The alignment of the nanofibers was controlled by changing the grounding of the collector from the edge conductors to the intermediate segment and vice versa. The grounding changes were done every 90 seconds to get 20 layers. The alignment did not affect the nanofibers' diameter since the randomly

oriented nanofibers (R) and the cross-aligned nanofibers (W) had the same average nanofiber diameter with a similar distribution, 718±184 and 720±177 µm, respectively (*p-value*= 0.3). On the other hand, the addition of Tween 80 in the polymer solutions for electrospinning (0.1, 0.5, 2, and 4 v/v%) in the shell affected both the size and distribution of nanofibers (uniformity)- which is aligned with other reports, detailed discussion in the supporting document [345].

Regarding the alignment evaluation, the SEM images were pre-analyzed and unframed, and the size of the region of interest (ROI) was defined. Then, with the ImageJ plugin (OrientationJ), each image was analyzed to get a color-coded map in which the hue corresponds to the degree of alignment. If cross-aligned nanofibers were successfully obtained, only two primary colors should appear on the map (with different ΔΘ˚). **Figure 4-1** shows a schematic of the designed collector for collecting cross-aligned nanofibers, color-coded maps, and a distribution graph of orientation for different samples.

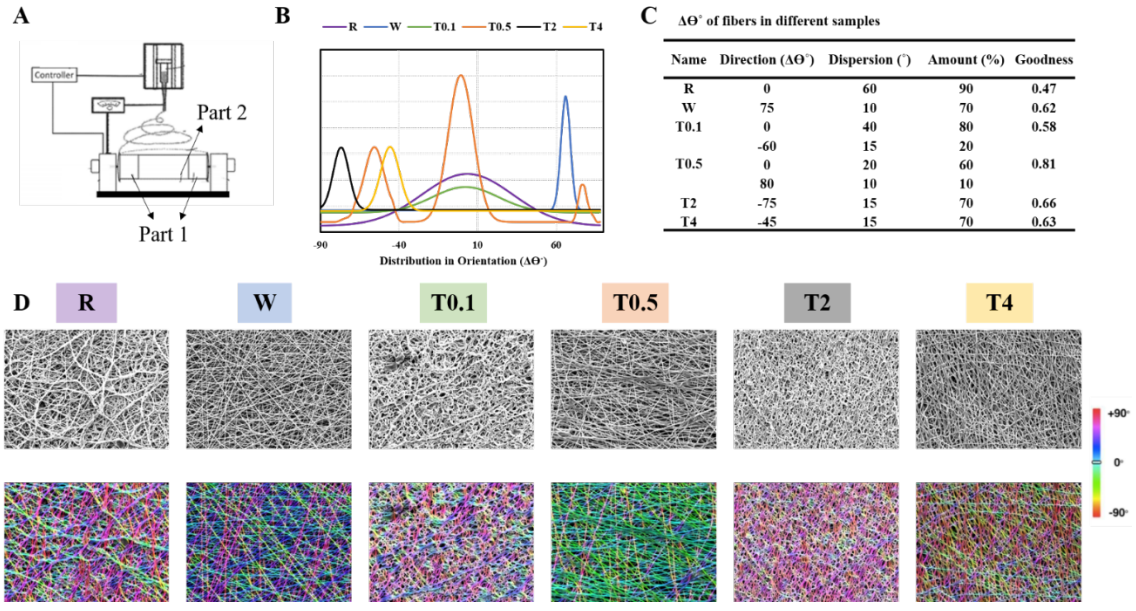

Figure 4-1 A) The schematic of the designed collector for obtaining cross-aligned nanofibers, B) Distribution of nanofiber orientation, C) direction and STDV of nanofiber angle, and D) Color-coded sample maps based on nanofiber orientation showing cross-align structure.

Sample W, which is only based on polymers and dye without Tween 80, maintained its alignment, and a cross-aligned structure was observed. The color map consisted of blue-pink and green-purple (65˚<ΔΘ˚<85˚) nanofibers showing the cross-aligned structure for 70% of nanofibers with 0.62 goodness in fit. But, adding Tween 80 with the lowest concentration (T0.1) interfered with the alignment, and random nanofibers were collected (80% of nanofibers in the range -40˚<ΔΘ˚<40˚); additionally, instead of straight nanofibers, curly nanofibers were obtained. However, increasing the Tween 80 concentration to 0.5% helped keep the alignment and nanofibers' structure. Although the dominant colors for T0.5 were not the same as W, the three dominant ranges were -75˚<ΔΘ˚<-45˚ or 70˚<ΔΘ˚<90˚ and -20˚<ΔΘ˚<20˚. Therefore, the cross-aligned structure was also present in this sample. The T2 sample was also aligned based on color coding, but the nanofibers were curly, making it hard to observe the alignment. The color map showed purple-pink with -90˚<ΔΘ˚<-60˚ for 70% of nanofibers. Increasing Tween 80 to 4% led to changes in orientation, and most of the nanofibers (70%) were aligned in the range of -60˚<ΔΘ˚<-30˚. The interaction of Tween 80 with polymers in the solution can impact the solution's properties, such as conductivity, surface tension, and viscosity [345–347]. These factors would ultimately affect the structure of nanofibers. Therefore, different alignments, fiber sizes, and fiber shapes were obtained.

4.3.3 Limit of Bacterial Detection via Nanobiosensors

The major objective of this work was to boost the sensitivity of *in situ* bacterial detection of the HCy dye-containing nanobiosensor. It has been reported that surfactants such as Tween 80 increase the water-lipid interfacial area and lead to a higher reaction rate for lipase [344]. Since lipase is the main contributor to the color change of our biosensors, we aimed to increase their activity by incorporating Tween 80 in the structure of the biosensors. The bacterial lipases are

from the α-β hydrolase fold proteins family, and their activity depends on the catalytic triad, including Serin, Histidine, and Aspartic acid [348]. Most lipases have an unstable domain known as the Lid structure. The Lid is an amphipathic structure in which the hydrophilic side faces water in the close conformation while the hydrophobic side is directed toward the triad pocket [349]. Interaction of the Lid with its microenvironment makes the active site accessible for the substrate, known as interfacial activation [105,350]. In a water-oil interface, the Lid structure changes and activates the lipase; otherwise, the Lid covers the triad most of the time, and the lipase is inactivated [351]. The water-oil interface creates a large hydrophobic patch around the triad, causing the Lid to open through rotational movements around two hinge regions. As the lipase changes its conformation to the open state, the hydrophobic side becomes available and unmasks the substrate-binding region. Therefore, the water-oil interface can help expose the binding domain easily. Tween 80, as a surfactant, can provide this water-oil interface and enhance the Lid unmasking, followed by boosted lipase activity [343]. Hence, in this paper, in addition to controlling the alignments of nanofibers, we added Tween 80 in the shell composition to boost the sensitivity of the biosensors.

To test the detection response threshold, we prepared different concentrations of three main bacteria responsible for wound infection, namely *E. coli*, *P. aeruginosa*, and MRSA. **Figure S8-4** presents the threshold concentrations and the minimum time needed for the color to change for each bacterium. At a low concentration of bacteria, around 4.0-6.0E+03 CFU/cm^2 in all species (*E. coli*, MRSA, and *P. aeruginosa*), the occurrence of a color change took a long time to be detected: *E. coli* 6 hr., MRSA 4 hr. and *P. aeruginosa* 3 hr. Increasing the concentration of the MRSA and *P. aeruginosa* by less than one log (around 3.0E+4.0 CFU/cm^2), still below the clinical threshold of bacterial infection (1.0E+05 CFU/cm^2), led to immediate

changes in certain Tween 80 containing samples. It should be mentioned that the behavior of samples with different Tween 80 concentrations differed. T0.5 and T2 showed the fastest and most vivid color change for all bacteria. For *E. coli*, the effect of Tween 80 in increasing the sensitivity, was not as significant as the other two species. When *E. coli* was at a concentration of around 3.3E+04 CFU/cm^2, it took 3 hr. for Tween 80 incorporated samples to change their color, while for the W sample, a longer duration was needed (5 hr.). By increasing the concentration of *E. coli* (4.20E+05 CFU/cm^2), the color change occurred after 1 hr. of exposure. **Figure 4-2** displays each membrane's color at the threshold point when the fastest color change was observed among the samples for each bacterium. All samples with Tween 80 showed a faster color change compared to W, and among Tween 80 incorporated samples, the membrane containing 0.5% and 2% Tween 80 showed a faster response. Interestingly, different bacteria responded differently to the presence of Tween 80 and its concentration. For instance, the high Tween 80 (4%) concentration did not lead to a fast color change for MRSA. However, it facilitated faster color change for *P. aeruginosa.*

Figure 4-2 Color-changing behavior of sample in the presence of different bacteria (Threshold of detection).

In **Figure 4-3A**, the color array of various samples (W, T0.1, T0.5, T2, and 4) is presented at different concentrations of bacteria. As indicated in the results, each sample exhibited a distinct color shift from yellow to green upon reaching its respective threshold point.

Overall, based on the behavior of samples in the presence of different bacteria types, the low concentration of Tween 80 (T0.1) increased the sensitivity, and the color change from yellow to green happened faster than W; however, the color change is not sufficiently intense to ensure dependable detection. It can be said that the Tween 80 with 0.1% concentration could not increase the lipase activity significantly, and the amount of active lipase present on the site was not high enough to lead to a vivid color change. Increasing the Tween 80 concentration to 0.5% and 2% led to noticeable color changes from yellow to green, which can be observed with untrained eyes for all bacteria types. Therefore, it can be said that the optimal concentration of Tween 80 for reaching the highest lipase activity is in the range of 0.5-2%. Increasing the concentration of Tween 80 to 4% did not change the quality or speed of color change for samples exposed to *E. coli* and *P. aeruginosa* compared to T0.5 and T2, but it adversely affected the sensitivity in the presence of MRSA. These aspects can be related to the fact that each type of bacteria reacts differently to the presence of Tween 80. Exceeding the optimal concentration of Tween 80 impedes lipase activity by forming strong hydrogen bonds and hydrophobic interactions with the enzyme, leading to its denaturation [344]. A lower lipase activity in the presence of a high concentration of Tween 80 correlated to a less cleaved ester bond of the dye. A mixed microenvironment containing various bacteria at both low and high concentrations was prepared to illustrate the color-changing behavior of all samples in a multi-species context. As depicted in **Figure 4-2**, at a low concentration, only samples with Tween 80, especially T0.5, exhibited a discernible green color change. These results suggest that a more pronounced green hue can be achieved when a mixture of bacteria is present. However, consistent with our earlier observations, the highest concentration of Tween 80 (4%) adversely impacted the color change in the presence of MRSA, and this effect was evident in mixed cultures as well, resulting in a

lighter color change. In mixtures with high bacterial concentrations, a dark green color was observed for all samples, particularly noticeable for T0.5 and T2 but less intense for T4 and T0.1. It is noteworthy that at high bacterial concentrations, the presence of Tween did not significantly influence the color change, as evidenced by the consistent color exhibited by the control sample (W). Therefore, it is evident that Tween 80 plays a pivotal role at low bacterial concentrations in accelerating color change and improving the detection threshold.

To assess the cleavage of the dye, the green-changed membranes were utilized for dye extraction purposes. The isolated dye was used for mass spectrometry analysis to determine the presence of cleaved dye fragments (the methods in the supporting document). As depicted in **Figure 4-3B**, the mass spectrum revealed a peak corresponding to the intact HCy dye at 400 m/z and a distinct peak representing the cleaved dye at 302 m/z. These observations verified that the HCy dye was cleaved in the presence of lipase secreted by bacteria at a low concentration. Furthermore, the extent of cleavage appears to be influenced by lipase activity, with an approximate cleavage rate of 6.4% observed at low bacterial concentrations.

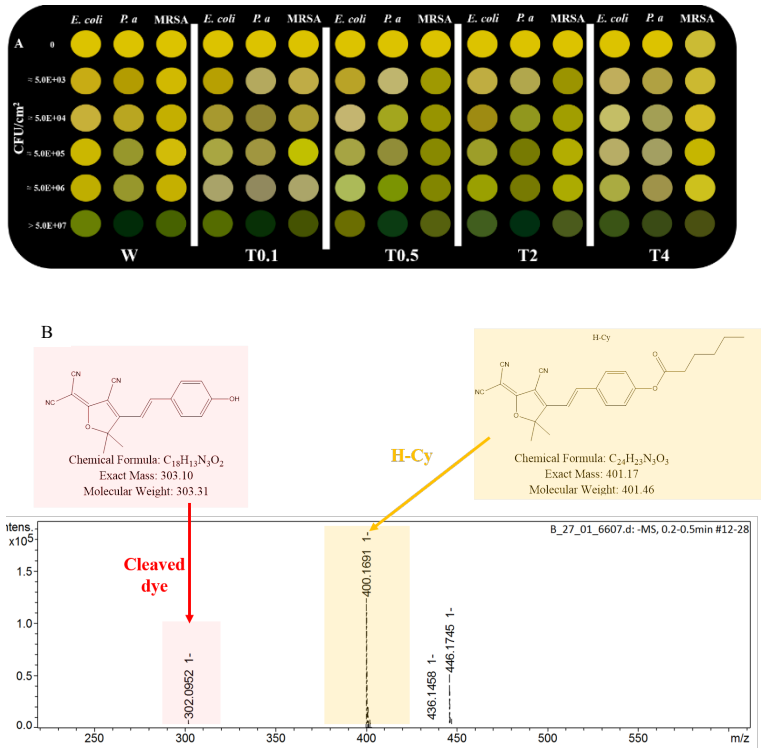

Figure 4-3 Color array showcasing various samples (W, T0.1, T0.5, T2, and T4) in response to varying concentrations of bacteria, including E. coli, P. aeruginosa, and MRSA. B) The mass spectra of the green membrane exposed to a low concentration of bacteria.

4.3.4 Colorimetric Behavior of Nanobiosensors in The Presence of Bacteria

In addition to taking digital images of biosensors to evaluate their color change, we used the GretagMacbeth ColorEye 2180UV spectrophotometer to quantify the color changes. The colors of samples at the threshold and high bacterial concentrations are illustrated in **Figure 4-4**. These colors were quantified based on ΔE and Δh for better comparison. ΔE shows color differences compared to the control sample on TSA (each membrane is compared to its control), and it is based on the CMC formula, which is a reliable way to compare colors in the textile industry. We chose the default ratio for lightness: chroma 2:1 for this project since human eyes generally accept larger differences in lightness than chroma. Moreover, the commercial tolerance

factor (CF) was set to 1, meaning a ΔE greater than 1 indicates a noticeable color difference to the human eye [352,353].

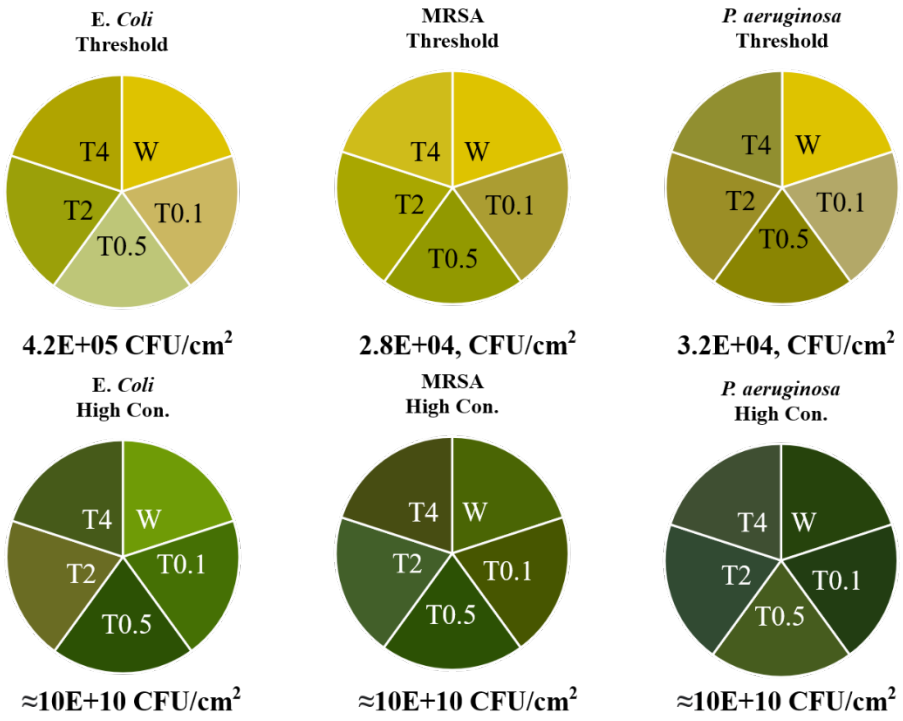

Figure 4-4 Palette of biosensors in the presence of different bacteria at a low concentration (limit of detection) compared to a high concentration.

Figure 4-5 shows the ΔE of samples exposed to various bacteria at the threshold concentrations. In the presence of all bacteria, sample W showed the lowest ΔE of around 1, with hardly any noticeable changes visible to the naked eye compared to the control sample. Adding Tween 80 at its lowest concentration (T0.1) led to an increase in ΔE. However, the difference in color between this sample (T0.1) and its control (sample on TSA without bacteria) was not substantial, especially for *E. coli* and MRSA. For all the tested bacteria, T0.5 and T2 displayed the most distinct color changes, thus resulting in the highest ΔE. These results were consistent with the threshold data presented in **Figure 4.2**. This supports the hypothesis that including Tween 80 can elevate the color difference at lower bacteria concentrations and improve the

detection threshold limit and response time. In addition to ΔE (color difference) based on the CMC tolerancing system, the difference in hue (Δh) of samples was quantified (**Figure S8-5**) to evaluate the color-changing behavior of samples with respect to Tween 80 concentrations. The differences in Δh for the sample without Tween 80 (W) and the sample with the lowest concentration of Tween 80 (T0.1) were significant in all types of bacteria, and Δh increased more for the samples with 0.5 and 2% Tween 80. However, the differences between T0.5 and T2 were insignificant, and these two concentrations enhanced the color-changing ability at the same level. Aligned with ΔE results, increasing the concentration to 4% did not further enhance the behavior; notably, the high concentration of Tween 80 reduced the Δh significantly for MRSA. Both ΔE and Δh results pointed to the importance of having the optimum concentration of Tween 80 for boosting the sensitivity of biosensors. Since the aim was to detect multi-species bacteria, the optimum concentration should lead to a noticeable color change for various strains of bacteria. In this case, T0.5 and T2 were chosen as the optimum concentrations for their exemplary behavior of color-changing and for having cross-aligned structures.

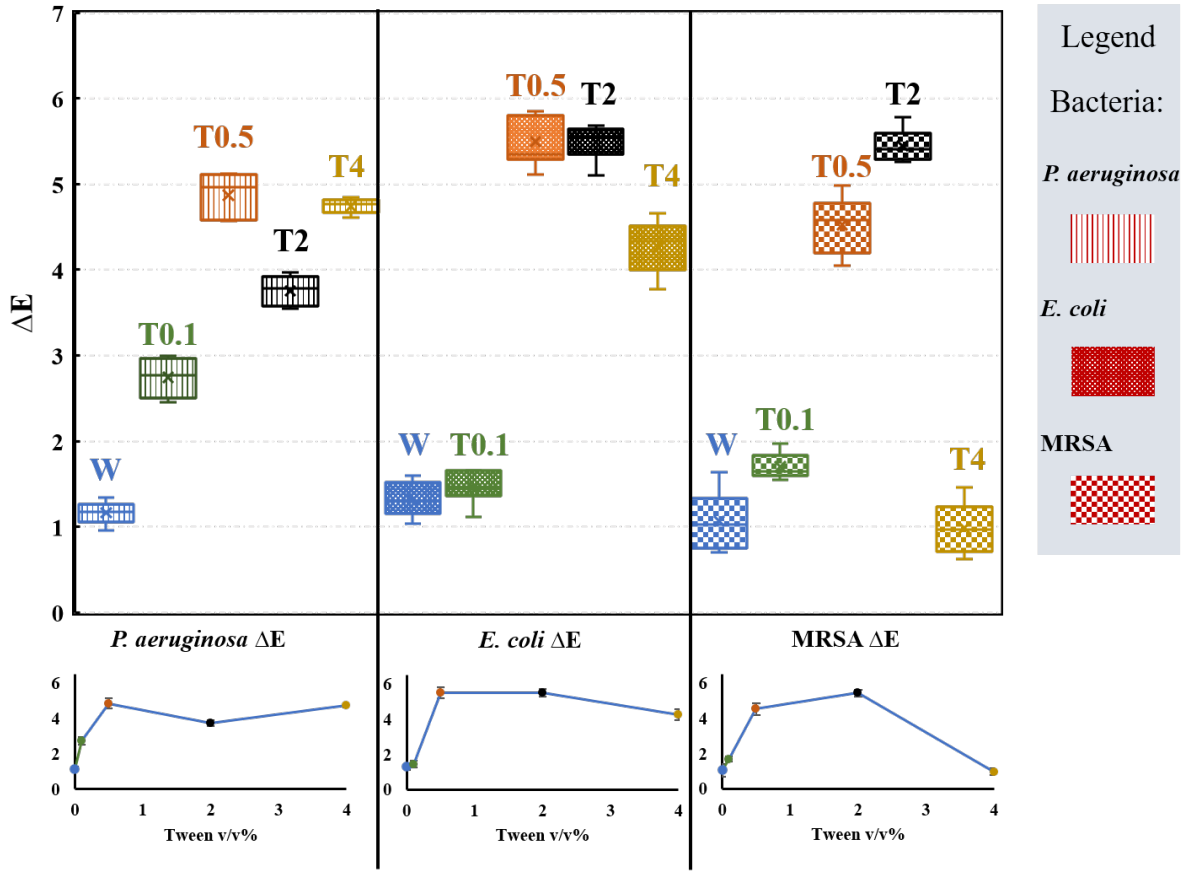

Figure 4-5 The color change (ΔE) of samples after exposure to various bacteria at the threshold concentrations.

4.3.5 Effect of Nanobiosensors on Lipase Activity

Tween 80 was chosen as an additive and a chemical cue in the biosensors compositions to enhance the sensitivity of biosensors as an activator of lipase, leading to a higher lipase activity. In addition to incorporating Tween 80, we hypothesized that the nanofibers' alignment (physical cue) could also boost the sensitivity. Therefore, a lipase activity assay was conducted to test lipase activity in the presence of four different membranes: randomly oriented electrospun nanofibers (R), cross-aligned nanofibers without Tween 80 (W), and cross-aligned nanofibers with optimum concentrations of Tween 80 (T0.5 and T2). The results were compared to bacteria without any sample (B). The obtained results of lipase activity and the relationship between

lipase activity and the bacterial concentrations are illustrated in **Figure 4-6**. To ensure that the increase in lipase activity was not because of increased bacterial concentrations, we prepared all bacterial lawns with the same bacterial suspension and incubated them with membrane samples simultaneously. Moreover, the initial and final bacteria concentrations for each sample were calculated, and as shown in **Figure 4-6B**, all samples were almost equal in terms of their bacterial concentrations. Therefore, the lipase activity in the presence of membranes is independent of environmental parameters and the concentration of bacteria. The obtained data supports our hypothesis that better localization of bacteria leads to a higher rate of lipase activity. The randomly oriented electrospun nanofibers (R) did not change the lipase activity significantly(p-value=0.295) compared to bacteria alone (B), but the cross-aligned membrane increased the activity 2.5 folds and 3.6 folds for MRSA (≈7.7E+07 ± 3.5E+06 CFU/cm^2) and *P. aeruginosa* (≈3.5E+07 ± 2.6E+06 CFU/cm^2), respectively. As we expected, the presence of Tween 80 elevated the lipase activity drastically by 10.4 folds for MRSA and 2.5 folds for *P. aeruginosa* compared to the aligned samples. However, the lipase activity in the presence of T0.5 and T2 in the aligned samples was almost the same. Therefore, based on the alignment of nanofibers as shown in SEM images and color-changing responses to different bacteria and lipase activity, the chosen optimum concentration of Tween80 was 0.5%.

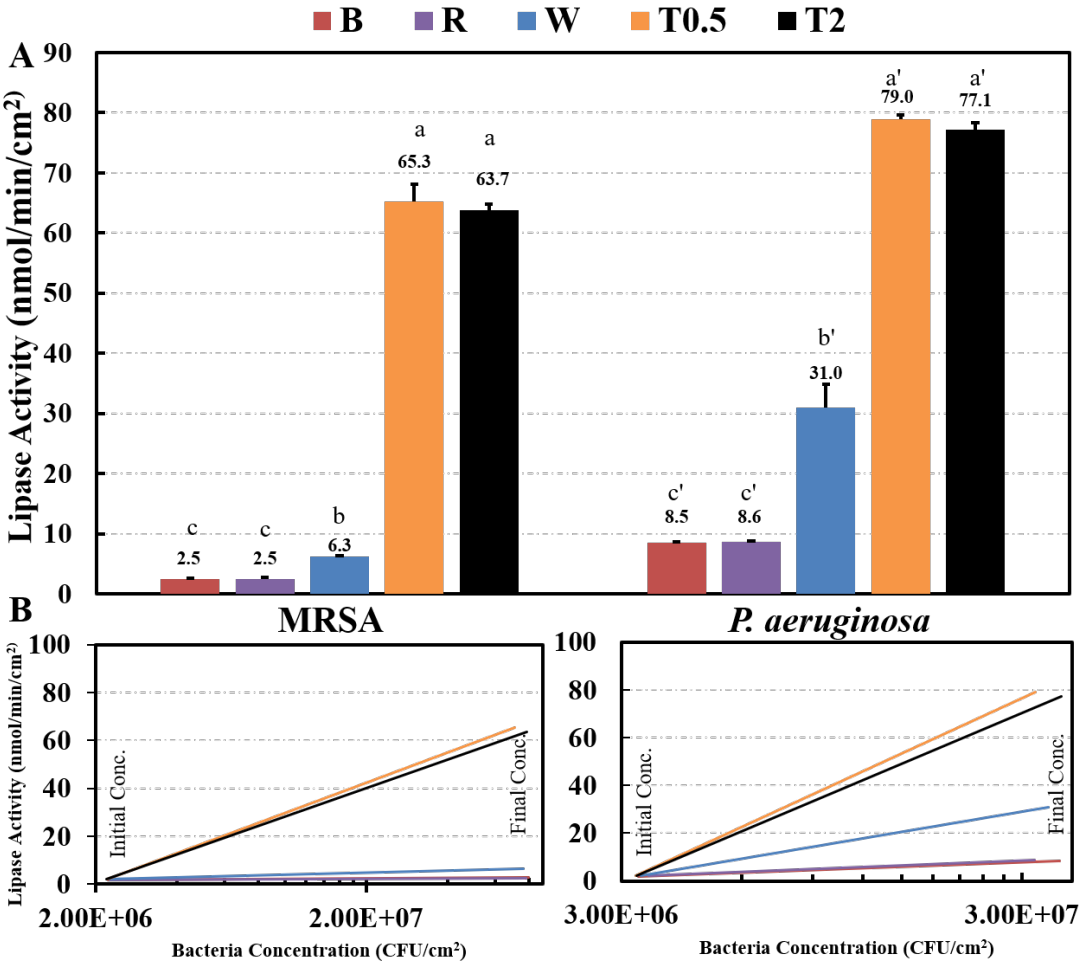

Figure 4-6 Lipase activity in the absence (only bacteria (B)) or presence of fabricated Biosensors: randomly oriented electrospun nanofibers (R), cross-aligned nanofibers (W), cross-aligned nanofibers with 0.5% Tween 80 (T0.5) and cross-aligned nanofibers with 2% Tween 80 (T2).

4.3.6 Interaction of Bacteria and Nanobiosensors (Effect of Alignments on Bacteria Localization)

To further investigate the role of alignment on the bacteria's interaction with samples, we assessed the morphology of bacteria exposed to various membranes. Randomly oriented nanofibers (R), cross-aligned nanofibers (W), and cross-aligned nanofibers with 0.5% Tween 80 (T0.5) were placed on a high concentration of MRSA bacteria lawn for 1 hr. and then were fixed

for analysis with SEM. The concentration of bacteria lawns was calculated before applying the membranes (5.52E+08 ± 5.29E+06 CFU/cm^2) and after 1 hr. of exposure using the drop-plating technique (8.94+08 ± 4.32E+06 CFU/cm^2) and ImageJ analysis. The SEM images of samples are presented in **Figure 4-7**, which showed the tendency of bacteria to attach to the cross-aligned sample more significantly ($p<0.01$) compared to the R sample (attached bacteria The enhanced localization of bacteria on aligned fibers can be attributed to the increased porosity and spacing resulting from cross-alignment, which provides more opportunities for bacterial entrapment. Moreover, the presence of Tween 80 in the structure (T0.5) led to the agglomeration of bacteria on nanofibers (attached bacteria 7.13E+07 ± 1.17E+06 CFU/cm^2), which was significantly higher than both R and W ($p<0.01$). Areas containing Tween 80 aggregates appeared to promote increased bacterial interaction with the nanofiber surface. In these regions, bacterial cells exhibited early signs of attachment and intercellular interaction, suggesting the initiation of biofilm formation. These findings also aligned with the colorimetric results, as well as the lipase activity results. Overall, we can claim that the alignment and Tween 80 led to an increase in the sensitivity of the biosensor, and we could reduce the concentration and time of detection from 2 hr. exposure to 1.0E+06 CFU/cm^2 and 2.5E+05 CFU/ cm^2 for MRSA and *P. aeruginosa* to an immediate color change response to 2.8E+04 CFU/cm^2 and 3.2E+04 CFU/cm^2 for MRSA and *P. aeruginosa.*

	R	W	T0.5
Before Bacterial exposure	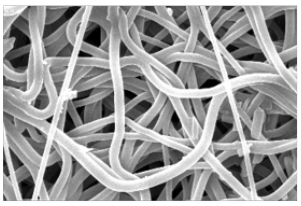	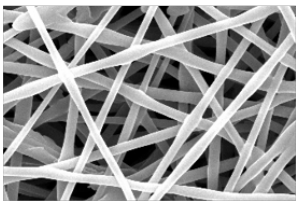	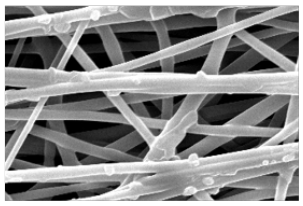
Alignment	**Random**	**Cross-Aligned**	**Cross-Aligned**
After bacterial exposure	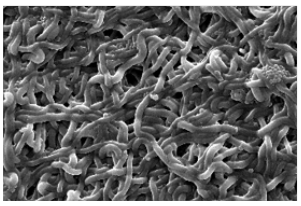	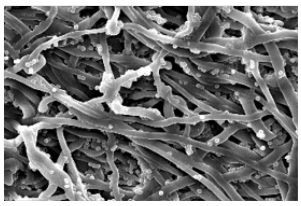	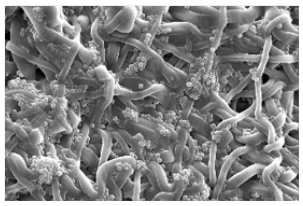
Bacterial concentration CFU/cm²	**5.31E+08**	**5.23E+08**	**5.21E+08**
Attached bacteria CFU/cm²	**1.55E+07**	**6.19E+07**	**7.13E+07**

Figure 4-7 Interaction of MRSA with different samples after 1 hr. of incubation

4.3.7 Colorimetric Behavior of Nanobiosensors in an *ex vivo* Burn Model

The response of membranes in a realistic situation was evaluated using an *ex vivo* porcine burn model. The burn wounds were inoculated with MRSA and *P. aeruginosa* separately and mixed. After one hour of incubation, the membranes were placed on the inoculated pig skins, and the initial bacterial concentration was determined. As presented in **Figure 4-8**, both W and T0.5 samples had an immediate color-changing response upon being placed on the burnt pig skin and continued to become darker as time passed. For the R sample, no initial and immediate color change was observed; the color change took 30 min. Since the initial concentrations of bacteria

were higher than their threshold of detection, all samples showed a color-changing response. The Tween 80 incorporated cross-aligned sample showed the fastest change and exhibited a darker initial response, making it more easily observable with the naked eye. These prompt and vivid colors occurred due to higher lipase activity in the samples containing Tween 80 and better bacteria localization on the biosensors due to the alignment of the nanofibers. After 30 minutes, all membranes were sandwiched between two glass slides and used for colorimetric analysis with the spectrophotometer. All samples showed a high color difference (ΔE) compared to the control, and the highest ΔE was for the T0.5 sample.

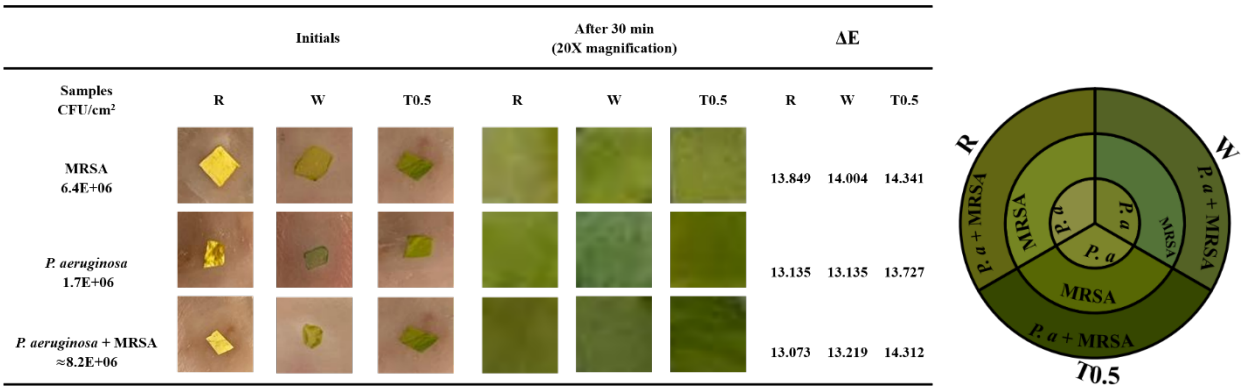

Figure 4-8 The color-changing response of different samples (randomly oriented electrospun nanofibers, cross-aligned nanofibers, and Tween 80 incorporated cross-align nanofibers) to the ex-vivo infectious burn wound on a porcine model and the color pallet of samples.

4.4 Conclusions

The gold standard techniques for infection detection, such as biopsy and bacterial culture swabbing, present significant shortcomings that highlight the need for a new approach. These methods are invasive, necessitating the removal of wound dressings to obtain results, which in itself can be detrimental to the healing process. Furthermore, they require a 24-hour incubation period to yield results, a duration in which the condition of the wound may significantly alter, potentially leading to complications or delayed treatment. This lag in diagnosis underscores the

urgent demand for a more efficient, less invasive technique that can provide immediate and accurate assessments of wound infections.

Our study presents an *in situ* colorimetric biosensor capable of detecting bacteria at low concentrations (<1.0E+05 CFU/cm^2) in real-time, thereby enabling early identification of potential infections to overcome the mentioned limitations. This biosensor offers the advantage of not requiring advanced technology for result interpretation, and healthcare workers can roughly determine the severity of infection by monitoring the relative darkness of the green color of the biosensor.

To enhance biosensor sensitivity, we introduced chemical cues (Tween 80) and physical cues (fiber cross-alignment) to amplify bacterial lipase activity without increasing bacterial concentration. It is the first work to evaluate the role of nanofibrous membranes' fiber alignment on bacterial behavior. Our findings demonstrate the influence of fiber alignment on bacterial behavior, indicating that cross-aligned nanofibers promote favorable bacteria interaction by better localization. Additionally, we determined that the lipase-boosting effect of Tween 80 in the solid state is concentration-dependent, with 0.5% concentration (in the initial electrospinning solution) yielding optimal performance. The resulting cross-aligned biosensors, incorporating Tween 80, enable real-time and *in situ* (3.0E+04 CFU/cm^2) early detection of *P. aeruginosa* and MRSA. Future investigations will evaluate different surfactants to detect infection caused by various ESKAPE bacteria.

4.5 Supporting Information.

“This material is available free of charge via the Internet at http://pubs.acs.org."

The following data are provided in the supporting document: Detailed information about reagents and materials, solution preparation steps for biosensors fabrication, the design section

for the modified electrospinning machine for fabricating aligned fibers, detailed steps of sample preparation for SEM imaging and mass spec, all bacterial suspension preparation and bacterial test steps, color system equations.

Regarding the results, all detailed discussions about chemical characterization, the morphology of biosensors, and the limit of detection are provided in the supporting document.

4.6 CRediT Authorship Contribution Statement

Farinaz Jonidi Shariatzadeh: Writing – review & editing, Writing – original draft, Visualization, Validation, Methodology, Data Curation, Formal analysis, Conceptualization. . **Sarvesh Logsetty:** Writing – review & editing, Validation, Conceptualization. **Song Liu:** Writing – review & editing, Validation, Supervision, Methodology, Funding acquisition, Conceptualization.

4.7 Funding Sources

The authors appreciate and acknowledge the financial support from the MITACS Grant (IT30856) and ParaNano Wound Care, LLC, the Natural Sciences and Engineering Research Council of Canada (NSERC) Discovery Grant (RGPIN-2019-06094), and the Canada Foundation for Innovation (award number: 23679).

5 Chapter 5: Antibacterial Biosensors for Early Detection and Elimination of Bacteria

Nanofibrous Theranostic Biosensor for Visual Detection of Infections and Triggered Drug Release: Utilizing ROS-Responsive Nanoparticles to Combat Bacterial Resistance

*Farinaz Jonidi Shariatzadeh[1], Sarvesh Logsetty[2] and Song Liu[1,3]**

1) Biomedical Engineering, Faculty of Engineering, University of Manitoba, Winnipeg, Manitoba, Canada, R3T 2N2

2) Departments of Surgery and Psychiatry, Rady Faculty of Health Sciences, University of Manitoba, Winnipeg, Manitoba, Canada, R3E 3P5

3) Department of Biosystems Engineering, Faculty of Agricultural and Food Sciences, University of Manitoba, R3T 2N2

* Corresponding Author: E.mail) song.liu@umanitoba.ca; +1) 204-474-9616).

Contribution as the first author: **Farinaz Jonidi Shariatzadeh:** Writing – review & editing, Writing – original draft, Visualization, Validation, Methodology, Data Curation, Formal analysis, Conceptualization. .

Abstract

The need for new technologies to detect and treat infections in wound care is increasingly urgent, especially with the rise of antibiotic-resistant bacteria. In this study, we developed a nanofibrous theranostic biosensor that provides both visual infection detection and on-demand drug release to combat bacterial resistance. The biosensor incorporates a hemicyanine dye, citric acid and ciprofloxacin (CIP)-loaded NPs within a nanofibrous matrix. The cleavage of the hemicyanine dye in the presence of bacteria triggers a colorimetric response, while the responsive release of CIP from the NPs upon exposure to elevated ROS enables targeted antibacterial agent delivery. The biosensor's color-changing properties were evaluated under different conditions, demonstrating compatibility with various wound dressing foams and cleaning solutions without interference. The results indicated no false positives were detected in the presence of salts and proteins. With a detection limit of 1.0E+5 CFU/cm², the biosensor provided vivid visual results within 5 hours. In direct antibacterial tests, 100% bacterial reduction for *E. coli,* MRSA, and *P. aeruginosa* was achieved within 4 hours in the presence of H_2O_2 (1 mM). Citric acid provided untargeted antibacterial action (99.9% for *E. coli* and 99.999% for MRSA and *P. aeruginosa*). While ROS-responsive CIP release, in addition to citric acid, ensured sustained triggered bacterial elimination (100% and 8 log reduction), significantly enhancing overall efficacy. Cytocompatibility tests with 3-day elution confirmed that the biosensor was non-cytotoxic, maintaining over 90% fibroblast viability even after complete drug release. This theranostic biosensor effectively prevents untargeted antibiotic release, reducing the risk of bacterial resistance while supporting fibroblast health and proliferation. These results suggest that this biosensor is a promising tool for wound care, offering real-time infection monitoring and targeted antibacterial treatment.

Keywords: nanofibrous membranes, responsive nanoparticles, lipase, antibiotics, colorimetric, targeted release

5.1 Introduction

Wound management is an essential aspect of clinical care, primarily due to the complications that arise from infections, which can significantly hinder the healing process and increase the likelihood of severe scarring [354]. Infections at wound sites typically trigger an inflammatory response that can delay tissue repair and promote excessive collagen deposition, ultimately resulting in pronounced and extensive scar formation [10,354–356]. The emergence of drug-resistant bacteria, such as methicillin-resistant *Staphylococcus aureu*s (MRSA), poses a challenge in treating bacterial infections, contributing to elevated mortality rates and a higher incidence of resistant strains [357]. In 2019, antibiotic resistance was linked to approximately 4.95 million deaths globally, with 1.27 million directly attributable to drug-resistant infections. This number is projected to rise to 10 million annually by 2050. In the United States alone, drug-resistant bacteria infect at least 2 million people each year, resulting in at least 23,000 deaths [358–360]. The misuse and overuse of antibiotics are significant contributors to the proliferation of these resistant bacteria [361]. This growing concern underscores the urgent need for advanced therapeutic strategies, such as the development of smart wound dressings capable of proactively identifying bacterial infections and delivering precise treatments in a timely and effective manner, thereby mitigating the risk of developing drug-resistant infections [362].

Smart and responsive wound dressings are designed to respond to environmental changes within the wound site, such as pH and temperature changes or the presence of specific biochemical markers like lipases and reactive oxygen species (ROS) [363,364]. These environmental biomarkers facilitate both detection and treatment. The integration of biosensing capabilities within dual-responsive wound dressings is crucial for real-time detection of infections, especially at low bacterial concentrations that traditional methods might not promptly

identify. Such dressings also allow for immediate therapeutic responses, potentially preventing severe complications associated with wound infections. This responsiveness ensures that antibacterial agents are released precisely when pathogens are present, thereby maximizing efficacy and minimizing side effects [365,366].

While most theranostic wound dressings developed to date have primarily utilized fluorescent probes or pH indicators for infection detection, they generally require additional equipment for the activation of their antibacterial activity, thus limiting their clinical utility. Regarding responsive treatment of bacterial infection, several responsive dressings have been designed to release drugs upon external stimuli such as light or magnetic fields. For instance, Li's group engineered a theranostic injectable hydrogel that detects infections through pH changes and combats bacteria after laser illumination, generating ROS that not only acts as a crosslinking agent for hydrogel formation but also possesses antibacterial properties [367]. Similarly, Shi's group utilized photodynamic technology for *in situ* bacterial detection and eradication using a dressing made from carboxymethyl chitosan and oxidized sodium alginate, incorporating 4-methylumphulone beta-D-glucoside (MUG) nanoparticles coated with titanium dioxide. In the presence of bacteria, MUG interacts with pathogenic enzymes(β-glucuronase) to produce 4-methylumbellione, which emits blue fluorescence. After detection, near-infrared irradiation can be used to activate the nanoparticles to regenerate ROS, which serves as the antibacterial agent [368]. Although both dressings show promising detection capabilities and antibacterial properties, their reliance on additional light sources for detection and activation limits their broader application.

Addressing the limitations of external radiation units, Wu's group developed a bilayer wound dressing incorporating the radiation source in the dressing by the addition of diodes. The

top layer comprises PDMS integrated with flexible electronics for temperature sensing and diodes for UV light emission, and the bottom layer features a hydrogel responsive to UV light with UV-cleavable linkages between gentamicin and poly (ethylene glycol). Upon detecting an infection-induced temperature rise (above 40°C), data is transmitted to a smartphone via Bluetooth, triggering an alert. The software includes a switch to activate the UV diodes in the top layer, subsequently releasing the antibiotic from the bottom layer through UV-induced degradation [369]. This system eliminates the need for an external light source. However, its accuracy in activation is limited, as various factors can influence the temperature at the wound site. Additionally, its reliance on smartphone connectivity presents challenges for effective wound care management.

Given the limitations of existing theranostic wound dressings, there is a pressing need for an innovative solution that utilizes bacterial by-products for detection and wound environmental biomarkers for targeted drug release. In this project, we enhanced our colorimetric dressing that changes its color from yellow to green in the presence of bacteria [106]. The hemicyanin dye incorporated in the biosensor undergoes a hydrolytic reaction in the presence of bacterial lipase, causing cleavage of an ester bond, thus enhancing intramolecular charge transfer and hence the color change. This mechanism allows for the detection of bacteria without external equipment, simplifying usage and reducing system complexity [108,318]. For clinical applications, *in situ* biosensors must be free of false positives while remaining sensitive and accurate in detecting bacterial infections. However, the previously developed biosensor in our lab showed an occasion of false positives due to the presence of salts (e.g. Na salts) and increased pH (pH> 7.5). In this project, we attempted to eliminate these false-positive results through the incorporation of different acids.

Simultaneously, the dressing is designed to release antibiotics in response to ROS, a biomarker significantly elevated in infected wounds as the body's immune response intensifies. In typical human plasma, the concentrations of hydrogen peroxide usually range from 1 to 8 μM, whereas in the presence of activated macrophages, these levels can escalate to between 10 and 1000 μM [370,371]. In this project, the antibiotic ciprofloxacin is encapsulated within responsive nanoparticles made from polyethylene glycol b-polypropylene sulfide (mPEG45-b-PPS60), which changes its structure in the presence of ROS, effectively releasing the drug. This responsive delivery system not only prevents premature drug release but also addresses potential issues of bacterial resistance and toxicity toward human cells. Additionally, the incorporation of citric acid, known for its safety and biocompatibility, supports wound healing by maintaining an acidic environment. By integrating both diagnostic and therapeutic functions that operate based on the wound's biological environment, this approach provides a streamlined, cost-effective solution that enhances clinical outcomes through timely and targeted treatment, aligning with the goals of precision medicine in wound care.

5.2 Material and Methods

5.2.1 Materials

Polyvinylpyrrolidone (PVP, Mw 40,000), tetrahydrofuran (THF, ≥99.9%), N,N-dimethylformamide (DMF, ≥99.8%), Amano Lipase PS from Burkholderia cepacia (≥30,000 U/g), Amano Lipase from Pseudomonas fluorescens (≥20,000 U/g), Lipase from Pseudomonas cepacia (30 U/mg), Lipase from Candida rugosa, HEPES, Tricine, Bricine, MES, m-PEG, triethylamine, methacryloyl chloride, dichloromethane, AIBN, thioacetic acid, diethyl ether, sodium methoxide, propylene sulfide, ciprofloxacin, and Muller Hinton agar and broth were purchased from Sigma Aldrich (St. Louis, MO, USA). Tween® 80, Integra Miltex Standard

biopsy punches, BD Bacto™ Tryptic Soy Broth (Soybean-Casein Digest Medium), BD Difco™ Dehydrated Culture Media: Tryptic Soy Agar (Soybean-Casein Digest Agar), 10X PBS Buffer (pH 7.4, 0.2 μm filtered), citric acid, salts, hydrogen peroxide, and aluminum foil were procured from Fisher Scientific (Nepean, ON, Canada). Tecophilic HP-60D-35 (hydrophilic aliphatic polyurethane, PU) was obtained from Lubrizol Advanced Materials (Cleveland, OH, USA). HCy was synthesized by Alberta Research Inc. (Alberta, AB, Canada) following a protocol developed in our lab.

Methicillin-resistant Staphylococcus aureus (MRSA) ATCC 33592, Pseudomonas aeruginosa ATCC 27853, and Escherichia coli ATCC 25922 were acquired from the American Type Culture Collection (ATCC) (Manassas, VA, USA). Human primary dermal fibroblasts (ATCC® PCS-201-012) and Fibroblast Basal Media supplemented with the Fibroblast Growth Kit were also obtained from ATCC. The MTT assay kit (CyQUANT™ MTT Cell Viability Assay), dialysis tubes (Pur-A-Lyzer™ Mega Dialysis Kit), Trypan blue, BSA, and FBS were purchased from Gibco, Thermo Fisher Scientific (USA).

5.2.2 Nanofiber Fabrication

The first step was to develop responsive biosensors for detecting bacteria. For this step, electrospinning was used.

5.2.2.1 Electrospinning of The Biosensors

Core-shell PU: PU/PVP/HCy/Citric acid membranes were fabricated with a co-axial spinneret apparatus (NE300 electrospinner). For core solution, 6.0 w/v% PU was dissolved in DMF: THF 1:1 solution overnight at 45.0 ˚C, and for shell solutions, 7.0 w/v % PU, 3.5 w/v % PVP, 4.0% Citric acid and 1.0 w/v % HCy were dissolved in DMF: THF overnight at 45.0 ˚C. The 0.5 v/v% Tween 80 solution was mixed thoroughly with the shell solutions before

electrospinning. The electrospinning conditions were maintained at a constant voltage of 20.0 kV, a needle-to-collector distance of 15.0 cm, and pump rates of 0.6 mL/hr for the core solution and 1.0 mL/hr for the shell solution. The morphology of nanofibers was evaluated with a scanning electron microscope at a voltage of 20.0 kV. The membranes were sputtered with gold/palladium prior to scanning.

5.2.2.2 Response to Different Solutions

To assess the performance of the biosensors under varying conditions, different buffers, salts, and protein solutions were prepared at various pH levels. The buffers used included artificial wound fluid (AWF, composed of $CaCl_2$, NaCl, and Tris), phosphate-buffered saline (PBS, containing NaCl, KCl, Na_2HPO_4, and KH_2PO_4), Tris (trisaminomethane, $(HOCH_2)_3CNH_2$), Tricine ($C_6H_{13}NO_5$), Bicine ($C_6H_{13}NO_4$), MES (2-(N-morpholino) ethanesulfonic acid, $C_6H_{13}NO_4S$), and HEPES (4-(2-hydroxyethyl)-1-piperazineethanesulfonic acid, $C_8H_{18}N_2O_4S$). These buffers were tested at pH levels of 4.0, 7.0, 8.0, and 11.0. The salt solutions were prepared with specific cations: For sodium (Na^+), the salts included NaCl, $Na_5O_{10}P_3$, $NaHCO_3$, NaH_2PO_4, and Na_2HPO_4. For potassium (K^+), the salts used were KCl, KI, KH_2PO_4, and $K(CH_3COOH)$. Magnesium (Mg^{2+}) was tested using $MgCl_2$ and $Mg(CH_3COOH)$, while CuBr and $FeCl_2$ were also included in the tests. Each solution contained a cation concentration of 500 μL. To determine whether ion concentration influenced the biosensor's color-changing properties, Na^+/Cl^-, Mg^{2+}/Cl^-, and K^+/Cl^- were tested at concentrations of 5.0, 10.0, 100.0, and 150.0 nM. Additionally, mixtures of two or three of these ions at the same final concentrations were also evaluated.

For protein solutions, bovine serum albumin (BSA, 2%) was added to AWF or solutions containing different salts ($NaHCO_3$, NaCl, KCl, and $CaCl_2$). Fetal bovine serum (FBS) was

mixed with AWF (1:1) or peptone water (peptone: NaCl) to investigate further the role of proteins in the biosensors' color-changing properties.

5.2.2.3 Response to Different Lipases and Sensitivity of The Biosensor

The color-changing behavior of the biosensors in the presence of different bacterial and fungal lipases was evaluated using a pure water solution. Five different dilutions were prepared for the experiment: 10.0, 5.0, 1.0, 0.5, and 0.1 mg/mL. The lipases used in this study included Amano Lipase PS from *Burkholderia cepacia* (≥ 30,000 U/g), Amano Lipase from *Pseudomonas fluorescens* (≥ 20,000 U/g), Lipase from *Pseudomonas cepacia* (30 U/mg), and Lipase from *Candida rugosa* (≥ 2 U/mg). After adding the lipases, the biosensors were monitored after one hour at 30.0 ºC to evaluate any color change. Additionally, to assess the effect of time on color change, Amano Lipase PS from *Burkholderia cepacia* was selected for further testing. The membranes were monitored at 15-minute intervals (30.0 ºC) for one hour at various concentrations (0, 0.25, 0.5, 0.75, 1, 3, and 10 mg/mL).

5.2.2.4 Bench Testing the Biosensors

A bench test was designed as a final quality control measure before proceeding to bacterial testing to ensure the biosensors' responsiveness to lipase and minimize the occurrence of false positives. In this test, biosensors (1.0×1.0 cm^2) were placed in either pure water or AWF solution with or without the addition of lipase (500 µL, Lipase PS from *Burkholderia cepacia*, 10 mg/mL). The samples were incubated at 40.0 ºC for 30.0 minutes. Following incubation, the color of the membranes was observed, and digital photographs were taken under different lighting conditions (daylight, cool light, and biosafety cabinet light) at 45º and straight angles. Additionally, the membranes' color was quantitatively evaluated using a spectrophotometer

(GretagMacbeth ColorEye 2180UV), and CIELAB (C2˚) data, including L*, a*, and b* values, were recorded. The corresponding color was also identified using the HEX# color code as a control reference.

5.2.2.5 Bacteria Response

The color change of the biosensors in the presence of bacteria was evaluated using three different bacterial strains: MRSA, *E. coli*, and *P. aeruginosa*. Bacterial plates were prepared to achieve a theoretical concentration of 10^5 CFU/cm² based on previously reported procedures. Briefly, 57 µL of a 10^8 CFU/mL bacterial solution was spread on each plate and incubated at 37 ˚C for 1 hour. Following incubation, biopsy punches were taken from all plates to determine the initial bacterial concentration. For each bacterial strain, three biological replicates were tested, and for each biological replicate, three technical replicates were used for bacterial counting. Once the membranes exhibited a color change to green, they were placed on a glass slide, and the color data (L*, a*, b*) were measured using a spectrophotometer. These values were then converted to a standard color based on the HEX# code. Additionally, the final bacterial concentration was determined using a biopsy punch.

5.2.2.6 Compatibility of The Biosensor with Commercial Foams

Given that the biosensors are intended for commercial application and might not be directly applied to wounds, we evaluated their compatibility with various foam dressings covered with Tegaderm®. Nine different types of foams were tested: AQUACEL® Foam (Convatec Forever Caring), Curafoam Dressing (Dynarex®), HEALQU® Non-Adhesive Waterproof Foam, Hydrofera Blue Classic®, McKesson® Hydrocellular Foam Dressing Non-Adhesive, Medline® Optifoam-Basic, Medline® Optifoam Non-Adhesive, Medline® Quick, and PolyMem® Non-Adhesive Pad.

The compatibility of the biosensors with these foams was assessed based on color change in the presence of commercial lipase and during bacterial tests. For the lipase test, the amount of lipase solution used was determined by the swelling capacity of each foam. The swelling capacity was measured by incrementally adding the solution and weighing the foams until a plateau was reached.

Two approaches were employed for the bacterial tests. In the first approach, the foam was placed on top of the agar without any additional solution. In the second approach, a wound-like environment was simulated by curving the agar, placing the foam inside the agar, and adding Simulated Wound Fluid (SWF), which comprised 50% fetal bovine serum (FBS) and 50% peptone water. The peptone water (0.1% peptone, 0.9% NaCl) was autoclaved for sterilization before being mixed with FBS. Furthermore, to confirm that the observed color change was explicitly due to the presence of bacteria in direct dry contact with the biosensors, the foams and biosensors were examined using SEM. This analysis was conducted to verify the presence of bacteria on the surface of the biosensors.

5.2.2.7 Compatibility of The Biosensor with a Wound-Cleaning Solution

The performance of the biosensors was further evaluated for compatibility with Hypochlorous Acid (HPA), a common wound-cleaning solution. Agar plates were prepared as previously described. After placing the biosensors on the agar, the plates were incubated overnight to allow for a high concentration of bacteria to develop ($\sim 10^{14}$ CFU/cm^2). The following day, each plate was divided into four sections. The first quadrant served as a bacteria control to determine bacterial concentration, while the second quadrant was splashed with 1 mL of HPA. The third quadrant was cleaned using gauze soaked in HPA, and the fourth quadrant served as a biosensor control. Following these treatments, a new biosensor was placed on each

quadrant, and the color change performance was monitored over time to ensure that the presence of HPA did not interfere with the biosensors. If a color change was observed, a biopsy punch was used to determine the bacterial concentration at that specific time point.

5.2.2.8 Performance of Biosensors after Sterilization

In addition to evaluating the biocompatibility of the biosensors for commercial use, it is crucial to assess their performance following sterilization. E-beam sterilization was selected as the appropriate method, with three different intensity levels (low, medium, and high doses) applied for the sterilization process. The sterilized samples were subjected to bench testing and compared to non-sterilized samples. Furthermore, the bacterial performance of the sterilized samples was evaluated using the previously described bacterial testing procedure. This comparison with non-sterilized samples ensured that the gamma radiation did not compromise the functionality of the colorimetric probe.

5.2.2.9 Leaching Test

Given the potential for the dye to leach into the environment after cleavage, the leachability of the biosensors was assessed using different foams in two separate conditions. In the first test, 500 µL of lipase solution was added to the foams, while in the second test, the foams were immersed in 5 mL of the solution. Both setups were maintained overnight. Subsequently, the foams were dried in an oven at 40°C, sectioned, and the depth of dye penetration into the foam was measured.

5.2.2.10 Cell viability

The biocompatibility of the biosensors was evaluated using the MTT assay following ISO 10993-5 guidelines. Sterilized samples, each with an area of 2 cm ×2 cm, were immersed in 333 µL of complete fibroblast media (Supplement: HSA 500 µg/mL, linoleic acid 0.6 mM, lecithin

0.6 µg/mL, L-Glutamine 7.5 mM, rh FGF basic 5 ng/mL, rh EGF/TGF-1 Supplements 5 ng/mL and 30 pg/mL, rh Insulin 5 µg/mL, Hydrocortisone 1 µg/mL, Ascorbic acid 50 µg/mL, antibiotics (Penicillin-Streptomycin-Amphotericin B Suspension), and 5% FBS). Five replicates were prepared for each sample. The samples were incubated at 37°C, 5% CO2, and 95% humidity for 72 hours to allow for extraction.

For cell preparation, 100 µL of complete growth media was added to each well of a 96-well plate, followed by the addition of 100 µL of a 1.0×10^5 cells/mL suspension, resulting in a final concentration of 1.0×10^4 cells/well. The cells were incubated under the same conditions for 24 hours. After incubation, the media was replaced with the extracted solutions (in four dilutions: 1.0, 0.1, 0.01, and 0.001 X), with DMSO serving as a negative control and media as a positive control.

After a further 24 hours of incubation, the extracts were removed, and an MTT assay was performed. Fresh media (100 µL) was added to each well, followed by the addition of 10 µL of 12 mM MTT stock solution (5 mg in 1 mL PBS). The cells were incubated for 3 hours, after which the media was removed, leaving 25 µL in each well. Subsequently, 50 µL of DMSO was added to dissolve the formazan crystals. The mixture was pipetted up and down and incubated for 10 minutes. Finally, the absorbance of each well was read at 540 nm, and cell viability was determined by comparing the optical density (OD) of each sample to that of the control (untreated cells).

5.2.3 Nanoparticle Fabrication

After successfully fabricating and examining biosensors, the second step was to fabricate responsive nanoparticles to load ciprofloxacin. For this step, a responsive polymer was synthesized, and then NPs were fabricated using the emulsion technique.

5.2.3.1 Synthesizing methoxy poly(ethylene glycol) methacrylate (mPEG45 methacrylate)

mPEG (1.0 g), triethylamine (0.6 mL), and methacryloyl chloride (1.0 mL) were added into dichloromethane 20 mL, and the reaction continued at room temperature for 48 hr. Then after, the rotary evaporator was used to concentrate the solution, followed by filtering and precipitating the products with cold diethyl [372].

5.2.3.2 Synthesizing methoxy poly(ethylene glycol) thioacetate (mPEG45 thioacetate)

mPEG methacrylate (0.2 g) was dissolved in 5 mL THF and was stirred for an hour. Then, AIBN (0.0065 g) and thioacetic acid (110 µL) were added to the solution, and the reaction chamber was filled with nitrogen gas for 30 seconds. After that, the reaction chamber was degassed by freezing the mixture under liquid nitrogen, evacuating it under a high vacuum, and filling it with nitrogen. The freezing-pumping-thawing cycle was redone until no bubbles formed at the thawing stage. The reaction chamber was heated to reach room temperature, and then the solution was mixed for 24 h at 60 °C. After 24 hours, the chamber was placed in the rotary evaporator. The final step was filtering and precipitating by cold diethyl ether to obtain powders. The obtained powder was used for chemical characterization and future steps [372].

5.2.3.3 Synthesizing of methoxy poly(ethylene glycol)-b-poly- (propylene sulfide) (mPEG45-b-PPS60)

mPEG thioacetate (0.37g) was dissolved in 10.0 mL THF under nitrogen gas in the Schlenk tube. Then sodium methoxide (0.012 gr in 445 µL methanol) was added to the solution by a syringe and stirred for 30 min at room temperature. Then propylene sulfide (0.87 mL) was added to the mixture and stirred overnight at 60 °C. After 24 hours, the solvent was removed using the rotary evaporator, and the final product was obtained by precipitating with cold diethyl ether and

filtering. The dried powder was placed in a dialysis tube (12-14 kDa cut off) filled with ultrapure water (30 mL) and immersed in 500 mL ultrapure water for 48 hr at continuous stirring. The medium water was changed frequently. After 48 hr, the solution was transferred to two 50 mL tubes and placed in the freezer for freeze-drying [372].

For each step of synthesizing, NMR and FTIR were used to characterize the final product chemically, and the yield of each step was calculated using the following formula.

$$yield\ of\ synthesize = {Final\ Weight\ of\ obtained\ Product\ (g)}\Big/{Theorical\ Weight\ of\ final\ Product\ (g)} \quad \textit{Equation 5-1}$$

5.2.3.4 Fabrication of NPs and Drug Loading

The synthesized PEG-co-PPS (80 mg) was used to fabricate the ROS-responsive NPs with different Ciprofloxacin (Cip) contents (6.25, 39, and 244 mg in 1 mL PBS 7.4). The drug solutions were added dropwise to the polymer solution (5 mL Chloroform), and the final solution was sonicated for 3 min in an ice bath, 20 W. Then, the obtained emulsion was added dropwise to the 20 mL PBS (containing 0.5% PVA) while mechanically stirring (1000 rpm). The emulsion was sonicated for 1 min in an ice bath, 40W. The rotary evaporator was used to remove the oil phase of the obtained emulsion. The final product was centrifuged to obtain the nanoparticles. Transmission Electron Microscopy (TEM) with negative staining was employed to evaluate the morphology of the NPs, while dynamic light scattering (DLS) was used to determine their hydrodynamic diameter. Also, the NPs were exposed to H_2O_2 (0.5 mM) to evaluate the changes in the morphology with TEM. The stability of the NPs in PBS buffer (pH=7.4, T=4 ºC) was also assessed after three months of storage with DLS.

5.2.4 Loading NPs in The Nanofibers

The NFs (10cm×10cm) were immersed in the 2 mL NPs solution (200 mg/mL) overnight and then washed three times with PBS to eliminate the non-loaded NPs and were dried in a vacuum oven (37 ºC) overnight. The dried NP-loaded NFs were used for morphology characterization by SEM.

5.2.5 Drug Loading Efficiency and Drug Release Behavior from NPs

0.6 mg/mL of NPs was treated with 100 µL H_2O_2 (30%) overnight and used for UV absorbance at 325 nm to find the loading efficiency (LE) and loading capacity (LC) of ROS NPs based on the following equations.

$$EE\% = \left(\frac{Initial\ added\ drug - Free\ drug}{Initial\ added\ drug}\right) \times 100 \quad \textit{Equation 5-2} \qquad LC\% = \left(\frac{Totall\ entraped\ Drug(mg)}{Totall\ NPs\ weigth\ (mg)}\right) \times 100 \quad \textit{Equation 5-3}$$

10 mg of drug-loaded NPs and 1cmx1cm NP-loaded NFs in 2mL PBS were used for the release profile in the absence and presence of H_2O_2 (1mM) as a reactive oxygen agent. The suspensions were placed in a dialysis tube and immersed in 23 mL PBS. At each interval, 1 mL of solution was collected and replaced with fresh PBS. The collected solution was used for absorbance reading at 325 nm. Different release profiles, zero-order, first-order, Korsmeyer-peppas, and Higuchi, were used to fit the release data using the formula in **Table 5-1**.

Table 5-1 The release profiles

Model	Formula
Zero-order	$M_t = M_0 + Kt$
First-order	$\ln M_t = \ln M_0 + Kt$
Korsmeyer-Peppas	$M_t/M_\infty = Kt^n$
Higuchi	$M_t/M_\infty = K\sqrt{t}$

5.2.6 Antibacterial tests

The antibacterial properties of the fabricated NPs and NFs and NP-loaded NFs were assessed using different techniques.

5.2.6.1 The Minimum Inhibitory Concentrations (MICs) and Minimum Bactericidal Concentrations (MBCs)

The MICs and MBCs of the NPs were determined for three different bacterial strains: *E. coli*, *P. aeruginosa*, and MRSA. MICs are defined as the lowest concentration of an antimicrobial agent that inhibits visible microbial growth after overnight incubation, and MBCs refer to the lowest concentration that prevents growth after subculturing onto antibiotic-free media [373]. These measurements were conducted both in the presence and absence of H_2O_2 (0.5 mM), with ciprofloxacin (CIP) at varying concentrations used as a control. The MIC of the antimicrobials was determined using the microdilution method in culture broth, following the guidelines set by the Clinical and Laboratory Standards Institute (CLSI) of the United States. A range of NP and Cip concentrations (128–0.06 μg/mL) were tested. The antimicrobial components were added to sterilized Mueller-Hinton broth to prepare different concentrations.

To prepare the bacterial suspension, a single colony of each bacterial strain was inoculated into 3 mL of Mueller-Hinton broth and incubated at 37°C for 18 hours. The turbidity of the suspension was then measured using the McFarland standard and adjusted to 0.5, corresponding to approximately 10^8 CFU/mL. Following the preparation of bacterial and component suspensions, 50 μL of each concentration was added to the wells of a 96-well plate, followed by the addition of 50 μL of bacterial suspension (reaching 5×10^5 CFU/mL). A sterility control, consisting of 100 μL of broth without bacteria, was included as a positive control, and a growth control, containing 50 μL of bacterial suspension and 50 μL of broth without any

antimicrobial agents, served as a negative control. The plates were then incubated overnight at 37°C. The MIC was determined by identifying the well with the lowest concentration of the antimicrobial component that exhibited a clear solution, indicating inhibition of bacterial growth, while the sterility control remained clear, and the growth control showed turbidity.

To determine the MBC, the wells that exhibited no visible bacterial growth from the MIC assay were selected for further analysis. 100 µL of these wells was plated onto Mueller-Hinton agar and incubated at 37°C overnight. The MBC was identified as the lowest concentration of the antimicrobial agent, which resulted in no bacterial growth on the agar plates.

5.2.6.2 Zone of inhibition (ZOI)

Biosensors were punched into discs using a 6.0 mm biopsy punch to evaluate the ZOI. Three types of biosensors were tested: one group without citric acid in the shell, a second group with citric acid in the shell, and a third group loaded with NPs. Bacterial plates were prepared by adjusting the inoculum concentration to 10^8 CFU/mL (equivalent to 0.5 McFarland standard). A cotton swab was dipped into the bacterial suspension, and after removing excess broth by pressing the swab against the tube's wall, the swab was used to streak the plate three times, rotating it 60 degrees after each streak. After a five-minute wait, the prepared discs were placed on the agar with a minimum distance of 24 mm between them. For each bacterial strain, three sets of plates were prepared: one set without hydrogen peroxide (H_2O_2), another set with H_2O_2 (1 mM) added to the broth before plating, and a third set where the biosensors were dipped in 1 mL of H_2O_2 (1 mM) for 2 seconds prior to placement on the agar. The plates were then incubated at 37°C overnight, and the clear zones surrounding each disc were measured the following day.

5.2.6.3 Direct Antibacterial Test

In this antibacterial test, 200 μL of bacterial suspension (10^5 CFU/mL) was added to different biosensors (6.0 mm in diameter), with or without the addition of H_2O_2 (1 mM), and incubated at 37°C for 4 hours. After incubation, the membranes were rinsed and vortexed to detach any adhered bacteria. The resulting suspension was then subjected to serial dilution plating to determine the bacterial concentration. For each sample, the bacterial concentration was compared to the control (with or without H_2O_2), and the log reduction in the bacterial count was calculated.

5.2.6.4 Time Dependent Antibacterial Test

Three bacterial strains were prepared with an initial concentration of 10^6 CFU/mL. Samples, including CIP, NPs, and NP-loaded NFs, were added to 3 mL of the bacterial suspension with and without H_2O_2, at a concentration equivalent to ¼ of the MIC for both CIP and NPs. Bacterial concentrations were determined at 0, 5, and 24 hours using sampling and serial dilution plate counting. These concentrations were then compared to the controls, and log reduction was calculated to evaluate the bactericidal efficacy over time.

5.2.7 Cytocompability

The biocompatibility of the final biosensors containing ROS-responsive NPs was assessed using various tests involving the MTT assay kit and human fibroblast cells.

5.2.7.1 Cell Culture

Human primary dermal fibroblasts (ATCC® PCS-201-012) were cultured in Fibroblast Basal Media supplemented with Fibroblast Growth Kit and 100 μg/mL antibiotics cocktail at 37 ˚C in a 5% CO_2 atmosphere. Cells were harvested with the Trypsin enzyme before the cellular test. Briefly, cells were washed with cold PBS three times, and then trypsin was added. Cells

were incubated at 37 ˚C for 5 minutes and then transferred to a tube containing complete media. The cell suspensions were centrifuged for 10 minutes at 1,000 g, and the cell pellet was resuspended in a complete media. The resuspended cells were used for cell counting. 20 µL of cells were mixed with 20 µL of Trypan blue solution, and 10 µL of cell suspension was used for cell counting. The suspension was added to the hemocytometer, and the number of live cells was found. The procedure was done three times for each cellular test.

5.2.7.2 IC50 for Cip, NPs with and without H_2O_2

To assess the cytocompatibility of the ROS-responsive NPs, various concentrations of Cip, NPs, and NPs exposed to 1 mM H_2O_2 overnight were tested. The concentrations tested for NPs were 0, 0.5, 1.0, 1.5, 2.0, 5.0, 10.0, and 100 mg/mL. For CIP, concentrations were selected based on the LC% of the NPs and included 0, 0.18, 0.36, 0.54, 0.72, 1.8, 3.6, and 36 mg/mL. The IC50 value, which represents the concentration at which 50% of the cells were dead, was determined for all samples.

A suspension of 2×10^5 cells was added to each well in complete media and incubated for 24 hours to allow for complete adhesion. The following day, the media was replaced with fresh media containing the test samples (Cip, NPs, and NPs exposed to H_2O_2), and the cells were incubated for an additional 24 hours. Subsequently, the MTT assay kit was used to quantify cell viability, following the manufacturer's instructions.

5.2.7.3 Cytocompability of NP-Loaded NFs

The biocompatibility of biosensors loaded with ROS-responsive NPs was evaluated both in the absence and presence of H_2O_2 using the elution technique. A 1 cm x 1 cm membrane was immersed in 5 mL of complete media for three days, with or without H_2O_2, and the resulting extraction was applied to the cells as described previously. Cell viability was assessed on days 1,

3, and 7, and the results were compared to a control group without any treatment (proliferation rate was measured compared to control on day 1).

5.2.7.4 A Mixture of Bacteria and Cells

A total of $1x10^5$ cells were added to each well and incubated overnight. Diluted bacterial suspensions in complete culture media (10^3 CFU/mL) were then prepared and added to each well at a ratio of 1:10, followed by incubation for 4 hours. After this period, 100 µL extracts from NP-loaded NFs, both with and without H_2O_2 treatment, were added to each well and incubated overnight. A positive control was included by adding a cocktail of antibiotics to one well, while a negative control consisted of a well without any treatment. Additionally, a growth standard consisting of non-infected cells was used. After 24 hours, the cell monolayer was lysed with Triton X-100, and the suspension was diluted for serial dilution plating to count bacterial colonies. Furthermore, the number of live cells was assessed using trypan blue after thoroughly washing the cell monolayer with cold PBS and trypsinizing.

5.3 Results and Discussion

5.3.1 Increased Accuracy of Biosensors: Elimination of False Positives in HCy Containing Biosensors

Real-time monitoring and point-of-care testing for wound infections are essential for improving patients' quality of life and reducing healthcare costs. Traditional bacterial detection methods, both conventional and biosensor-based, typically require the removal of wound dressings to obtain swabs or tissue biopsy samples. However, this removal can damage newly formed tissue, disrupt the healing process, and cause additional pain and discomfort. Wearable colorimetric sensors integrated into wound dressings have been developed to address these challenges. These colorimetric sensors enable continuous monitoring of vital wound parameters and provide real-time feedback to clinicians or patients, allowing timely interventions without further compromising the healing process [374]. For colorimetric biosensors to be effectively utilized in different clinical and non-clinical settings, several key factors must be considered. First, they should produce a visible response that can be easily distinguished by the naked eye, even by non-trained individuals. Second, they should not require complex technology for data interpretation. Additionally, two of the most critical factors for successful bacterial detection are sensitivity and accuracy. High sensitivity is essential for detecting bacteria at an early stage before infection progresses, while accuracy ensures that the biosensor performs reliably in complex wound environments [375,376].

The accuracy of a biosensor is defined by its ability to detect bacterial biomarkers selectively without interference from other environmental factors. The wound microenvironment is rich in salts, enzymes, and proteins, which can potentially affect sensor performance. An ideal biosensor should: yield a positive test result in infected patients, generate a negative result in

uninfected patients, remain independent of other non-bacterial biomarkers, serve as a predictor of infection outcomes, provide rapid and easy-to-interpret results with minimal error, and be cost-effective for widespread clinical use [374–376].

Many biosensors developed in laboratory settings fail to perform accurately in real-world conditions due to insufficient testing in complex wound environments. Lack of accuracy often leads to false positive results in clinical applications. Moreover, one commonly used biomarker for wound infection detection is pH. While normal skin pH ranges from 4.2 to 5.6, an infection increases the pH to a more alkaline level. However, pH alone is not a reliable infection indicator, as it fluctuates throughout different stages of healing, even in the absence of bacteria, thus causing false positives. To address these issues, we tested our fabricated biosensors in artificial wound fluid (AWF), which contains various salts and proteins with different pHs, to assess their accuracy and to minimize false positives in clinical settings.

Preliminary tests demonstrated that the biosensor did not exhibit any color change in AWF up to pH 7.5 in the absence of bacterial lipase, even when enriched with proteins and a mixture of $CaCl_2$ and NaCl. However, at pH levels above 7.5, some occasions of false positive results were observed in AWF. To determine the specific cause of these false positives, we individually assessed the effects of salts, pH, and proteins on the biosensor. The results indicated that proteins did not trigger a false positive response. And neither pH alone (water at $8<pH<11$) nor salts alone (various concentrations of NaCl, $CaCl_2$, or their combinations) caused false positives. The combination of alkaline pH and salts was responsible for the false positive results. Further testing of the dye solution alone under the same conditions showed no observable colorimetric false positives. The result suggests that the false positive results were not due to the dye itself but rather its interaction within the nanofiber matrix and microenvironment. A

thorough literature review led us to speculate that dye aggregation in the nanofiber structure, influenced by the presence of salts at alkaline pH, was possibly responsible for these unexpected color changes.

Based on the literature review, it was inferred that various environmental factors, such as alkaline pH and the presence of mixed salts at specific concentrations can affect the aggregation behavior of the dye and alter the way electrons circulate within these aggregates [377]. When dye monomers aggregate in a face-to-face configuration (**Figure 5-1A**), they form H-aggregates, leading to a blue shift in the spectrum. Conversely, when the interaction is head-to-tail (**Figure 5-1B**), J-aggregates are formed, resulting in a redshift. These different configurations modify intramolecular interactions, which are highly dependent on the packing arrangement of the dye molecules, ultimately causing a color change in the system. [378,379]. Shifts in dye aggregation can be evaluated using fluorescence spectroscopy. **Figure 5-1C** presents the fluorescence spectra of samples excited at 488 nm, measured in water at pH 8, artificial wound fluid (AWF: AWF ($CaCl_2$ (10mM), NaCl (200mM), Tris (40mM), and 2% BSA in distilled water)) at pH 6 and 10, and a water solution containing lipase at pH 8. As shown, the second fluorescence peak at 580 nm, observed in water and AWF at pH 6 and 8, shifts in the AWF solution at pH 10. This shift is attributed to the presence of salts in the AWF and the alkaline environment, which disrupt dye aggregation, causing a transition from H-aggregation (side-by-side configuration) to J-aggregation (head-to-tail configuration) with a redshift. Interestingly, the membrane exposed to lipase (orange spectrum) exhibited a single broad peak instead of the double peak in yellow samples. All samples (yellow, green, and orange) displayed fluorescence under UV light at 365 nm, as shown in Figure **5-1D**. To confirm whether salt-induced changes in aggregation were responsible for the observed spectral differences, SEM was used to examine samples in AWF at

pH 6 and 10. As shown in **Figure 5-1E**, salt deposits were visible only in the sample at pH 10. The increase in salt presence may be due to increased membrane swelling at alkaline pH, which facilitates salt entrapment within the structure.

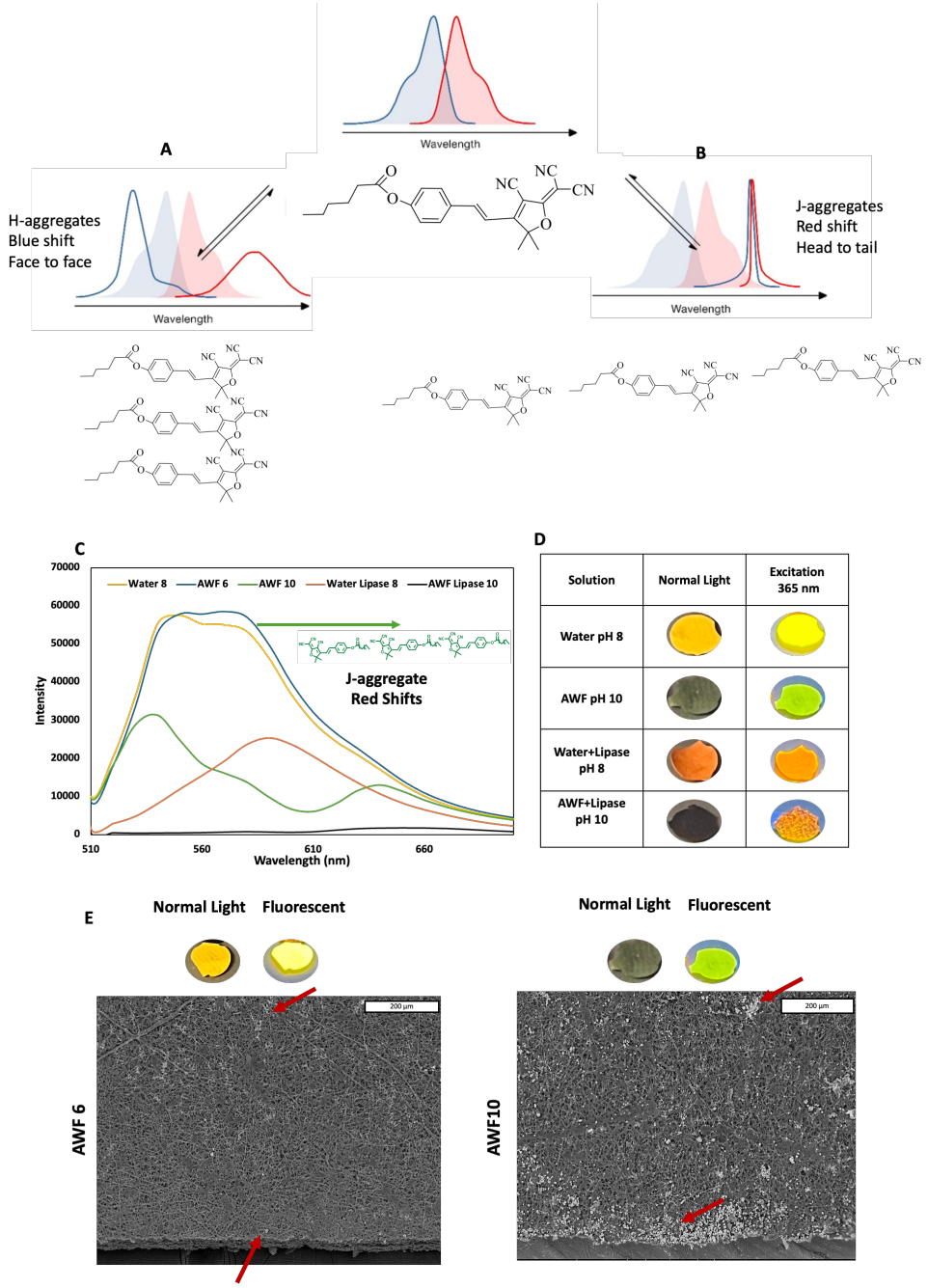

Figure 5-1 A-B) Different aggregate configurations of the dye, which causes different color changes C) Fluorescent spectra (at 488 nm excitation) of biosensors in different solutions at different pHs such as water, AWF (having NaCl and $CaCl_2$) and lipase indicating the red shift in the presence of AWF at pH 10. D) The fluorescent behavior of samples in different solutions at 365 nm excitation and E) SEM images of the biosensors in AWF at pH of 6 and 10, showing the presence of the salts.

We ingeniously employed both chemical and physical methods to counteract these environmental factors and eliminate false positives. The chosen additives for the biosensor in this project were acids known for their wound-healing properties: citric acid, palmitic acid, humic acid, gallic acid, and tranexamic acid. These acids can react with excess basic salts in the medium, neutralizing them and possibly preventing changes in the dye's aggregate configuration. After the addition of each acid, a quick test was performed at pH 8.0 to ensure false positives did not occur. The initial color of the membranes varied based on the added acid: citric and palmitic acids produced a yellow color, humic acid black, gallic acid orange, and tranexamic acid red. Following the addition of AWF without lipase at pH 8.0, the membrane containing citric acid did not show any color change. In contrast, palmitic acid turned green, humic acid brown, gallic acid dark orange, and tranexamic acid brown. Among all the samples, only the membrane with citric acid exhibited a distinct color change in the presence of lipase, indicating that the other acids interfered with the membrane's lipase responsiveness (**Figure S9-1**). Consequently, citric acid, which showed the most promising results in preventing false positives, was selected for the fabrication of the final biosensors.

In regard to preventing false positive color change by the addition of acid to the biosensor, the thickness of the biosensors is of paramount importance since the concentration of the citric acid in the solution is fixed. The thickness affects the amount of citric acid that can be loaded into the membrane. As thickness increases, more citric acid can be incorporated, which can both enhance the biosensor's performance and accuracy but also pose challenges during extended electrospinning, potentially disrupting continuous spinning. Moreover, citric acid, being a potent antibacterial agent, can also hinder the biosensor's sensitivity by killing bacteria

upon contact. To determine the optimal parameters for biosensor fabrication, different citric acid concentrations (0.5–6%) and electrospinning times (1–3 hours), resulting in thicknesses ranging from 50 to 500 µm, were tested in the presence of AWF at pH 8.0. The ideal parameters were determined to be 4% citric acid (as higher concentrations did not improve performance), a spinning time of 3 hours and a thickness of approximately 350–450 µm. The time of electrospinning was determined with a series of tests, and it was shown that shorter electrospinning times result in thinner membranes, which are prone to false positives. The results of testing the biosensors' color change prepared under different spinning times and citric acid concentrations in AWF in the absence of lipase, and the presence of salt and proteins at pH=8.0, which can cause false positives, are presented in **Figure 5-2A**.

The biosensors fabricated with the optimal parameters were further analyzed for fiber diameter and distribution, **Figure 5-2B**. The fiber diameters ranged from 200 nm to 800 nm, with an average diameter of 412 ± 140 nm. The membrane thickness was approximately 415 µm, **Figure 5-2C**. The best-performing sample was selected for further testing in various solutions and salt concentrations to ensure that no false positives occurred.

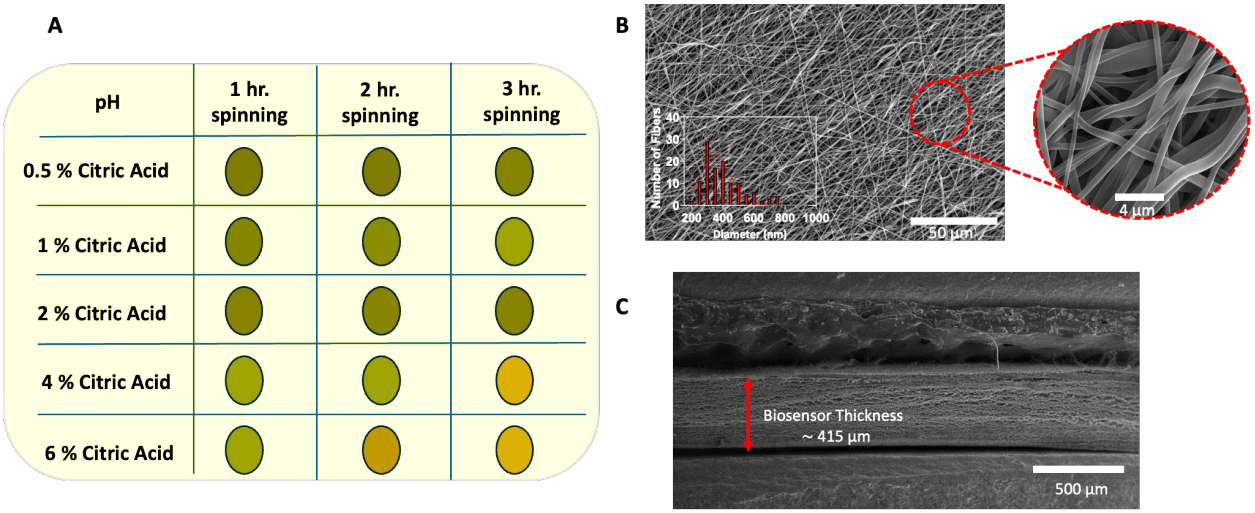

Figure 5-2 A) The effect of citric acid concentration and electrospinning time on the color-changing property of the biosensor in the absence of lipase. B) The morphology of the biosensor in SEM image and fiber diameter distribution. C) The SEM image from the cross-section of the biosensor showing the thickness of the biosensor

5.3.1.1 Response to Different Solutions

To better simulate the complex wound environment, which is rich in proteins and salts, and to ensure that no false positives occur in actual wound settings, we tested the fabricated citric acid-loaded biosensor under realistic conditions. Testing involved evaluating the biosensors' accuracy and precision using various buffers, salts, and protein solutions at different concentrations and pH levels. The results indicated that no false positives were observed in the presence of various buffers, including AWF, PBS, Tris, Tricine, Bicine, MES, and HEPES, at pH levels of 4.0, 7.0, and 8.0. However, at pH 11.0, all buffers caused a color change from yellow to green due to ester bond hydrolysis, which enhances internal charge transfer and facilitates the color shift, as depicted in **Figure S9-2**.

Additionally, the presence of ions (Na^+, Mg^{2+}, and K^+), whether alone or in combination, did not induce any color change towards green across concentrations ranging from 5.0 mM to 150.0 mM, as shown in **Figure S9-3**. These results confirm that the fabricated biosensor does not produce false positives in response to different ions and buffers.

To further evaluate the sensor's selectivity, various salts of these ions were also tested, including NaCl, Na_2HPO_4, $Na_5P_3O_{10}$, $NaHCO_3$, NaH_2PO_4, KCl, KI, KH_2PO_4, $K(CH_3COOH)$, $MgCl_2$, $Mg(CH_3COOH)$, CuBr, and $FeCl_3$. No green color change was observed with any of these salts, demonstrating the biosensor's selectivity for lipase (**Figure S9-4**).

Moreover, testing in the presence of proteins such as FBS and BSA in different buffers also yielded no color change (**Figure S9-5**), showing that the biosensor does not react with

proteins. These findings highlight the biosensor's potential for specific bacterial detection, with no false positives from other environmental factors, underscoring its reliability.

5.3.1.2 Response to different lipases and sensitivity of the biosensor

In addition to preventing false positives, it is essential to ensure that the biosensor consistently produces positive results regardless of the bacterial source of lipase. Commercially available lipases from different bacterial sources with different concentrations were tested to evaluate the selectivity and accuracy of the biosensor. This test specifically aimed to determine the selectivity of the biosensor; therefore, solutions were prepared without salts to eliminate potential interference. In the absence of salts, the observed color change was from yellow to orange. As shown in **Figure 5-3A**, after 1 hour of exposure to different lipase concentrations—Amano Lipase PS from *Burkholderia cepacia* (L_1), Amano Lipase from *Pseudomonas fluorescens* (L_2), Lipase from *Pseudomonas cepacia* (L_3), and Lipase from *Candida rugosa* (L_4)—all biosensors exhibited a noticeable color change. At the lowest concentration of 0.1 mg/mL, the color change was subtle, but at 0.5 mg/mL, all lipases induced an orange color visible to the naked eye. Although L_4, derived from fungi, caused a color change, it was less pronounced compared to bacterial lipases. These results indicate that the biosensor can detect various lipases, even at low concentrations like 0.1 mg/mL, though higher concentrations produce more distinct color changes.

To further evaluate the biosensor's performance, L_1 was chosen to assess the effect of time on color change at a fixed concentration, **Figure 5-3B**. The color change occurred almost instantly at the highest concentration (10 mg/mL). As the concentration decreased, time became a more critical factor in the color change process, as the dye concentration exceeded that of the

available lipases at each time point. For all concentrations tested, a color change was observed within 1 hour, demonstrating the biosensor's sensitivity.

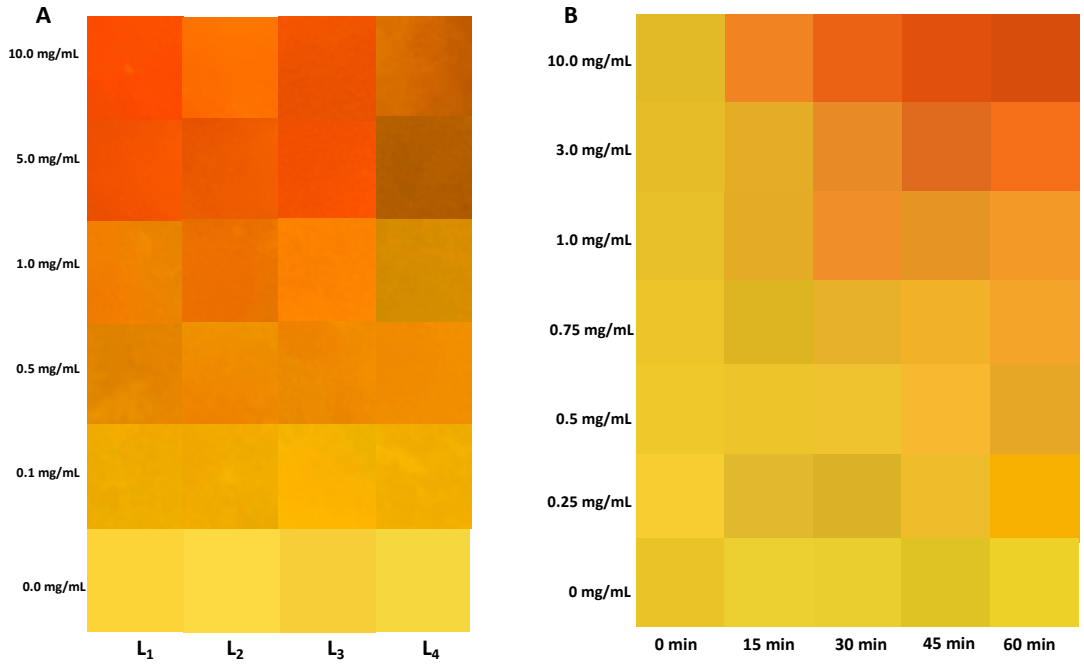

Figure 5-3 biosensors color changing A) after one hr. in the presence of different lipases from bacteria and fungi sources. B) during one hr. at different concentrations of L_1.

5.3.1.3 Bench Testing of the biosensors

As a quality control step, a bench test was designed to ensure the engineered biosensors do not yield false positives in the absence of lipase and reliably exhibit a color change in its presence. Since the biosensor is intended for various settings, including hospitals, home care, battlefields, and household use, it is important to assess the visibility of the color change under different lighting conditions. As shown in **Figure 5-4A**, variations in the color temperature of the light source exerted a minor influence on color perception. Similarly, the angle of observation did not noticeably affect the visibility of the color change. These findings were consistent for both biosensors in AWF (no lipase) and AWF with lipase.

The biosensors in AWF and AWF with lipase were also analyzed using spectrophotometry to determine their L*, a*, and b* values and to generate reflectance graphs. As shown in **Figure 5-4B**, the AWF samples exhibited a yellow color with a positive b* value (L* = 78.2, a* = 1.8, b* = 66.72), while the AWF with lipase samples shifted towards the red spectrum with a positive a* value (L* = 61.3, a* = 34.9, b* = 44.8). The L*, a*, and b* data were used to generate HEX color codes for reference in future bench tests as part of quality control during mass production. **Figure 5-4C** illustrates the clear distinction between the two samples in terms of reflectance and wavelength. The AWF sample had a reflection peak at 550 nm, corresponding to the yellow range, while the AWF with lipase peaked at around 600 nm, indicating an orange hue. This orange color results from a combination of cleaved dye (red) and non-cleaved dye (yellow), confirming the biosensor's functionality.

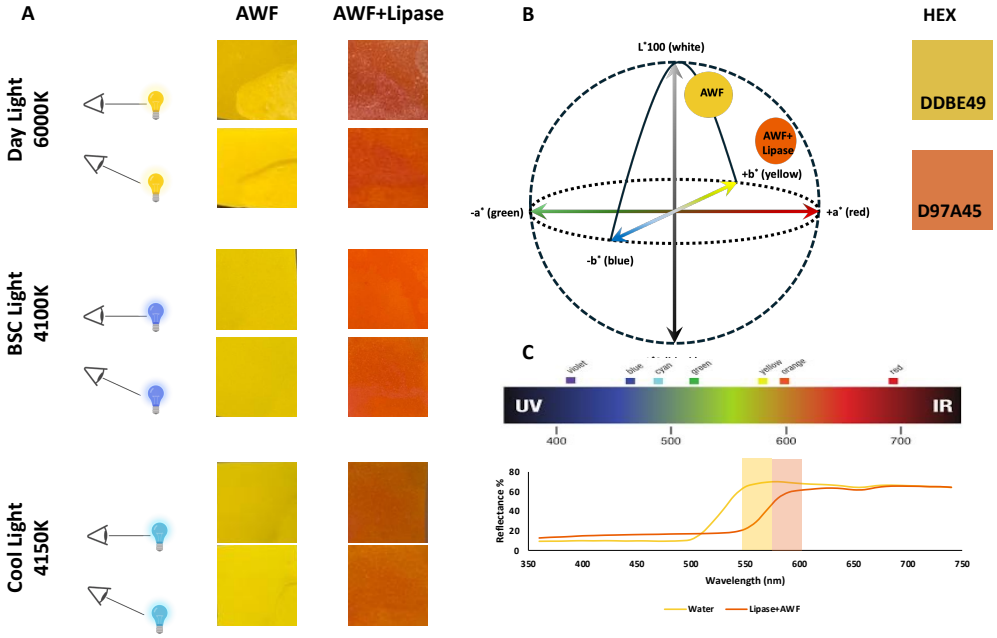

Figure 5-4 A) Bench test study of biosensors color in the absence (AWF) and the presence (AWF+lipase) of lipase under different lighting settings and at two different angles. B) the color space and color of biosensors in AWF and AWF+lipase. C) the reflection spectra of AWF and AWF+lipase samples indicate the differences between these two samples.

5.3.1.4 Response of the Biosensors to Bacteria

The performance of the biosensors in detecting bacteria was assessed using the agar method. To ensure the observed color changes fell within an acceptable range, the same lighting conditions as those used in the bench test were applied. The color was examined both directly at eye level (90º angle) and at a 45º angle. The biosensors exhibited a noticeable color change for all three tested bacteria (*P. aeruginosa*, *E. coli*, and MRSA), as shown in **Figure 5-5A**. However, the color change appeared slightly different under varying light sources. All changes were clearly distinguishable from the control, which showed no color change. The color shifts occurred within 5 hours of sample placement; a timeframe suitable for clinical applications. The initial bacterial concentration was 3 x 10^5 CFU/cm², but after 5 hours, significant growth was inhibited due to the presence of citric acid, which has antibacterial properties. Following the 5-hour incubation, the biosensors were used to isolate and culture the bacteria to further assess bacterial concentrations in the presence of the biosensor. The bacterial concentration around the biosensors remained close to the initial level, between 5-6 x 10^5 CFU/cm².

The color-changed biosensors were also analyzed using spectrophotometry to determine their color spectra. As shown in **Figure 5-5B**, a shift toward the green spectrum was observed at a wavelength of 525 nm, compared to the control sample, which showed a yellow color at 550 nm. In terms of color space, the green-shifted biosensors had L* values between 66-72, b* values between 42-48, and negative a* values ranging from -3 to -6, indicating a shift toward green.

Finally, based on these results, a flash card was developed to help end users differentiate between infected and non-infected wounds by showing the color changes associated with bacterial presence under different light sources, as demonstrated in **Figure 5-5C**.

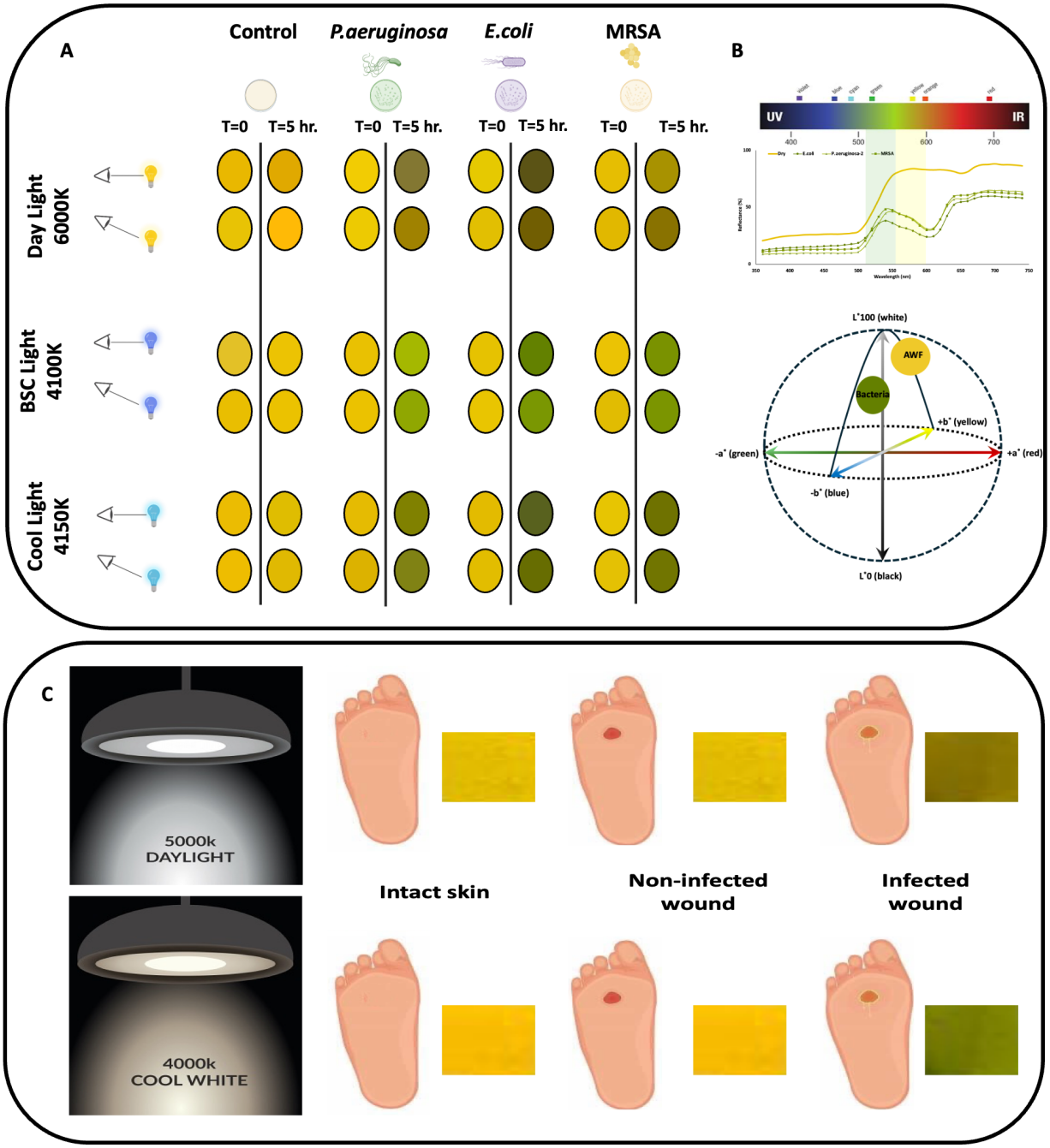

Figure 5-5 The performance of the biosensors in the presence of different bacteria. A) the color changing of the Biosensor in the presence of P. aeruginosa, E. coli, and MRSA under different light sources compared to control with no bacteria. B) the color wavelength spectra of biosensors after exposure to the bacteria and control. And the color space of the control and bacteria exposed sample. C) the flashcard for differentiating infected wounds from non-infected wounds based on the color change.

In addition to preventing false positives and ensuring high accuracy and sensitivity, a biosensor intended for clinical use in actual wound environments must also be compatible with commercially available wound dressings and cleaning solutions. Depending on clinical circumstances, the fabricated biosensor may not be applied directly to the wound. Therefore, we tested its compatibility with different commercially available foams to determine whether the color change would still occur even when the biosensor was not in direct contact with the wound. The names and properties of these foams are provided in **Table S9-1**, while the results and discussion on biosensor compatibility with different dressings and cleaning solutions are included in the Supporting Information (**Chapter 9**). Furthermore, for clinical applications, sterilization and its potential effects on biosensor performance are crucial factors. A detailed discussion of biosensor performance after sterilization is also provided in the Supporting Information (**Chapter 9**). Another often overlooked aspect in bench experiments is dye leachability in the wound environment. To address this, we designed an experiment to evaluate dye leaching, and the results are also included in the Supporting Information (**Chapter 9**).

5.3.1.5 Cell Viability

As the final step in evaluating the feasibility of using the biosensor in clinical conditions, its cytocompatibility was assessed. Fibroblast viability in the presence of the released dye was evaluated after three days of extraction. As shown in **Figure 5-6A**, biosensors without dilution (1X) exhibited 81.2 ± 5% cell viability, which falls within the acceptable biocompatibility range (80-95%). However, with increasing dilutions—reflecting more realistic wound conditions due to the presence of wound fluids—cell viability significantly improved, reaching 97-100%. **Figure 5-6B** demonstrates the increase in the population of healthy cells as dilution factors increased. While the number of healthy cells in the undiluted sample was lower than in the

control group (fibroblasts in growth media), it was still significantly higher than in the negative control (DMSO). Elongated, healthy cells observed across all diluted samples (0.1X, 0.01X, and 0.001X) confirmed the biocompatibility of both the biosensors and the released dye.

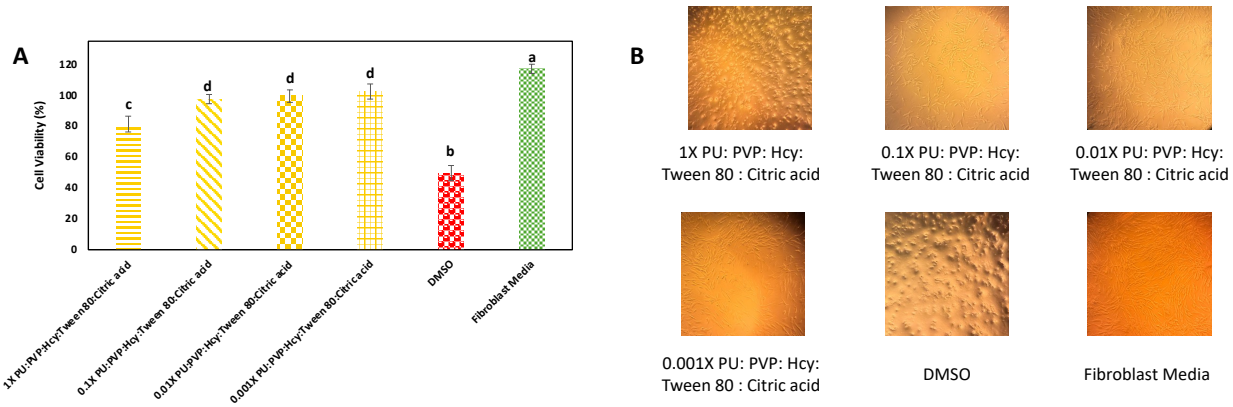

Figure 5-6 A) The cell viability of Human Adult Skin Fibroblast in the presence of three-day extracted biosensors with different dilutions (1-0.001X) compared to only growth media and DMSO. B) The morphology cells in the presence of extracts.

5.3.2 Theranostic Biosensors Fabrication

To fabricate theranostic biosensors capable of detecting bacteria without false positives and eliminating their presence, reactive oxygen species (ROS) were chosen as the target biomarkers. ROS levels correlate with induced stress at the wound site and are closely associated with infection. ROS-responsive nanoparticles were incorporated into the biosensors to achieve this dual functionality. These nanoparticles enable the development of a theranostic system that not only detects bacterial infection through a visible color change—providing real-time feedback to physicians, nurses, and patients—but also releases antibiotics in response to bacterial presence. The triggered antibiotic release helps prevent infection while avoiding sustained drug release, which could contribute to bacterial resistance. The following sections present the characterization results of NPs and the nanoparticle-loaded nanofibers (NP-NFs). The ROS-

responsive NPs were fabricated using a $mPEG_{45}$-b-PPS_{60} polymer, which was synthesized in-house.

5.3.2.1 Chemical Characterization of PEG-PPS

The ROS-responsive polymer ($mPEG_{45}$-b-PPS_{60}) was synthesized in a three-step process, as outlined in **Figure S9-11A**. First, methoxy poly(ethylene glycol) methacrylate ($mPEG_{45}$ methacrylate) was synthesized. This step was followed by thioacid modification to produce methoxy poly(ethylene glycol) thioacetate (mPEG45 thioacetate), and finally, copolymerization yielded methoxy poly(ethylene glycol)-b-poly(propylene sulfide) ($mPEG_{45}$-b-PPS_{60}).

In the first step, the successful functionalization of m-PEG to PEGMA is demonstrated by the appearance of three new peaks in the FTIR spectrum (**Figure S9-11B**) at 1740 cm^{-1} (C=O stretching), 1650 cm^{-1} (C=C stretching) and 980 cm^{-1} (C=C bending). Additionally, a peak at 1260 cm^{-1} related to C-O stretching in an ester group further confirms the reaction. This step of synthesizing had a yield of 80%. In the second step, the appearance of a peak at 630 cm^{-1}, attributed to the S-CH_3 group, indicates successful thioacid modification. A reduction in the intensity of peaks associated with the C=C group suggests that some m-PEGMA reacted with thioacetic acid. This step yield was 76.6%.

Finally, NMR data for mPEG45-b-PPS60 (**Figure S9-11C**) shows a quadruplet peak at 1.81-1.9 ppm (integration 1.93) corresponding to two hydrogens from the O-(CO)HCH_2CH_2S group and a singlet at 2.35 ppm indicating three hydrogens from the -$SCOCH_3$ group, confirming the successful synthesis of PEG-thioacetate. Additionally, the presence of a peak at 1.35-1.45 ppm in the PEG-PPS spectrum, attributed to CH_3 hydrogens in PPS, further confirms the successful synthesis. The final step had a yield of 50%.

5.3.2.2 Fabrication of NPs and Drug Loading

After successfully synthesizing $mPEG_{45}$-b-PPS_{60}, NPs were fabricated using a double emulsion technique, as shown in **Figure S9-12A**. The hydrophilic portion of the polymer, PEG, an FDA-approved material, enhances the serum half-life of the NPs and reduces protein adsorption due to its shielding effect. The final nanostructure morphology depends on the fraction of the PEG component: micelles form when the PEG fraction exceeds 45%, inverted structures form below 25%, and filaments form between 25% and 45%. In this project, micelles were chosen as the desired structure [380,381]. The dense PEG-based outer layer of these NPs imparts a neutral charge, making them non-immunogenic and non-inflammatory. This outer layer also prevents nonspecific cellular interactions by regulating protein corona formation. The hydrophobic portion of the polymer, PPS, is responsible for the self-assembly of the NPs and contributes to their stability, **Figure S9-12B**. PPS is reactive to ROS, and under oxidative conditions, it undergoes structural changes that facilitate the release of the encapsulated cargo [380,381].

TEM was used to evaluate the morphology of the freshly fabricated NPs, revealing spherical particles with an average diameter of 213.9 ± 29.5 nm, as depicted in **Figure 5-7A**. The NPs were fully disassembled after treatment with H_2O_2, and no spherical particles were observed, as shown in **Figure 5-7B,** some polymer agglomeration however, was observed. DLS also indicated a hydrodynamic diameter peak of around 200 nm for fresh NPs. However, when stored in the PBS buffer at 4ºC for three months, the size of the NPs increased to approximately 500 nm, **Figure 5-7C**. In contrast, freeze-dried samples maintained consistent size and morphology even after three months of storage.

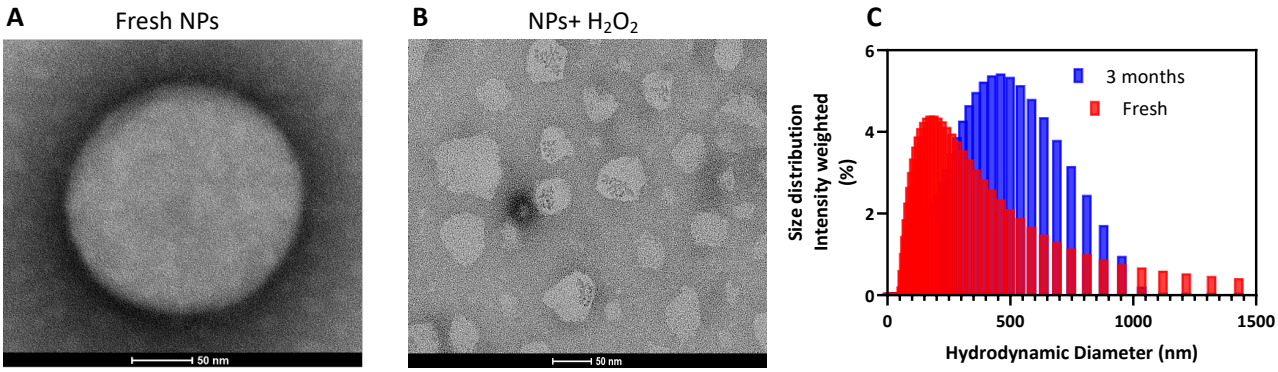

Figure 5-7 A) TEM image of freshly fabricated NPs, B) The TEM image of NPs after treatment with H_2O_2, and C) the hydrodynamic diameter of fresh NPs and NPs stored in the fridge in PBS for three months.

5.3.3 Loading NPs into the Nanofibers

Since the loading of NPs into NFs was achieved by immersing the fabricated biosensors into an NP solution, there was a possibility that this process could alter the morphology of both NFs and NPs. To assess this, SEM was conducted after loading and drying the theranostic biosensors. As shown in **Figure 5-8**, the distribution and average size of the nanofibers (435 ± 17 nm) remained unchanged, with no significant difference (p-value = 0.27) to biosensors without treatment. The SEM images also revealed that the NPs were dispersed between the NFs, and their size showed no significant variation compared to freshly prepared NPs.

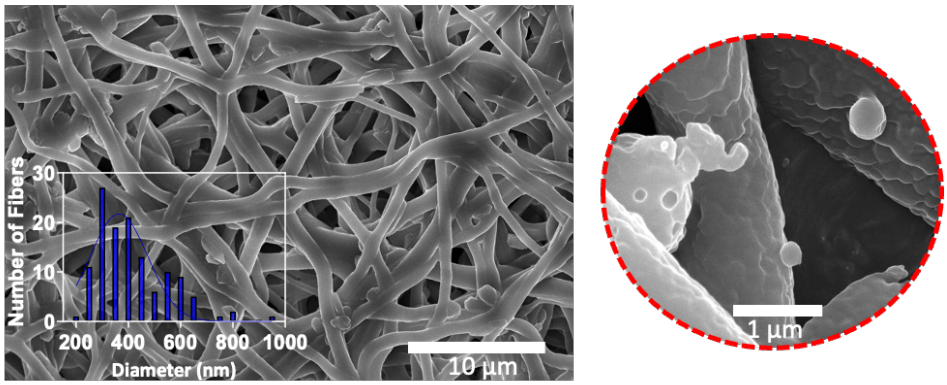

Figure 5-8 The morphology of the theranostic biosensor after immersing in NPs solution and drying.

5.3.3.1 Drug Loading Efficiency and Drug Release Behavior from NPs and NF-loaded NPs

Since three different concentrations of CIP were selected for loading into the NPs, the LE and LC were calculated to determine the optimal concentration for incorporating NPs into the NFs. As shown in **Figure S9-13A**, the lowest concentration (6.25 mg) resulted in both LE and LC values below 20%. At the highest concentration (244 mg), the LC reached approximately 25%, and the LE was around 53%. Although these values are higher than those observed for the 6.25 mg sample, they are significantly lower than those for the NPs loaded with 39 mg of CIP, which exhibited LE and LC values of 73% and 36%, respectively. The difference between the 39 mg and 244 mg samples may be attributed to the excess drug at higher concentrations, which could lead to saturation of the NP matrix. There appears to be a limit to how much drug can be incorporated into the NPs, and exceeding this limit results in reduced LE and LC. Only drugs with optimal interactions within the NP network remain, while the excess drug is removed during the washing steps in the fabrication process.

The release of CIP from all three NP formulations, as well as from NPs loaded in the biosensor (NP/NF), was evaluated in the absence and presence of hydrogen peroxide (H_2O_2) as a ROS agent. In the absence of H_2O_2, less than 20% of the drug was released from the NPs over 72 hours, and this amount was even lower for the NP/NF samples, **Figure S9-13A**. The delay is likely because the drug released from the NPs became further entrapped between the nanofibers, reducing the amount detected in the media at each time point. Overall, this indicates that drug release took longer when NPs were embedded in the biosensor.

However, when H_2O_2 was introduced into the release medium, the drug release profile changed significantly. The assembly and disassembly of the polymer chains drive the release mechanism from PEG-b-PPS NPs. During NP fabrication, self-assembly occurs due to the

hydrophilic nature of PEG and the hydrophobic nature of PPS. During NP fabrication, self-assembly occurs due to the hydrophilic nature of PEG and the hydrophobic nature of PPS. In the presence of ROS, however, the PPS segment undergoes a transition from hydrophobic to hydrophilic, as illustrated in **Scheme 5-1**, converting into hydrophilic poly(propylene sulfone). This structural change leads to the disassembly of the nanoparticles, triggering the release of the encapsulated drug. [382][383]. Although the NP/NF samples required more time, both NPs and NP/NF systems achieved 100% release within 72 hours. In the case of NPs alone, more than 50% of the drug was released within 6 hours, while the NP/NF system required 12 hours to reach 60% release. The release behavior for all samples exposed to the ROS agent followed a zero-order profile, indicating constant drug release after being triggered by the ROS. These results suggest that the NPs were successfully loaded into the NFs and that the majority of the drug release occurred only in the presence of stimuli, with less than 20% untriggered release in 72 hours.

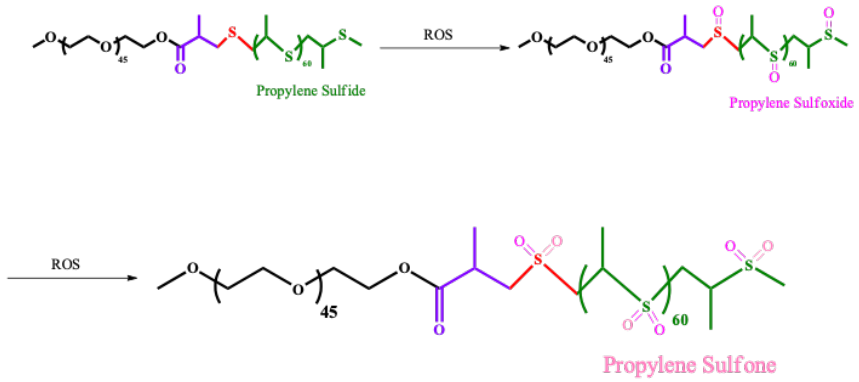

Scheme 5-1 Changes in the structure of m-PEG$_{44}$-b-PPS$_{60}$ in the presence of a ROS agent.

5.3.4 Antibacterial Tests

5.3.4.1 The Minimum Inhibitory Concentrations (MICs) and Minimum Bactericidal Concentrations (MBCs)

MIC and MBC of the drug-loaded NPs were evaluated against three different bacterial strains—*E. coli*, MRSA, and *P. aeruginosa*—both in the absence and presence of H_2O_2 as a ROS agent. These results were compared to CIP as a reference. As shown in **Figure 5-9**, the MIC values for the NPs without H_2O_2 were significantly higher for all three bacteria, with MICs being 32, 16, and 16 times greater than those of CIP for *E. coli*, MRSA, and *P. aeruginosa*, respectively. However, in the presence of H_2O_2, these differences were notably reduced, with MIC values only 8, 4, and 4 times higher than CIP for the same bacteria.

These findings suggest that CIP encapsulated within the NPs can be released in response to ROS, specifically H_2O_2. This targeted release mechanism effectively inhibits bacterial growth at concentrations of 0.4 µg/mL for *E. coli*, 0.5 µg/mL MRSA, and 0.4 µg/mL *P. aeruginosa*. The MBC values followed a similar pattern, with required concentrations for NPs in the presence of H_2O_2 being 1.6, 1, and 1.6 µg/mL for *E. coli*, MRSA, and *P. aeruginosa*, respectively, compared to 0.25, 0.2, and 0.4 µg/mL for CIP. Overall, both the MIC and MBC data demonstrate that the fabricated CIP-loaded NPs possess effective antibacterial activity with acceptable inhibitory and bactericidal properties, particularly in the presence of ROS.

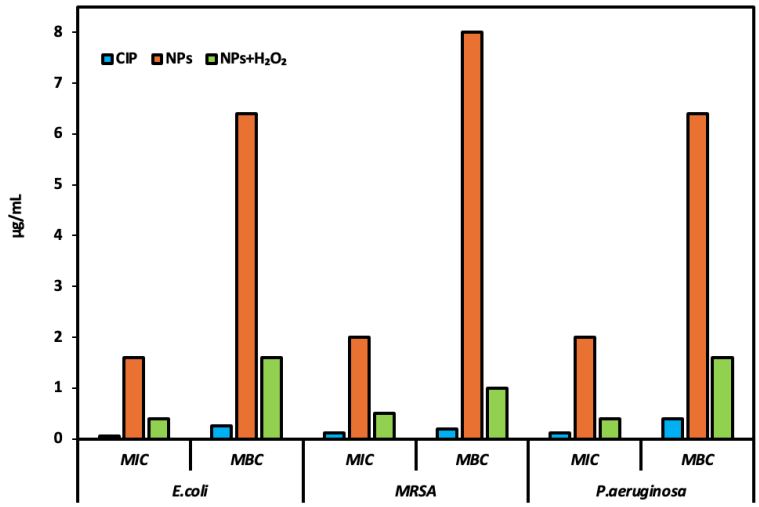

Figure 5-9 MIC and MBC of CIP-Loaded ROS-responsive NPs and CIP in the absence and the presence of H_2O_2 as ROS agent.

5.3.4.2 Zone of Inhibition (ZOI)

ZOI experiment was conducted under three different conditions: without H_2O_2, with H_2O_2 added to the broth, and with localized immersion of the biosensor in H_2O_2 to evaluate the antibacterial effect of the theranostic biosensors. As shown in **Figure 5-10**, the biosensors without NPs or citric acid (NFs) did not show any ZOI for any of the bacterial strains.

The biosensors containing only citric acid (C-NFs) demonstrated an antibacterial effect, showing a ZOI for MRSA and *P. aeruginosa* (10 mm) but not for *E. coli*. Interestingly, the addition of H_2O_2 did not significantly alter the ZOI of the citric acid-containing samples. The use of topical acidic solutions to eliminate bacteria, particularly antibiotic-resistant strains, is a well-established practice in wound care management. Acids such as diluted acetic acid, ascorbic acid, and salicylic acid have been used for this purpose. However, due to their potential to harm skin cells, their use has been limited. Citric acid, a natural compound derived from citrus fruits, has emerged as a promising alternative. Its antibacterial mechanism primarily involves altering the

pH of the wound environment, making it less suitable for bacterial growth. Additionally, citric acid disrupts bacterial cells by transitioning from its undissociated to dissociated form upon entering the bacteria. This process leads to an internal pH reduction, ultimately causing bacterial cell death. A low intracellular pH damages bacterial DNA, proteins, and cell membranes across various bacterial strains. It has also been proposed that organic acids inhibit nicotinamide adenine dinucleotide (NADH) oxidation by lowering the pH and further promoting cell death. Two additional mechanisms have been suggested for citric acid's antibacterial activity: the first involves direct disruption of bacterial outer membranes, where citrate binds to cell wall components, impairing membrane function and leading to cell death. The second mechanism requires citrate's chelating effect, which captures essential divalent ions like Ca^{2+} and Mg^{2+}, both of which are critical for bacterial growth.

Several studies have demonstrated the effectiveness of citric acid against MRSA and *P. aeruginosa*, showing promising results in inhibiting their growth. However, its effect on *E. coli* is highly concentration- and pH-dependent. While citric acid can inhibit *E. coli* growth at very low pH levels (around pH 3), it cannot eliminate the bacteria. As the pH increases to 4 or 5, citric acid's effectiveness against *E. coli* decreases significantly. Based on the data obtained, the amount of citric acid present in the biosensors was insufficient to substantially alter the agar's pH, which explains why no ZOI was observed for *E. coli*.

For the theranostic biosensors containing NPs (CNPs-C-NFs), the ZOI was observed even without ROS due to the presence of citric acid. In the absence of added H_2O_2, the zones of ZOI were 30 mm for *E. coli* and 15 mm for both MRSA and *P. aeruginosa*. These data represent a 5 mm increase in ZOI for MRSA and *P. aeruginosa* compared to samples containing only citric acid and a substantial inhibition for *E. coli*. These results may be attributed to the

untriggered release of CIP (10%) from the NPs. It is known that bacteria can produce ROS as a byproduct of their metabolic processes, and this endogenous ROS production can increase upon exposure to antibiotics. Therefore, the enhanced ZOI observed even without externally added ROS may be linked to ROS generated by the bacteria themselves. However, the introduction of H_2O_2 significantly increased the ZOI compared to samples without H_2O_2 (40 mm for *E. coli*, 25 mm for MRSA and 30 mm *P. aeruginosa*). For *E. coli* and MRSA, there was no significant difference in ZOI whether the H_2O_2 was introduced locally or added to the broth, both showing 25 mm ZOI. In contrast, for *P. aeruginosa*, the locally immersed samples exhibited a larger ZOI of 30 mm compared to locally added with 25 mm ZOI. Although the citric acid-containing samples without NPs did not produce a ZOI for *E. coli*, the theranostic biosensors, even without H_2O_2, showed a larger ZOI for *E. coli* than for the other two bacterial strains. The significant differences in the ZOI of the theranostic biosensors with and without H_2O_2 indicate that the triggered release of the antibacterial agent was successfully achieved.

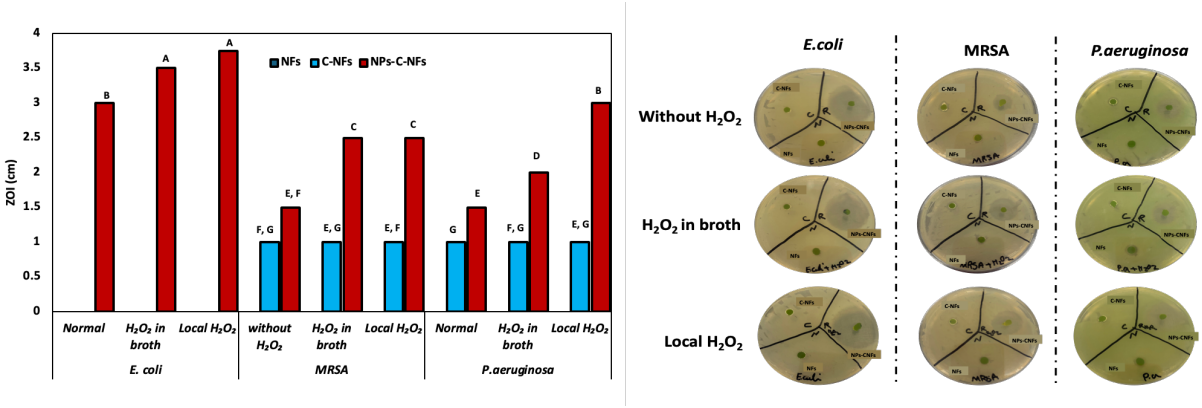

Figure 5-10 A) The ZOI data for different bacteria for biosensors (NFs), citric acid-containing biosensors (C-NFs), and theranostic biosensors (NPs-C-NFs) having both citric acid and NPs. All samples were tested in the absence of H_2O_2 and the presence of H_2O_2 in the broth or locally. B) the ZOI on agars.

5.3.4.3 Direct Antibacterial Test

The antibacterial efficacy of different biosensors—alone (NFs), containing citric acid (C-NFs), and containing both citric acid and nanoparticles (NPs-C-NFs)—was evaluated through direct antibacterial testing to assess the reduction in bacterial counts. As shown in **Figure 5-11A**, the biosensors alone (NFs) achieved less than 1 log reduction in bacterial counts within 4 hours. However, the addition of citric acid to the membrane (C-NFs) resulted in a significant log reduction, with 5 logs for MRSA and 4.6 logs for *P. aeruginosa*, consistent with the ZOI data. There was no significant difference in these reductions with or without H_2O_2. As previously noted in the ZOI experiments, citric acid had a lesser effect on *E. coli*, leading to only a 3-log reduction.

In the NPs-C-NFs samples, even without the addition of H_2O_2, the log reduction for *E. coli* increased significantly to 5.5 logs, aligning with the ZOI data, which can be related to the untriggered release of CIP from NPs initially and an increase in endogenous ROS that can trigger release of more CIP. However, for MRSA and *P. aeruginosa*, the absence of H_2O_2 did not lead to a significant improvement in log reduction. In contrast, when H_2O_2 was added as a ROS trigger, the log reduction increased dramatically for all bacterial strains, reaching almost 8 logs.

These results demonstrate that the ROS-responsive nanoparticles incorporated into the biosensors can effectively eliminate bacteria when exposed to a ROS agent such as H_2O_2. This mechanism offers an alternative to the prolonged release of antibiotics, thereby reducing the risk of developing bacterial resistance. Additionally, in situations where bacterial concentrations are below the infection threshold, and the immune system is not actively responding, the citric acid in the biosensors can help control bacterial growth and assist in their elimination even without

ROS-triggered release. This dual approach ensures both immediate bacterial control via citric acid and selective antibiotic release in response to elevated ROS levels associated with infection.

5.3.4.4 Time Dependent Antibacterial Test

The continuous antibacterial effect of the theranostic biosensors, as well as NPs and CIP, was monitored at concentrations below their respective MICs over 24 hours. As shown in **Figure 5-11B,** except for the NPs-C-NFs in the presence of *E. coli*, all other samples for all bacterial strains showed a significantly higher log reduction at 24 hours compared to 5 hours (almost 1 log increase). This data suggests sustained antibiotic release in the samples exposed to H_2O_2 and the prolonged antibacterial effect of citric acid in the theranostic biosensors, even in the absence of H_2O_2. Furthermore, for all bacterial strains, the NPs without H_2O_2 exhibited a lower log reduction, indicating that minimal untargeted release occurred in the absence of the ROS stimulus (3 log increase for *E. coli*, and 2 log increase for MRSA and *P. aeruginosa*). Among all bacteria, *E. coli* showed the highest log reduction, including CIP (6 log reduction), NPs (3 log reduction), NPs with H_2O_2 (7 log reduction), and NPs-C-NFs with H_2O_2 (7 log reduction), suggesting that this antibiotic is particularly effective against *E. coli* compared to MRSA and *P. aeruginosa*. For MRSA, during the initial 5 hours, pure CIP (3.5 log reduction) showed a greater log reduction compared to NPs with H_2O_2 (3 log reduction), indicating that not all the CIP had been released from the NPs. However, in the case of NPs-C-NFs with H_2O_2 (4 log reduction), the log reduction exceeded that of pure CIP, suggesting that citric acid also contributes synergistically to the antibacterial activity. After 24 hours, the effect of NPs-C-NFs (4.5 log reduction) remained greater than NPs alone (4 log reduction) but similar to that of pure CIP (4 log reduction), indicating that more CIP was released over time from the NPs.

For *P. aeruginosa*, during the first 5 hours, CIP and NPs with H_2O_2 showed similar 4 log reductions, but both were lower than that of NPs-C-NFs (5.5 log reduction), again due to the presence of citric acid. This indicates that the amount of CIP released from the NPs during the initial 5 hours was as effective as pure CIP and more effective than CIP for MRSA. However, after 24 hours, pure CIP achieved a higher log reduction (5 log reduction).

Overall, these findings indicate that loading CIP into ROS-responsive NPs did not significantly reduce the antibiotic's effectiveness against bacteria. Additionally, the combination of CIP with citric acid enhanced the antibacterial properties of the biosensors, leading to a higher likelihood of bacterial elimination, even at lower bacterial concentrations and earlier time stages.

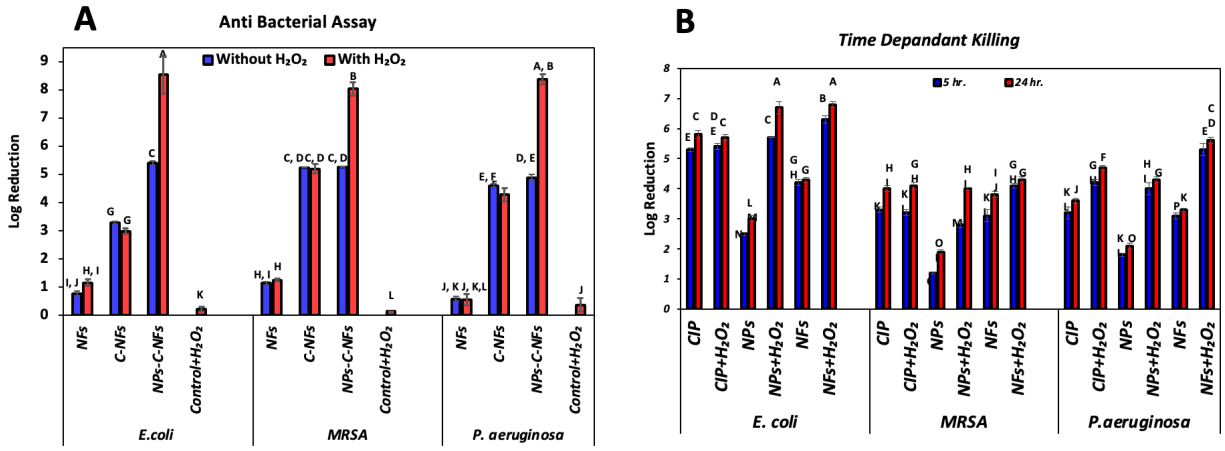

Figure 5-11 A) Direct antibacterial effect of biosensors with different compositions in the presence and absence of H_2O_2.(4 hours) And B) The time-dependent antibacterial effect of CIP, NPs, and NPs-C-NFs in the presence and absence of H_2O_2 for 5 and 24 hours, different alphabets indicate significant differences.

5.3.5 Cytocompability

The Cytocompability of the fabricated NPs and NPs-loaded theranostic biosensors were evaluated for human adult fibroblasts to ensure that the synthetic polymer is not cytotoxic.

5.3.5.1 IC50 for Cip, NPs with and without H2O2

The IC50 of CIP and CIP-loaded NPs was evaluated in both the absence and presence of H_2O_2, ensuring that the amount of CIP loaded into the biosensor was consistent across all tests. As shown in **Figure 5-12A**, there were no significant differences in cell viability between the presence and absence of H_2O_2 at each CIP concentration, with the IC50 for pure CIP calculated at 0.72 µg/mL.

For the NPs, the concentrations were selected to match the available CIP at each level tested for pure CIP. As indicated in **Figure 5-12B**, in the absence of H_2O_2, the cell viability for the NPs remained above 80%, even at concentrations as high as 10 µg/mL. A notable decrease in viability, to around 60%, was only observed when the concentration was increased tenfold. This demonstrates that the fabricated NPs are cytocompatible and effectively prevent CIP release, resulting in higher cell viability compared to pure CIP. However, upon the addition of H_2O_2, which triggered the release of CIP from the NPs, cell viability began to decrease as the concentration of available CIP increased.

For the ROS-responsive NPs in the presence of H_2O_2, the IC50 for CIP-loaded NPs was determined to be 2 µg/mL, which corresponds to the same level of effectiveness as 0.72 µg/mL of pure CIP, based on LC. Both the IC50 values for pure CIP and CIP-loaded NPs are above the concentrations used in this project, indicating that cytotoxicity is not a concern for the doses applied in the experiment.

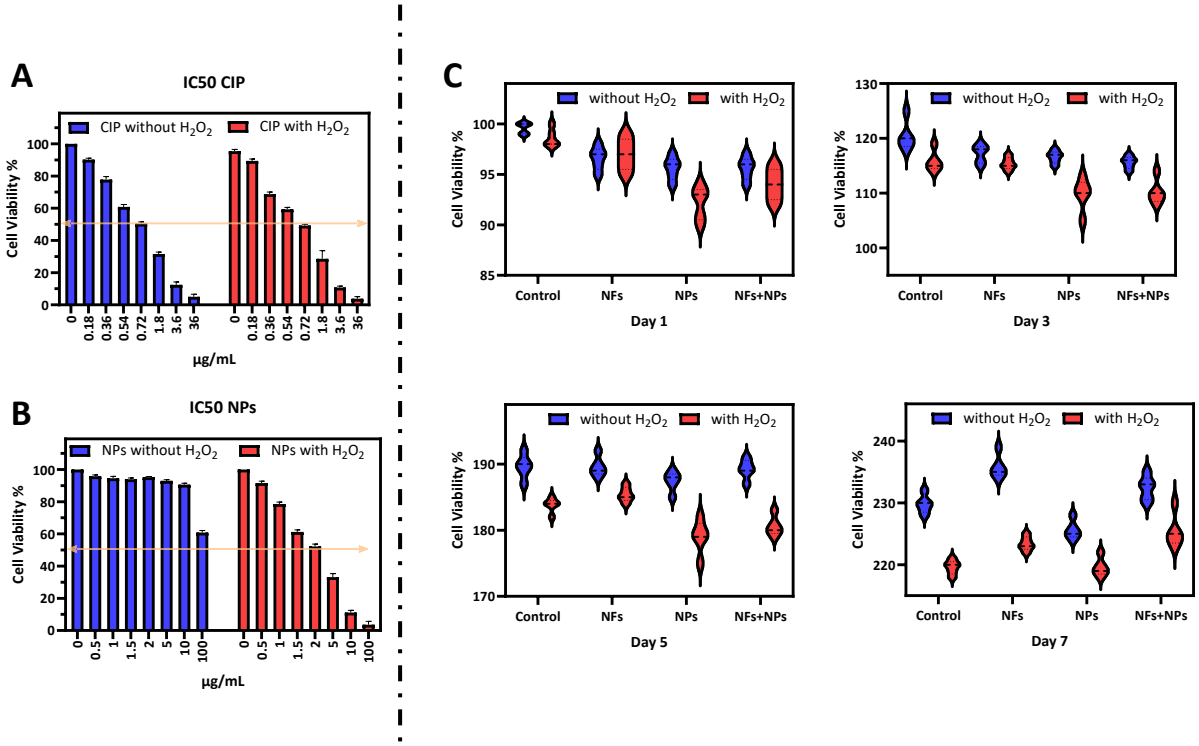

Figure 5-12 A) IC50 of pure CIP in the absence and presence of H_2O_2, B) IC50 of CIP-loaded NPs in the absence and presence of H_2O_2, and C) The Cell viability in the presence of different biosensor extracts at different time points.

5.3.5.2 Cytocompability of NP-Loaded NFs

A three-day extract from the biosensor (without NPs), NPs, and theranostic biosensor (NFs + NPs) was used to assess the cytocompatibility of the fabricated biosensors in both the presence and absence of H_2O_2 (1mM). As shown in **Figure 5-12C**, the presence of H_2O_2 did not result in a significant decrease in cell viability (cell viability remained more than 90%). Over the course of a week, the viability of cells exposed to NPs and NFs + NPs was slightly lower than that of NFs alone and the control group, likely due to the untargeted release of CIP that occurred during the three-day extraction. Despite this slight reduction (5-10%) in viability compared to the control, the theranostic biosensor maintained approximately 90% cell viability.

In terms of cell proliferation, there were no significant differences in the growth rates of cells exposed to NPs, NFs, NFs + NPs, and the control over the one week period, whether H_2O_2 was present or not. Since the release data indicated that the entire drug load would have been released during the three-day extraction, the one-week cytocompatibility tests with these extracts suggest that the theranostic biosensors are non-cytotoxic, even after complete drug release. Additionally, the lack of any observed changes in cell proliferation rates compared to the control compared to day 1 indicates that the biosensor does not impede fibroblast growth, further supporting its biocompatibility.

5.3.5.3 A Mixture of Bacteria and Cells

The cell-bacteria co-culturing experiment was conducted to evaluate the antibacterial properties of the theranostic biosensor in the presence of fibroblasts. The results, shown in **Figure 5-13**, are presented in terms of log reduction for both bacterial and fibroblast cells. In the controls treated with antibiotics, all three bacterial strains (MRSA, *P. aeruginosa*, and *E. coli*) showed complete bacterial elimination (8 log reduction), and no reduction in fibroblast viability was observed, indicating that the antibiotics eradicated the bacteria while maintaining cell viability. In contrast, the untreated negative controls exhibited almost no log reduction for normal bacteria and less than 1 log reduction for bacteria exposed to H_2O_2. However, the log reduction for fibroblasts was 2, 2, and 3 when being co-cultured with MRSA, *P. aeruginosa*, and *E. coli*, respectively, indicating that the presence of these bacteria resulted in significant cell death.

For biosensors without NPs, the presence of citric acid increased bacterial log reduction compared to the untreated samples, and fibroblast log reduction decreased to 1 for both MRSA

and *P. aeruginosa*. These results suggest that the citric acid-loaded biosensors had some antibacterial effect, although not complete.

In the NP-loaded samples with H_2O_2, bacterial log reduction was significantly higher than in the NFs-only samples (with H_2O_2), and fibroblast log reduction was significantly lower, indicating that the release of CIP from the NPs effectively reduced bacterial load, allowing more fibroblasts to remain viable. The combined effect of NPs and citric acid was even more pronounced in the NFs + NPs samples. For instance, in the case of *E. coli*, bacterial log reduction was 5 for NFs + NPs, 4 for NPs and 3 for NFs alone. For *P. aeruginosa* and MRSA, the log reduction was around 5 for NFs + NPs and 2 for NFs alone, while around 3 and 4 for NPs alone, respectively.

In the presence of NFs + NPs with H_2O_2, fibroblast viability improved due to the significant reduction in bacterial load. For all bacterial strains, fibroblast log reduction was less than 1, and in the case of MRSA and *P. aeruginosa*, fibroblasts even began to proliferate, similar to the positive control. These data demonstrate that the theranostic biosensors effectively combat bacterial infections while preserving fibroblast health, making them a promising tool for managing wound infections.

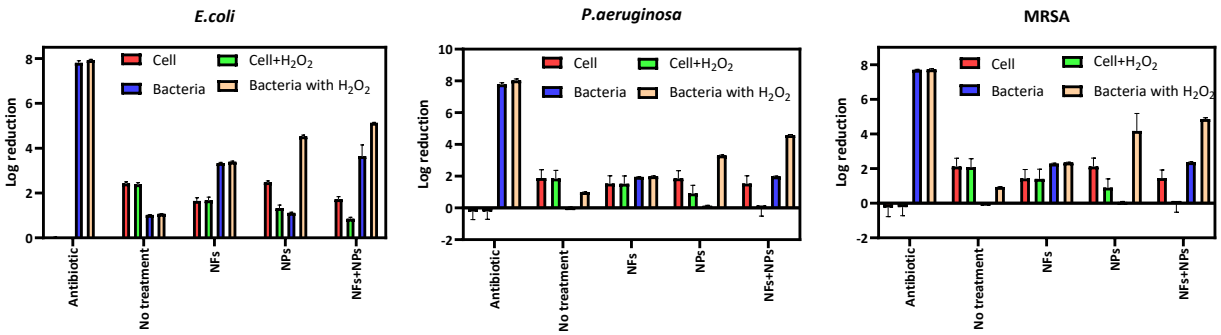

Figure 5-13 Log reduction in the number of bacteria and fibroblasts in different conditions in the presence and absence of H2O2: cocktail of antibiotics, No treatment, NFs, NPs, and NFs+NPs.

5.4 Conclusions

The development of theranostic dressings, particularly those with colorimetric signaling capabilities, is of critical importance for advancing wound care. These smart dressings not only provide real-time feedback on infection status but also enable timely intervention by signaling the presence of bacteria through visible color changes. This feature can assist healthcare providers, patients, and caregivers in monitoring wounds more effectively, reducing the need for invasive diagnostics or frequent dressing changes. In addition, the ability to combine diagnostic functions with therapeutic actions, such as the targeted release of antibiotics, enhances treatment efficiency and reduces the likelihood of prolonged infections or the development of antibiotic resistance. A theranostic dressing that offers both detection and treatment can significantly improve patient outcomes by ensuring timely and appropriate care.

In this study, we developed and evaluated a theranostic biosensor designed to detect bacterial infections, signal their presence via a visible color change, and release antibiotics in a controlled, ROS-responsive manner. Our results demonstrate the biosensor's potential for use in wound care, combining effective antibacterial action with biocompatibility.

The nanofibrous biosensors with a hemicyanin dye as a probe showed highly effective, color-changing properties, providing a clear and reliable visual signal in response to bacterial presence. The biosensor demonstrated excellent compatibility with different wound dressing foams and cleaning solutions, maintaining its colorimetric response without interference. Additionally, its performance remained accurate under various conditions, such as the presence of salts and proteins typically found in wound environments. Importantly, no false positives were observed, even in the presence of these complex biological materials, ensuring the biosensor's reliability in detecting infections and its robustness for practical clinical applications.

For the therapeutic part of the theranostic biosensors, the ROS-responsive NPs, based on PEG-PPS, showed stable encapsulation of CIP and a triggered release mechanism upon exposure to oxidative conditions, such as the presence of H_2O_2 with less than 20% release in the absence of ROS. This triggered release for 80% of the loaded drug was confirmed by significant increases in bacterial log reduction and ZOI when H_2O_2 was introduced, indicating that the system can prevent untargeted drug release and thereby reduce the risk of bacterial resistance. The combined action of citric acid and CIP-loaded NPs further enhanced antibacterial efficacy, as demonstrated by higher log reductions for MRSA, *P. aeruginosa*, and *E. coli* compared to the use of either agent alone.

Cytocompatibility tests confirmed that the biosensors, both with and without NPs, maintained fibroblast viability at over 90%, with no significant cytotoxicity observed even after a complete release of CIP over three days. The co-culture experiments demonstrated that the biosensor's antibacterial properties did not compromise fibroblast health, showing significant reductions in bacterial load while allowing fibroblasts to remain viable and, in some cases, proliferate.

Overall, the theranostic biosensor developed in this study offers a promising solution for managing wound infections. It effectively eliminates bacteria through a combination of ROS-triggered antibiotic release and citric acid's pH-altering properties while preserving cell viability. The ability to control antibiotic release in response to ROS not only reduces the risk of prolonged antibiotic exposure and resistance but also ensures targeted treatment in infected areas. This dual-action biosensor could be a valuable tool for improving outcomes in wound healing and infection management.

5.5 Supporting Information

The supplementary data provides additional insights into the performance and characterization of the developed systems. It includes color-changing figures of the biosensors in various solutions, illustrating their functionality under different conditions. The combability of the biosensor with different commercially available wound dressings both in the bench test and different bacteria tests are discussed in detail in the supporting information. Moreover, the effects of sterilization methods and wound cleaning solutions on the biosensors' performance are also examined. Furthermore, the data evaluates the water absorbency capabilities of different foam materials and the penetration of dye through these foams from the biosensors. Chemical characterization of the synthesized ROS-responsive polymer is presented, along with the fabrication steps for the nanoparticles. Additionally, the release behavior of the nanoparticles with different kinetic models applied to understand the mechanisms governing drug release are included.

5.6 CRediT Authorship Contribution Statement

Farinaz Jonidi Shariatzadeh: Writing – review & editing, Writing – original draft, Visualization, Validation, Methodology, Data Curation, Formal analysis, Conceptualization. . **Sarvesh Logsetty:** Writing – review & editing, Validation, Conceptualization. **Song Liu:** Writing – review & editing, Validation, Supervision, Methodology, Funding acquisition, Conceptualization.

5.7 Funding Sources

The authors appreciate and acknowledge the financial support from the MITACS Grant (IT30856) and ParaNano Wound Care, LLC, the Natural Sciences and Engineering Research

Council of Canada (NSERC) Discovery Grant (RGPIN-2019-06094), and the Canada Foundation for Innovation (award number: 23679).

6 Chapter 6: Targeted Delivery of Anti-Scar Drug

Enhanced Targeted Drug Delivery for Scar Prevention: Clathrin-Coated Solid Lipid Nanoparticles for Model Drug Encapsulation

Farinaz Jonidi Shariatzadeh[1], Vinith Yathindranath[2,6], Yang Liu[3], Donald W. Miller[2,6], Francis Lin[3], Sarvesh Logsetty[4] and Song Liu[1,5]*

1)Biomedical Engineering, Faculty of Engineering, University of Manitoba, Winnipeg, Manitoba, Canada, R3T 2N2

2) Department of Pharmacology and Therapeutics, University of Manitoba, Winnipeg, MB R3E 0Z3, Canada

3)Department of Physics and Astronomy, University of Manitoba, Winnipeg, MB R3T 2N2, Canada

4)Departments of Surgery and Psychiatry, Rady Faculty of Health Sciences, University of Manitoba, Winnipeg, Manitoba, Canada, R3E 3P5

5)Department of Biosystems Engineering, Faculty of Agricultural and Food Sciences, University of Manitoba, R3T 2N2

6)PrairieNeuro Research Centre, Rady Faculty of Medicine, University of Manitoba, Winnipeg, MB R3E 0Z3, Canada

* Correspondence to: song.liu@umanitoba.ca; +1) 204-474-9616).

Revised from the research article published in Adv. Therap. 2024, 7, 2400185. https://doi-org.uml.idm.oclc.org/10.1002/adtp.202400185
(https://onlinelibrary-wiley-com /doi/full/10.1002/adtp.202400185)

Contribution as the first author **Farinaz Jonidi Shariatzadeh:** Writing – review & editing, Writing – original draft, Visualization, Validation, Methodology, Data Curation, Formal analysis, Conceptualization, Project administration.

Abstract

Excessive scar formation is a major complication of wound healing. Premature release of anti-scarring drugs can negatively impact healing. This study aims to develop a targeted delivery system for the controlled release of anti-scarring drugs during the scar formation stage. We developed solid lipid nanoparticles (SLNs) coated with Clathrin, a cage-like protein, to prevent premature drug release. Insulin-like growth factor (IGF) was conjugated to the SLNs for targeted delivery via its affinity for connective tissue growth factor (CTGF), a protein overexpressed during scar formation. The IGF-Clathrin-SLNs exhibited a size of 300±20 nm and a zeta potential of 9.23±0.4 mV. *In vitro* studies demonstrated sustained release of the encapsulated drug- kynurenic acid; less than 10% of kynurenic acid was released within three days, while over 50% was released within 10 hours upon Clathrin removal using a surfactant at pH 8. Cellular uptake studies confirmed targeting efficacy. Fibroblasts with low CTGF expression displayed low uptake (<10%), whereas MCF7 cells with high CTGF expression showed significantly higher uptake (80%). This work demonstrates a promising targeted delivery platform for the controlled release of anti-scarring drugs during scar formation.

Keywords: scarless healing; targeted delivery; nanoparticles; triggered delivery; premature release

Graphical abstract:

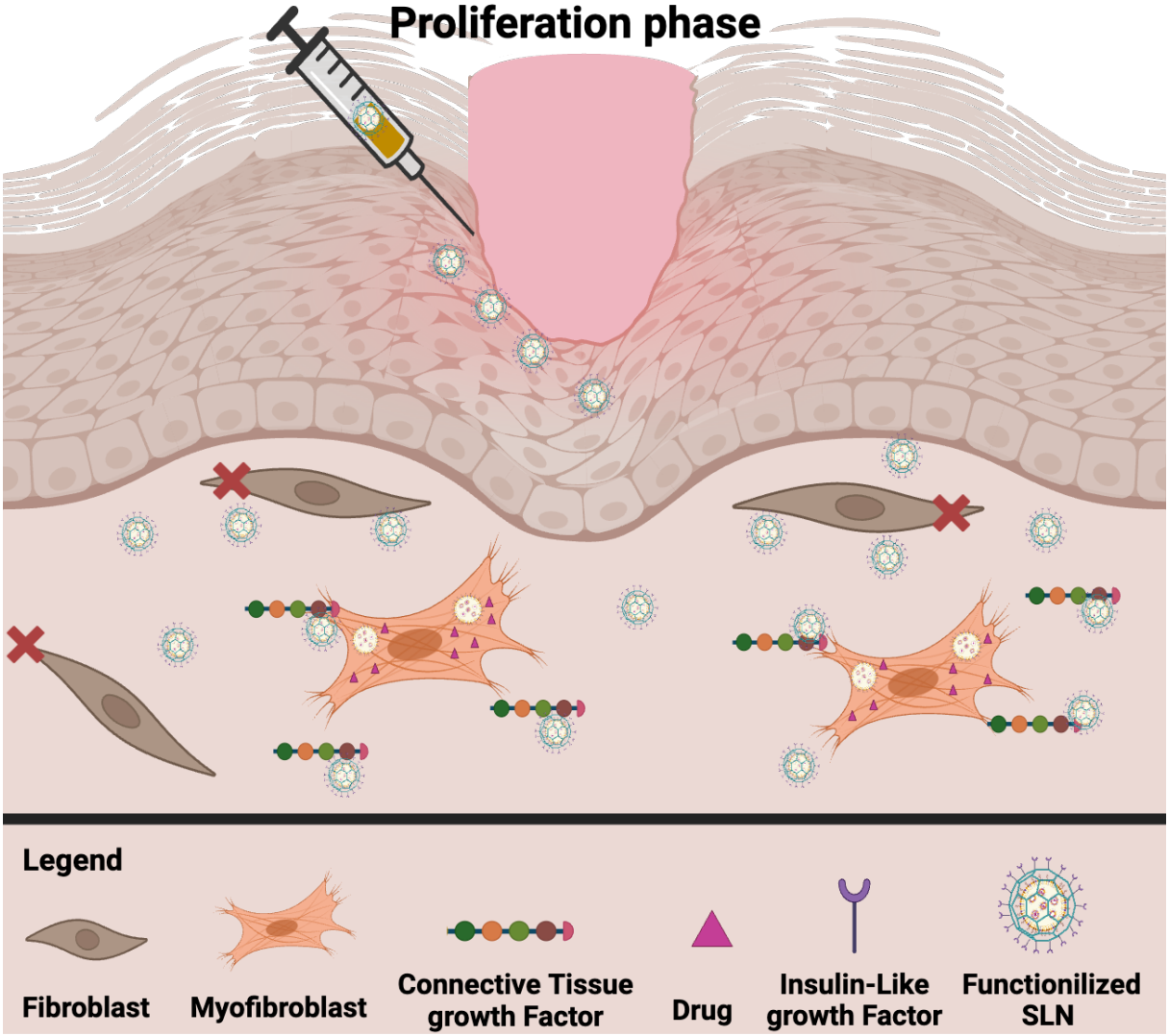

Created with BioRender.com

6.1 Introduction

Adult skin wound healing is a complex process requiring a delicate balance between rapid restoration of the skin's protective barrier and the prevention of excessive scar formation. An overactive healing response can lead to pathological scarring, which is marked by increased patient discomfort, restricted mobility, and elevated healthcare costs [52,384]. Myofibroblasts are one of the primary cells responsible for scar formation during wound healing. These cells contribute to wound closure and contraction. Moreover myofibroblast can influence surrounding cells through both direct interactions and the secretion of extracellular matrix (ECM) components, including collagen, growth factors, and cytokines [3]. However, an overabundance of myofibroblasts at the injury site can lead to excessive collagen production, resulting in scar formation [385,386].

In contrast to the "basket-weave" pattern of collagen fibers found in healthy skin, scar tissue has collagen fibers aligned parallel to the skin surface [387]. This parallel alignment, along with an increased collagen density and larger fiber size, distinctly differentiates scarred tissue from normal tissue [201]. During natural healing processes, enzymes such as matrix metalloproteinase (MMPs) break down temporary parallel collagen scaffolds, allowing for the replacement with a "basket-weave" collagen pattern [388]. However, in severe wounds with elevated collagen content, MMPs activity may be insufficient to replace the random temporary collagen scaffolds leading to the formation of rigid scar tissue [52,389].

Despite advancements in wound management, including surgery, pressure therapy, and stem cell interventions, scarless healing remains an unmet clinical need. Developing innovative drug delivery systems to modulate enzymatic activity and collagen synthesis presents a promising avenue for scar reduction [390]. Current advancements in drug delivery systems for

scar prevention are centered around using nano/microcarriers for localized drug delivery, providing sustained release while reducing the need for frequent wound dressing changes [89,391]. For example, Ghahary's group [392] developed a microcarrier system using poly(lactic-co-glycolic acid) (PLGA) and a diblock copolymer (methoxy polyethylene glycol-block-poly(D, L-lactide), MePEG-b-PDLLA) to control the release of kynurenic acid (KyA), an anti-scarring compound, for post-surgical wounds. Results showed that wounds treated with KyA-loaded microcarriers exhibited less fibrotic tissue and reduced collagen levels [392]. While sustained delivery of anti-scarring drugs offers a promising approach, the therapeutic application of these agents during wound healing poses significant challenges due to potential adverse effects on newly formed tissue, particularly the collagen matrix [391]. These drugs often increase the activity of enzymes that degrade the ECM, such as MMPs, which can disrupt the healing process if released prematurely during critical stages like inflammation and early proliferation [263,390,393]. Thus, a targeted drug delivery system capable of precisely delivering anti-scarring therapeutics at the appropriate stage of wound healing is essential to mitigate adverse scar formation [391,394].

Scar formation typically initiates in the mid-proliferation stage, characterized by elevated levels of biomarkers such as transforming growth factor (TGF-β) and connective tissue growth factor (CTGF), and the differentiation of fibroblasts into myofibroblasts [3,389,395–398]. To effectively reduce scarring, the therapeutic interventions must target biomarkers exclusively expressed during this phase, avoiding interference with other stages of the repair process. CTGF meets this criterion as it is significantly overexpressed during scar formation. CTGF contains four main domains, including an insulin-like growth factor binding protein (IGF-BP) domain, which has a specific affinity for binding to insulin-like growth factors (IGF) [399] (**Figure S10-**

1). The IGF-BP domain may be exploited for the specific targeting of drug-loaded carriers to CTGF.

Given that CTGF is an ECM protein, targeting therapeutic agents to this molecule offers a dual benefit: enhancing carrier stability within the wound environment and promoting cellular uptake by myofibroblasts. Although specific CTGF receptors have not been definitively identified, various pathways, such as integrin binding and epidermal growth factor receptor (EGFR) endocytosis, can facilitate the targeting of myofibroblast via CTGF. This strategy presents a promising approach for delivering therapeutic agents directly to myofibroblasts, thereby inhibiting scar formation [400–402].

In the field of skin drug delivery, solid lipid nanoparticles (SLNs) have gained prominence because of their unique structures and ability to penetrate both epidermal and dermal layers [403]. The successful development of drug delivery systems based on SLNs necessitates meticulous formulation and optimization to achieve optimal loading capacity, efficiency, and particle size tailored to specific therapeutic applications [404]. Various fabrication methods for SLN fabrication include high-pressure homogenization, hot/cold homogenization, solvent emulsification/evaporation, microemulsion, solvent injection, and microfluidic techniques, with the choice of method dictated by the application's specific needs [405,406]. In our research, we utilized solvent injection and microfluidic techniques to develop SLNs for skin wound treatment, with a focus on optimizing particle size and loading efficiency. To address the challenge of premature drug release, we incorporated a Clathrin cage that disassembles post-endocytosis, thereby protecting the drug until it reaches the intracellular environment for release [407].

For this study, we used KyA as a model anti-scarring drug to demonstrate the system's effectiveness. We evaluated the cellular uptake of our specifically designed SLNs in two

different cell types: human fibroblasts with low CTGF expression and MCF7 breast cancer cells, which serve as a model for a cell with high CTGF expression [408,409]. Our findings revealed a significantly higher uptake of the functionalized SLNs in cells with elevated CTGF expression. Moreover, we conducted *in vitro* release experiments to evaluate the efficacy of Clathrin coatings in minimizing premature drug release. The Clathrin-coated SLNs significantly reduced the initial burst release by a factor of six.

6.2 Results and Discussion

6.2.1 Clathrin Extraction and Characterization

Clathrin extraction from pig brain tissue involved a sequential tissue homogenization process, buffer exchange, and ultracentrifugation [407]. The yield from pig brain tissue was determined to be 10 mg/kg of wet tissue. Following extraction, the concentration of Clathrin was assessed using the Bradford assay (**Figure 6-1A**) to be 0.92 mg/mL (1.39 mg) based on a standard curve of Bovine Serum Albumin (BSA).

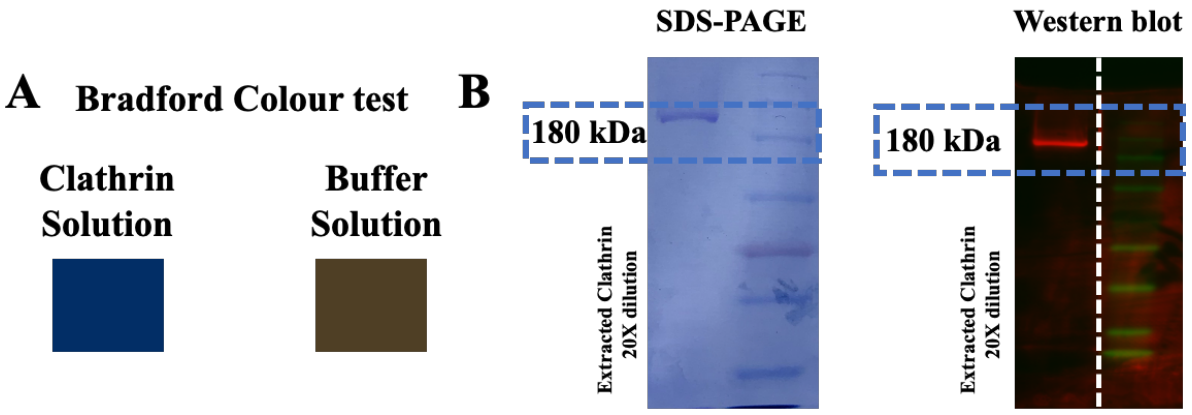

Figure 6-1 Clathrin extraction characterizations: A) Bradford colorimetric assay results for the purified Clathrin solution and the buffer solution without proteins. B) SDS-PAGE and Western blot images (8.0% gel) showing bands at 180 kDa (heavy chain of Clathrin) for 20X diluted extracted Clathrin compared to the Prestained Protein Ladder (10–245 kDa). The Western blot images were from the same membrane but have been cropped.

Clathrin extraction was further investigated by SDS-PAGE and Western blot, and Clathrin heavy chain, with a molecular weight of 180 kDa, was detected in both SDS-PAGE and Western blot results (**Figure 6-1B**), indicating successful extraction. The extracted Clathrin was used in future steps for coating SLNs to prevent premature release of the drug from the system.

6.2.2 SLNs Fabrication and Characterization

6.2.2.1 Fabrication

The SLNs were synthesized using ethanol injection and microfluidic techniques, with the goal of optimizing lipid composition, concentration, and flow rates to achieve maximum loading capacity (LC), efficiency (LE), and a particle size range of 200-300 nm conducive to effective skin penetration [410,411]. Three flow rates were initially selected—1.5, 8, and 12 mL/min—along with three lipid concentrations (4, 8, and 10 mg/mL) and four compositions (A-D). Preliminary assessments revealed that compositions A and C were unsuitable for microfluidic applications due to incomplete dissolution in ethanol at room temperature. Consequently, these compositions were excluded from further microfluidic processes. A total of 60 experimental runs were conducted, with some failing to result in the collection of SLNs. For instance, in the ethanol injection technique, high ethanol injection speeds (8 and 12 mL/min) led to the formation of a thin film rather than NPs, and sonication of this film produced micron-sized particles instead. Furthermore, no SLNs were collected after centrifugation in runs using a lipid concentration of 10 mg/mL or a flow rate of 1.5 mL/min using microfluidic techniques. For these experiments, the suspensions were concentrated by rotary evaporation and subsequently analyzed using transmission electron microscopy (TEM) to determine particle size. TEM analysis revealed that the particle sizes in these samples ranged from 10 to 50 nm.

Our response analysis (**Table S10-5** and **Figure S10-2**) revealed the interplay between formulation parameters (technique, low rate, lipid concentration, and composition) and their influence on SLN size, LE, and LC. According to the graphs and the equations derived from fitting the D-optimal Poisson quadratic model, it can be concluded that with the ethanol injection technique, the flow rate had an antagonistic effect on the size (nm) of SLNs, while lipid concentration had a synergistic effect. Specifically, increasing the flow rate reduced the size of SLNs across all compositions, whereas increasing the lipid concentration increased it. For the compositions A-D, the size ranges of SLNs fabricated with different flow rates and lipid concentrations were 30-270 nm (average: 99.5 nm), 40-1200 nm (average: 305 nm), 30-900 nm (average: 316 nm), and 10-700 nm (average: 147 nm), respectively.

However, the lipid concentration had an antagonistic effect on the microfluidic samples with compositions B and D, and the flow rate had a synergistic effect on the size of SLNs. This means that increasing the flow rate increased the size of SLNs while increasing the lipid concentration decreased it. For compositions B and D, the size ranges of SLNs fabricated with different flow rates and lipid concentrations were 10-60 nm (average: 30.3 nm) and 10-100 nm (average: 45 nm), respectively.

For LE, both flow rates and lipid concentrations had a synergistic effect for all compositions and techniques, leading to an increase in LE with higher values of these independent factors. The average LEs for ethanol injection for compositions A-D were 26.7±14%, 15.4±5.8%, 23.7±10.54%, and 16.5±5.96%, respectively. For the microfluidic technique, the LEs for compositions B and D were 17.7±10.5% and 34.8±26%, respectively. LC showed the same trend as LE, with all independent factors having a synergistic effect. The

average LCs for the ethanol injection technique for compositions A-D were 11.7±10.42%, 6.2±2.8%, 9.1±2.72%, and 6.1±1.44%, respectively, while for the microfluidic technique, they were 9.3±5.3% for composition B and 15.8±11.34% for composition D.

Considering the objectives of maximizing LE and LC while achieving a size in the 200-300 nm range, run 32 (ethanol injection, composition A, flow rate of 1.5 mL/hr, and lipid concentration of 10 mg/mL) was selected for functionalization and coating. This run demonstrated an LE of approximately 60% and an LC of around 40%.

6.2.2.2 Physicochemical Characterization

The morphology of the selected SLNs was assessed using negative staining and TEM. TEM images showed a spherical morphology for all fabricated SLNs, as illustrated in **Figure 6-2A-B**. The diameters of both the SLNs and the SLNs-KyA were measured from TEM images (n>30). The average diameter of the SLNs-KyA was 262 ± 66 nm, as shown in **Figure 6-2C**. Notably, there was no statistically significant difference in the size and distribution between the SLNs (250 ± 23 nm) and the SLNs-KyA (*p-value*=0.55).

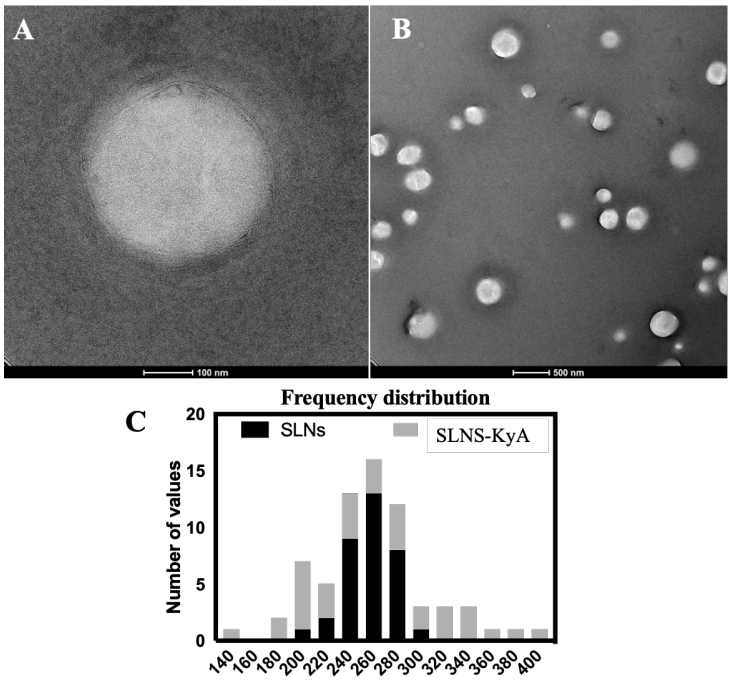

Figure 6-2 TEM images of SLNS with two magnifications (A and B) and C) SLNs diameter distribution without and with drug (SLNs-KyA) n>100.

The hydrodynamic diameter of the SLNs, measured using dynamic light scattering (DLS), was found to be 290 ± 40 nm, consistent with the findings from TEM analysis. Additionally, the zeta potential of both SLNs and SLNs-KyA was measured with values of 13.4 ± 1.1 mV and 11.5 ± 1.2 mV, respectively. These values align with previous studies utilizing a similar lipid composition [412]. The observed reduction in zeta potential for SLNs-KyA may be attributed to the negative charge of KyA at physiological pH (pH = 7.4, PBS), suggesting potential drug deposition on the SLNs' surface.

The chemical composition of the SLNs-KyA was analyzed using Fourier-transform infrared spectroscopy (FTIR). **Figure S10-3** displays the spectra of lipids, the drug (KyA), and SLNs-KyA. Characteristic KyA peaks at 1631, 1595, 1415, and 1247 cm^{-1} corresponding to

stretching of C=O, asymmetric stretching of COO, symmetric stretching of COO, and stretching of C-N, respectively, were present in the SLN-KyA spectrum. The presence of these KyA-specific peaks indicates successful drug loading within or adsorption onto the surface of the SLNs. Notably, the absence of a peak at 3474 cm^{-1} suggests potential hydrogen bonding interactions between the drug and lipids. The SLNs-KyA spectrum also exhibited characteristic peaks of lipids, with additional details provided in the Supporting Document.

The thermal properties of SLNs-KyA were evaluated using differential scanning calorimetry (DSC). **Table S10-6** presents the melting points of various lipids and the drug, and **Figure S10-4** displays the DSC thermogram, highlighting distinct peaks and varying enthalpies. According to the literature, interactions between lipids and lipids/drugs can alter enthalpy and melting temperature. The shifts in endothermic melting points observed in the SLNs-KyA thermogram may be attributed to the dispersion state of lipids, drug incorporation, particle size, and the surfactant used [413]. Moreover, the presence of the drug can lead to increased surface energy and surface area, as well as defects in the crystalline lattice, contributing to a decrease in melting point and enthalpy [414]. These factors likely account for the observed differences in peaks and shifts in SLNs-KyA compared to bulk lipids. Furthermore, the decrease in enthalpy for the drug peak suggests that a significant amount of the drug was dissolved in the lipid phase during fabrication [413], which can facilitate sustained release in the SLN structure post-formation.

The LC and LE of the SLNs-KyA were evaluated by lysing the SLNs. Despite the relatively low loading capacity, the system remains viable, assuming the majority of the drug is released at the target site within the desired timeframe. The fabricated SLNs demonstrated an LC of 40 ± 5%, with an LE of 60 ± 7%.

The drug release profile from SLNs was assessed at 37 ˚C with constant shaking over 72 hours by dialyzing technique, **Figure 6-3A**. A standard curve for KyA was established to analyze the drug's release behavior from SLNs. The release profile exhibited two distinct phases. In the initial phase, lasting approximately 40 hours, 50% of the total drug was released, likely due to water diffusion. This phase can be described by both the Higuchi model (**Figure 6-3B**), which explains time-dependent drug release from a hydrophilic matrix based on Fick'ss diffusion law, and the Korsmeyer-Peppas model (**Figure 6-3C**), which accounts for both water/drug diffusion and particle erosion. In cases of anomalous transport, drug release is influenced by both Fickian diffusion and the swelling and relaxation of the drug delivery system matrix. The data from fitting these two models to the release kinetics are summarized in **Figure 6-3D**. Neither the zero-order nor the first-order models provided an acceptable fit ($R^2 < 0.95$). The latter phase of drug release, occurring after 48 hours, was attributed to the disassembly of the SLNs, resulting in a burst release that led to the release of nearly all the remaining drugs (**Figure 6-3A**). This disassembly of SLNs after 48 hours was also confirmed by the SEM image (**Figure 6-2A**).

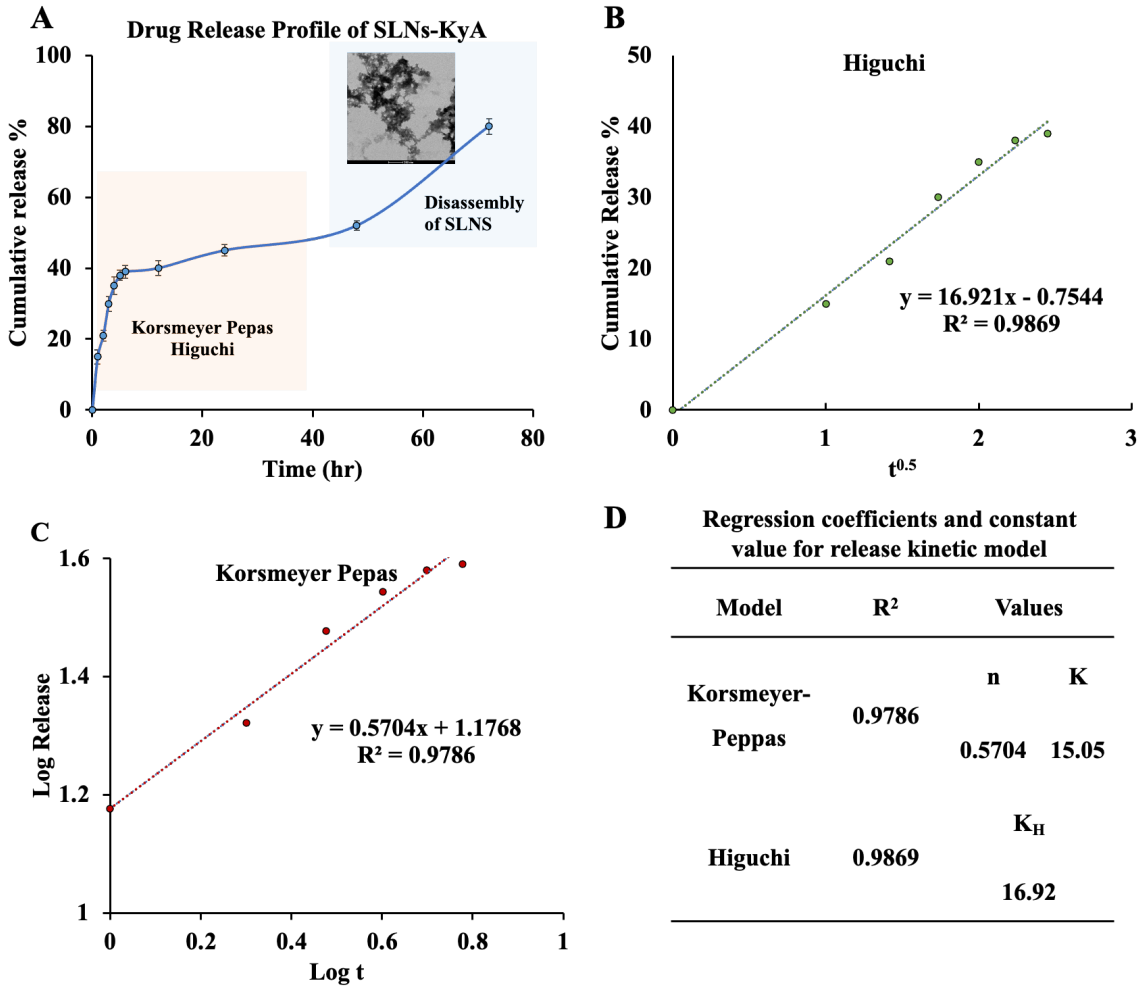

Figure 6-3 Drug-related behavior: A) The release profile of the drug(KyA) from SLNs within 72hrs (n=3) and SEM image of disassembled SLNs (scale bar 200 nm). B) Higuchi Model fitting, C) Korsmeyer-Peppas fitting, and D) regression coefficients for the release kinetics.

6.2.3 SLNs Coating and Functionalization

6.2.3.1 SLNs Coating with Clathrin:

The issue of premature drug release and the stability of SLNs was mitigated by implementing a protective cage named Clathrin. Drug release from SLNs typically occurs due to water penetration, which leads to increased internal pressure and subsequent ejection of the drug

from the lipid layers. Clathrin, as a cage protein, counteracts this pressure increase, inhibiting SLN expansion and preventing premature drug release into the surrounding media [407].

After successful Clathrin extraction, this cage protein was used *in vitro* to coat SLNs. Two methods were employed to reassemble the cage protein on the surface of SLNs. The first method involved biomimetic assembly, requiring a conducive surface (such as a Golgi-like lipid structure), cytosolic components, ARF1 (a GTP-binding protein), adaptor proteins, and GTP. The second method involved using different buffers with chelating agents [415]. However, the purification steps of cytosol for the biomimicking technique pose a limitation, as the extracted cytosol might lack essential recruiting proteins. TEM images obtained after attempting biomimetic assembly with the synthetic buffer confirmed the absence of coating (**Figure 6-4B**), indicating that critical components such as ARF1 and AP-1 were missing. Consequently, the metal ions (chelating) assembly approach was adopted as an alternative [415,416]. The effectiveness of Clathrin cage assembly without biomimicking *in vivo* conditions depends on three factors1) The presence of Ca^{2+}, 2) the presence of heat-labile agents like protease inhibitors (PMSF), and 3) the presence of a polypeptide chain known as fraction II (110 kDa).

The chelating assembly process was conducted using three distinct buffers, each affecting Clathrin reassembly differently based on its final composition. Buffer #2 facilitates reassembly only if Fraction II is present in the structure of the extracted Clathrin independent of the Ca^{2+}, relying solely on the crosslinker protein. However, reassembly in the presence of buffers #1 and #3 occurs even without Fraction II. In these buffers, Ca^{2+} binds different chains, enhancing reassembly efficiency. Notably, buffers #1 and #3 differ in the presence of a heat-labile agent (PMSF), contributing to a more efficient reassembly process.

All reassembly experiments were conducted using the dialyzing technique, and TEM images of uncoated and coated SLNs using various methods are presented in Figure **6-4A-E**. TEM image analysis and Bradford assay measurements (**Figure 6-4F**) indicated that Fraction II was present in the Clathrin extraction but at insufficient concentrations for complete coating, with only 50% of the Clathrin used for coating in buffer #2. In contrast, the addition of Ca^{2+} in buffer #3 significantly enhanced the crosslinking of the chains, resulting in 80% of Clathrin being utilized for coating. The presence of PMSF further increased coating efficiency by 60% compared to buffer #1. Consequently, buffer #3 was selected as the optimal environment for Clathrin assembly on SLNs.

The coated SLNs were centrifuged to remove unreacted Clathrin, followed by dialysis to eliminate excess salts. The purified coated SLNs (C-SLNs) were analyzed using Bradford dye and SDS-PAGE to confirm the presence of protein, as depicted in **Figure 6-4G-H**. For SDS-PAGE, the assembled cage on SLNs could not migrate through the gel. Therefore, Triton X-100 was used to disassemble the SLNs, and Clathrin was disassembled by a Tris buffer at pH 8.0. The appearance of the same band at 180 KDa in coated samples confirmed successful coating. The Bradford assays exhibited a discernible color change for coated SLNs, verifying protein presence even after rigorous washing of the pellet. TEM images of samples treated in buffer #3, which led to coating, were used to measure the sizes of both SLNs and the coating. The core (SLNs) had an average size of 239 ± 13, while the shell (coating) measured 33 ± 6. Notably, Clathrin-coated SLNs exhibited no significant difference in size compared to untreated SLNs (*p-value* = 0.13), indicating that the coating process preserved SLN morphology and size.

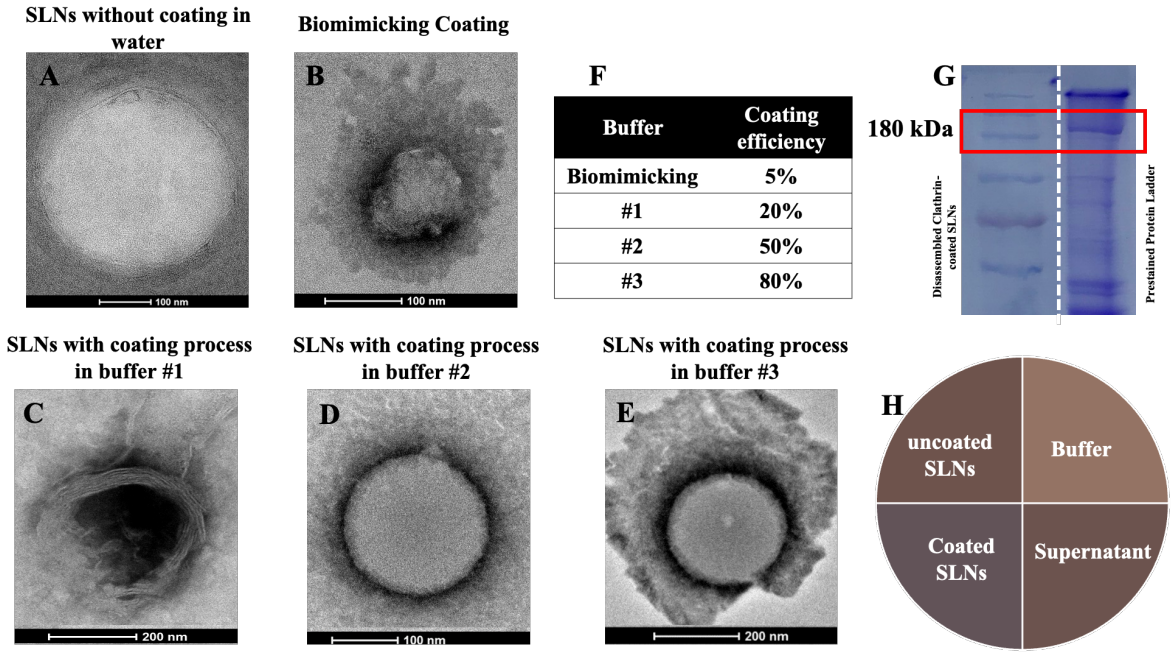

Figure 6-4 TEM images of uncoated SLN (A) and coated SLNs in different buffers (B-E). F) Coating efficiency is calculated based on the presence of protein. G) the presence of Clathrin in SDS-PAGE of Clathrin-coated SLN (8.0% gel). SDS-PAGE images were from the same membrane but have been cropped. and H) color difference (Bradford Dye) of coated suspension with uncoated suspensions and buffer without SLNS,

6.2.3.2 Functionalizing The Coated SLNs with IGF

To effectively target the critical window of scar formation, we identified the extracellular biomarker CTGF, which is markedly overexpressed during this stage and can bind to an IGF. The surface of the Clathrin-coated SLNs was functionalized with IGF to serve as a targeting moiety for the specific delivery of the antiscar drug. The IGF functionalized Clathrin coated SLNs loaded with KyA drug (IC-SLNs-KyA) were characterized using DLS and a zeta sizer to evaluate the size and charge variations resulting from coating and functionalization. The results presented in **Table 6-1** demonstrate that coating and functionalization did not impact the size or distribution of the SLNs. No significant differences were observed in the size and diameter of SLNs-KyA, C-SLNs-KyA, and IC-SLNs-KyA. In terms of the zeta potential, the coating

treatment resulted in a slight decrease in the zeta potential (approximately 3.5 mV) due to the negative charge of the Clathrin protein. However, the difference between the functionalized sample (IC-SLNs-KyA) and the coated sample (C-SLNs-KyA) was insignificant, indicating that IGF functionalization did not alter the surface charge.

Furthermore, introducing IGF was expected to elevate the protein content in the samples. As depicted in **Figure S10-5**, the results of the Bradford assay confirmed the successful IGF functionalization with a substantial increase in protein concentration—approximately 30-fold for C-SLNs-KyA and 80-fold for IC-SLNs-KyA—compared to untreated SLNs (SLNs-KyA) without functionalization or coating.

Table 6-1 Hydrodynamic diamtere and zeta poteintial of samples.

Name	HD (nm)	Zeta Potential mV	PDI
SLNs-KyA	290±40	11.5±1.4	0.25
C-SLNs-KyA	270±16	7.93±0.6	0.29
IC-SLNs-KyA	300±19	9.23±0.4	0.26

The drug release behavior of the IC-SLNs-KyA was assessed using the same protocol as for SLNs. As depicted in **Figure 6-5A**, the Clathrin cage effectively mitigated premature drug release, with less than 10% of the drug being released within the initial 72 hours. Following the disassembling of the Clathrin cage by introducing Tris and Triton X-100 and adjusting the pH from 7.4 to 8.0, a sustained release profile was observed, which conformed well to the Higuchi and Korsmeyer-Peppas models, **Figure 6-5B-D**. The difference in the *n* value of the Korsmeyer-Peppas model between SLNs-KyA (n=0.57) and IC-SLNs-KyA (n=0.48) suggested structural alterations in the coated SLNs that contributed to the prevention of premature drug release. A

value of $n < 0.5$ indicated that the drug release was primarily diffusion-based following the disassembly of the coating. The sustained drug release from SLNs after Clathrin cage disassembly was observed over a period of 3 days, with 50% of the drug being released within the first 10 hours.

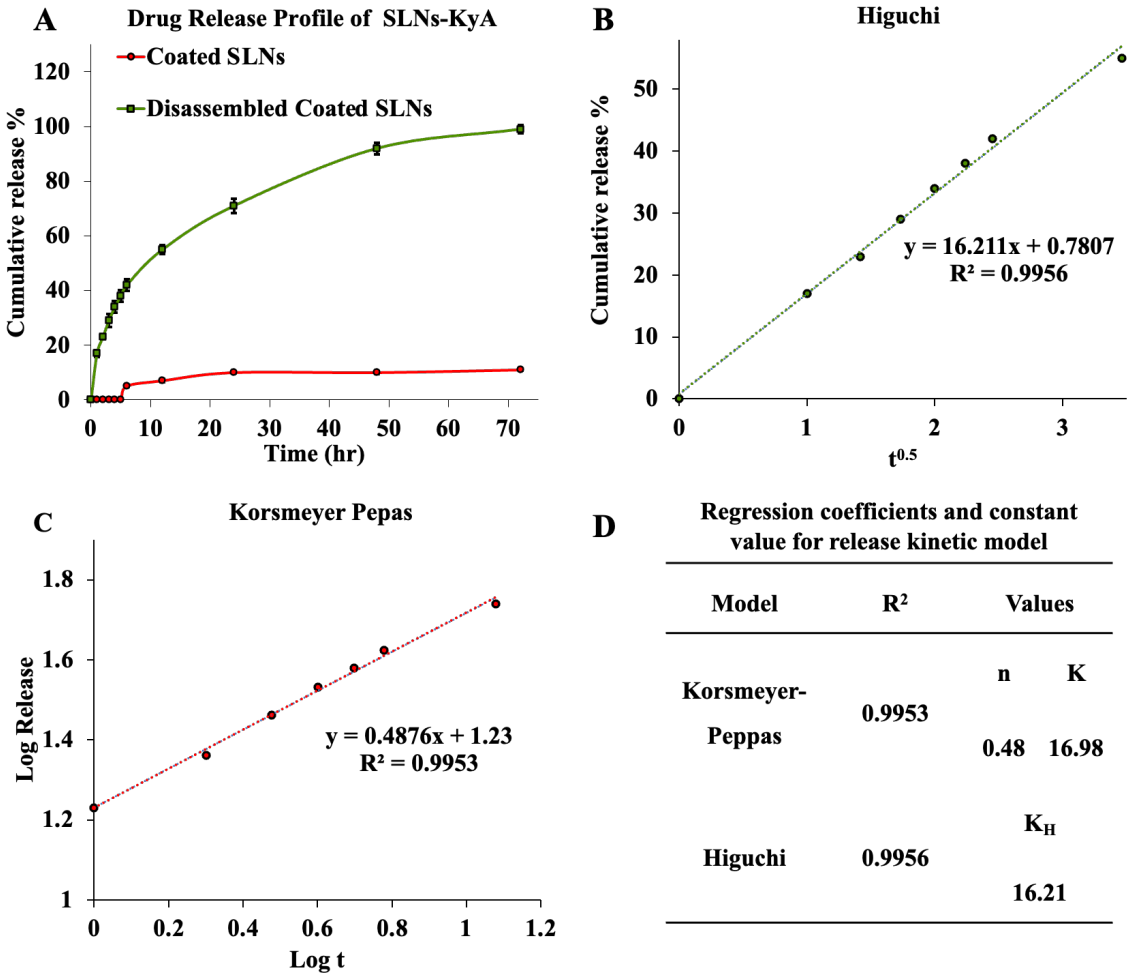

Figure 6-5 Drug-related behavior: A) The release profile of the drug (KyA) from coated SLNs and disassembled Clathrin SLNs (n=3) within 72hrs (n=3). B) Higuchi Model fitting, C) Korsmeyer-Peppas fitting, and D) regression coefficients for the release kinetics

.

The stability of IC-SLNs-KyA was evaluated after three months of storage as freeze-dried samples at 4°C. Analysis showed that the morphology of stored IC-SLNs-KyA remained consistent with fresh IC-SLNs-KyA, with no changes in size (295 ± 10 nm based on DLS) and charge (9.53 ± 0.3 based on zeta potential) after resuspension in PBS (physiological pH 7.4) at room temperature. The *p-value*, when compared to fresh samples, was greater than 0.05. Furthermore, the release behavior in PBS at pH 7.4 was similar to that of freshly prepared samples, with less than 10% release over 72 hours, indicating a stable coating. When the coating was disassembled by increasing the pH to 8.0 and adding Tris and Triton X-100, more than 60% of the KyA was released within the first day.

Additionally, resuspended IC-SLNs-KyA in PBS (pH 7.4) were kept for 5 days, during which their charge and size were evaluated using DLS and a zetasizer and compared to SLNs-KyA. A slight increase in the charge of IC-SLNs-KyA suspended in PBS for 5 days was observed compared to freshly prepared IC-SLNs-KyA (10.02 ± 0.5 and 9.23 ± 0.4, respectively); however, the *p-value* was greater than 0.05, indicating the changes were not significant. The same trend was observed for the size (310 ± 4 nm). These data indicate that IC-SLNs-KyA are stable under physiological conditions. Notably, for SLNs-KyA, after 5 days of suspension in PBS, almost no nanoparticles were observed, and no size or charge could be measured, indicating that the SLNs were fully disassembled.

6.2.4 Cellular Assays

6.2.4.1 Cytotoxicity

The cell viability of fibroblasts was evaluated over 24 hours using various concentrations of free drug, blank SLNs, SLNs-KyA, C-SLNs-KyA, and IC-SLNs-KyA (0, 1, 2, 5, 10, 50, and

100 µg/mL), as shown in **Figure S10-6**. The blank SLNs showed no significant reduction in cell viability, even at the highest concentration (100 µg/mL), demonstrating biocompatibility with over 90% cell viability. KyA is known to inhibit fibroblast proliferation, and even the lowest concentrations of free KyA (1 and 2 µg/mL) significantly decreased cell numbers compared to the control (*p-value*<0.01) with a 10% reduction in cell viability. The viability of SLNs loaded with KyA (LC 40%) was similar to that of free drugs at the same concentrations. For example, 5 µg/mL SLNs-KyA (containing 2 µg/mL KyA) and 2 µg/mL free KyA both showed viability rates of 92 ± 0.5% and 90 ± 1.5%, respectively, with a *p-value* of 0.44. However, incorporating a clathrin coating improved viability by preventing premature drug release. For instance, at 100 µg/mL C-SLNs-KyA (comparable to 50 µg/mL free drug), the viability of clathrin-coated drug-loaded SLNs was 82 ± 2%, while for free KyA was 68 ± 3% (*p-value* = 0.003). Notably, there was no significant difference in cell viability between the blank SLNs and IC-SLNs-KyA at any concentration, indicating that the functionalized SLNs were not taken up by the cells. Based on these findings, an SLN concentration of 2 µg/mL was selected for a week-long viability and proliferation assay to evaluate the sustained release impact of KyA on fibroblast viability and proliferation. This concentration was chosen because it was the lowest at which blank SLNs and IC-SLNs-KyA showed no significant difference regarding fibroblast viability, while SLNs-KyA and IC-SLNs-KyA exhibited significant differences without being cytotoxic. This indicates that successful targeted delivery of KyA would effectively alter the behavior of the targeted cells. Therefore, the cytotoxicity of SLNs-KyA, C-SLNs-KyA, and IC-SLNs-KyA (2 µg/mL) was assessed over a one-week period on fibroblast cells. As represented in **Figure 6-6A**, SLNs-KyA, C-SLNs-KyA, and IC-SLNs-KyA showed high cell viability on day one with 84%, 87%, and 91%, respectively. The viability on days 3 and 7 for all three samples was also higher than 85%,

indicating that the viability of cells was high during the week with no significant differences for each sample over a week (*p-value*> 0.5). To effectively minimize scar formation and promote wound healing, KyA must selectively target myofibroblasts to reduce their proliferation without adversely affecting the general fibroblast population [417–419]. This necessitates targeted delivery of KyA from SLNs to prevent premature release and off-target effects on fibroblasts. A one-week proliferation was employed to determine if the developed IGF-functionalized Clathrin-coated KyA-loaded SLNs prevented fibroblast uptake. We investigated the impact of drug-loaded SLNs on fibroblast proliferation with and without Clathrin coating and IGF functionalization. Given KyA's nature, its internalization is expected to reduce fibroblast proliferation. Successful targeting would result in no decrease in fibroblast proliferation, indicating no uptake of IGF-C-SLNs-KyA. **Figure 6-6B** shows that IC-SLNs-KyA maintained the same proliferation rate as the control (no treatment) with no statistically significant difference, confirming that fibroblasts did not internalize the nanoparticles. This indicates successful targeting to prevent fibroblast uptake. In contrast, C-SLNs-KyA and SLNs-KyA showed decreased proliferation, indicating drug delivery to fibroblasts and subsequent internalization influenced their behavior. These results suggest that IC-SLNs-KyA is biocompatible, and that coating and functionalization achieved targeted delivery, preventing uptake by fibroblasts with low CTGF expression. The differences in proliferation rates between the control and IC-SLNs-KyA were not significant (*p-value* > 0.05), but significant differences were found between IC-SLNs-KyA and both SLNs-KyA and C-SLNs-KyA (*p-value* < 0.05). Interestingly, Clathrin coating initially resulted in the same fibroblast proliferation rate as the control and IC-SLNs-KyA for up to two days. However, after an initial burst release of the drug, a decline in proliferation was observed. These outcomes illustrate that the coating effectively

prevented premature drug release, and that functionalization successfully prevented undesired cellular uptake, achieving the primary objectives of this project.

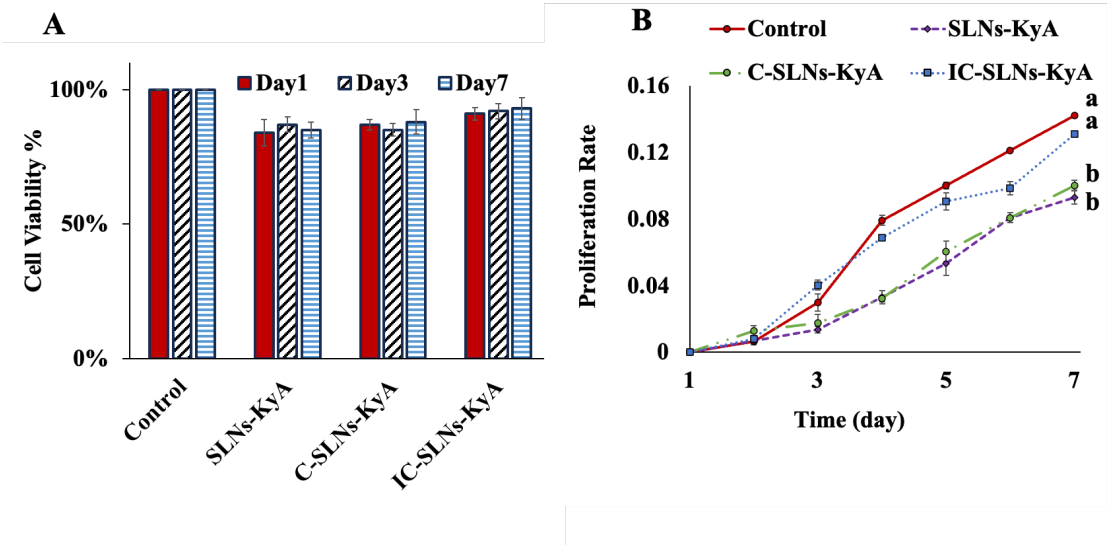

Figure 6-6 A) MTT cytotoxicity assay of samples with fibroblast over a week (n=5). B) Proliferation of fibroblast treated with different SLNs over a week. a and b indicate significantly different data (n=5) based on One-way ANOVA with posthoc Tukey.

6.2.4.2 Fluorescent Imaging (Cellular Uptake)

The targeted delivery system is engineered to prevent the uptake of IGF-functionalized Clathrin-coated FITC-loaded SLNs (IC-SLNs-FITC) by normal fibroblasts, given their low expression of CTGF. Conversely, MCF7 cells, characterized by their overexpression of CTGF, are expected to exhibit uptake in response to the designed targeting [420]. To track the uptake of these SLNs by the two cell types, FITC was encapsulated within the SLNs instead of the drug. As presented in **Figure 6-7A**, both cell types internalized non-functionalized SLNs (SLNs-FITC), and no statistically significant differences were observed (*p-value* > 0.05). DAPI and LysoTracker™ Deep Red staining revealed that the SLNs-FITC entered the cytosol (indicated by red and green fluorescence) but not the nucleus (indicated by blue fluorescence). Following functionalization, it was observed that IC-SLNs-FITC was exclusively taken up by MCF7 cells,

while fibroblast cells did not internalize the functionalized SLNs. These findings demonstrate the successful targeting of IC-SLNs-FITC, wherein only cells exhibiting a high expression of CTGF could uptake the functionalized SLNs. The IGF functionalization exhibits an affinity for binding to CTGF. This binding not only enhances the likelihood of SLN internalization through a specific pathway but also reduces the rate of SLN washout. Following the IGF-CTGF bind, facilitated by the IGF-BP domain on CTGF [399,421], there is an increased probability that SLNs will remain at the injury site and be internalized by the targeted cells.

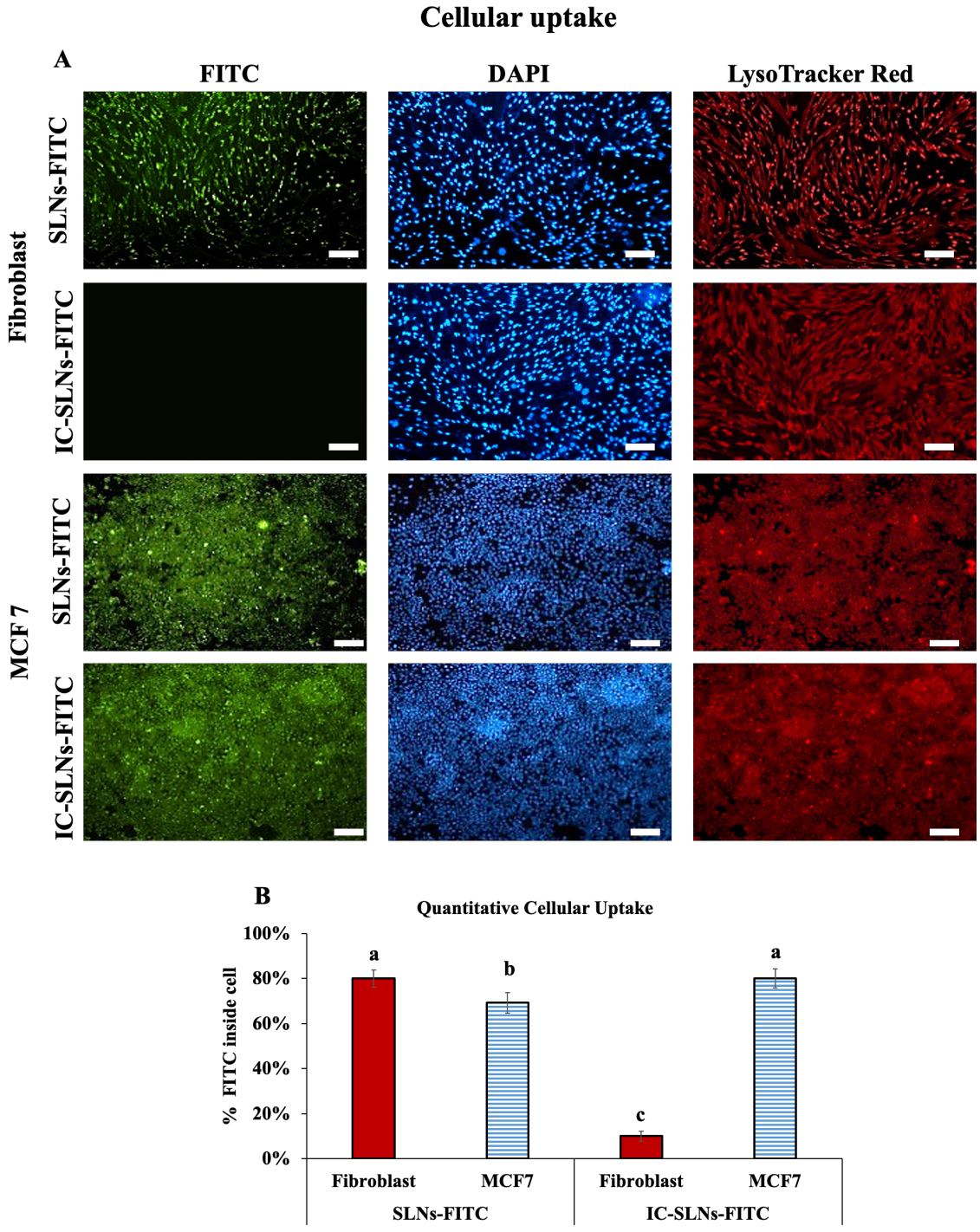

Figure 6-7 A) The fluorescent imaging of fibroblasts and MCF7 after treating for 24 hr with SLNS and functionalized SLNS (green: FITC, blue: DAPI and red: LysoTracker™ Deep Red), Scale bar=100 µm, B) Cellular uptake of FITC inside cells measured after lyzing cells. a, b, and c indicate significantly different data (n=5) based on One-way ANOVA with posthoc Tukey.

In addition to the qualitative assessment of FITC uptake, cellular lysis was performed, and the intracellular and supernatant FITC levels were quantified. As demonstrated in **Figure 6-7B**, SLNs-FITC facilitated significant FITC delivery to both cell types. The uptake of FITC was notably high in both cells, reaching 80% for fibroblasts and 70% for MCF7, with a statistically significant difference (*p-value* < 0.01), indicating a higher tendency for fibroblasts to uptake the SLNs. Conversely, IC-SLNs-FITC demonstrated a low uptake by fibroblasts, resulting in less than 15% released FITC attributed to the targeting moiety (IGF), indicating that the internalization of IC-SLNs-FITC in the absence of the targeting growth factor (CTGF) is not facilitated. The IC-SLNs-FITC were effectively internalized by MCF7, leading to FITC release within the cells. This successful targeting was reflected in the uptake of IC-SLNs-FITC, which was 10% higher than the uptake of SLNs-FITC by MCF7 (*p-value* < 0.01), emphasizing the enhanced uptake due to targeting. The increased internalization may also be associated with a higher availability of SLNs in the area following their binding to CTGF.

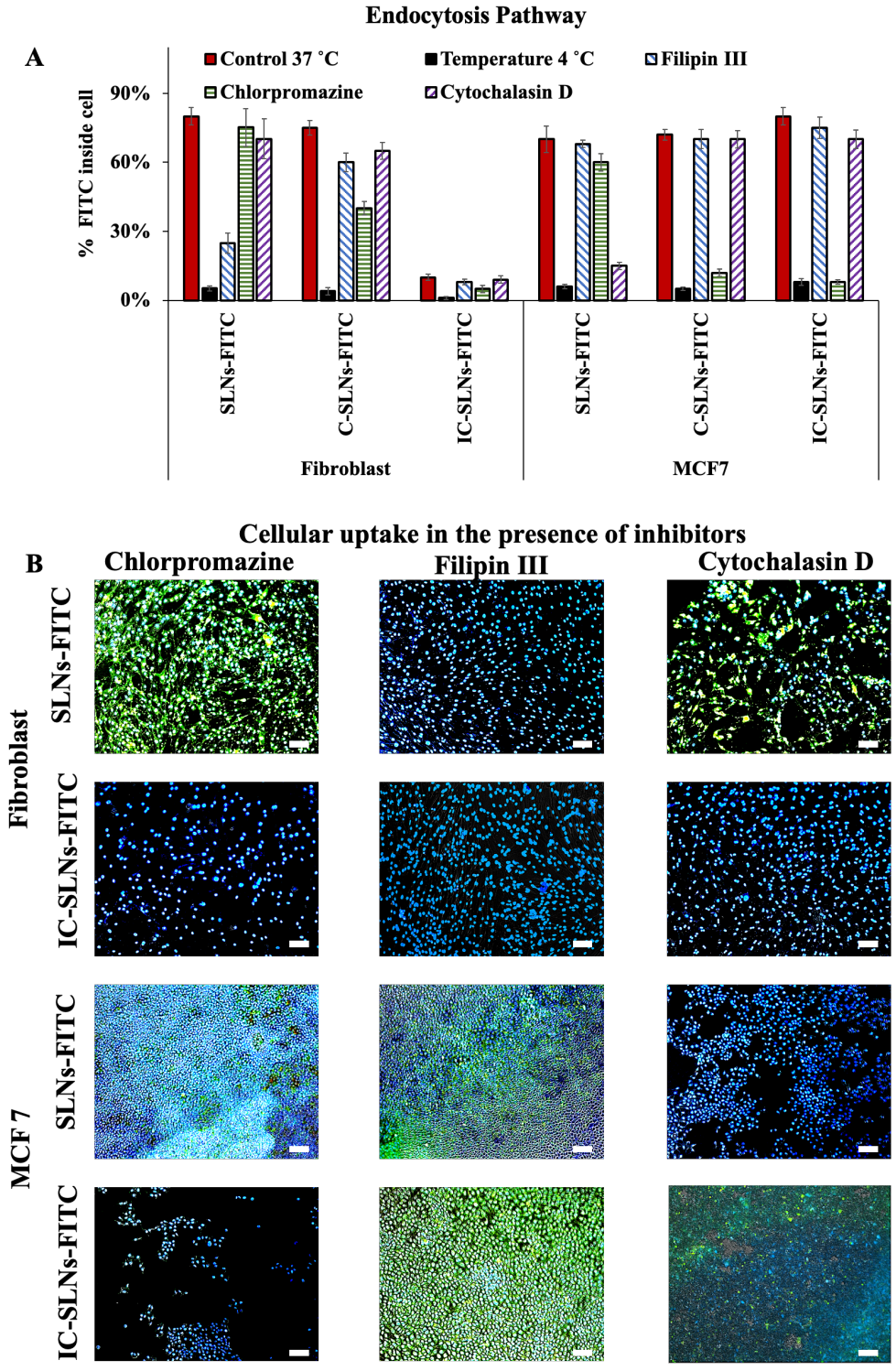

Figure 6-8 A) Endocytosis pathway, uptake of FITC loaded samples in fibroblasts and MCF7 in the presence of different inhibitors, n=5. B) Fluorescent images of cellular uptake in the presence of inhibitors for both cell types. The green shows the uptaken SLNs and the blue shows the nucleus. The absence of green means no uptake happened, Scale bar=100 µm.

6.2.4.3 Endocytosis Pathway

Energy-dependent internalization was tested to indicate which pathway is the dominant pathway for SLN internalization. The uptake of each sample (SLNs-FITC, C-SLNs-FITC, IC-SLNs-FITC) was assessed at 37 °C for both fibroblast and MCF7 cells, with a comparative analysis of uptake at 4 °C to establish a baseline. As illustrated in **Figure 6-8A**, none of the samples exhibited complete uptake at 4 °C for either cell type, highlighting the energy-dependent nature of SLN internalization, specifically through endocytosis. The uptake of samples at 4 °C was consistently less than 10%, contrasting sharply with the controls at 37 °C, where uptake exceeded 70%. This significant reduction in uptake at 4 °C is attributed to an elevation in cell membrane rigidity, impeding both active, energy-dependent uptake and passive diffusion processes [422]. Notably, the uptake of IC-SLNs-FITC by fibroblasts at both temperatures was limited, attributable to the targeting moiety, with uptake levels of 10% and 1% at 37 °C and 4 °C, respectively. Accordingly, diverse endocytosis inhibitors were used to assess the primary pathway for each SLN.

In the case of fibroblasts, SLNs-FITC exhibited substantial uptake in the presence of Chlorpromazine and Cytochalasin D (75% and 70%, respectively), with no significant difference from the control (80%- *p-value*>0.05), suggesting uptake independence from Clathrin-mediated or macropinocytosis pathways, **Figure 6-8B**. However, a 75% reduction in endocytosis was observed in the presence of Filipin III, indicating a reliance on caveolin-mediated pathways for uptake. In this mechanism, cells with elevated surface cholesterol levels form a flask-shaped membrane to internalize particles [423]. Given the high cholesterol content on fibroblast surfaces, this caveolin-mediated pathway emerges as a primary route for uptake in these cells. The disruptive action of Filipin III on cholesterol impedes this pathway, hence hindering particle

uptake [424]. Given that a 25% uptake was observed even when the caveolin-mediated pathway was blocked, and this level surpassed the uptake observed at 4 °C, it is evident that passive diffusion also contributed to the uptake process [425]. In the case of Clathrin-coated FITC-loaded SLNs (C-SLNs-FITC), significant reductions were observed across all pathways for fibroblasts (40-60% uptake, suggesting the absence of a specific internalization route for this formulation. However, the highest reduction occurred with chlorpromazine (60% reduction), an inhibitor of Clathrin formation, indicating that the Clathrin-mediated pathway might be the predominant route, **Figure 6-8A-B**. This emphasized that most SLNs enter cells primarily through the Clathrin-mediated pathway [424]. For uptake of IC-SLNs-FITC in fibroblasts, the low uptake observed in the control group (only 10% uptake), attributed to targeting, did not exhibit any significant differences in the presence of inhibitors (less than 10% uptake). The observed low uptake of the SLNs suggests that passive diffusion was the primary mechanism involved, as indicated by the lack of significant effects from the inhibitors. This reduced uptake may be attributed to the IGF functionalization, which could have interacted with specific surface receptors on fibroblasts, thereby inhibiting endocytosis [426].

Although CTGF's presence and its affinity for IGF increased the uptake of IC-SLNs-FITC in MCF7, the exact mechanism remains elusive [427]. The interaction of CTGF with cell receptors and its subsequent effects are highly dependent on the cell type and location, such as epithelial cells, muscle cells, or myo/fibroblasts in the liver, cornea, and skin [428]. While a specific cell receptor for CTGF has not been conclusively identified, various pathways may facilitate its binding to the cell surface or internalization. Potential receptors include integrins (ITGs), heparan sulfate proteoglycans (HSPGs), lipoprotein receptor-related proteins (LRPs), and tyrosine kinase (TK) receptors [428]. In myo/fibroblasts, CTGF primarily interacts with

ITGs and HSPGs via the thrombospondin type I domain, with ITG α6β1 being a key receptor in human adult myo/fibroblasts. This interaction plays a crucial role in mediating CTGF's influence on cellular behavior [428].

Additionally, CTGF may be internalized through the clathrin-mediated pathway via LRPs, such as α2-macroglobulin, for these cells, although it is unclear whether this uptake is necessary for CTGF's function or merely leads to its degradation in the endosome [429–431]. Furthermore, another way for CTGF to bind to the cell surface or to be internalized is through other extracellular proteins. For instance, CTGF can enhance the binding of TGF-β to cell receptors through the von Willebrand domain and increase its affinity for TGF-β receptors on cells [430]. The endocytosis pathway and ultimate localization of SLNs are highly dependent on the cell type, as well as the composition and functionalization of nanoparticles. Therefore, distinct pathways exist for MCF7 cells in comparison to fibroblasts. In the case of the SLNs-FITC sample, macropinocytosis emerged as the primary route of endocytosis in MCF7, resulting in a reduction of over 50% compared to the control, as shown in **Figure 6-8A-B**. Macropinocytosis, a non-specific and actin filament-dependent process, is favored for internalization due to the relatively large size of the SLNs used in this study (approximately 200-300 nm). The disruption of micropinocytosis was done by using cytochalasin D, which inhibits actin filament polymerization. Passive diffusion also played a role in the uptake of SLN in MCF7 cells, contributing to about 15% of the total uptake, **Figure 6-8A-B**. In the case of C-SLNs-FITC, the Clathrin-mediated pathway became the dominant internalization route, with a 60% reduction in uptake, indicating that the Clathrin coating effectively facilitated specific internalization. Notably, while functionalization did not alter the mode of endocytosis, it enhanced the overall endocytosis of IC-SLNs-FITC by approximately 10% compared to coated samples without

functionalization due to the presence of expressed CTGF by MCF7. The results indicated that the functionalization of SLNs with IGF led to targeted delivery to only cells expressing a higher level of CTGF (MCF7).

6.3 Conclusions

Severe skin wounds often lead to the formation of abnormal scar tissue, characterized by reduced elasticity and mechanical functionality compared to normal skin. Additionally, scar tissue has diminished heat tolerance and water retention capabilities. Despite the availability of various scar management techniques, including surgical interventions and stem cell therapies, these methods have limitations that underscore the need for advanced research in drug delivery systems for scar reduction and prevention. However, the destructive nature of anti-scarring drugs poses challenges, as their improper timing can compromise the healing trajectory and potentially lead to chronic wounds with increased infection risk. Targeted drug delivery systems offer a solution by preventing such complications and promoting complete skin regeneration.

In this study, we developed a targeted delivery system based on SLNs designed explicitly for the scar formation stage, with the aim of effectively targeting cells with high CTGF expression, such as myofibroblasts. CTGF is known to be prominently expressed during the scar formation window. To mitigate the risk of premature drug release, we employed a protective coating using the cage protein Clathrin, which prevents untimely drug release. Upon reaching the stage of high CTGF expression, the coated SLNs are internalized by the target cells, where the Clathrin coating disassembles within the cell cytosol, enabling a sustained drug release over 72 hours with an initial burst release in the first 10 hours.

Our findings demonstrate that the cage protein effectively prevents drug release, with less than 10% of the drug being released even after 3 days, thereby protecting the SLNs from degradation,

which typically occurs within this timeframe. Furthermore, utilizing FITC-loaded SLNs, we illustrated selective dye uptake of functionalized SLNs by cells with high CTGF expression, such as MCF7 cells. In contrast, fibroblasts with low CTGF expression exhibited less than 10% uptake.

This designed delivery system holds potential for a wide range of anti-scarring agents, including drugs, DNA, proteins, genes, and siRNAs. Additionally, by customizing the targeting moiety the system's specificity for myofibroblasts can be further enhanced, optimizing its efficacy in scar prevention and reduction.

6.4 Material and Methods

6.4.1 Chemicals and Reagents

Hydrogenated soya phosphatidylcholine (HSPC) and Distearoylphosphatidylethanolamine (DSPE-PEG) were generously provided as gift samples by Lipoid (Ludwigshafen, Germany). Triolein was purchased from Fisher Scientific (Hampton, NH, USA) and all other lipids (Cholesterol, 1,2-dioleoyl-3-trimethylammonium-propane (DOTAP), 1,2-distearoyl-sn-glycero-3-phosphocholine (DSPC) and 1,2-Dimyristoyl-rac-glycero-methoxy polyethylene glycol (DMG-PEG) were purchased from Sigma Aldrich (St. Louis, MO, USA). Bovine Serum Albumin (BSA), Kynurenic Acid, phosphotungstic, Fluorescein isothiocyanate isomer I (FITC), Chlorpromazine hydrochloride, and Filipin were procured from Sigma Aldrich (St. Louis, MO, USA).

Bradford assay kit, the MTT assay kit (CyQUANT™ MTT Cell Viability Assay), Dialysis tubes (Pur-A-Lyzer™ Mega Dialysis Kit), and Cytochalasin B were obtained from Thermo Scientific (Waltham, MA, USA). The protein ladder, primary antibody (Anti-Clathrin

heavy chain antibody), and secondary antibody (Goat Anti-Rabbit IgG H&L, HRP) were sourced from Abcam (Cambridge, UK). EDC was procured from G Biosciences (St. Louis, MO, USA), and NHS, Lyso-Tracker Red, paraformaldehyde (in PBS), and ",6-diamidino-2-phenylindole (DAPI) were obtained from Fisher Scientific (Hampton, NH, USA). Human IGF-I Recombinant ProteinDulbecco'ss Modified Eagle Medium (DMEM) media and Fetal Bovine Serum (FBS) were sourced from Gibco™. All chemicals used in the study were of analytical grade.

6.4.2 Cell Lines

Human primary dermal fibroblasts (ATCC PCS-201-012), the human breast cancer cell line MCF7, and Fibroblast Basal Media supplemented with Fibroblast Growth Kit were purchased from ATCC (Manassas, VA, USA).

6.4.3 Instrumentation

The instruments used for the fabrication of SLNs included a syringe pump (New Era Pump Systems, Inc., NY, USA), NanoAssemblr® Benchtop (Precision NanoSystems Inc., BC, Canada), a mechanical stirrer (Caframo Compact Digital, Caframo LabSolutions, ON, Canada), a sonicator (q700, Qsonica L.L.C, NT, USA), and a centrifuge (Sorvall Legend Micro 21, Thermo Scientific, MA, USA). The fabricated SLNs were freeze-dried using a Christ freeze dryer (Martin Christ Gefriertrocknungsanlagen GmbH, Germani) for further evaluation.
The morphology of the SLNs was evaluated by Transmission Electron Microscopy (TEM FEI Talos F200X S/TEM, Thermo Scientific, MA, USA), and their size and charge were analyzed using a zeta sizer (Litesizer 500, Anton Paar, QC, Canada).

Chemical characterization was performed by Fourier Transform Infrared Spectroscopy (FTIR) (IS10, Thermo Scientific, MA, USA). KBR was used to prepare a pellet, and samples were scanned from the 4,000 to 4,00 cm^{-1} wavenumber range.

The thermal properties of SLNs were evaluated using a Differential Scanning Calorimetry (TA instrument, NC, USA). The samples were heated from 20 to 200 °C at a heating rate of 10 °C/min.

All cellular tests and uptake evaluations were conducted using a fluorescence microscope (Nikon Ti-U, Nikon Instruments Inc., NY, USA) and a fluorescence spectrometer (Biotek Synergy 4, Agilent, CA, USA).

6.4.4 Clathrin Extraction and Characterization

Clathrin was extracted from pig brains (bought fresh from a local plant) using a two-step procedure [415]: the initial step involved isolating natural Clathrin-coated vesicles, and the second step involved separating Clathrin Triskelia.

For the first step, the tissue was minced, and small pieces of tissue were frozen with liquid nitrogen for further breakdown. The broken tissues were homogenized with the same amount of isolation buffer (**Table S10-1**) on ice for 5 minutes and 1000 rpm (10 seconds with 30-second breaks). The homogenized tissue was sonicated for cell lysis at 40% amplitude for 15 cycles. The homogenates were centrifuged at 10,000 g for 30 min at 4.0 ˚C, and the supernatant was filtered with cheesecloth to remove floating fat debris. The supernatant was centrifuged at 120,000 g for 30 minutes at 4.0 ˚C, and the obtained pellet was resuspended in the minimum volume of isolation buffer (3 mL/pellet) with a Dounce tissue grinder. The resuspended pellet was mixed with the same amount of Ficoll-400/sucrose (12.5% wt. in isolation buffer) and was centrifuged for 40 minutes at 25,000 g and 4.0 ˚C. The cloudy supernatant was collected and diluted with the

isolation buffer three times. Then, the solution was centrifuged at 120,000 g and 4.0 ˚C for 1 hour, and the obtained pellet was resuspended in a small isolation buffer and kept at 4.0 ˚C for the second step.

In the second step, the coated vesicle pellet was resuspended in 3.0 mL dissociation buffer (**Table S10-1**) and homogenized for 10 minutes, followed by incubation on ice for 1 hour. The solution was clarified by ultracentrifuging at 120,000 g for 1 hour at 4.0 ˚C. The supernatant was concentrated with ultrafiltration unit (14 kDa)-VivaSpin at 4,000 g for 30 min at 4.0 ˚C and stored at -80 ˚C.

The Bradford test was utilized to confirm the presence of protein in the final suspension, and the concentration of extracted Clathrin was determined using the Bradford test at 595.0 nm based on a standard curve using BSA.

The SDS-PAGE test was employed to evaluate the efficiency of Clathrin extraction, specifically targeting the Clathrin heavy chain (180 kDa) using an 8.0% gel. Sample preparation involved mixing the extracted Clathrin (20X diluted) with running buffer followed by heating at 95.0 ˚C for 5 minutes. After heating, the samples were centrifuged for 2 minutes at 1,000 g, and 20 µL of each sample was loaded into the gel wells. A protein ladder served as a molecular weight reference, and the test was conducted for 75 minutes at a current of 2 amperes. Subsequently, the gel was stained with Coomassie Blue and heated for 2 minutes. The destaining process occurred overnight on a rocking shaker. Gel evaluation was performed under light to identify proteins.

For the western blot test, the samples were prepared as explained, and instead of staining, the gels were transferred to nitrocellulose membranes. These membranes were incubated in a 1 µg/mL primary antibody solution (Anti-Clathrin heavy chain antibody) overnight at 4.0 ˚C.

Following washing with TBST (RNAase-free), 1 μL of the secondary antibody (Goat Anti-Rabbit IgG H&L, HRP) was added, and the membranes were shaken on a rocking shaker for 2 hours at room temperature. Finally, the membranes were stained and utilized for fluorescent imaging.

6.4.5 SLNs Fabrication and Characterization

6.4.5.1 Fabrication

The synthesis of SLNs was done by ethanol injection and microfluidic technique, as outlined in the literature [405,432]. Briefly, For the preparation of SLNs through ethanol injection, lipids (in a molar ratio of 4:3.4:2.5:1.3) and a model drug (3 nM KyA) were dissolved in hot ethanol at 70.0 ˚C. The lipid phase was added into a preheated aqueous solution (Tris buffer with 0.5 v/v% Tween 80) using a syringe pump. Meanwhile, the aqueous phase was under mechanical stirring (1000 rpm) at 45.0 ˚C. Mechanical stirring was maintained for 30 minutes, followed by sonication for 5 minutes at an amplitude of 40%. The resulting suspension was centrifugated for 30 minutes at 14,000 g, and the SLNs were collected.

For microfluidic methods, lipids in a molar ratio of 5:20:12:1 were dissolved in the organic phase (ethanol), while a model drug (3 nM KyA) was dissolved in Tris buffer (pH=8.0). The aqueous and organic phases were mixed in a 1:1 ratio with different flow rates and kept at room temperature overnight. Subsequently, the final suspension was centrifugated for 30 minutes at 14,000 g, and the SLNs were collected.

For both techniques, to remove the unloaded drug, the collected SLNs were passed through Sephadex G-50. The final product was dialyzed against deionized water, with frequent water changes to remove buffer salts. The filtered SLNs were freeze-dried and stored at 4.0 ˚C until further use.

A Design of Experiments (DOE) randomized D-optimal model for the response surface method (RSM) was used (Stat-Ease® 22.0) to achieve the highest loading efficiency (LE%), loading capacity (LC%), and desired size (nm). The independent variables (factors) included two fabrication techniques, four distinct lipid compositions (**Table 6-2**), three lipid concentrations, and three flow rates, **Table 6-3**.

Table 6-2 SLNs lipid compositions

Composition	Structural Lipid	Filling Lipid	Helper Lipid	Coating Lipid
A	HSPC[1]	Triolein	Cholesterol	DSPE-PEG[2]
B	HSPC	DOTAP[3]	Cholesterol	DSPE-PEG
C	DSPC[4]	Triolein	Cholesterol	DMG-PEG[5]
D	DSPC	DOTAP	Cholesterol	DMG-PEG

1) HSPC: Hydrogenated soya phosphatidylcholine 2) DSPE-PEG: Distearoylphosphatidylethanolamine

3) DOTAP: 1,2-dioleoyl-3-trimethylammonium-propane 4) DSPC: 1,2-distearoyl-sn-glycero-3-phosphocholine

5) DMG-PEG: 1,2-Dimyristoyl-rac-glycero-methoxy polyethylene glycol

With these parameters, 60 experimental runs were defined. The responses of each run were fitted to various models, such as linear, 2FI, and quadratic models, to determine the best fit. The generated quadratic polynomial equation (for each concentration and each technique) was used to evaluate the synergistic or antagonistic effects of each independent variable on the dependent variables. The polynomial regression results were illustrated using 3-D plots. The quadratic equation is as follows in **Equation 6-1**:

$$Ln(y) = \alpha_0 + \alpha_1 A + \alpha_2 B + \alpha_3 AB + \alpha_4 A^2 + \alpha_5 B^2 \qquad \textit{Equation 6-1}$$

Where y was the response, α_0 was an intercept and α_{1-3} were linear coefficient, α_{4-5} were squared coefficients, A was the flow rate and B was the lipid concentration.

Table 6-3 Variables for fabrication of SLNs to find the optimum parameters

Variables						
Independent Categorical	Technique			Composition		
	Ethanol injection	Microfluidic		A	B	C	D
Independent Quantitative	A (Flow rate mL/min)			B (Lipid concentration mg/mL)		
	1.5	8	12	4	8	10
Dependent variable	y_1: Size (nm)		y_2: LE%		y_3: LC%	
Aim	200-300 nm		Maximize		Maximize	

6.4.5.2 Physiochemical Characterization

The morphology of SLNs was assessed using TEM at 20 kV. The diameter of SLNs was measured using ImageJ. Before imaging, samples were negatively stained by mixing an equal amount of SLN suspension (in water) and a 2% aqueous solution of phosphotungstic (20 µL each). A droplet of the mixed solution (10 µL) was placed on a TEM grid for 20 seconds, and the excess solution was removed by filter paper. The grid was air-dried and used for TEM imaging. Moreover, for evaluating the hydrodynamic diameter, polydispersity index (PDI), and zeta potential of the diluted SLN, they were suspended in PBS (pH 7.4) and subjected to sonication for 30 minutes before the measurements.

The drug content within the SLNs was determined by lysing the SLNs (using 0.1% v/v Triton X-100) and quantifying the entrapped drug content through a UV-Vis spectrophotometer at 252.0 nm based on a standard curve of different concentrations of KyA. The free drug was assessed based on the UV of the supernatant. The loaded drug quantity was determined by **Equations 6-2** and **6-3**, and LE% and LC% were calculated.

$$LE\% = \left(\frac{Initial\ added\ drug - Free\ drug}{Initial\ added\ drug}\right) \times 100 \quad \textit{Equation 6-2}$$

$$LC\% = \left(\frac{Totall\ entraped\ Drug(mg)}{Totall\ SLNs\ weigth\ (mg)}\right) \times 100 \quad \textit{Equation 6-3}$$

The drug release profile from SLNs was analyzed using the dialysis technique. The SLNs were weighed and placed in 2 mL dialysis tubes with phosphate-buffered saline (PBS, 0.01 M, pH = 7.4) against 18.0 mL PBS (0.01 M, pH = 7.4). These samples were then placed in a shaking bath (100 rpm) at 37 ˚C. At designated intervals, 1.0 mL of PBS was collected and replaced with 1.0 mL of fresh PBS. The collected solution was assessed using a UV-Vis spectrophotometer to determine the drug concentration at 252.0 nm. The accumulated release (R) was calculated based on **Equation 6-4**.

$$R = \frac{V \times \sum_1^i C_i}{m}$$ *Equation 6-4*

where **V** represents the total media volume (20.0 mL), **C** indicates the concentration of the drug in each interval, and **m** represents the mass of the drug in SLNs. The release kinetics were assessed by fitting various models to the data, including zero-order, first-order, Higuchi, and Korsmeyer-Peppas. The evaluation involved utilizing the regression coefficient (R^2) to determine the best-fitting model.

6.4.6 SLNs Coating and Functionalization

6.4.6.1 SLNs Coating with Clathrin

Coating with Clathrin involves the reassembly of disassembled Clathrin on the surface of SLNs. Clathrin reassembly can occur under two conditions: 1) Biomemitic method using cytosol and proteins and 2) using different chelator factors.

For the first technique, cytosol was extracted from rat livers (detailed steps in the Supporting Document). For coating the SLNs with Clathrin, the extracted Clathrin was dialyzed against synthetic buffer (**Table S10-3**) and fabricated SLNs (3.5 mg/mL), Clathrin (120 µg/mL), GTP (4

mM) and cytosol (6 mg/mL) were added to the synthetic buffer and incubated at 37 ˚C for 15 minutes while shaking. The solution was centrifuged for 20 minutes at 14,000 g, and the pellet (coated SLNs) were collected for further characterization.

For the second technique, different buffers (**Table S10-4**) were used to reassemble Clathrin on the surface of SLNs. The extracted Clathrin was added to the fabricated SLNs with 2 mL of the desired buffer and placed in a dialysis bag against the buffer overnight at room temperature with constant shaking. The 2 mL suspension was centrifuged (14,000 g, room temperature, 20 minutes), and the pellet was collected for further characterization.

The SLNs coated using these techniques were characterized to assess the successful reassembly of Clathrin on the SLN surfaces. The evaluation included calculating the percentage of successful coating by measuring the protein contents of each batch. Additionally, the morphology of the coated SLNs was examined using TEM with negative staining, as described earlier. As the final evaluation to determine the success of the coating step, the supernatants and pellets from each coating technique were employed for SDS-PAGE characterization. Before the test, the SLNs were treated with Tris-HCl (pH=8.0) and Triton X-100 to disassemble both the SLNs and the coating.

6.4.6.2 Functionalizing The Coated SLNs with IGF

Clathrin-coated SLNs were functionalized with IGF using EDC-NHS chemistry. The initial step involved activating the Clathrin-coated SLNs with EDC-NHS. 1 mL of the coated sample was combined with EDC (1 mg/mL), NHS (1 mg/mL), and 3500 µL PBS. This suspension was left at room temperature with continuous shaking overnight. Subsequently, the suspension was centrifuged (20 minutes, 14,000 g) to remove excess EDC and NHS, and the

pellet was collected and resuspended in a PBS solution. The Clathrin-coated SLNs treated with EDC-NHS were introduced to 100 µL of IGF-I (100 µg in 1 mL PBS) and shaken for 4 hours at room temperature, followed by overnight incubation at 4 ˚C. The final suspension was centrifuged at 16,000 g and 4 ˚C for 20 minutes, and the resulting pellet was resuspended in 5 mL PBS.

The success of IGF-functionalizing Clathrin-coated SLNs was assessed using the Bradford assay. A sample of coated SLNs served as the blank, and functionalized SLNs were compared against it. Concentrations were determined based on the previously established standard curve using BSA.

Furthermore, the size and charge of drug-loaded SLNs (SLNs-KyA), Clathrin-coated drug-loaded SLNs (C-SLNs-KyA), and IGF-functionalized Clathrin-coated drug-loaded SLNs (IC-SLNs-KyA) were evaluated as previously described.

Additionally, the drug release profile from IC-SLNs-KyA samples was examined in PBS (pH=7.4, with 0.1% Triton X-100) and Tris-HCl (pH=8.0 with 0.1% Triton X-100).

Lastly, the stability of SLNs was evaluated after three months of storing dry samples at 4.0 ˚C. The hydrodynamic diameter and drug content were investigated and compared to fresh SLNs.

6.4.7 Cellular Assays

6.4.7.1 Cell Culture

Two cell types were selected to assess the targeting efficacy of the engineered SLNs. Human primary dermal fibroblasts (PCS cells) and the human breast cancer cell line were employed in the study.

PCS cells were cultured in Fibroblast Basal Media supplemented with Fibroblast Growth Kit and 100 µg/mL antibiotics cocktail at 37 ˚C in a 5% CO_2 atmosphere. On the other hand,

MCF7 cells were cultured in high glucose DMEM media with 10% FBS and 100 µg/mL antibiotics cocktail under the same conditions of 37 ˚C and 5% CO_2 atmosphere. Cells were harvested with the Trypsin enzyme before the cellular test. Briefly, cells were washed with cold PBS three times, and then trypsin was added. Cells were incubated at 37 ˚C for 5 minutes and then transferred to a tube containing complete media. The cell suspensions were centrifuged for 10 minutes at 1,000 g, and the cell pellet was resuspended in a complete media. The resuspended cells were used for cell counting. 20 µL of cells were mixed with 20 µL of Trypan blue solution, and 10 µL of cell suspension was used for cell counting. The suspension was added to the hemocytometer, and the number of live cells was found. The procedure was done three times for each cellular test.

6.4.7.2 Cytotoxicity

The cytotoxicity of the samples for PCS cells was assessed using the MTT assay kit. Different concentrations of KyA, various concentrations of SLNs-KyA, C-SLNs-KyA, and IC-SLNs-KyA were used to evaluate the cytotoxicity of samples for fibroblast for 24 hrs (0-100 µg/mL).

Moreover, the desired concentrations of each sample (2 µg/mL) were used for one one-week test for both cytotoxicity and proliferation tests. In brief, SLNs-KyA, C-SLNs-KyA, and IC-SLNs-KyA were introduced into cell wells and incubated for 1 to 7 days. Following the desired incubation period, the culture media was replaced with MTT dye and incubated for 4 hours at 37 ˚C. DMSO was added to the wells upon forming formazan crystals, and the plate was read using a microplate reader at 570 nm. The viable cell percentage was calculated based on a control without any sample.

6.4.7.3 Fluorescent Imaging (Cellular Uptake)

Instead of the drug, FITC dye was incorporated inside SLNs to assess cellular uptake. The fabrication technique (ethanol injection) remained the same, and instead of the drug, 10 nM FITC was added to the lipid phase. The resulting FITC-loaded SLNs (SLNs-FITC) were dialyzed against DI water to separate any unloaded FITC. The FITC-loaded SLNs were examined with a fluorescent microscope at various stages (coating and functionalizing) to ensure that FITC remained encapsulated within the SLNs before proceeding to cellular tests. The quantity of loaded FITC in SLNs was determined based on a standard curve.

SLNs-FITC, Clathrin-coated FITC-loaded SLNs (C-SLNs-FITC), and IGF-functionalized Clathrin-coated FITC-loaded SLNs (IC-SLNSs-FITC) were utilized for the cellular uptake assay. Considering the growth rate of MCF7 and PCS, the optimal cell density per well was determined to be 5×10^5 cells/well. After a 2-hour pre-incubation period, 200 µL of each sample was added to the media, and the plate was placed in the incubator for 24 hours. Subsequently, all wells were washed with cold PBS three times to eliminate any remaining SLNs not internalized by cells. The washed cells were then utilized for cellular uptake characterization.

To assess cellular uptake, 50 nmol/L Lyso-Tracker Red was introduced to each well, and the plates were incubated at 37 ˚C for 30 minutes. Following this, Lyso-Tracker Red was replaced with 4% paraformaldehyde (in PBS), and the plates were incubated for 10 minutes at 4 ˚C. After fixation, the cells were washed with PBS three times, and 1% Triton X-100 (in PBS) was added to the wells, with plates incubated at 4 ˚C for an additional 10 minutes. Following another three washes, 1% BSA was introduced to the wells for 30 minutes at 37 ˚C. After the

final wash, DAPI was added to stain the cell nuclei. The plates were observed using a fluorescent microscope. Image analysis was performed using NIS-Elements viewer.

In addition to the qualitative assessment of cellular uptake, quantitative data were acquired from the supernatant (culture media). Furthermore, the cells were lyzed with 1% Triton X-100 and centrifugated at 14,000g for 10 minutes. The quantity of FITC within the cells was determined based on the supernatant. The percentage of cellular uptake was calculated by considering the amount of FITC in the cytosol and culture media. FITC excitation occurred at 490 nm, and emission was measured at 525 nm [433].

*6.4.7.4 **Endocytosis Pathway**:*

FITC-loaded samples (SLNSs-FITC, C-SLNSs-FITC, IC-SLNSs-FITC) were used to determine the uptake pathway in fibroblast cells and MCF7. Cells were seeded at 5×10^5cells/well in 48-well culture plates and cultured for 24 hours in the specified culture media. The media were replaced with media containing 200 µL samples, and plates were incubated at 4 ˚C for 2 hours to assess the energy dependence of SLNs internalization. Additionally, cells were seeded as described to investigate various endocytosis pathways. Following 24 hours of incubation, different chemical inhibitors were introduced to each well 1 hour before adding the samples (Chlorpromazine (20 µM): Clathrin inhibitor, Filipin (5 µg/mL): Caveolin inhibitor, Cytochalasin B (5 µg/mL): Micropinocytosis and phagocytosis inhibitor) [407,434]. Following inhibitor treatments, the cells were washed with PBS, fresh media containing 200 µL of each sample was added to each well, and the plates were incubated at 37 ˚C for 2 hours. After 2 hours, cells were washed with PBS and fixed and stained with DAPI as described previously.

6.4.8 Statistical Analysis

For all data, the mean and standard deviation (SD) were calculated (n>3). One-way ANOVA (Analysis of Variance) with posthoc Tukey was employed to compare significant differences between groups (GraphPad Prism Versio 10.2.0), and a p-value<0.05 was considered statistically significant.

6.5 CRediT Authorship Contribution Statement

Farinaz Jonidi Shariatzadeh: Writing – review & editing, Writing – original draft, Visualization, Validation, Methodology, Data Curation, Formal analysis, Conceptualization, Project administration. **Vinith Yathindranath:** Methodology- Supporting, Writing – review & editing. **Yang Liu:** Methodology- Supporting, Writing – review & editing**. Donal W.Miller:** Methodology- Supporting, Writing – review & editing, Resources-Supporting**. Fransic Lin:** Methodology- Supporting, Writing – review & editing, Resources-Supporting**. Sarvesh Logsetty:** Writing – review & editing, Conceptualization. **Song Liu:** Writing – review & editing, Validation, Supervision, Methodology, Funding acquisition, Conceptualization, Resources.

6.6 Funding Sources

The authors appreciate and acknowledge the financial support of the Natural Sciences and Engineering Research Council of Canada (NSERC) Discovery Grant (RGPIN-2019-06094), the Canada Foundation for Innovation (award number 23679), the University of Manitoba GETS program, and the University of Manitoba Graduate Fellowship (UMGF).

6.7 Supporting Information

Detailed information on cytosol and clathrin extraction, as well as discussions about DSC and FTIR data, are provided in the supporting documents. Additionally, the supporting

documents include FTIR spectra, surface responses, DSC spectra, Bradford results, and additional MTT results.

7 Chapter 7: Summary, Conclusions and Future Works

7.1 Summary

This thesis addresses challenges in wound healing, focusing on scenarios that contribute to delayed healing and scar formation. The study explores strategies to promote the natural healing trajectory, accelerating regeneration while minimizing complications and the chance of scar formation. A comprehensive literature review identified key factors responsible for delayed healing and scarring, highlighting cellular, molecular, and external influences that disrupt the healing process. These disruptions: impaired hemostasis, exaggerated inflammation, prolonged re-epithelialization, excessive ECM deposition, excessive formation of new blood vessels, abnormal ECM remodeling, or reduced apoptosis may occur during any of the four stages of healing. Environmental and external factors, such as bacterial infection, wound size and location, and patient demographics (e.g., sex and race), further influence these processes [435–438]. For example, bacterial presence exacerbates inflammation, depletes oxygen and nutrients, and increases ROS, ultimately prolonging inflammation and contributing to scar formation [439,440].

This project specifically targeted exaggerated inflammatory responses. Prolonged inflammation promotes scar formation through cytokines secreted by immune cells, particularly macrophages. Cytokines like PDGF, TGF-β, and IL-4/IL-13 activate fibroblasts via pathways such as SMAD signaling, converting them into myofibroblasts. These myofibroblasts overexpress α-SMA and collagen, leading to excessive ECM deposition and scarring [441–444]. Bacterial infections are a primary driver of prolonged inflammation. They not only increase immune cells but also compete for resources and generate ROS, further damaging healthy tissue. A biosensor was developed that detects bacterial presence at concentrations as low as 3×10^4 CFU/cm^2, triggering a visible color change from yellow to green to address the infection

problem. This alert mechanism allows patients and clinicians to take timely action to control infections, thereby reducing immune cell infiltration and shortening the inflammatory phase.

Furthermore, a theranostic biosensor was designed to both detect bacteria (10^5 CFU/cm^2) and release antibacterial agents in response to ROS. The decrease in the sensitivity of the biosensor is rooted in changes in the design to increase the accuracy of the final outcome of color change and prevent false positives. This targeted delivery reduces bacterial loads and minimizes immune cell activation, preventing prolonged inflammation and subsequent scarring. The use of on-demand antibacterial release helps prevent antimicrobial resistance while promoting controlled wound healing.

Scar formation is also driven by excessive ECM deposition, particularly collagen with parallel fibrils instead of a basket-weave structure. An imbalance between ECM synthesis and degradation, often due to reduced MMP activity, contributes to scarring. The project explored the delivery of anti-scar drugs that enhance MMP activity and reduce collagen expression to address the scar problem. However, premature or delayed drug release can disrupt the healing process, leading to chronic wounds [436,437,444]. To improve precision, in this project, we identified CTGF, a downstream effector of TGF-β, as a promising biomarker for targeting anti-scar therapies. CTGF is predominantly expressed during scar formation (proliferation stage) and directly influences ECM production by increasing fibronectin and collagen expression while inhibiting MMP activity. Targeting CTGF enables selective drug delivery during the scar formation phase, improving therapeutic outcomes.

Overall, this work employed diverse strategies to manage various stages of wound healing, aiming to achieve accelerated regeneration and reduce the likelihood of scarring. By controlling

inflammation, targeting bacterial infections, and modulating ECM dynamics, the study contributes to advancing scarless healing approaches.

7.2 Conclusions

This project implemented three distinct but interrelated strategies to address critical stages in wound healing. The main conclusions of each approach, as well as the overall findings of the study, are summarized below.

7.2.1 Ultra-Sensitive Biosensor for Bacteria Detection

Rapid bacterial detection in wounds is essential to prevent the progression of chronic wounds or systemic infections. Traditional methods often require invasive sampling and complex technologies, which are unsuitable for detecting low bacterial concentrations ($< 1\times10^5$ CFU/ /cm^2). To address this limitation, we developed a colorimetric nanofibrous biosensor for real-time, in situ monitoring of bacterial infections.

Key findings:

- **Colorimetric Mechanism**: The biosensor utilizes hemicyanine dye (HCy), which undergoes a visible color change in response to bacterial lipase activity, a biomarker for wound infection.
- **Enhanced Sensitivity**: Cross-aligned nanofibers were incorporated to localize bacteria more effectively, and Tween 80, a surfactant, was added to amplify bacterial lipase activity (26-fold for MRSA and 9-fold for *P. aeruginosa*).
- **Detection Threshold**: The biosensor detects bacteria at concentrations as low as 3×10^4 CFU/cm^2, with the inclusion of Tween 80 increasing the visual response fourfold, ensuring clear detection.
- **Optimization**: A Tween 80 concentration of 0.5% in the electrospinning solution was identified as optimal for enhancing biosensor performance.

These innovations demonstrate that the combination of nanofiber alignment and chemical modification significantly improves bacterial detection, enabling early intervention to manage wound infections effectively.

7.2.2 Antibacterial Biosensors for Early Detection and Elimination of Bacteria

Infections in wounds remain a significant challenge, particularly with the rise of antibiotic-resistant bacteria. This study developed a theranostic biosensor capable of simultaneously detecting infections visually and delivering antibiotics in a controlled, ROS-responsive manner.

Key findings:

- **Dual Functionality**: The biosensor combines citric acid for immediate antibacterial action with PEG-PPS-based NPs loaded with CIP for sustained, ROS-triggered drug release.
- **Controlled Release**: In the presence of ROS (e.g., H_2O_2), CIP release increased from 20% at 72 hours without ROS to 50% in the first 6 hours and 100% at 72 hours, ensuring precise delivery.
- **Antibacterial Effectiveness**: Citric acid achieved a 3-log reduction in *E. coli* and a 5–6 log reduction in *P. aeruginosa* and MRSA. ROS-triggered CIP release further enhanced bacterial reduction, achieving an 8-log reduction across all strains.
- **Targeted Action**: ROS-triggered antibiotic release increased the ZOI threefold, confirming its ability to limit untargeted drug release and reduce bacterial resistance risks.

- **Biocompatibility**: The biosensor demonstrated over 90% fibroblast viability post-drug release, and co-culture experiments showed that bacterial elimination did not compromise fibroblast health or proliferation.

This dual-action biosensor provides an effective solution for wound infection management by combining immediate and sustained antibacterial actions while minimizing the risk of resistance and supporting healthy tissue recovery.

7.2.3 Targeted Delivery of Anti-Scar Drug

Excessive ECM production and scarring pose significant complications in wound healing. Premature release of anti-scarring drugs can further disrupt the healing process. This study developed a targeted delivery system to control drug release, specifically during the scar formation phase.

Key findings:

- **Targeting Mechanism**: SNLs were coated with clathrin to prevent premature release and conjugated with IGF to target CTGF, a protein overexpressed during scar formation.
- **Release Profile**: Less than 10% of the encapsulated drug (kynurenic acid) was released within three days, while over 50% was released within 10 hours upon clathrin removal at pH 8.
- **Cell-Specific Uptake**: Fibroblasts with low CTGF expression exhibited minimal uptake (<10%) of the clathrin-coated, IGF-conjugated SNLs, while cells with high CTGF expression (e.g., MCF7 cells) demonstrated significantly higher uptake (80%).

This targeted delivery system shows promise for precisely administering anti-scarring therapies, including small molecules, DNA, proteins, or siRNAs, during the scar formation phase.

7.2.4 Overall conclusion

This thesis highlights the importance of providing a suitable microenvironment to guide wound healing toward regeneration, addressing critical challenges such as infection detection, bacterial elimination, and scar formation. Chronic wounds, often characterized by prolonged healing and scarring, impose a significant financial burden globally, with infections alone contributing to increased morbidity, mortality, and healthcare costs. To address these challenges, the research explored innovative strategies to improve wound healing outcomes by targeting key stages of the healing process.

One of the major contributions of this work is the development of an ultra-sensitive colorimetric biosensor capable of detecting bacteria at low concentrations. The biosensor exhibits a visible color change in response to bacterial lipase activity, making it easily readable to untrained individuals, including patients themselves. This technology has broad implications, as it can be employed in various settings, from home care to battlefield scenarios, to alert physicians and caregivers about bacterial presence before it reaches critical colonization thresholds. The simplicity of the biosensor's readout makes it particularly advantageous for remote areas and low-income countries, where access to advanced diagnostic tools is limited. By enabling early infection detection, this biosensor not only reduces the financial burden associated with prolonged infections but also lowers detection costs compared to current diagnostic standards. Beyond skin wound applications, the biosensor can be adapted for other uses, such as urinary tract infection detection, catheter infection monitoring, and dental infection diagnosis. However, while the biosensor demonstrated compatibility with commercially available wound dressings, further optimization is required to enhance its sensitivity and accuracy for these alternative applications.

In addition to infection detection, timely elimination of bacteria remains a significant challenge in wound healing. Systemic antibiotics or sustained local drug delivery systems often pose disadvantages, including cytotoxicity to healthy tissues, reduced efficacy requiring higher dosages, and the increased risk of bacterial resistance. This thesis introduced a responsive nanoparticle system capable of releasing antibiotics, specifically in the presence of elevated ROS, a key indicator of bacterial infection to address these limitations. This technology ensures targeted drug release, reducing the likelihood of systemic infection progression and minimizing the development of antibiotic resistance. Ciprofloxacin was used as a model drug; however, the platform is versatile and can accommodate various biocides or therapeutic agents. For example, in wounds characterized by excessive inflammation, anti-inflammatory agents could be loaded into the nanoparticles to mitigate tissue damage. While the nanoparticles can be administered directly via injection, their incorporation into membranes or scaffolds enhances their retention at the wound site, further improving therapeutic outcomes. This technology has significant potential to reduce hospitalization times and, when combined with the biosensor, offers a comprehensive solution for both infection detection and treatment in diverse settings. Although this study focused primarily on skin wounds, the responsive nanoparticles could also be applied to internal wounds, provided additional in vivo validation is conducted.

Beyond addressing infection and inflammation, this thesis also focused on targeting scar formation during the proliferation phase of wound healing. To selectively target cells responsible for scar formation, nanoparticles were decorated with a specific targeting moiety, enabling precise drug delivery to cells overexpressing CTGF, such as myofibroblasts. While time constraints and experimental complexities limited the testing of cancer cells, successful targeting was demonstrated, indicating strong potential for wound healing applications. This technology

could be particularly transformative for burn patients, where extensive scar formation disrupts essential skin functions such as temperature regulation and hydration. By promoting skin regeneration, this approach could reduce the need for surgical interventions and additional therapies, significantly improving patient outcomes. Furthermore, the developed nanoparticles can be adapted for cancer therapies, particularly breast cancer, where CTGF overexpression is common. The versatility of the solid lipid nanoparticle platform allows for the loading of both hydrophobic and hydrophilic agents, as well as biological molecules such as DNA or siRNA, depending on the fabrication technique (e.g., ethanol injection or microfluidics) and lipid composition. However, further work is needed to enhance targeting accuracy and optimize the system for specific applications.

7.2.4.1 Broader Implications

The findings of this thesis have significant implications for wound healing and beyond. The developed biosensor and responsive nanoparticles offer a framework for early infection detection, targeted therapy, and the potential for scar prevention, which could transform current clinical practices. By enabling timely intervention, these technologies have the potential to reduce healthcare costs, improve patient outcomes, and minimize complications associated with chronic wounds. Additionally, the adaptability of the biosensor and nanoparticle platforms opens avenues for applications in other medical fields, including infection monitoring in urinary catheters, dental treatments, and targeted cancer therapies. The ability to customize these systems for different therapeutic agents further enhances their translational potential.

7.2.4.2 Limitations

Despite the promising outcomes, this study has several limitations. The direct effects of the developed technologies on wound healing were not evaluated *in vivo*, which is a critical step for

clinical translation. Future studies should focus on preclinical and clinical validation to assess efficacy, biocompatibility, and safety. Additionally, while the biosensor demonstrated sensitivity to bacterial lipase activity, its performance in complex biological environments requires further optimization. For the nanoparticle systems, improving targeting accuracy and ensuring stability under physiological conditions remain essential for their practical application.

7.3 Future Works

Although wound healing, particularly the scar formation phase, involves highly complex processes, this project aimed to implement various strategies to influence different stages of healing, with the goal of achieving accelerated and scar-free regeneration. Future directions for the different components of this project can be outlined as follows:

1. **Enhancing Biosensor Sensitivity**

   Incorporate additional lipase inducers, such as specific ions, to further increase the sensitivity of the biosensor for bacterial detection.

2. **Developing Bacterial Differentiation Biosensors**

   Design biosensors capable of distinguishing between different bacterial types, such as gram-negative and gram-positive bacteria, to provide more targeted diagnostic information.

3. **Improving Targeted Delivery Systems**

   Test SLNs with alternative targeting moieties, such as anti-CTGF antibodies, to enhance specificity for scar-related biomarkers.

4. **Myofibroblast Testing of SLNs**

   Differentiate fibroblasts into myofibroblasts *in vitro* and evaluate the uptake and efficacy of decorated SLNs in cells with high CTGF expression to confirm targeted delivery capabilities.

5. **3D Bioprinted Scar Models**

   Develop a 3D bioprinted scar model comprising both fibroblasts and myofibroblasts. Use this model to test the efficacy of targeted anti-scar drug delivery systems under controlled conditions.

6. ***In Vivo* Models**

   Conduct *in vivo* studies (potential model rabbit ear) to validate the biosensors for infection detection and elimination, as well as the targeted anti-scar drug delivery system for preventing scar formation in animal models.

These future steps will help refine the strategies developed in this project, ensuring their robustness, specificity, and translational potential for clinical applications.

8 Chapter 8 Appendix 1

Supporting Information

Ultra-Sensitive Nanofiber Biosensor: Rapid in situ Chromatic Detection of Bacteria for Healthcare Innovation

*Farinaz Jonidi Shariatzadeh[1], Sarvesh Logsetty[2] and Song Liu[1,3]**

1) Biomedical Engineering, Faculty of Engineering, University of Manitoba, Winnipeg, Manitoba, Canada, R3T 2N2

2) Departments of Surgery and Psychiatry, Rady Faculty of Health Sciences, University of Manitoba, Winnipeg, Manitoba, Canada, R3E 3P5

3) Department of Biosystems Engineering, Faculty of Agricultural and Food Sciences, University of Manitoba, R3T 2N2

* Corresponding Author: E.mail) song.liu@umanitoba.ca; +1) 204-474-9616).

KEYWORDS: Colorimetric probe, color-changing sensor, real-time infection detection, nanofibers, bacterial lipase, Tween80.

8.1 Material and Methods

8.1.1 Materials

Polyvinylpyrrolidone (PVP, Mw 40,000), tetrahydrofuran (THF, ≥99.9%), and N, N-dimethylformamide (DMF, ≥99.8%) were purchased from Sigma Aldrich (St. Louis, MO, USA). Tween® 80, Integra Miltex Standard biopsy punches, BD Bacto™ Tryptic Soy Broth (Soybean-Casein Digest Medium), BD Difco™ Dehydrated Culture Media: Tryptic Soy Agar (Soybean-Casein Digest Agar), 10X PBS Buffer (pH= 7.4- 0.2 µm filtered) and Aluminum foil were purchased from Fisher Scientific (Nepean, ON, Canada). The Lipase Activity Assay Kit (Colorimetric-ab 10254) was purchased from Abcam Inc. (Toronto, ON, Canada). Tecophilic HP-60D-35 (hydrophilic aliphatic polyurethane, PU) was purchased from Lubrizol Advanced Materials (Cleveland, OH, USA). HCy was synthesized by Alberta Reaserch Inc. (Alberta AB, Canada) based on the developed protocol in our lab. MRSA ATCC 33592, *P. aeruginosa* ATCC 27853, and *E. coli* ATCC 25922 were obtained from the American Type Culture Collection (ATCC) (Manassas, VA).

8.1.2 Designing The Electrospinning Machine for Collecting Cross-Aligned Nanofibers

To increase surface contact, reach optimal porosity, and enhance bacteria-nanofibers interaction, we used a commercially available electrospinning machine with a modified collector system to obtain cross-aligned nanofibers. The modified electrospinning machine was designed and provided by ParaNano Wound Care, LLC. Briefly, the collector comprises first, second, and intermediate segments, **Figure 4-1A**: parts 1 and 2, respectively. The first and second segments are connected to the intermediate segments on opposite ends and work as circumferential conductors at each edge. The first and second segments have electrically chargeable edge

conductors, electrically isolated from intermediate segments. The charge state of the segments is cycled to collect cross-aligned nanofibers formed in a plurality of radial structures.

8.1.3 Fabrication of Nanobiosensors

Nanobiosensors were fabricated with electrospinning. Overall, 6 samples were prepared as follows: 1) Random nanofibers without surfactant (R), 2) cross-aligned nanofibers without surfactant (W), 3) cross-aligned nanofibers with 0.17 w/v% Tween 80, 4) cross-aligned nanofibers with 0.53 w/v % Tween 80, 5) cross-aligned nanofibers with 2.12 w/v % Tween 80 and 5) cross-aligned nanofibers with 4.24 w/v % Tween 80. The electrospinning parameters and the membranes' chemical composition are presented in **Table S8-1**.

Table S8-1 Samples compositions and electrospinning parameters.

Name	Composition		Electrospinning parameter				
	Core w/v %	Shell w/v%	Voltage kV	Distance cm	Speed rpm	Flow rate mL/hr	Interval seconds
R	6% PU	7%PU 3.5% PVP 1.02% HCy	19	11	60	1	NA
W	6% PU	7%PU 3.5% PVP 1.02% HCy	19	11	60	1	90
T0.1	6% PU	7%PU 3.5% PVP 1.02% HCy 0.17% Tween 80	19	11	60	1	90
T0.5	6% PU	7%PU 3.5% PVP 1.02% HCy 0.530 Tween 80	19	11	60	1	90
T2	6% PU	7%PU 3.5% PVP 1.02% HCy 2.12% Tween 80	19	11	60	1	90
T4	6% PU	7%PU 3.5% PVP 1.02% HCy 4.24% Tween 80	19	11	60	1	90

As discussed in the machine design section, obtaining the cross-aligned structure relies on switching the grounding between edge conductors and an intermediate segment. The spinning time in each state (edge conductors or intermediate segment) before switching is called an interval, and the complete duration of one intermediate segment grounding and one edge conductor grounding is called one layer. If the number of layers exceeds the optimum number, the cross-aligned structure will not be obtained. Therefore, the optimum intervals and layer number were established as 90 seconds and 20 layers, respectively, to have a cross-aligned structure.

In addition to keeping the optimum number of layers, a non-conductive film should cover the collector to get aligned nanofibers; otherwise, a conductive film (aluminum film) interferes with alternating collector segment grounding, and aligned nanofibers cannot be obtained. **Table**

S8-2 presents the amount of Tween 80 used compared to the amount of dye and polymers used for each sample. The ratio of HCy and Tween 80 is important because HCy is the chromogenic probe that facilitates the color change due to lipase, and Tween 80 is the surfactant that increases lipase activity.

Table S8-2 The concentrations of Tween 80 in samples and its ratio to the main polymers and HCy dye.

Sample name	Tween 80 v/v%	Tween 80 wt%	Tween 80/ polymers	Tween 80/ HCy
R	0	0	0	0
W	0	0	0	0
T0.1	0.1	0.17	0.06	1.04
T0.5	0.5	0.53	0.32	5.20
T2	2	2.12	1.28	20.78
T4	4	4.24	2.57	41.57

8.1.4 Morphological Characterization of Nanobiosensors

Morphology and alignment of the electrospun nanofibers were characterized using scanning electron microscopy (SEM, FEI Quanta FEG 650). Samples were sputter coated for 45 s with gold−palladium (60:40), and SEM was conducted with an accelerating voltage of 10.0 kV. Nanofiber diameters were measured from SEM images using ImageJ, and nanofiber diameter distribution was found based on 300 nanofiber measurements. The alignment of the membrane was observed from the SEM images with 1,000 X magnification. The images were analyzed with the ImageJ-OrientationJ plugin to get a colored map presenting the orientation of nanofibers in color. After setting the scale of images and finding δ (the mean diameter of nanofibers in pixel ratio), the SEM images were de-framed. The other parameters, such as coherency and energy, were

set at 10%. The final colored map shows the direction of nanofibers, and the hue represents the angle of local nanofiber orientation (-90˚to 90˚) [445].

Moreover, the ImageJ particle analyzer was used to find the porosity of membranes. After setting the scale of images and converting them to 8-bit images, the threshold of each image was adjusted to red for the background and black for the nanofibers [446]. When all nanofibers were black, the void area was calculated with the particle analyzer, and the percent of porosity was obtained based on **Equation 8-1**.

$$Prosity\ \% = (\frac{void\ area}{totall\ area}) \times 100 \qquad \textit{Equation 8-1}$$

8.1.5 Bacteria Culture

Two leading bacteria causing wound infection were chosen for bacterial tests in this study, namely MRSA ATCC 33592 (gram-positive), *P. aeruginosa* ATCC 27853 (gram-negative) [447,448], and antibiotic-resistant bacteria named *E. coli* ATCC 25922(gram-negative) [449]. All bacteria solutions were prepared in Tryptic Soy Broth (TSB), and Tryptic Soy Agar (TSA) was used for bacteria inoculation.

The initial bacteria solutions were prepared by suspending colonies of each species in 2.0 mL 0.01 M PBS to obtain turbidity of 0.5 McFarland (MF). Then, each solution was diluted 100× in 0.01 M PBS, and 15 µL of the diluted solution was added to 45.0 mL TSB. The broth solutions were incubated for 18 hr. at 37 ˚C, shaking at 140 rpm (reaching 10^8 CFU/mL).

The overnight solutions were used to prepare bacterial lawns. The solutions were diluted by a factor of 100×. Then 100 µL of diluted solutions were spread on TSA plates and incubated for different time intervals (0, 2, 5, and 12 hr.) to reach different concentrations of bacteria.

8.1.6 Limit of Bacteria Detection via Nanobiosensors

Bacteria lawns on TSA with different concentrations of bacteria were used to find the threshold of color change regarding the concentration of bacteria (limit of detection). Different concentrations of bacteria were prepared by pre-incubating bacterial lawn at 37 ˚C for different time intervals. Pre-incubation is essential for bacteria to pass the lag phase, proliferate, and produce lipase. It also mimics the wound infection condition by providing a desired temperature and food source for bacteria growth. After the pre-incubation, the biosensors 1×1 (cm×cm) were placed on the bacteria lawns, incubated at 32 ˚C (skin temperature), and monitored for color changes every 15 minutes. The concentration of each plate was measured right after pre-incubation, and the required time for color change was recorded. Samples were placed on agar, and digital images were taken initially. The final digital images were taken when the first color change was observed, and the plate concentration was calculated with a standard drop-plating technique. Briefly, agar plugs were removed from the plates (n=4-6) with Integra Miltex Standard biopsy punches (d= 0.4 cm) sonicated for 2 min in 1 mL PBS to detach the bacteria from the surface of the agar. Then, 10× serial dilutions were plated drop by drop on the agar plates and incubated for 18 hr. at 37 °C. The number of colonies for each dilution was counted, and the concentration was found based on **Equations 8-2 and 8-3**.

$$Concentration\ of\ Bacteria\ \left({}^{CFU}/_{mL}\right) = \frac{Number\ of\ colones}{Used\ Volume\ (mL)\times 10^{Dilution}} \qquad \textit{Equation 8-2}$$

$$Concentration\ of\ Bacteria\ \left({}^{CFU}/_{cm^2}\right) = \frac{number\ of\ colones\ extracted\ from\ the\ biopsy\ \ (CFU)}{\pi r^2} \qquad \textit{Equation 8-3}$$

8.1.7 Colorimetric Behavior of Nanobiosensors in The Presence of Bacteria

We used the CMC system to find the color information, and CF=1 was considered for the ΔE data. In addition to the quantitative data for the color change, a color pallete was prepared for

each bacterium and each membrane at the threshold concentrations and high concentrations that can be used as a reference for the color-changing behavior of the biosensors. It should be noted that the data was compared to its own control on an agar plate for each sample.

$$\Delta E = \sqrt{\left(\frac{\Delta L}{lS_L}\right)^2 + \left(\frac{\Delta C}{cS_C}\right)^2 + \left(\frac{\Delta H}{S_H}\right)^2}$$

Where

$$\Delta C = C_1 - C_2 \qquad C_{1=}\sqrt{{a_1}^2 + {b_1}^2} \qquad C_2 = \sqrt{{a_2}^2 + {b_2}^2}$$

$$\Delta H = \sqrt{\Delta a^2 + \Delta b^2 - \Delta c^2} \qquad \Delta L = L_1 - L_2 \qquad \Delta a = a_1 - a_2 \qquad \Delta b = b_1 - b_2$$

$$S_L = o.511 \; if \; L_1 < 16 \qquad S_L = \frac{0.040975 L_1}{1 + 0.017654 L_1} \; if \; L_1 \geq 16$$

$$S_c = \frac{0.0638 C_1}{1 + 0.0131 C_1}$$

$$S_H = S_C(FT + 1 - F)$$

$$T = 0.56 + |0.2\cos(H_1 + 168°)| \; if \; 164° \leq H_1 \leq 345°$$

$$T = 0.36 + |0.4\cos(H_1 + 35°)| \; otherwise$$

$$F = \sqrt{\frac{{C_1}^4}{{C_1}^4 + 1900}} \qquad H = Arctan(\frac{b_1}{a_1}) \quad H_1 = H \; if \; H \geq 0 \quad H_1 = H + 360° \; otherwise$$

CMC is a common way to compare colors in the textile industry and is a tolerancing system. The provided formula defines an ellipsoid around the standard color that the semi-axis resembles hue, chroma, and lightness. For this study, we chose CF=1, which means $\Delta E \geq 1$ corresponds to a significant color change from yellow. In addition to ΔE, the difference in the hue of samples is also reported as an absolute color change, and larger Δh presents a more decent color change.

8.1.8 Cleaved Dye Characterization

The composition of HCy after being exposed to bacteria ($3.0E{\times}10^4 CFU/cm^2$) was examined using ESI MS to verify its cleavage. Following exposure to bacteria, the dye was extracted from the electrospun membranes by immersing them in ethyl acetate for 24 hours and then filtering the solution through a 0.2 μm syringe filter. Since there was a chance of cleavage during the ionization, the pure HCy dye was used for normalizing the data, and the cleavage rate was calculated based on the following formula (**Equation 8-4**):

$$Cleavage\ rate = \left(\frac{\left(\frac{Intensity\ of\ BD\ at\ 302\frac{m}{z}}{Intensity\ of\ BD\ at\ 302\frac{m}{z} + Intensity\ of\ BD\ at\ 400\frac{m}{z}}\right)\times 100 - \left(\frac{Intensity\ of\ PD\ at\ 302\frac{m}{z}}{Intensity\ of PD\ at\ 302\frac{m}{z} + Intensity\ of\ PD\ at\ 400\frac{m}{z}}\right)\times 100}{\left(100 - \left(\frac{Intensity\ of\ PD\ at\ 302\frac{m}{z}}{Intensity\ of PD\ at\ 302\frac{m}{z} + Intensity\ of\ PD\ at\ 400\frac{m}{z}}\right)\times 100\right)}\right)\times 100$$

Equation 8-4

Where BD is the Bacterial exposed dye, and PD is the Pure yellow dye

8.1.9 Assay of Lipase Activity

An assay of lipase activity was conducted as follows. The bacteria plates were prepared as described previously, and after 5 hr. of incubation at 37 ˚C, samples were placed on the plates. The initial concentration of each plate was calculated based on the biopsied agar plug upon placing the samples, and the final concentration of each plate was calculated based on the biopsied agar plug after 5 hr. of incubation at 37 ˚C. Regarding the lipase activity, the initial activity was calculated for pre-incubated agar based on the biopsied agar plug, and the final activity was calculated for bacteria in contact with the collected membranes. The bacteria were separated from the membranes/agar plugs with ultrasonication for 2 min, then centrifuged at 10,000 g for 15 min. 50 μL of each solution was added to a well in a 96-well plate containing assay buffer and reagents. The plate was read with a microplate reader (BioTek-PowerWave XS2) in kinetic mode at 37 °C

with readings every 2 min for 1 hr. A standard curve was prepared based on the manufacturer's protocol, and the lipase activity was calculated for each sample (n=6). The kit quantified the lipase activity through the interaction of cleaved substrate (triglycerides) with mixed enzymes and a colorimetric probe (oxi-red).

8.1.10 Interaction of Bacteria and Nanobiosensors (Effect of Alignments on Bacteria Localization)

The high concentration plate of MRSA (5.2×10^8 CFU/cm^2) was used to evaluate the interaction between bacteria and biosensors. Biosensors with 1×1 (cm×cm) dimensions were placed on agar and incubated for 1 hr. at 32 ˚C. Then biosensors were collected and immersed in glutaraldehyde solution (0.25 %) for the fixation procedure (30 min, room temperature). Then, the biosensors were washed with 0.01M PBS three times and immersed in a series of ethanol (30%, 50%, 70%, 80%, 90%, 100%) for 10 min; the 100% solution was changed twice. Then, the samples were air dried for 18 hr. before analyzing with SEM (FEI Quanta FEG 650). Samples were sputter coated for 45 s with gold−palladium (60:40), and SEM was conducted with an accelerating voltage of 10.0 kV. The SEM images were analyzed with ImageJ software to count the number of bacteria and evaluate their interaction with membranes. For each sample, one image with 1,000X, one image with 2,000X, one image with 5,000X, and three images with 10,000X magnification were used for counting the bacteria.

8.1.11 Colorimetric Behavior of Nanobiosensors in an *ex-vivo* Burn Model

Pig skins were cut into 4×4 (cm×cm) pieces and were burnt with a heated brass rod (2× 2 (cm×cm)- 9.2 N) for 1 min, and then the burnt skins were placed in a NaCl (0.9%) solution for 10 min, followed by 70% Ethanol. The skins were air-dried and sterilized with UV prior to bacterial inoculation.

8.2 Results and Discussion

8.2.1 Chemical Characterization of Nanobiosensors

This study aimed to increase the sensitivity of bacterial detection by chemical means, incorporating Tween 80 in the shell composition and physical means, controlling nanofiber alignment. Various nanofibrous membranes based on tecophilic HP-60D-35 (hydrophilic aliphatic polyurethane, PU) were fabricated with a core-shell nanofiber structure. All membranes had PU as their core and PU: PVP with a 2:1 ratio as their shell. Randomly oriented electrospun nanofibers and cross-aligned electrospun nanofibers only based on PU and PVP were fabricated as controls to evaluate the role of alignment. Moreover, membranes with different concentrations of Tween 80 from 0% to 4% (w/v) were prepared to investigate the role of the surfactant in boosting sensitivity.

The chemical composition of the membranes was characterized by ATR-FTIR. The chemical structures of components and the main peaks of each membrane are presented in **Figure S8-1**. The spectrum of the aligned membrane (W) was subtracted from that of the membrane containing 4% v/v Tween 80 (T4) (T-W) to evaluate the presence of Tween 80 in the membrane. The absence of the peak related to the C≡N stretch at 2250 cm^{-1} demonstrated that the subtraction was done correctly since this peak of HCy dye should have the same intensity in both samples. The remaining peaks are characteristic of Tween 80, including $–H_2C–O–CH_2–$ (946 cm^{-1}), $–CO–O–CH_2–$ (1100 cm^{-1}), $–CH_2–CH_3$ (2855 $cm^{-1}$and 2900 cm^{-1}), O–H (3600 cm^{-1}), and C=O stretch at 1732 cm^{-1} [450]. These peaks demonstrated that Tween 80 was successfully incorporated into the shell of nanofibers without any chemical interaction with other polymers or the dye.

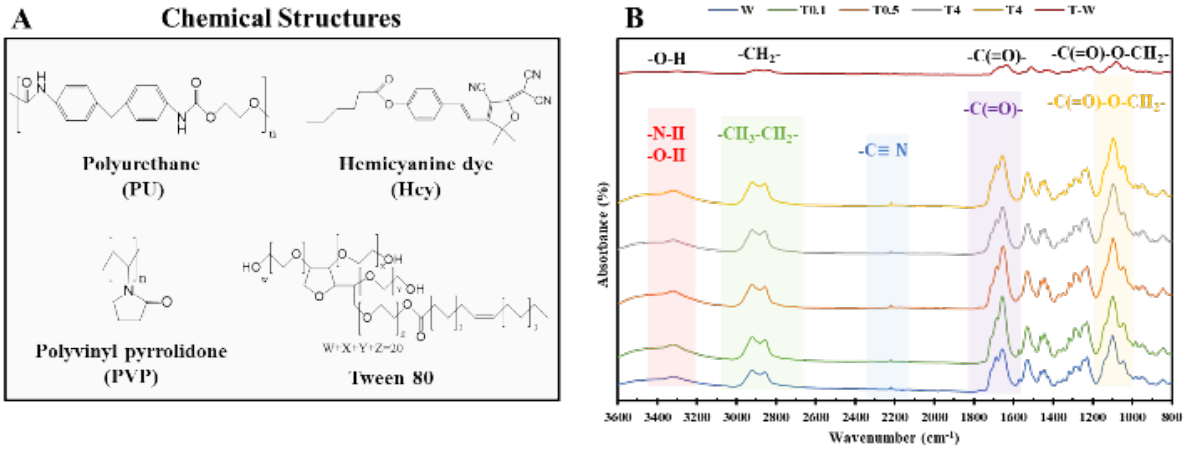

Figure S8-1 A) Chemical structures of components, B) ATR-FTIR spectra of membranes: cross-aligned nanofibers (W), cross-aligned nanofibers with 0.1% Tween 80 (T0.1), cross-aligned nanofibers with 0.5% Tween 80 (T0.5), cross-aligned nanofibers with 2% Tween 80 (T2), cross-aligned nanofibers with 4% Tween 80 (T4), and difference spectrum of T4 and W (T4-W).

8.2.2 Morphological Characterization of Nanobiosensors

SEM images of the nanofibrous membranes were taken with different magnifications to evaluate the diameter and alignment of the nanofibers. **Figure S8-2** presents the SEM images of the samples (R, W, T0.1, T0.5, T2, and T4) with two magnifications (1,000× and 10,000×).

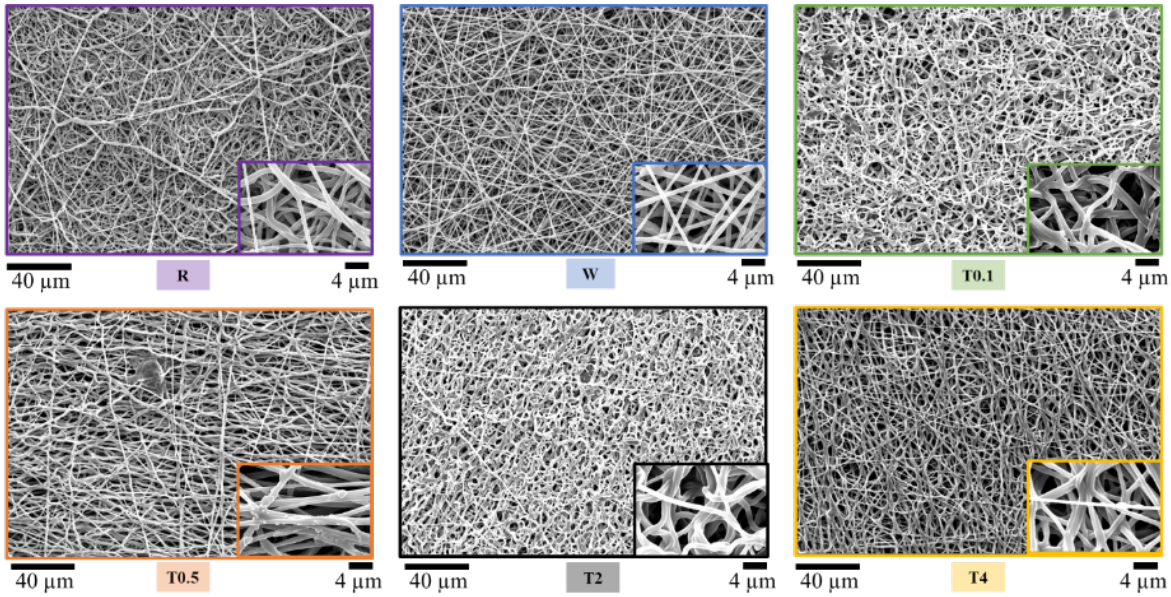

Figure S8-2 SEM images of samples with two magnifications (1,000× and 10,000×): randomly oriented electrospun nanofibers (R), cross-aligned nanofibers (W), cross-aligned nanofibers with 0.1% Tween 80 (T0.1), cross-aligned nanofibers with 0.5% Tween 80 (T0.5), cross-aligned nanofibers with 2% Tween 80 (T2), cross-aligned nanofibers with 4% Tween 80 (T4).

Each SEM image at 10,000 magnification was analyzed using ImageJ software to find nanofiber diameter, and more than 300 nanofibers from different regions were chosen for measurement. The nanofiber diameter distribution of each sample is presented in **Figure S8-3**.

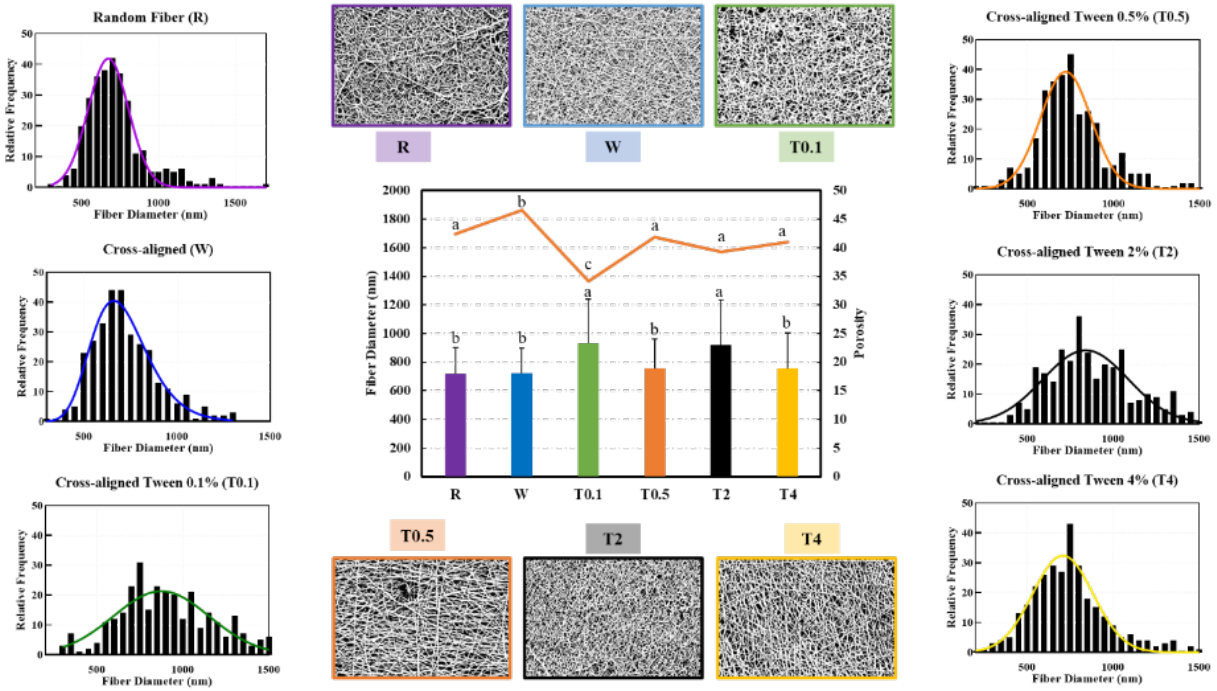

Figure S8-3 Distribution of nanofibers diameter, mean fiber diameter, and porosity calculated based on processed images with ImageJ (For all variables with the same letter on top, the difference between the means is not statistically significant. If two variables have different letters, they are significantly different).

Regarding the role of Tween 80 on fiber diameter and distribution, it can be said that by adding Tween 80 at a concentration of 0.1v/v%, the nanofiber diameter increased to 932±307 µm and exhibited a wider distribution. This was attributed to the presence of Tween 80 in the solution, which resulted in larger droplet formation and nanofibers with a larger diameter despite keeping the feeding rate and voltage constant for all samples. By increasing the concentration of Tween 80 to 0.5%, a smaller mean nanofiber diameter (757 ± 204 µm) than T0.1 but almost in the same range as W and R was obtained. Regarding the nanofiber distribution, a higher Tween 80 concentration (T0.5) led to the collection of more uniform nanofibers with a narrower nanofiber distribution than T0.1. Increasing the concentration to 2% again caused the same phenomenon as

T0.1, an increase in nanofiber diameter and distribution (919±317 μm). However, the diameter decreased to the initial size (757 ± 245 μm) again by adding more Tween 80 (4%).

Nanofiber diameter in electrospinning can be affected by various parameters such as concentration, viscosity, conductivity, and surface tension of the solution, and the presence of surfactant can change all of these parameters [451,452]. The effect of surfactants on the nanofiber diameter and distribution depends on the critical micelle concentration of surfactant (CMC) and critical aggregation concentration (CAC) of polymer-surfactant in the polymer solution [453]. The CMC of Tween 80 in an aqueous solution at room temperature is 0.015 mM; however, it changes by changing the solvent or addition of a cosolvent [454,455]. Tween 80 does not have CMC in pure DMF, but adding a cosolvent such as THF can cause micellization or reverse micellization, depending on the cosolvents' percentages. Santhanalakshmi [456] explored the role of organic cosolvents on the CMC of Tween 80 and showed that as the fraction of CCl_4 decreased in CCl_4:DMF solution, the CMC of Tween 80 also decreased (1:0 1.78 mM to 0.2:0.8 1.08 mM). Since there has not been an investigation of THF: DMF cosolvent, we could not compare the data, but probably 0.1% Tween 80 (0.8 mM) is lower than the CMC of Tween 80 in DMF: THF and micelles were not formed. However, the presence of Tween 80 in the solution might increase the viscosity due to interaction with polymers (CAC) and lead to a larger fiber formation [453]. When the concentration of Tween 80 was increased to 0.5% (4.0 mM), the micelles were probably formed. The presence of micelles might interrupt the PU, PVP, and dye complex (hydrophobic forces and hydrogen bonds between Tween 80 and polymers), leading to decreased viscosity and, therefore, decreased nanofiber diameter. However, Increasing the concentration of Tween 80 to 4% did not result in any further significant decrease in nanofiber diameter.

In addition to nanofiber diameter measurements, SEM images were used to measure the 2D porosity of the nanofibers. The 2D porosity of nanofibers, especially the surface layers, plays an essential role in the localization of bacteria. The 2D porosity was measured with ImageJ software by changing the images' threshold to separate the nanofibers from empty spaces. Based on the obtained result (**Figure S8-3**), the 2D porosities of different membranes were as follows 41.8±2.0% R, 46.2±1.3% W, 33.9±1.3% T0.1, 40.9±1.3% T0.5, 38.9±1.4% T2, and 39.7±1.5% T4.

8.2.3 Limit of Bacteria Detection via Nanobiosensors

To test the detection response threshold, we prepared different concentrations of three main bacteria responsible for wound infection, namely *E. coli*, *P. aeruginosa,* and MRSA. Different concentrations of bacteria were prepared by pre-incubating bacterial lawn at 37 ˚C for different time intervals. The pre-incubation is essential for bacteria to pass the lag phase and begin to proliferate, producing lipase. It also mimics the wound infection condition by providing a desired temperature and food source for bacteria growth. After the pre-incubation, the biosensors were placed on the bacteria lawns, incubated at 32 ˚C (skin temperature), and monitored for color changes every 15 minutes. The concentration of each plate was measured right after pre-incubation, and the required time for color change was recorded.

Table S 8-3 Bacteria Concentration at the time of color change

Bacteria	Threshold Concentration CFU/cm^2)	Exposure time
E. coli	$4.20\times10^{5*}$	1 hr.
MRSA	2.77×10^{4}	Immediate
P. aeruginosa	3.17×10^{4}	Immediate

*4.20E+05 is the initial concentration, and the final concentration post 1 hr. incubation is 5.2E+05

Figure S8-4 presents the threshold concentrations, and the minimum time needed for the color to change. The reported time corresponded to the first sample that underwent a color

change. For *E. coli*, all samples incorporated with Tween 80 exhibited a green color simultaneously. In the case of *P. aeruginosa*, all samples with Tween 80 showed a green color simultaneously, except for T0.1. As for MRSA, T0.5 and T2 demonstrated the fastest green color change.

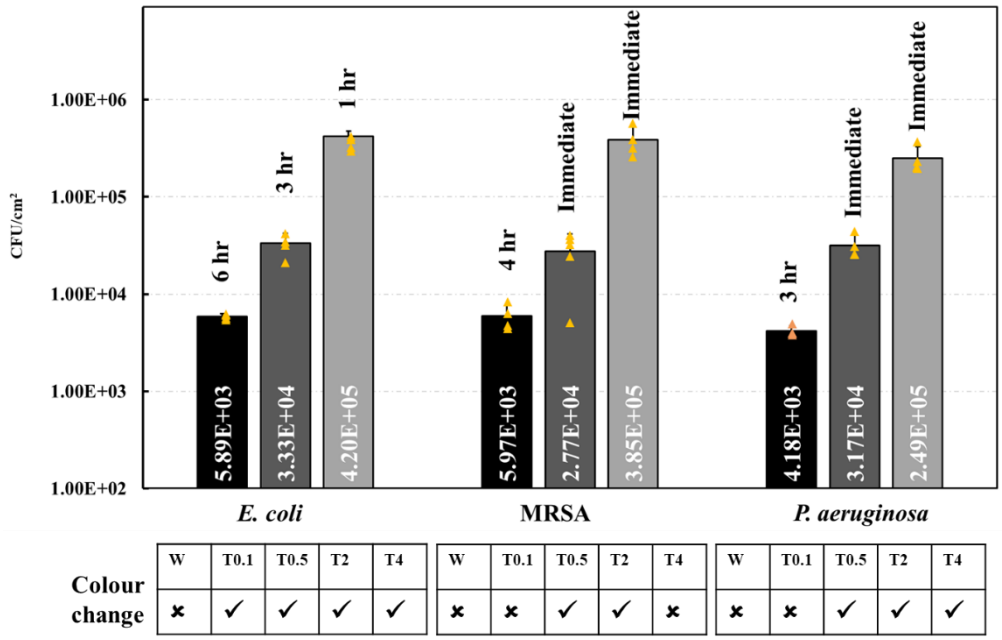

Figure S8-4 The Detection threshold for different bacteria at different concentrations and exposure times. Only the samples indicated with ✓showed the color change at the threshold.

8.2.4 Colorimetric Behavior of Nanobiosensors in The Presence of Bacteria

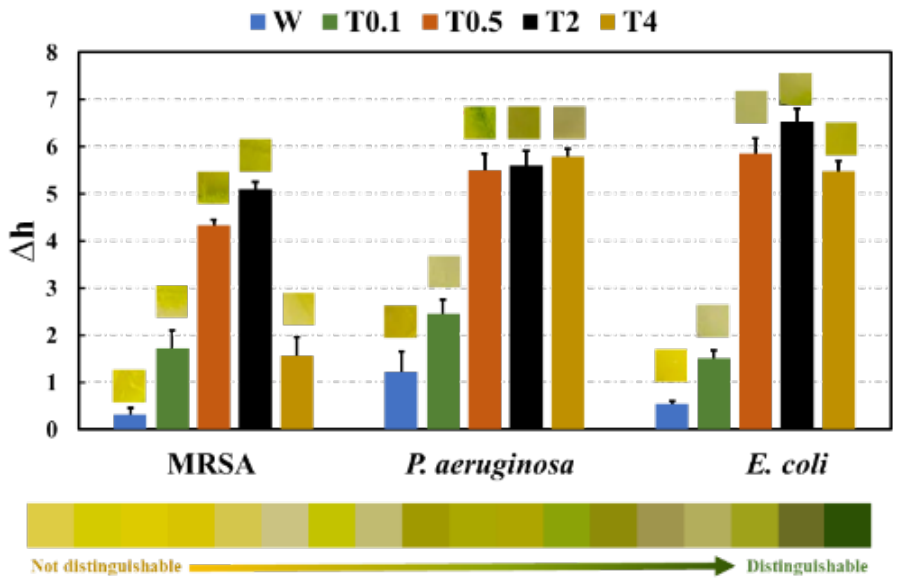

Figure S8-5 Δh (difference in hue) of various samples in the presence of the three bacteria

9 Chapter 9 Appendix 2

Supporting Information

Nanofibrous Theranostic Biosensor for Visual Infection Detection and Triggered Drug Release: ROS-Responsive Nanoparticles to Prevent Bacterial Resistance

*Farinaz Jonidi Shariatzadeh[1],, Sarvesh Logsetty[2] and Song Liu[1,3]**

1)Biomedical Engineering, Faculty of Engineering, University of Manitoba, Winnipeg, Manitoba, Canada, R3T 2N2

2)Departments of Surgery and Psychiatry, Rady Faculty of Health Sciences, University of Manitoba, Winnipeg, Manitoba, Canada, R3E 3P5

3)Department of Biosystems Engineering, Faculty of Agricultural and Food Sciences, University of Manitoba, R3T 2N2

* Correspondence to: song.liu@umanitoba.ca; +1) 204-474-9616).

KEYWORDS: nanofibrous membranes, responsive nanoparticles, lipase, antibiotics, colorimetric, targeted release

9.1 Figures

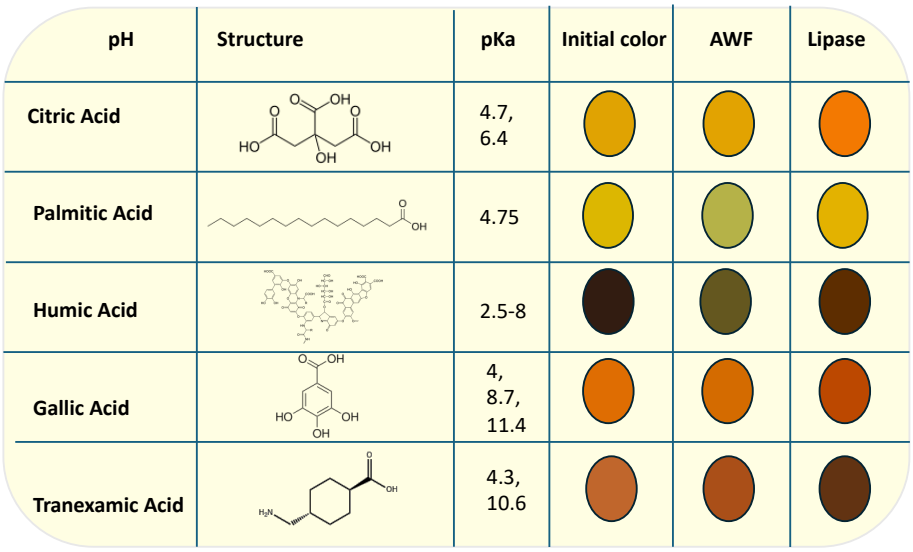

Figure S9-1 Effect of the addition of different acids to the biosensors and its performance in AWF solution with and without lipase.

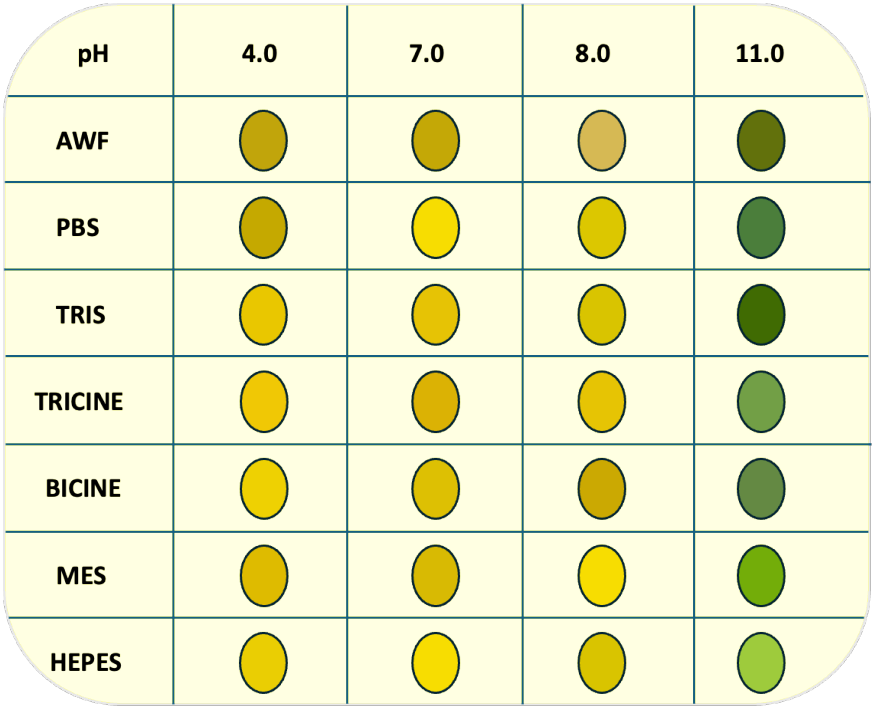

Figure S9-2 Color-changing response of the biosensor in the presence of different buffers at different levels of pH.

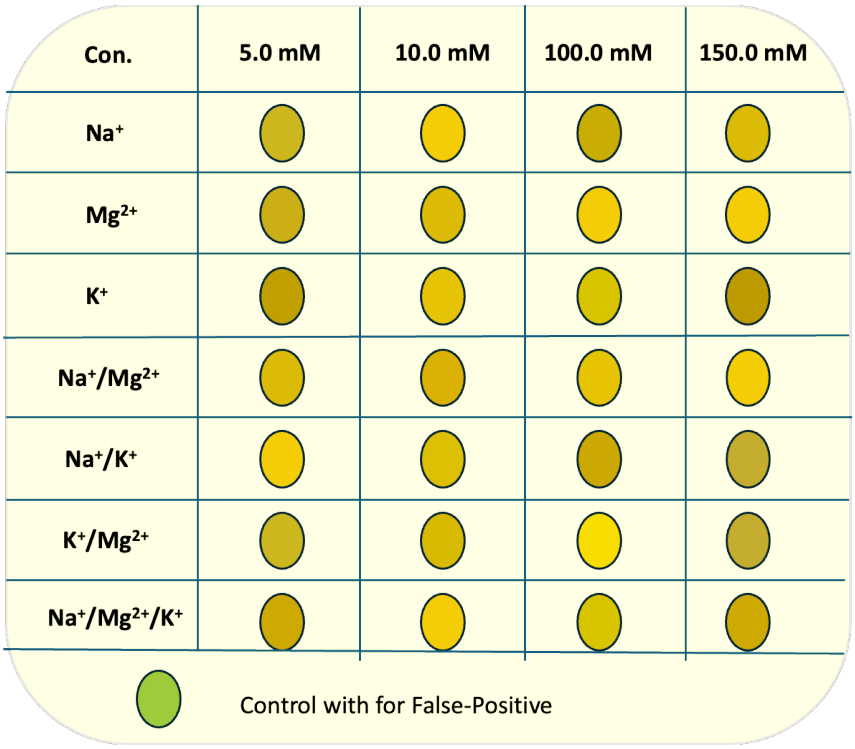

Figure S9-3 Color-changing response of the biosensor in the presence of different ions at different concentrations.

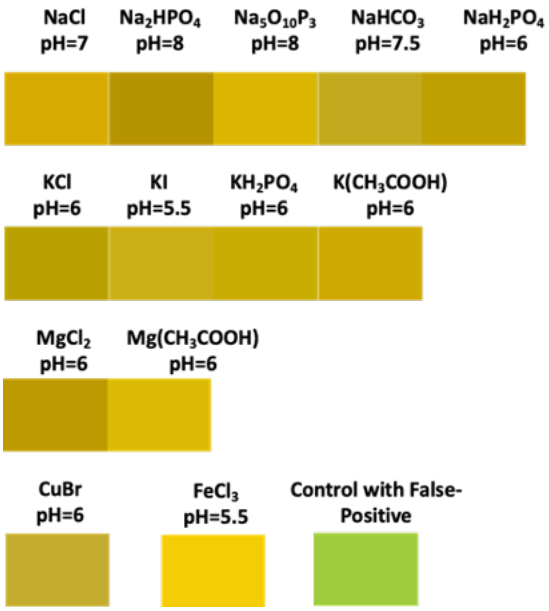

Figure S9-4 Color-changing response of the biosensor in the presence of different salts.

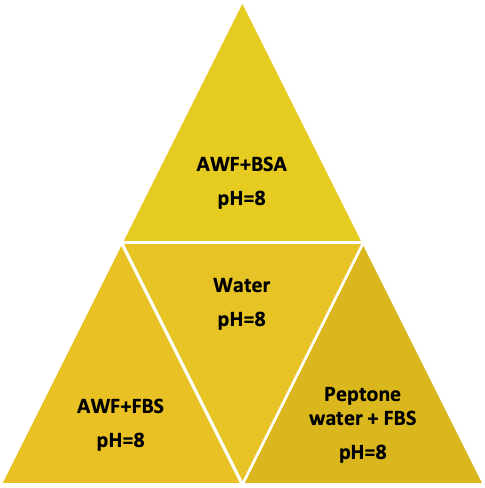

Figure 9-5 Color-changing response of the biosensor in the presence of different proteins.

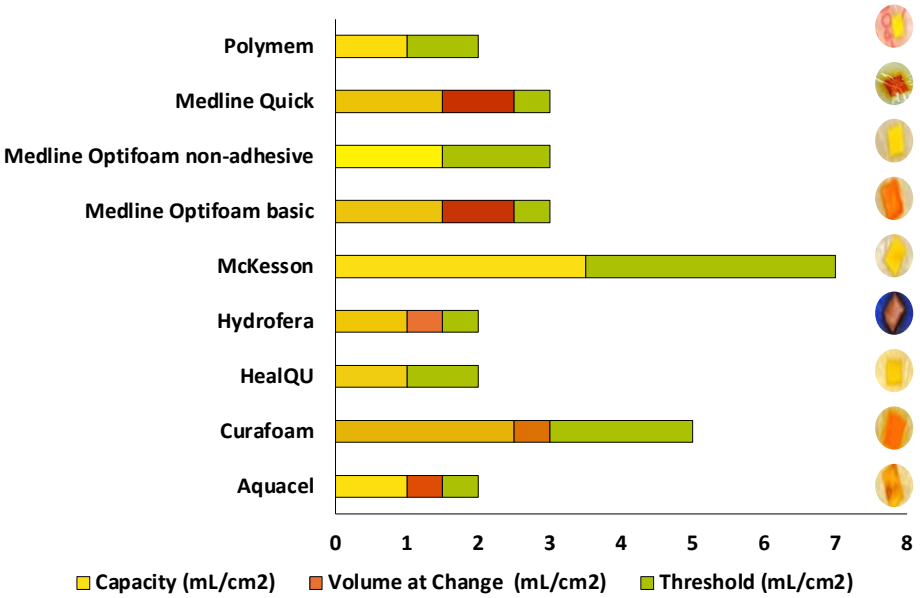

Figure 9-6 The water uptake capacities of the foam (yellow), the volume required for a positive color change (orange), and the threshold volume that triggered the false positive (green).

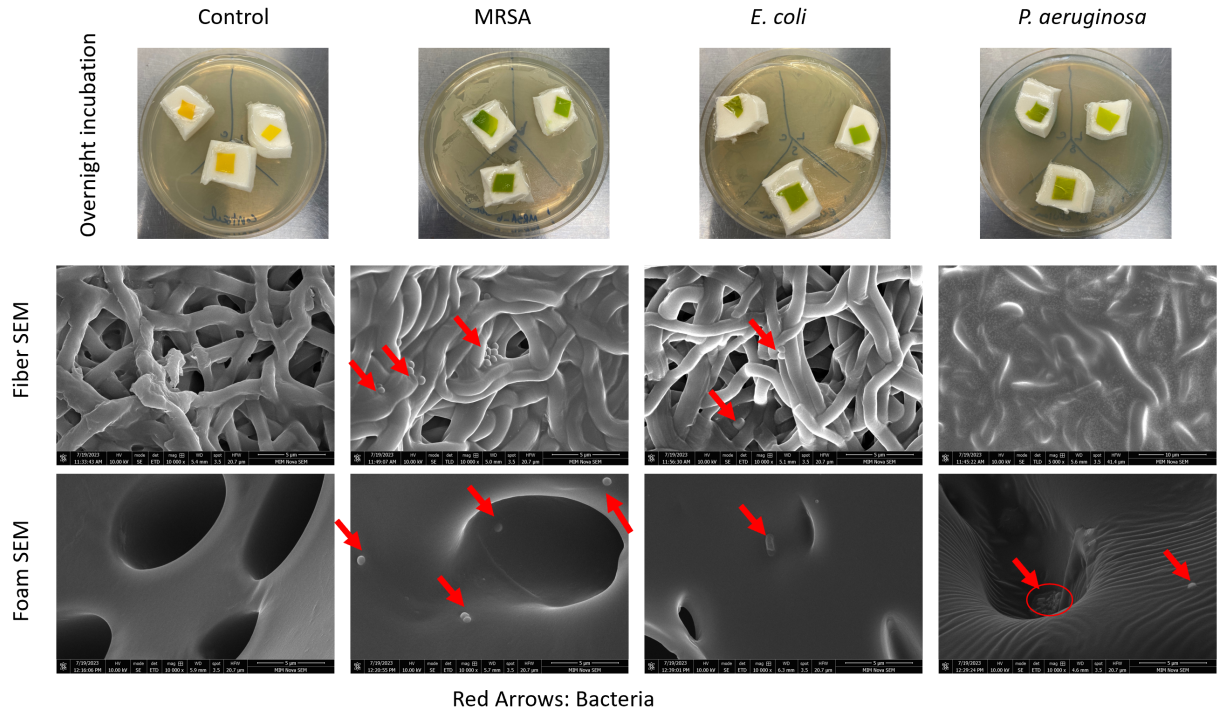

Figure S9-7 The plates after overnight incubation with Curafoam-paired biosensors and the SEM images of the foam and the biosensors to show the presence of bacteria.

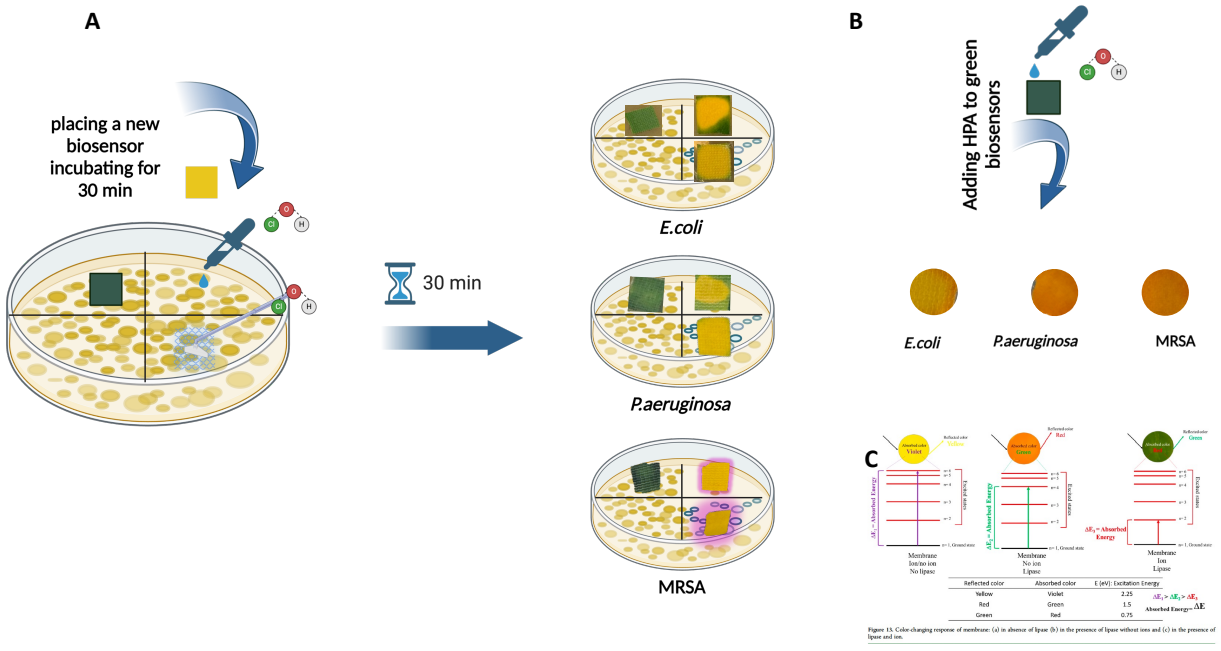

Figure 9-8 A) Treating the bacteria agar plates with HPA wound cleaning solution either directly pouring the solution or rubbing the agar with gauze soaked in the solution for three different strains of bacteria to evaluate the color change of the biosensors after treatment. B) immersing the color-changed biosensors in the HPA solution to evaluate the color stability. C) color theory regarding orange and green colors of the dye after cleavage in different environments.

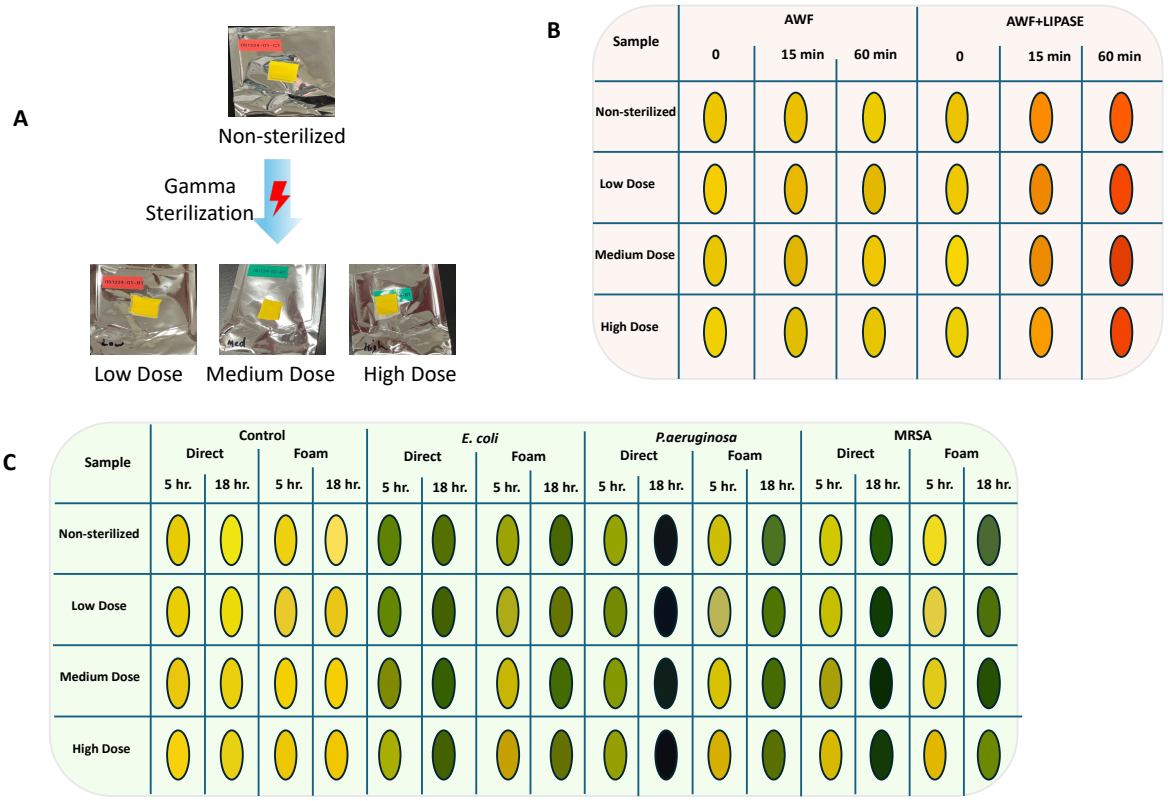

Figure 9-9 A) sterilized samples with three different dosages. B) the results of the bench tests of the sterilized samples, and C) the results of the bacteria tests for sterilized samples.

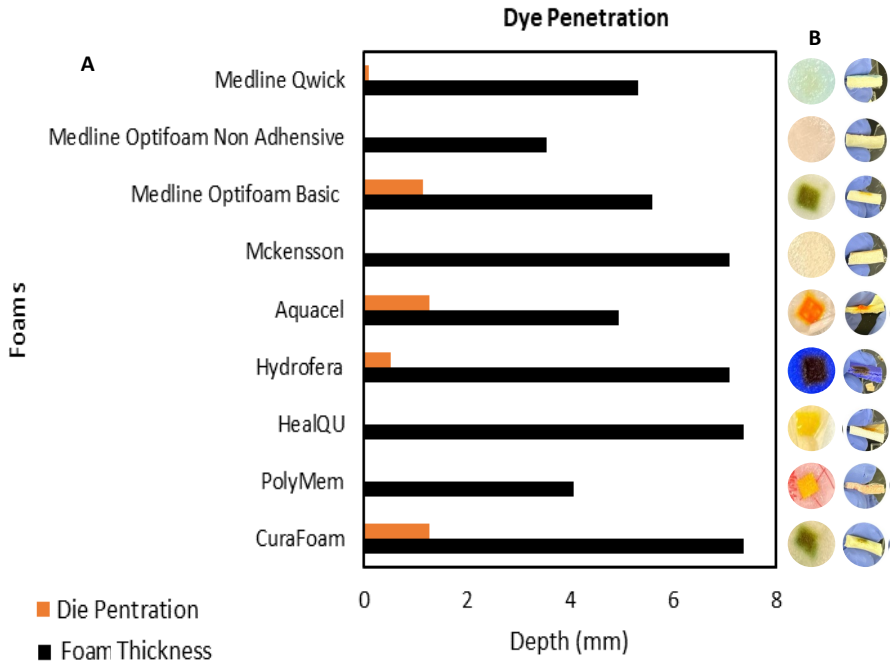

Figure 9-10 A) The foam thickness and penetrated dye through the foam height. B) the dye stains on top of the foams after removing the biosensors and cross-section of the foams to show the penetrated dye throughout the foams.

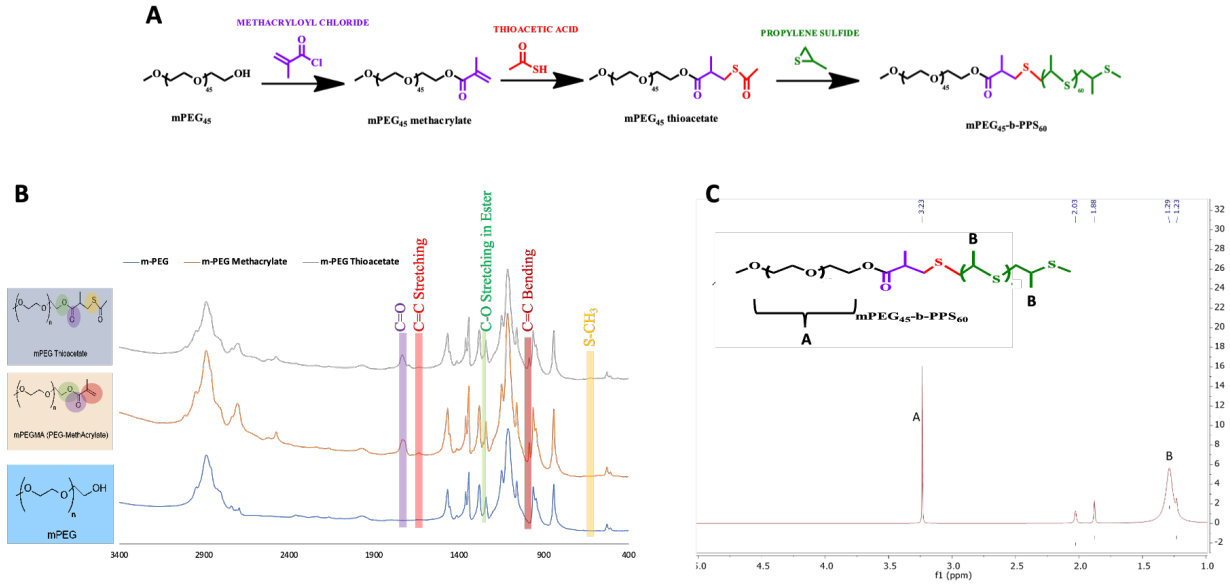

Figure S9-11 A) Schematic of reaction for synthesizing ROS-responsive PEG_{45}-b-PPS_{60} co-polymer. B) FTIR spectra of mPEG, mPEGMA, and m-PEG Thioacetate and C) The NMR spectrum of PEG_{45}-b-PPS_{60} co-polymer

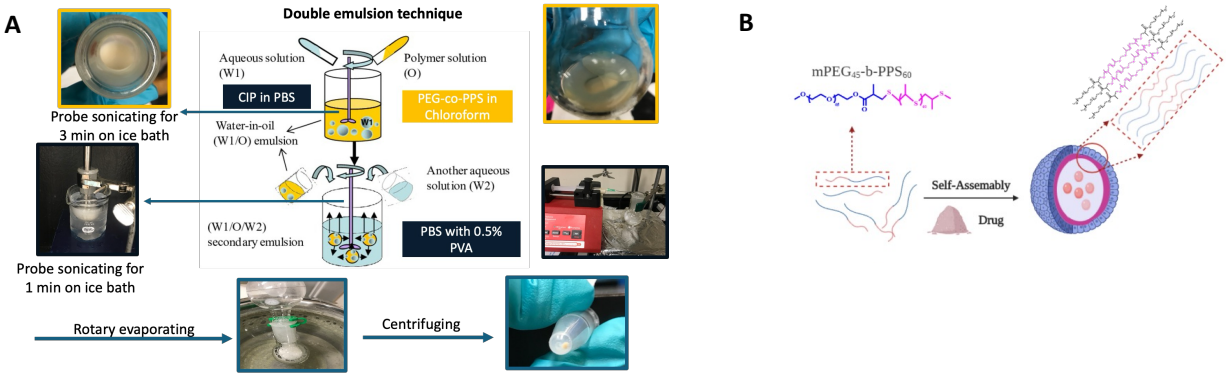

Figure S9-12 A) Double-emulsion technique for fabricating ROS-responsive NPs loaded with ciprofloxacin. B) Self-assembly of PGE_{45}-b-PPS_{60}.

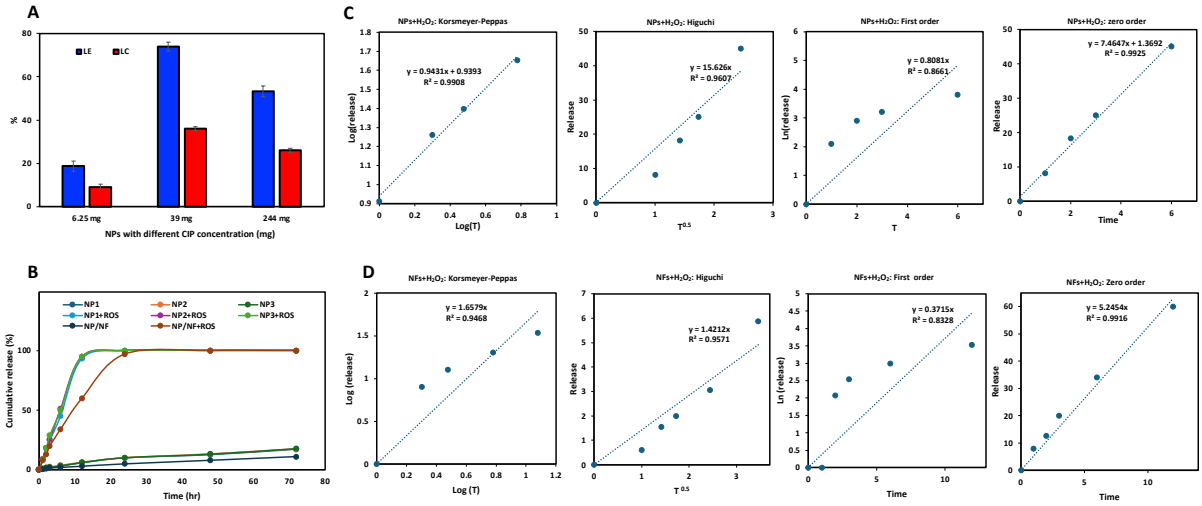

Figure 9-13 A) The loading efficiency and loading capacity of different concentrations of CIP loaded into NPs. B) The release profile of CIP from different NPs and NFs loaded with NPs ND C) The release models fitted on the release profile in the presence and absence of ROS agent.

9.2 Tables

Table 9-1 The properties of tested commercially available foam to test the compatibility of the biosensor.

Foams	Images	Foam Structure	Material Composition	Thickness
Aquacel		Semi-occlusive surface Multi-layer	PU foam layer Hydrofiber wound contact layer Waterproof film	~4mm
Curafoam		Occlusive surface Single layer	Polyurethane foam	~5.5 mm
HealQU		Closed surface Multi-layer	Silicon (wound contact layer) Foam layer and Waterproof film	~5mm
Hydrofera		Occlusive surface Single layer	Polyvinyl alcohol sponge foam	~3mm
McKesson		Closed surface Multi-layer	Hydrocellular foam Waterproof film	~7mm
Medline Optifoam basic		Occlusive surface Single layer	PU foam	~5.5mm
Medline Optifoam non-adhesive	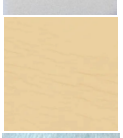	Closed surface Multi-layer	Hydrophilic foam Waterproof film	~4 mm
Medline Quick		Semi-occlusive surface Multi-layer	Polyacrylate fiber PU foam	~4mm
Polymem	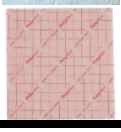	Closed Surface Multi-layer	PU foam Waterproof film	~3mm

Table 9-2 Color changing responses of paired biosensors with different foam on only agar bacterial test.

Foams	*E. coli*	*P.aeruginosa*	MRSA	Control
Aquacel				
Curafoam				
HealQU				
Hydrofera				
Medline Optifoam basic				
Medline Optifoam non-adhesive				
Medline Quick				
Polymem				
Biosensor				

Table 9-3 Color changing responses of paired biosensors with different foam on agar with SEF bacterial test.

Foams	*E. coli*	*P.aeruginosa*	MRSA	Control
Aquacel				
Curafoam				
HealQU				
Hydrofera				
Medline Optifoam basic				
Medline Quick				
Polymem				
Biosensor				

Table 9-4 The initial concentrations for each bacterium and concentration after each treatment at the time that color change was observed.

Bacteria	Initial Con.	Conc. Gauze treatment	Conc. Direct solution treatment
E. coli	2.73E+14 ±4E+13	1.27E+05 ±1.5E+04	2.77E+08 ±3.0E+07
P. aeruginosa	2.53E+14 ±4.0E+13	3.4E+06 ±3.0E+5	1.2E+09 ±1.0E+08
MRSA	2.67E+14 ±7.6E+13	3.4E+05 ±2.5E+04	2.37E+08 ±1.5E+07

9.3 Results and Discussion

9.3.1 Compatibility of The Biosensor with Commercial Foams

Since the color change mechanism of the biosensors relies on the presence of lipase, the penetration of water from the foam to the biosensor is critical. However, this presents a challenge regarding an excess of wound fluid. The wound fluid, which is rich in salts, could potentially trigger a false positive. A bench test was designed to evaluate the water uptake capacity of various foams, determine the minimum volume required to induce a color change in the presence of lipase and identify the amount of excess fluid that causes a false positive for each foam.

The results of this bench test are shown in **Figure S9-6**, where the displayed colors represent the actual biosensor responses. As indicated in the figure, several biosensors did not show any orange color change in the presence of lipase, including Polymem, Medline Optifoam Non-Adhesive, McKesson, and HealQU. The common feature of these foams is the presence of a protective waterproof layer, which prevents lipase from interacting with the biosensor. Thus, no color change occurs. For the remaining foams, a positive color change was observed before reaching the threshold for a false positive. Based on this, the foams were classified into three categories according to their exudate-handling capacity. Foams suitable for low-exudate wounds were to be paired with the biosensor for infection detection which included Hydrofera and Aquacel. Foams suitable for medium-exudate wounds include Medline Optifoam Basic and Medline Quick. Finally, the foam best paired with the biosensor for high-exudate wounds is Curafoam.

After bench-testing the compatibility of the biosensors with the foams, two versions of bacterial tests were conducted. In these tests, the biosensors were placed on top of the foams and covered with Tegaderm to simulate clinical conditions more accurately. In the first bacterial test, no

stimulated wound exudate was used, and the foams were placed on top of agar plates. Since the foams were not in direct contact with the agar and there was insufficient fluid to transport citric acid from the sensor to the agar, no inhibition zones were observed around the samples. This also delayed exposure of the dye to the lipase.

In this test, a biosensor without foam was used as a control to evaluate the color change of foam-incorporated biosensors. Among the tested foams, only Curafoam showed a noticeable color change within the first 6 hours for all three bacterial strains. For *E. coli*, additional foams, such as Aquacel, Hydrofera, and Medline Optifoam Basic, began to turn green at the edges, though the color change for *P. aeruginosa* and MRSA was not as prominent, **Table S9-2**. None of the other foam-paired samples exhibited a color change within the initial 6-hour period. After overnight incubation, other samples without a waterproof membrane, including Medline Quick and those that had already begun to change color, turned dark green. Meanwhile, the control, along with HealQU, Medline Optifoam Non-Adhesive, and Polymem, remained yellow. These results aligned with the bench test findings, confirming that the waterproof layer interferes with the biosensor's sensitivity and overall performance.

In the second bacterial test, SWF was used to replicate the presence of exudate in a wound. Curved agar plates were prepared to ensure the foam-paired biosensor was in direct contact not only with the wound's surface but also with its edges, better mimicking the wound environment. In this setup, the presence of fluid increased the exposure of lipase to the dye, enhancing the interaction between the two. As a result, the color change occurred faster for all samples, as shown in **Table S9-3.**

All foams without a waterproof layer, including Aquacel, Curafoam, Hydrofera, Medline Optifoam Basic, and Medline Quick, exhibited a color change for all three bacterial strains tested. Given that the amount of SWF added at each interval (50 µL) and in total (500 µL) was below the threshold for all samples, no false positives were expected. However, HealQU and Polymem foams did not show a color change due to insufficient fluid penetration. Although a green color change was noticeable in all foams, the color change was less distinguishable with Hydrofera because of its blue color. Overall, the results from these tests suggest that pairing the biosensor with foams that facilitate water penetration from the wound to the biosensor or absorb sufficient wound fluid to expose the biosensor to lipase is effective. The biosensor is compatible with these types of foam dressings. The foams and biosensors were fixed and analyzed using SEM to evaluate the presence of bacteria and confirm that the color change observed in the bacterial test without SWF was due to lipase activity.

As shown in **Figure S9-75-6**, even in the absence of SWF, bacteria were able to migrate through the foam and reach the biosensor. Therefore, the color change resulted from lipase secretion by these bacteria, as well as from lipase transferred from the agar to the biosensor via the same pathway. This result confirms that the color change was solely due to the presence of bacteria, with no false positives, as the control samples remained yellow.

9.3.2 Compatibility of the biosensor with a wound-cleaning solution

In clinical practice, wound washing is a standard procedure, with one of the primary solutions for this purpose being HPA [457]. Therefore, evaluating the performance of biosensors in the presence of this cleaning solution is crucial. Plates incubated overnight with biosensors were used. The following day, 1 mL of HPA was applied to one quadrant of each plate, while another quadrant was cleaned using gauze soaked in HPA to achieve high bacterial concentrations. New

biosensors were then placed on the treated areas and monitored for color change within the first 30 minutes, as shown in **Figure S9-8A**. After the color change in each quadrant, a biopsy punch was taken to measure the bacterial concentration after cleaning treatment to find out the new bacteria load. The control quadrants for all three bacterial strains had concentrations around 10^{14} CFU/cm², with the final concentrations of treated sections after observing the color change of the newly placed biosensors presented in **Table S9-4**.

For *E. coli* and *P. aeruginosa* samples, the biosensors turned green from the edges within 30 minutes. In both strains, the quadrants cleaned with HPA-soaked gauze exhibited a greater log reduction in bacterial load, resulting in less vivid and slower color changes compared to those treated directly with HPA. The log reductions for *E. coli* were 9 for the gauze-cleaned quadrant and 6 for the direct solution treatment, while for *P. aeruginosa*, the reductions were 8 and 5, respectively. These results suggest that using HPA-soaked gauze was more effective at reducing bacterial load, as it combined both mechanical and chemical cleaning. This data is aligned with other studies on this cleaning agent and shows that alone, it is not able to clean the wound completely [458]. However, in both methods, the biosensors detected the remaining bacteria after treatment. The results for MRSA were different. The biosensor did not change color, but a red halo appeared around it, indicating the release of cleaved dye from the biosensor into the agar. The same pattern of bacteria reduction was observed in the MRSA samples, with a log reduction of 8 for the gauze-cleaned quadrant and 6 for the direct solution treatment.

Additionally, biosensors that had changed color overnight due to bacterial exposure for all bacteria strains were immersed in HPA to assess their compatibility with the cleaning solution and evaluate the stability of the color. Because HPA has an acidic pH, immersion caused the biosensor color to shift to orange, a mixture of red and yellow, as shown in **Figure S9-8B**. This

occurred because the acid neutralized the salts' effects on dye aggregation. Both green and orange colorations indicate cleaved dye but in different environments. As discussed previously, the presence of salts influences dye aggregation and affects electron layers, as depicted in Figure S**9-8C**. The results of these tests indicated that both methods—cleaning the wound with the solution before applying the biosensors or applying the biosensors first and then cleaning the wound—are effective. The biosensors remain viable in both conditions. Furthermore, if the observed color differs from yellow (either orange or green), it signals the presence of bacteria.

9.3.3 Performance of Biosensors after Sterilization

For clinical applications, biosensors must withstand the sterilization process. The biosensors were exposed to three doses of E-beam (**Figure S9-9A**), to test performance of sterilized biosensors. Following sterilization, all samples were subjected to both bench tests and bacterial tests, and their performance was compared to non-sterilized samples to assess whether sterilization impacted detection limits, sensitivity, or accuracy. As shown in **Figure S9-9B**, there were no significant differences in the time required for color change between the sterilized and control samples in the bench test. Additionally, no false positives were observed in any of the sterilized samples. These results indicate that the sterilization process did not deactivate the dye or the citric acid, which is crucial for preventing false positives.

In the bacterial tests (*E. coli*, MRSA, and *P. aeruginosa*), both direct testing and the use of foams showed that sterilized samples had similar color change timelines as non-sterilized samples, as shown in **Figure S9-9C**. This suggests that sterilization did not compromise the sensitivity or accuracy of the biosensors. For all samples, the initial color change was observed within the first 5 hours, with a dark green color developing after overnight incubation. These findings

demonstrate that the biosensors are compatible with sterilization, a critical step in preparing products for clinical use.

9.3.4 Leaching Test

The penetration of the cleaved dye from the biosensor into the environment is crucial, and this was evaluated by applying the biosensor to foam, which was then immersed in 5 mL of AWF-containing lipase overnight. After drying, the foams and biosensors were removed, and the surface and cross-sections of the foams were examined to detect the presence of dye. As shown in **Figure S9-10A**, the dye did not fully penetrate any of the foams, indicating a low risk of dye migration to a wound. As expected, in foams with a waterproof layer (Medline Optifoam Non-Adhesive, McKesson, HealQU, and Polymem), no dye penetration or cleavage occurred. For Medline Optifoam Non-Adhesive and McKesson, no dye stains were observed on the surface (**Figure S9-10B**). However, in the HealQ and Polymem foams, yellow dye remained on the waterproof layer after the biosensor was removed.

Among the other foams, Medline Qwick showed the least penetration, with 3.5% of the dye penetrating through the foam's height, and no visible dye remained on the top surface. Hydrofera exhibited 9.5% penetration, with the dye residue on the surface forming the complete shape of the biosensor. Medline Optifoam Basic and Curafoam both showed 20% penetration, with the remaining dye matching the shape of the biosensor. Aquacel had the highest penetration, with 30% of the dye reaching the foam's depth, and vivid color remained on the surface due to dye absorption by the foam.

These results indicate that dye penetration from the biosensor to the foam and the surrounding environment is possible. However, the likelihood of dye entering a wound is low, as it does not fully pass through the foam—additionally, the residual dye on the foam after biosensor removal

aids in visualizing the color change. Since dye penetration does occur, it is essential to assess the toxicity of the released dye.

10 Chapter 10 Appendix 3

Supporting Information

Enhanced Targeted Drug Delivery for Scar Prevention: Clathrin-Coated Solid Lipid Nanoparticles for Model Drug Encapsulation

Farinaz Jonidi Shariatzadeh[1], Vinith Yathindranath[2,6], Yang Liu[3], Donald W. Miller[2,6], Francis Lin[3], Sarvesh Logsetty[4] and Song Liu[1,5]*

1)Biomedical Engineering, Faculty of Engineering, University of Manitoba, Winnipeg, Manitoba, Canada, R3T 2N2

2) Department of Pharmacology and Therapeutics, University of Manitoba, Winnipeg, MB R3E 0Z3, Canada

3)Department of Physics and Astronomy, University of Manitoba, Winnipeg, MB R3T 2N2, Canada

4)Departments of Surgery and Psychiatry, Rady Faculty of Health Sciences, University of Manitoba, Winnipeg, Manitoba, Canada, R3E 3P5

5)Department of Biosystems Engineering, Faculty of Agricultural and Food Sciences, University of Manitoba, R3T 2N2

6)PrairieNeuro Research Centre, Rady Faculty of Medicine, University of Manitoba, Winnipeg, MB R3E 0Z3, Canada

* Correspondence to: song.liu@umanitoba.ca; +1) 204-474-9616).

KEYWORDS: scarless healing; targeted delivery; nanoparticles; triggered delivery; premature release

10.1 Figures

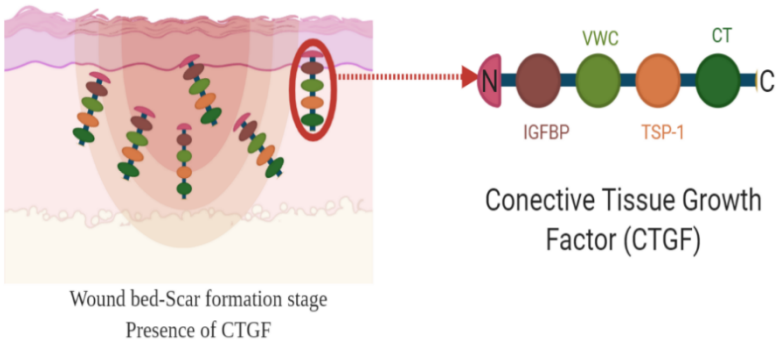

Figure 10-1 The Connective Tissue Growth Factor (CTGF) structure has four main domains: insulin-like growth factor-binding protein (IGFBP), von Willebrand factor type C repeat (VWC), thrombospondin type 1 repeat (TSP), and cysteine knot-containing carboxyl domain (CT).

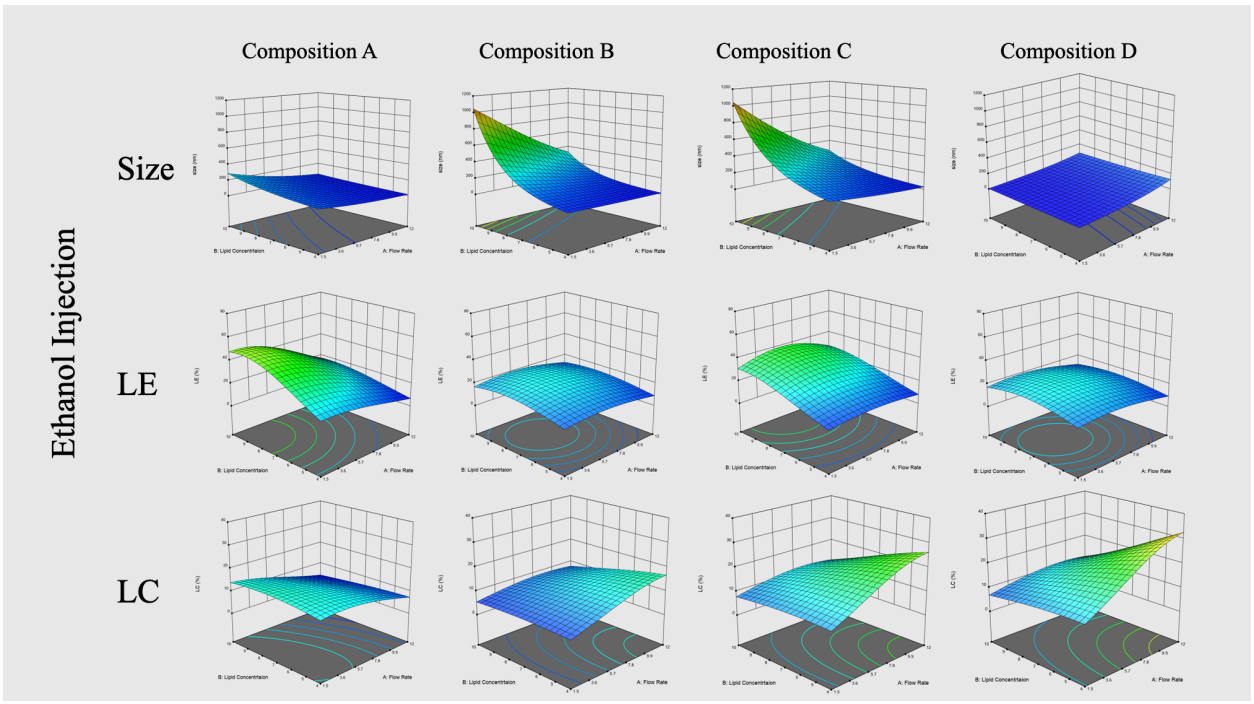

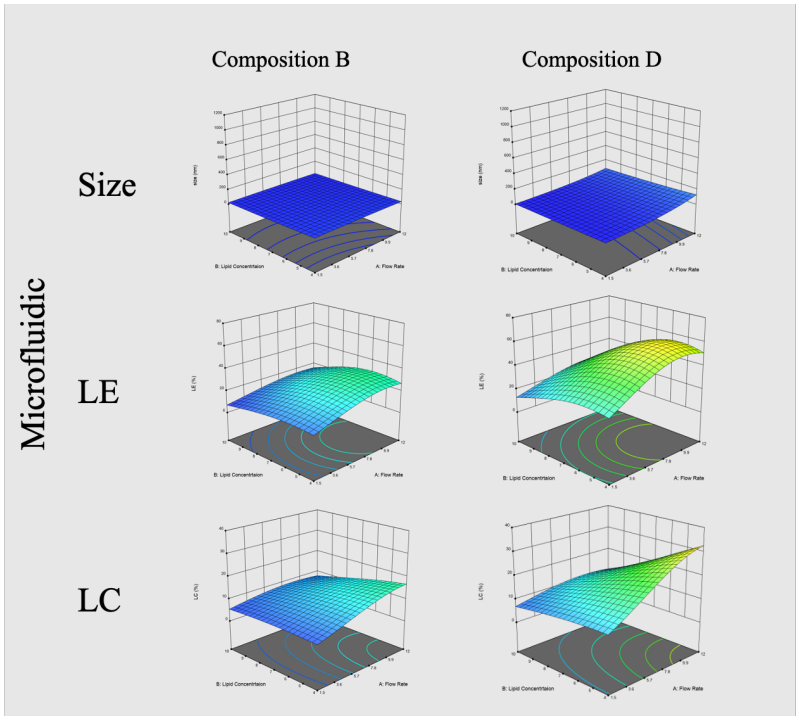

Figure10-2 Response Surface for size, LE, and LC regarding each fabrication technique's flow rate, lipid composition, and lipid concentration.

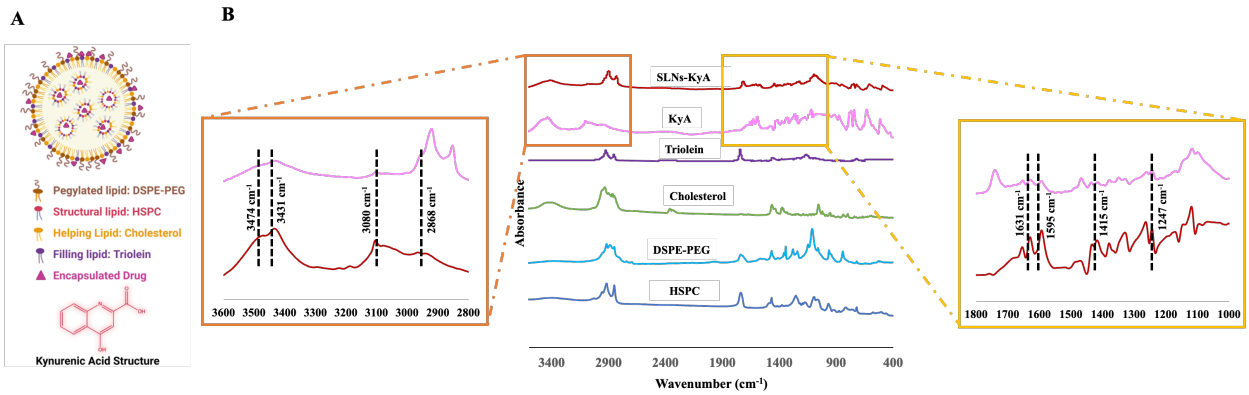

Figure10-3 A) Schematic of SLNs structure and chemical structure of KyA, B) FTIR spectra of lipids, drug, and SLNs.

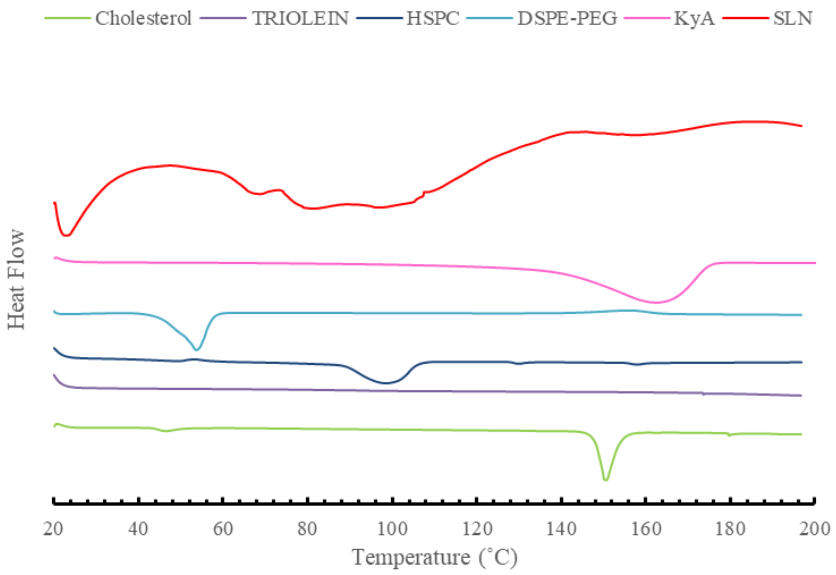

Figure10-4 DSC spectra of lipids, drug, and SLN.

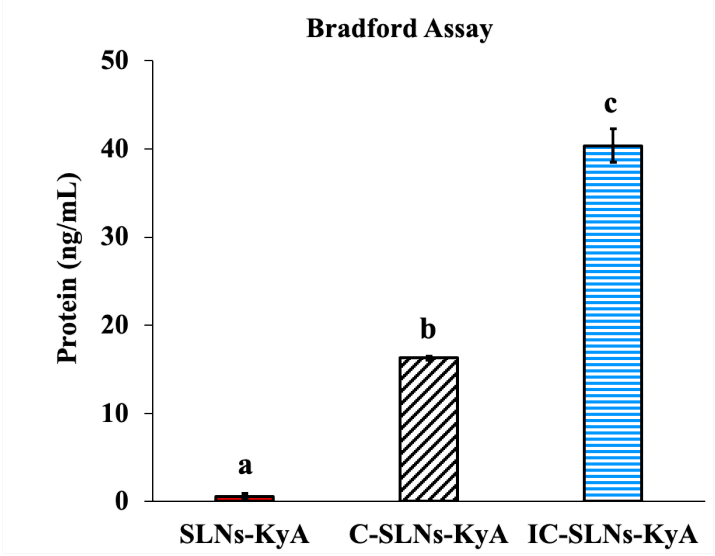

Figure10-5 The protein concentration of DS, C-DS, and IC-DS. a,b, and c indicate significantly different data (n=3) based on One-way ANOVA with posthoc Tukey.

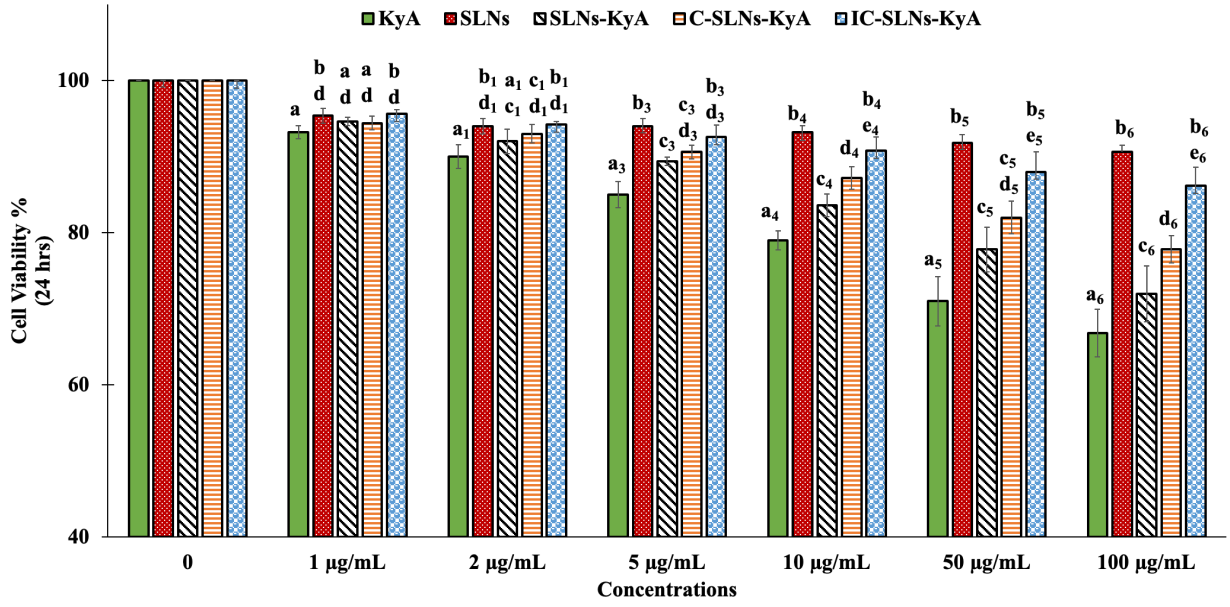

Figure10-6 The cell viability (fibroblasts) in the presence of different concentrations of free drug (KyA), blank SLNs, SLNs-KyA, C-SLNs-KyA, and IC-SLNs-KyA. Different alphabets indicate significantly different data (n=5) based on One-way ANOVA with posthoc Tukey.

10.2 Methods

10.2.1 Cytosol Extraction

Cytosol was extracted from rat livers and was characterized with Bradford assay and SDS-PAGE based on literature [459]. Briefly, the rat livers were minced and homogenized in cytosol buffer (**Table S10-2**) in the presence of protease inhibitors and then centrifuged for 30 minutes at 4 ˚C (12,000 g). the supernatant was centrifuged again at 100,000 g for 1 hour.

10.3 Results and Discussion

10.3.1 FTIR Results

In the KyA spectrum (pink), peaks at 3474 and 3431 cm^{-1} were assigned to the stretching of O-H in the carboxylic acid group and the quinoline ring, respectively [460]. The 3076 and 2968 $cm^{-1\ peaks}$ were associated with C-H and C=C stretching in the quinoline ring and benzyl group, respectively. In the HSPC spectrum, characteristic peaks at 2918 cm^{-1}, 2851 $cm^{-1,}$ and 1468 cm^{-1} are attributed to C-H stretching and bending of the fatty acid chain. Also peaks at 1741 cm^{-1}, 1234 cm^{-1}, 1065 cm^{-1} and 722 cm^{-1} are related to stretching of C=O, P=O, P-O-C and $N+(CH_3)_3$ [461]. In the Triolein spectrum, the bond at 3600 cm^{-1} is related to O-H. The peaks at 2925 cm^{-1} and 2858 cm^{-1} are attributed to C-H stretching, and peaks at 1749 cm^{-1} occurred due to stretching of C=O, $-CH_2$ scissoring, and stretching manifested at 1455 cm^{-1} and 1398 cm^{-1}, respectively. Also, the peak at 1285 cm^{-1} is related to the C-O-C [462]. In the cholesterol spectrum, the characteristic peaks at 2930 cm^{-1} and 2865 cm^{-1} are attributed to symmetrical stretching of the CH_2 group and CH_3 group; moreover, peaks around 1464 cm^{-1} and 1438 cm^{-1} are related to asymmetrical stretching of the CH_2 group and CH_3 group. A peak at 1378 cm^{-1} is related to the CH_2 group and CH_3 group bending. Finally, the peak at 1055 cm^{-1}

represents ring deformation in the cholesterol [463]. In the DSPE-PEG spectrum, the broad peak around 1000 cm^{-1} is related to C-O-C vibrations. The peak at 1700 cm^{-1} is attributed to carbonyl ketone, and peaks at 2900 cm^{-1} and 2800 cm^{-1} are attributed to the starching of C-H [464].

10.3.2 Thermal Characterization (DSC)

DSC was employed to examine the solid-state interactions among different components of DS. Bulk lipids exhibited distinct melting points: Cholesterol at approximately 150 °C with an enthalpy of 58.17 J/g, HSPC at around 53 °C with an enthalpy of 152 J/g, DSPE-PEG at approximately 89 °C with an enthalpy of 45 J/g, while Triolein remained in a liquid state. The drug (KyA) displayed a melting point of around 163 °C with an enthalpy of 181 J/g (Table S10-6).

Distinct peaks for melting and varying enthalpies were observed in the DS thermogram (Figure S3 and Table S6). Previous studies have established that interactions between lipids and lipid-drug formulations can alter enthalpy and melting temperature, with shifts in endothermic melting points in the DS thermogram attributed to factors such as the dispersion state of lipids, the presence of the drug, particle size, and the surfactant employed [413]. Incorporating the drug into the structure may enhance the likelihood of defects in the crystalline lattice, decreasing the melting point and enthalpy of the final SLNs [414] Nanoparticles' nanosize increases surface area and higher surface energy, causing a drop in the melting point and enthalpy [414]. Moreover, the surfactant can affect the thermal properties by increasing the solubility and miscibility of lipids, reducing the melting point and enthalpy [465]. These factors contribute to the observed differences in peaks and shifts in DS compared to bulk lipids.

Furthermore, the decrease in enthalpy for the drug peak indicates that most of the drug was dissolved in the lipid phase during fabrication, rendering it in its amorphous state. Only a small amount of the drug remained crystalline [413]. The presence of crystalline drugs in the structure of SLNs after formation can contribute to a burst release, whereas the drug in an amorphous state is conducive to sustained release.

10.4 Tables

Table S10-1 Composition of the isolation buffer and dissociation buffer for extracting Clathrin.

Isolation buffer pH= 6.5 MES-NaOH			
Name	**Concentration**	**Name**	**Concentration**
MES	10 mM	EGTA	1 mM
DDT	0.2 mM	$MgCl_2$	0.5 mM
NaN_3	0.02% (w/v)	PMSF*	50 mg/L
KCl	100 mM		
Dissociation buffer pH= 7 Tris-HCl 0.5 M			
Name	**Concentration**	**Name**	**Concentration**
EDTA	1 mM	NaN_3	0.02 %
PMSF	50 mg/L	DDT	0.2 mM

Table S10-2 The cytosol buffer composition for extracting cytosol.

Cytosol Buffer pH= 7.4			
Name	**Concentration**	**Name**	**Concentration**
HEPES	25 mM	Sucrose	250 mM
EDTA	2 mM	Leupeptin	0.5 μg/mL
PMSF	1 mM	Aprotinin	0.1 U/mL

Table S10-3 The synthetic buffer composition for in vivo assembly of Clathrin

Synthetic buffer pH= 7.4			
Name	**Concentration**	**Name**	**Concentration**
HEPES	25 mM	Potassium chloride	25 mM
Magnesium acetate	25 mM	Potassium Glutamate	150 mM

Table S10-4 Different Buffers composition for in Vitro re-assembly of Clathrin

Component	Buffer #1	Buffer #2	Buffer #3
Base	Na-MES pH= 6.5 5 mM	Na-MES pH= 6.5 100 mM	Na-MES pH= 6.2 20 mM
Salts	$CaCl_2$ 2 mM	$MgCl_2$ 2 mM	$CaCl_2$ 2 mM
Chelator	EDTA 1 mM	EGTA 1 mM	-
Reducing agent	-	-	DTT 0.5 mM
Preservative (preventing microbial growth)	-	NaN_3 0.02%	NaN_3 0.02%
Heat labile	-	-	PMSF 0.5 mM

Table S10-5 Predicated and actual responses for different independent factors.

Run	Factor1	F 2	F 3	F4	SIZE (nm)		LE (%)		LC (%)	
					A	P	A	P	A	P
1	Ethanol	1.5	8	A	250	201.59	30	46.6	10	23.14
2	Microfluidic	12	8	B	54	21.7	15	25.11	7	11.14
3	Ethanol	8	4	C	30	57.68	10	11.24	5	8.63
4	Ethanol	1.5	4	C	60	135.97	15	9.39	6	5.26
5	Microfluidic	8	8	B	45	25.2	35	24.47	19	11.13
6	Ethanol	12	8	D	400	245.61	12	14.16	6	6.28
7	Ethanol	12	4	D	10	32.59	10	9.16	4	6.58
8	Microfluidic	12	8	D	70	85.88	40	43.43	15	17.05
9	Ethanol	12	10	B	340	329.28	25	12.67	12	6
10	Ethanol	1.5	4	D	30	6.27	20	14.08	7	3.89
11	Ethanol	8	8	B	100	200.31	14	22.08	5	7.87
12	Ethanol	8	4	D	10	19.08	7	14.3	6	6.75
13	Microfluidic	1.5	8	D	10	5.01	25	21.76	10	8.79
14	Ethanol	1.5	4	D	30	6.27	20	14.08	7	3.89
15	Ethanol	8	10	C	470	497.69	32	37.86	10	11.54
16	Microfluidic	1.5	4	B	20	46.4	10	12.32	5	5.92
17	Ethanol	8	8	D	14	137.14	24	21.9	5	7.64
18	Microfluidic	12	4	B	60	35.29	33	26.93	17	16.78
19	Microfluidic	1.5	10	D	10	4.2	6	12.93	4	6.88
20	Ethanol	8	8	D	15	137.14	24	21.9	5	7.64
21	Ethanol	1.5	4	B	150	63.53	10	12.06	4	3.29
22	Ethanol	8	8	A	80	71.87	25	32.89	10	10.93
23	Ethanol	12	10	C	240	271.52	35	27.21	10	8.41
24	Microfluidic	12	10	D	25	76.61	10	26.14	6	10.67
25	Ethanol	8	8	C	340	229.08	30	33.57	12	11.53
26	Microfluidic	8	10	B	15	21.04	10	15.34	5	8.55
27	Ethanol	12	10	C	290	271.52	35	27.21	10	8.41
28	Ethanol	12	8	C	90	122.05	15	24.01	5	9.15
29	Ethanol	1.5	8	C	700	499.99	27	27.63	10	9.28
30	Ethanol	1.5	4	A	90	119.16	30	19.01	15	10.82
31	Ethanol	12	8	A	30	32.81	10	16.84	5	4.78
32	Ethanol	1.5	10	A	260	285.83	60	47.59	40	29.28
33	Microfluidic	8	4	B	36	42.96	30	26.5	15	14.14
34	Ethanol	8	10	B	600	560.97	20	18.67	10	8.17
35	Ethanol	1.5	8	B	230	388.17	23	19.93	6	6.25
36	Microfluidic	8	8	D	60	31.91	75	44.24	27	16.6
37	Microfluidic	8	8	D	60	31.91	75	44.24	27	16.6

38	Ethanol	8	4	B	40	30.35	10	13.15	5	5.47
39	Microfluidic	1.5	4	B	20	46.4	10	12.32	5	5.92
40	Microfluidic	1.5	4	D	40	8.48	10	26.23	4	10.73
41	Ethanol	12	4	C	40	29.31	8	7.96	12	8.12
42	Ethanol	1.5	10	C	900	1045.2	30	30.91	11	10.67
43	Microfluidic	1.5	8	B	23	25.2	12	11.21	9	6.15
44	Microfluidic	1.5	10	B	10	20.24	12	6.97	6	5.43
45	Ethanol	8	8	A	80	71.87	25	32.89	10	10.93
46	Ethanol	12	4	B	50	16.59	12	8.8	5	5.2
47	Ethanol	1.5	8	D	30	41.74	19	21.24	7	5.81
48	Ethanol	8	4	A	30	39.33	10	13.21	6	6.75
49	Microfluidic	12	4	D	100	128.23	50	51.05	35	32.6
50	Ethanol	12	4	A	35	17.13	12	6.7	5	3.5
51	Microfluidic	12	10	B	20	18.56	10	15.82	5	7.85
52	Ethanol	12	8	B	40	114.82	10	14.92	5	6.3
53	Ethanol	8	10	D	600	400.79	10	17.69	6	7.04
54	Ethanol	1.5	10	B	1200	1045.98	15	16.72	4	7.45
55	Ethanol	1.5	10	D	40	117.36	16	17.02	5	6.15
56	Ethanol	12	10	A	40	49.51	30	17.41	6	4.84
57	Ethanol	8	10	A	90	105.9	35	33.85	10	12.04
58	Microfluidic	8	4	D	50	49.97	44	52.5	23	26.75
59	Microfluidic	8	10	D	25	27.8	14	26.5	7	11.32
60	Ethanol	12	10	D	700	735	15	11.49	9	5.32

Table S10-6 Melting points and Enthalpies of bulk lipids, drug, and drug-loaded SLNs

Name	Enthalpy J/gr	Melting endothermic (˚C)	
		Peak onset	Peak maximum
Cholesterol	58.17	148.31	150.64
HSPC	152.8	48.06	53.71
DSPE-PEG	44.49	89.24	98.97
Triolein	NA	NA	NA
KyA	181.4	141.43	163.13
Drug-loaded SLN	1.341	75.29	79.42
	0.4895	63.67	66.30
	3.27	20.31	23.04
	2.446	147.33	158.76

11 REFERENCES

[1] World Health Organization. Burns. 2023.

[2] Block L, Gosain A, King TW. Emerging Therapies for Scar Prevention. Adv Wound Care (New Rochelle) 2015;4:607–14. https://doi.org/10.1089/wound.2015.0646.

[3] Jonidi Shariatzadeh F, Currie S, Logsetty S, Spiwak R, Liu S. Enhancing wound healing and minimizing scarring: A comprehensive review of nanofiber technology in wound dressings. Prog Mater Sci 2025;147. https://doi.org/10.1016/j.pmatsci.2024.101350.

[4] Rahimnejad M, Derakhshanfar S, Zhong W. Biomaterials and tissue engineering for scar management in wound care. Burns Trauma 2017;5. https://doi.org/10.1186/s41038-017-0069-9.

[5] Mulholland EJ. Electrospun Biomaterials in the Treatment and Prevention of Scars in Skin Wound Healing. Front Bioeng Biotechnol 2020;8. https://doi.org/10.3389/fbioe.2020.00481.

[6] Moore A, Marshall C, Longaker M. Minimizing Skin Scarring through Biomaterial Design. J Funct Biomater 2017;8:3. https://doi.org/10.3390/jfb8010003.

[7] Fernandes MG, da Silva LP, Cerqueira MT, Ibañez R, Murphy CM, Reis RL, et al. Mechanomodulatory biomaterials prospects in scar prevention and treatment. Acta Biomater 2022;150:22–33. https://doi.org/10.1016/j.actbio.2022.07.042.

[8] Gangemi EN, Gregori D, Berchialla P, Zingarelli E, Cairo M, Bollero D, et al. Epidemiology and Risk Factors for Pathologic Scarring After Burn Wounds. Arch Facial Plast Surg 2008;10:93–102. https://doi.org/10.1001/archfaci.10.2.93.

[9] Butzelaar L, Ulrich MMW, Mink van der Molen AB, Niessen FB, Beelen RHJ. Currently known risk factors for hypertrophic skin scarring: A review. Journal of Plastic,

Reconstructive & Aesthetic Surgery 2016;69:163–9. https://doi.org/10.1016/j.bjps.2015.11.015.

[10] Wilgus TA. Inflammation as an orchestrator of cutaneous scar formation: a review of the literature. Plast Aesthet Res 2020;7. https://doi.org/10.20517/2347-9264.2020.150.

[11] Cowin AJ, Bayat A, Murray RZ, Kopecki Z. Editorial: Inflammation in Healing and Regeneration of Cutaneous Wounds. Front Immunol 2021;12. https://doi.org/10.3389/fimmu.2021.806687.

[12] Wang ZC, Zhao WY, Cao Y, Liu YQ, Sun Q, Shi P, et al. The Roles of Inflammation in Keloid and Hypertrophic Scars. Front Immunol 2020;11. https://doi.org/10.3389/fimmu.2020.603187.

[13] Sachdeva C, Satyamoorthy K, Murali TS. Microbial Interplay in Skin and Chronic Wounds. Curr Clin Microbiol Rep 2022;9:21–31. https://doi.org/10.1007/s40588-022-00180-4.

[14] Tuttle MS. Association Between Microbial Bioburden and Healing Outcomes in Venous Leg Ulcers: A Review of the Evidence. Adv Wound Care (New Rochelle) 2015;4:1–11. https://doi.org/10.1089/wound.2014.0535.

[15] Canesso MCC, Vieira AT, Castro TBR, Schirmer BGA, Cisalpino D, Martins FS, et al. Skin Wound Healing Is Accelerated and Scarless in the Absence of Commensal Microbiota. The Journal of Immunology 2014;193:5171–80. https://doi.org/10.4049/jimmunol.1400625.

[16] Malone M, Schultz G. Challenges in the diagnosis and management of wound infection. British Journal of Dermatology 2022;187:159–66. https://doi.org/10.1111/bjd.21612.

[17] White RJ, Cooper R, Kingsley A. Wound colonization and infection: the role of topical antimicrobials. 2001.

[18] Eming SA, Krieg T, Davidson JM. Inflammation in wound repair: Molecular and cellular mechanisms. Journal of Investigative Dermatology 2007;127:514–25. https://doi.org/10.1038/sj.jid.5700701.

[19] Zhao G, Usui ML, Lippman SI, James GA, Stewart PS, Fleckman P, et al. Biofilms and Inflammation in Chronic Wounds. Adv Wound Care (New Rochelle) 2013;2:389–99. https://doi.org/10.1089/wound.2012.0381.

[20] Rezaie F, Momeni-Moghaddam M, Naderi-Meshkin H. Regeneration and Repair of Skin Wounds: Various Strategies for Treatment. International Journal of Lower Extremity Wounds 2019;18:247–61. https://doi.org/10.1177/1534734619859214.

[21] Naghavi M, Vollset SE, Ikuta KS, Swetschinski LR, Gray AP, Wool EE, et al. Global burden of bacterial antimicrobial resistance 1990–2021: a systematic analysis with forecasts to 2050. The Lancet 2024;404:1199–226. https://doi.org/10.1016/S0140-6736(24)01867-1.

[22] DiNubile MJ, Lipsky BA. Complicated infections of skin and skin structures: When the infection is more than skip deep. Journal of Antimicrobial Chemotherapy 2004;53. https://doi.org/10.1093/jac/dkh202.

[23] Bowler PG. Wound pathophysiology, infection and therapeutic options. Ann Med 2002;34:419–27. https://doi.org/10.1080/078538902321012360.

[24] Sheikhzadeh E, Beni V, Zourob M. Nanomaterial application in bio/sensors for the detection of infectious diseases. Talanta 2021;230. https://doi.org/10.1016/j.talanta.2020.122026.

[25] Colino CI, Lanao JM, Gutierrez-Millan C. Recent advances in functionalized nanomaterials for the diagnosis and treatment of bacterial infections. Materials Science and Engineering C 2021;121. https://doi.org/10.1016/j.msec.2020.111843.

[26] Pang Q, Jiang Z, Wu K, Hou R, Zhu Y. Nanomaterials-Based Wound Dressing for Advanced Management of Infected Wound. Antibiotics 2023;12. https://doi.org/10.3390/antibiotics12020351.

[27] Souto EB, Ribeiro AF, Ferreira MI, Teixeira MC, Shimojo AAM, Soriano JL, et al. New nanotechnologies for the treatment and repair of skin burns infections. Int J Mol Sci 2020;21. https://doi.org/10.3390/ijms21020393.

[28] Mihai MM, Dima MB, Dima B, Holban AM. Nanomaterials for Wound Healing and Infection Control. Materials 2019;12:2176. https://doi.org/10.3390/ma12132176.

[29] Lin Y, Chen Z, Liu Y, Wang J, Lv W, Peng R. Recent Advances in Nano-Formulations for Skin Wound Repair Applications. Drug Des Devel Ther 2022;16:2707–28. https://doi.org/10.2147/DDDT.S375541.

[30] Holzer-Geissler JCJ, Schwingenschuh S, Zacharias M, Einsiedler J, Kainz S, Reisenegger P, et al. Article The Impact of Prolonged Inflammation on Wound Healing. Biomedicines 2022;10. https://doi.org/10.3390/biomedicines10040856.

[31] Rahimnejad M, Derakhshanfar S, Zhong W. Biomaterials and Tissue Engineering for Scar Management in Wound Care. Burns Trauma 2017;5:1–9. https://doi.org/10.1186/s41038-017-0069-9.

[32] Sareen J, Erickson J, Medved MI, Asmundson GJG, Enns MW, Stein M, et al. RISK FACTORS FOR POST-INJURY MENTAL HEALTH PROBLEMS. Depress Anxiety 2013;30:321–7. https://doi.org/10.1002/da.22077.

[33] Spiwak R, Sareen S, Logsetty S. Techniques to Assess Long-Term Outcomes after Burn Injuries. European Burn Journal 2022;3:328–39. https://doi.org/10.3390/ebj3020028.

[34] Kaur G, Narayanan G, Garg D, Sachdev A, Matai I. Biomaterials-Based Regenerative Strategies for Skin Tissue Wound Healing. ACS Appl Bio Mater 2022;5:2069–106. https://doi.org/10.1021/acsabm.2c00035.

[35] Farahani M, Shafiee A. Wound Healing: From Passive to Smart Dressings. Adv Healthc Mater 2021;10:1–32. https://doi.org/10.1002/adhm.202100477.

[36] Safina I, Childress LT, Myneni SR, Vang KB, Biris AS. Cell-Biomaterial Constructs for Wound Healing and Skin Regeneration. Drug Metab Rev 2022;54:63–94. https://doi.org/10.1080/03602532.2021.2025387.

[37] Moore AL, Marshall CD, Barnes LA, Murphy MP, Ransom RC, Longaker MT. Scarless Wound Healing: Transitioning from Fetal Research to Regenerative Healing. Wiley Interdiscip Rev Dev Biol 2018;7:e309. https://doi.org/10.1002/wdev.309.

[38] Larouche J, Sheoran S, Maruyama K, Martino MM. Immune Regulation of Skin Wound Healing: Mechanisms and Novel Therapeutic Targets. Adv Wound Care (New Rochelle) 2018;7:209–31. https://doi.org/10.1089/wound.2017.0761.

[39] Chantre CO, Hoerstrup SP, Parker KK. Engineering Biomimetic and Instructive Materials for Wound Healing and Regeneration. Curr Opin Biomed Eng 2019;10:97–106. https://doi.org/10.1016/j.cobme.2019.04.004.

[40] Zhong SP, Zhang YZ, Lim CT. Tissue Scaffolds for Skin Wound Healing and Dermal Reconstruction. Wiley Interdiscip Rev Nanomed Nanobiotechnol 2010;2:510–25. https://doi.org/10.1002/wnan.100.

[41] Zurada JM, Kriegel D, Davis IC. Topical Treatments for Hypertrophic Scars. J Am Acad Dermatol 2006;55:1024–31. https://doi.org/10.1016/j.jaad.2006.03.022.

[42] Bloemen MCT, van der Veer WM, Ulrich MMW, van Zuijlen PPM, Niessen FB, Middelkoop E. Prevention and Curative Management of Hypertrophic Scar Formation. Burns 2009;35:463–75. https://doi.org/10.1016/j.burns.2008.07.016.

[43] Wysocki AB. Skin Anatomy, Physiology, and Pathophysiology. Nurs Clin North Am 1999;34:777–97, v.

[44] Venus M, Waterman J, McNab I. Basic Physiology of The Skin. Surgery (Oxford) 2010;28:469–72. https://doi.org/10.1016/j.mpsur.2010.07.011.

[45] Kolarsick PAJ, Kolarsick MA, Goodwin C. Anatomy and Physiology of the Skin. J Dermatol Nurses Assoc 2011;3:203–13. https://doi.org/10.1097/JDN.0b013e3182274a98.

[46] Powell J. Skin Physiology. Women's Health Medicine 2006;3:130–3. https://doi.org/10.1383/wohm.2006.3.3.130.

[47] Monteiro-Riviere NA. Comparative Anatomy, Physiology, and Biochemistry of Mammalian Skin. Dermal and Ocular Toxicology, 1991, p. 1–69.

[48] Dehdashtian A, Stringer TP, Warren AJ, Mu EW, Amirlak B, Shahabi L. Anatomy and Physiology of the Skin. In: Riker AI, editor. Melanoma, Cham: Springer International Publishing; 2018, p. 15–26. https://doi.org/10.1007/978-3-319-78310-9_2.

[49] Kolarsick PAJ, Kolarsick MA, Goodwin C. Anatomy and Physiology of the Skin. J Dermatol Nurses Assoc 2011;3:203–13. https://doi.org/10.1097/JDN.0b013e3182274a98.

[50] Chen S, Liu B, Carlson MA, Gombart AF, Reilly DA, Xie J. Recent Advances in Electrospun Nanofibers for Wound Healing. Nanomedicine 2017;12:1335–52. https://doi.org/10.2217/nnm-2017-0017.

[51] Gantwerker EA, Hom DB. Skin: Histology and Physiology of Wound Healing. Clin Plast Surg 2012;39:85–97. https://doi.org/10.1016/j.cps.2011.09.005.

[52] Jeschke MG, van Baar ME, Choudhry MA, Chung KK, Gibran NS, Logsetty S. Burn injury. Nat Rev Dis Primers 2020;6. https://doi.org/10.1038/s41572-020-0145-5.

[53] Przekora A. A Concise Review on Tissue Engineered Artificial Skin Grafts for Chronic Wound Treatment: Can We Reconstruct Functional Skin Tissue In Vitro? Cells 2020;9:1622. https://doi.org/10.3390/cells9071622.

[54] Rodrigues M, Kosaric N, Bonham CA, Gurtner GC. Wound Healing: A Cellular Perspective. Physiol Rev 2019;99:665–706. https://doi.org/10.1152/physrev.00067.2017.-Wound.

[55] Furie B, Furie BC. Mechanisms of Thrombus Formation. New England Journal of Medicine 2008;359:938–49. https://doi.org/10.1056/NEJMra0801082.

[56] Fox JEB, Phillips DR. Inhibition of Actin Polymerization in Blood Platelets by Cytochalasins. Nature 1981;292:650–2. https://doi.org/10.1038/292650a0.

[57] Sorrentino S, Studt J-D, Medalia O, Tanuj Sapra K. Roll, Adhere, Spread and Contract: Structural Mechanics of Platelet Function. Eur J Cell Biol 2015;94:129–38. https://doi.org/10.1016/j.ejcb.2015.01.001.

[58] Pradhan S, Khatlani T, Nairn AC, Vijayan KV. The Heterotrimeric G Protein Gβ1 Interacts with The Catalytic Subunit of Protein Phosphatase 1 and Modulates G Protein–Coupled Receptor Signaling in Platelets. Journal of Biological Chemistry 2017;292:13133–42. https://doi.org/10.1074/jbc.M117.796656.

[59] Steed DL. The Role of Growth Factors in Wound Healing. Surgical Clinics of North America 1997;77:575–86. https://doi.org/10.1016/S0039-6109(05)70569-7.

[60] Dwivedi C, Pandey H, C. Pandey A, W. Ramteke P. Nanofibre Based Smart Pharmaceutical Scaffolds for Wound Repair and Regenerations. Curr Pharm Des 2015;22:1460–71. https://doi.org/10.2174/1381612822666151215103553.

[61] van der Vliet A, Janssen-Heininger YMW. Hydrogen Peroxide as a Damage Signal in Tissue Injury and Inflammation: Murderer, Mediator, or Messenger? J Cell Biochem 2014;115:427–35. https://doi.org/10.1002/jcb.24683.

[62] Martin P. Wound Healing--Aiming for Perfect Skin Regeneration. Science (1979) 1997;276:75–81. https://doi.org/10.1126/science.276.5309.75.

[63] Cañedo-Dorantes L, Cañedo-Ayala M. Skin Acute Wound Healing: A Comprehensive Review. Int J Inflam 2019;2019:1–15. https://doi.org/10.1155/2019/3706315.

[64] Chen WYJ, Rogers AA. Recent Insights into The Causes of Chronic Leg Ulceration in Venous Diseases and Implications on Other Types of Chronic Wounds. Wound Repair and Regeneration 2007;15:434–49. https://doi.org/10.1111/j.1524-475X.2007.00250.x.

[65] de Oliveira S, Rosowski EE, Huttenlocher A. Neutrophil Migration in Infection and Wound Repair: Going Forward in Reverse. Nat Rev Immunol 2016;16:378–91. https://doi.org/10.1038/nri.2016.49.

[66] Bratton DL, Henson PM. Neutrophil Clearance: When The Party is Over, Clean-up Begins. Trends Immunol 2011;32:350–7. https://doi.org/10.1016/j.it.2011.04.009.

[67] Sorg H, Tilkorn DJ, Hager S, Hauser J, Mirastschijski U. Skin Wound Healing: An Update on the Current Knowledge and Concepts. European Surgical Research 2017;58:81–94. https://doi.org/10.1159/000454919.

[68] Garbuzenko E, Nagler A, Pickholtz D, Gillery P, Reich R, Maquart F -X., et al. Human Mast Cells Stimulate Fibroblast Proliferation, Collagen Synthesis and Lattice Contraction:

A Direct Role for Mast Cells in Skin Fibrosis. Clinical & Experimental Allergy 2002;32:237–46. https://doi.org/10.1046/j.1365-2222.2002.01293.x.

[69] Siebenhaar F, Syska W, Weller K, Magerl M, Zuberbier T, Metz M, et al. Control of Pseudomonas Aeruginosa Skin Infections in Mice is Mast Cell-Dependent. Am J Pathol 2007;170:1910–6. https://doi.org/10.2353/ajpath.2007.060770.

[70] Weller K, Foitzik K, Paus R, Syska W, Maurer M, Weller K, et al. Mast Cells are Required for Normal Healing of Skin Wounds in Mice. The FASEB Journal 2006;20:2366–8. https://doi.org/10.1096/fj.06-5837fje.

[71] Wang Z, Lai Y, Bernard JJ, MacLeod DT, Cogen AL, Moss B, et al. Skin Mast Cells Protect Mice against Vaccinia Virus by Triggering Mast Cell Receptor S1PR2 and Releasing Antimicrobial Peptides. The Journal of Immunology 2012;188:345–57. https://doi.org/10.4049/jimmunol.1101703.

[72] Younan G, Suber F, Xing W, Shi T, Kunori Y, Åbrink M, et al. The Inflammatory Response after an Epidermal Burn Depends on the Activities of Mouse Mast Cell Proteases 4 and 5. The Journal of Immunology 2010;185:7681–90. https://doi.org/10.4049/jimmunol.1002803.

[73] Wulff BC, Parent AE, Meleski MA, DiPietro LA, Schrementi ME, Wilgus TA. Mast Cells Contribute to Scar Formation during Fetal Wound Healing. Journal of Investigative Dermatology 2012;132:458–65. https://doi.org/10.1038/jid.2011.324.

[74] Wilgus TA, Wulff BC. The Importance of Mast Cells in Dermal Scarring. Adv Wound Care (New Rochelle) 2014;3:356–65. https://doi.org/10.1089/wound.2013.0457.

[75] Tamoutounour S, Guilliams M, Montanana Sanchis F, Liu H, Terhorst D, Malosse C, et al. Origins and Functional Specialization of Macrophages and of Conventional and

Monocyte-Derived Dendritic Cells in Mouse Skin. Immunity 2013;39:925–38. https://doi.org/10.1016/j.immuni.2013.10.004.

[76] Lumelsky NL. Commentary: Engineering of Tissue Healing and Regeneration. Tissue Eng 2007;13:1393–8. https://doi.org/10.1089/ten.2007.0100.

[77] Gurtner GC, Werner S, Barrandon Y, Longaker MT. Wound Repair and Regeneration. Nature 2008;453:314–21. https://doi.org/10.1038/nature07039.

[78] He L, Huang X, Kanisicak O, Li Y, Wang Y, Li Y, et al. Preexisting Endothelial Cells Mediate Cardiac Neovascularization after Injury. Journal of Clinical Investigation 2017;127:2968–81. https://doi.org/10.1172/JCI93868.

[79] Fathke C, Wilson L, Hutter J, Kapoor V, Smith A, Hocking A, et al. Contribution of Bone Marrow–Derived Cells to Skin: Collagen Deposition and Wound Repair. Stem Cells 2004;22:812–22. https://doi.org/10.1634/stemcells.22-5-812.

[80] Karra R, Walter AO, Wu SM. The Relationship between Cardiac Endothelium and Fibroblasts: It's Complicated. Journal of Clinical Investigation 2017;127:2892–4. https://doi.org/10.1172/JCI95492.

[81] Plikus M V., Guerrero-Juarez CF, Ito M, Li YR, Dedhia PH, Zheng Y, et al. Regeneration of Fat Cells from Myofibroblasts during Wound Healing. Science (1979) 2017;355:748–52. https://doi.org/10.1126/science.aai8792.

[82] Goffin JM, Pittet P, Csucs G, Lussi JW, Meister J-J, Hinz B. Focal Adhesion Size Controls Tension-Dependent Recruitment of α-Smooth Muscle Actin to Stress Fibers. J Cell Biol 2006;172:259–68. https://doi.org/10.1083/jcb.200506179.

[83] Tomasek JJ, Gabbiani G, Hinz B, Chaponnier C, Brown RA. Myofibroblasts and Mechano-Regulation of Connective Tissue Remodelling. Nat Rev Mol Cell Biol 2002;3:349–63. https://doi.org/10.1038/nrm809.

[84] van der Veer WM, Bloemen MCT, Ulrich MMW, Molema G, van Zuijlen PP, Middelkoop E, et al. Potential Cellular and Molecular Causes of Hypertrophic Scar Formation. Burns 2009;35:15–29. https://doi.org/10.1016/j.burns.2008.06.020.

[85] Desmoulière A, Redard M, Darby I, Gabbiani G. Apoptosis Mediates The Decrease in Cellularity during The Transition between Granulation Tissue and Scar. Am J Pathol 1995;146:56–66.

[86] Hobbs RM, Silva-Vargas V, Groves R, Watt FM. Expression of Activated MEK1 in Differentiating Epidermal Cells is Sufficient to Generate Hyperproliferative and Inflammatory Skin Lesions. Journal of Investigative Dermatology 2004;123:503–15. https://doi.org/10.1111/j.0022-202X.2004.23225.x.

[87] Xue M, Jackson CJ. Extracellular Matrix Reorganization During Wound Healing and Its Impact on Abnormal Scarring. Adv Wound Care (New Rochelle) 2013;4:119–36. https://doi.org/10.1089/wound.2013.0485.

[88] Drucker AM, Kleiner O, Manion R, Philip A, Dutz J, Barnard K, et al. Top Ten Research Priorities for Psoriasis, Atopic Dermatitis and Hidradenitis Suppurativa: The SkIN Canada Priority Setting Initiative. J Cutan Med Surg 2023;27:133–9. https://doi.org/10.1177/12034754231156103.

[89] Amini-Nik S, Yousuf Y, Jeschke MG. Scar Management in Burn Injuries using Drug Delivery and Molecular Signaling: Current Treatments and Future Directions. Adv Drug Deliv Rev 2018;123:135–54. https://doi.org/10.1016/j.addr.2017.07.017.

[90] Walmsley GG, Maan ZN, Wong VW, Duscher D, Hu MS, Zielins ER, et al. Scarless Wound Healing: Chasing The Holy Grail. Plast Reconstr Surg 2015;135:907–17. https://doi.org/10.1097/PRS.0000000000000972.

[91] Liu A, Moy RL, Ozog DM. Current Methods Employed in The Prevention and Minimization of Surgical Scars. Dermatologic Surgery 2011;37:1740–6. https://doi.org/10.1111/j.1524-4725.2011.02166.x.

[92] Berman B, Villa AM, Ramirez CC. Novel Opportunities in The Treatment and Prevention of Scarring. J Cutan Med Surg 2004;8:32–6. https://doi.org/10.1007/s10227-004-0806-0.

[93] Bloemen MCT, van der Veer WM, Ulrich MMW, van Zuijlen PPM, Niessen FB, Middelkoop E. Prevention and Curative Management of Hypertrophic Scar Formation. Burns 2009;35:463–75. https://doi.org/10.1016/j.burns.2008.07.016.

[94] Berman B, Villa AM, Ramirez CC. Novel Opportunities in The Treatment and Prevention of Scarring. J Cutan Med Surg 2004;8:32–6. https://doi.org/10.1007/s10227-004-0806-0.

[95] Chen MA, Davidson TM. Scar Management: Prevention and Treatment Strategies. Curr Opin Otolaryngol Head Neck Surg 2005;13:242–7. https://doi.org/10.1097/01.moo.0000170525.74264.f8.

[96] Hu MS, Maan ZN, Wu JC, Rennert RC, Hong WX, Lai TS, et al. Tissue Engineering and Regenerative Repair in Wound Healing. Ann Biomed Eng 2014;42:1494–507. https://doi.org/10.1007/s10439-014-1010-z.

[97] Suamte L, Tirkey A, Barman J, Jayasekhar Babu P. Various Manufacturing Methods and Ideal Properties of Scaffolds for Tissue Engineering Applications. Smart Materials in Manufacturing 2023;1:100011. https://doi.org/10.1016/j.smmf.2022.100011.

[98] Chen J, Fan Y, Dong G, Zhou H, Du R, Tang X, et al. Designing Biomimetic Scaffolds for Skin Tissue Engineering. Biomater Sci 2023;11:3051–76. https://doi.org/10.1039/D3BM00046J.

[99] Garg T, Rath G, Goyal AK. Biomaterials-Based Nanofiber Scaffold: Targeted and Controlled Carrier for Cell and Drug Delivery. J Drug Target 2015;23:202–21. https://doi.org/10.3109/1061186X.2014.992899.

[100] Abrigo M, McArthur SL, Kingshott P. Electrospun Nanofibers as Dressings for Chronic Wound Care: Advances, Challenges, and Future Prospects. Macromol Biosci 2014;14:772–92. https://doi.org/10.1002/mabi.201300561.

[101] Young JL, Holle AW, Spatz JP. Nanoscale and mechanical properties of the physiological cell–ECM microenvironment. Exp Cell Res 2016;343:3–6. https://doi.org/10.1016/j.yexcr.2015.10.037.

[102] Juncos Bombin AD, Dunne NJ, McCarthy HO. Electrospinning of Natural Polymers for The Production of Nanofibres for Wound Healing Applications. Materials Science and Engineering C 2020;114:110994. https://doi.org/10.1016/j.msec.2020.110994.

[103] Memic A, Abudula T, Mohammed HS, Joshi Navare K, Colombani T, Bencherif SA. Latest Progress in Electrospun Nanofibers for Wound Healing Applications. ACS Appl Bio Mater 2019;2:952–69. https://doi.org/10.1021/acsabm.8b00637.

[104] Afsharian YP, Rahimnejad M. Bioactive Electrospun Scaffolds for Wound Healing Applications: A Comprehensive Review. Polym Test 2021;93:106952. https://doi.org/10.1016/j.polymertesting.2020.106952.

[105] Miguel SP, Figueira DR, Simões D, Ribeiro MP, Coutinho P, Ferreira P, et al. Electrospun Polymeric Nanofibres as Wound Dressings: A Review. Colloids Surf B Biointerfaces 2018;169:60–71. https://doi.org/10.1016/j.colsurfb.2018.05.011.

[106] Singh H, Li W, Kazemian MR, Yang R, Yang C, Logsetty S, et al. Lipase-Responsive Electrospun Theranostic Wound Dressing for Simultaneous Recognition and Treatment of Wound Infection. ACS Appl Bio Mater 2019;2:2028–36. https://doi.org/10.1021/acsabm.9b00076.

[107] Alipour R, Khorshidi A, Shojaei AF, Mashayekhi F, Moghaddam MJM. Skin Wound Healing Acceleration by Ag Nanoparticles Embedded in PVA/PVP/Pectin/Mafenide Acetate Composite Nanofibers. Polym Test 2019;79:106022. https://doi.org/10.1016/j.polymertesting.2019.106022.

[108] Currie S, Shariatzadeh FJ, Singh H, Logsetty S, Liu S. Highly Sensitive Bacteria-Responsive Membranes Consisting of Core–Shell Polyurethane Polyvinylpyrrolidone Electrospun Nanofibers for In Situ Detection of Bacterial Infections. ACS Appl Mater Interfaces 2020;12:45859–72. https://doi.org/10.1021/acsami.0c14213.

[109] Garcia-Orue I, Gainza G, Gutierrez FB, Aguirre JJ, Evora C, Pedraz JL, et al. Novel Nanofibrous Dressings Containing rhEGF and Aloe Vera for Wound Healing Applications. Int J Pharm 2017;523:556–66. https://doi.org/10.1016/j.ijpharm.2016.11.006.

[110] Choi JS, Choi SH, Yoo HS. Coaxial electrospun nanofibers for treatment of diabetic ulcers with binary release of multiple growth factors. J Mater Chem 2011;21:5258–67. https://doi.org/10.1039/c0jm03706k.

[111] Abdali Z, Logsetty S, Liu S. Bacteria-Responsive Single and Core-Shell Nanofibrous Membranes Based on Polycaprolactone/Poly(ethylene succinate) for On-Demand Release of Biocides. ACS Omega 2019;4:4063–70. https://doi.org/10.1021/acsomega.8b03137.

[112] Chouhan D, Janani G, Chakraborty B, Nandi SK, Mandal BB. Functionalized PVA–Silk Blended Nanofibrous Mats Promote Diabetic Wound Healing via Regulation of Extracellular Matrix and Tissue Remodelling. J Tissue Eng Regen Med 2018;12:e1559–70. https://doi.org/10.1002/term.2581.

[113] Choi JS, Leong KW, Yoo HS. In vivo wound healing of diabetic ulcers using electrospun nanofibers immobilized with human epidermal growth factor (EGF). Biomaterials 2008;29:587–96. https://doi.org/10.1016/j.biomaterials.2007.10.012.

[114] Lai HJ, Kuan CH, Wu HC, Tsai JC, Chen TM, Hsieh DJ, et al. Tailored design of electrospun composite nanofibers with staged release of multiple angiogenic growth factors for chronic wound healing. Acta Biomater 2014;10:4156–66. https://doi.org/10.1016/j.actbio.2014.05.001.

[115] Yao CH, Lee CY, Huang CH, Chen YS, Chen KY. Novel Bilayer Wound Dressing Based on Electrospun Gelatin/Keratin Nanofibrous Mats for Skin Wound Repair. Materials Science and Engineering C 2017;79:533–40. https://doi.org/10.1016/j.msec.2017.05.076.

[116] Xie Z, Paras CB, Weng H, Punnakitikashem P, Su LC, Vu K, et al. Dual Growth Factor Releasing Multi-Functional Nanofibers for Wound Healing. Acta Biomater 2013;9:9351–9. https://doi.org/10.1016/j.actbio.2013.07.030.

[117] Malgarim Cordenonsi L, Faccendini A, Rossi S, Bonferoni MC, Malavasi L, Raffin R, et al. Platelet Lysate Loaded Electrospun Scaffolds: Effect of Nanofiber Types on Wound

Healing. European Journal of Pharmaceutics and Biopharmaceutics 2019;142:247–57. https://doi.org/10.1016/j.ejpb.2019.06.030.

[118] Li W, Cicek N, Levin DB, Logsetty S, Liu S. Bacteria-triggered release of a potent biocide from core-shell polyhydroxyalkanoate (PHA)-based nanofibers for wound dressing applications. J Biomater Sci Polym Ed 2020;31:394–406. https://doi.org/10.1080/09205063.2019.1693882.

[119] Hamdan S, Pastar I, Drakulich S, Dikici E, Tomic-Canic M, Deo S, et al. Nanotechnology-Driven Therapeutic Interventions in Wound Healing: Potential Uses and Applications. ACS Cent Sci 2017;3:163–75. https://doi.org/10.1021/acscentsci.6b00371.

[120] Miguel SP, Sequeira RS, Moreira AF, Cabral CSD, Mendonça AG, Ferreira P, et al. An Overview of Electrospun Membranes Loaded with Bioactive Molecules for Improving The Wound Healing Process. European Journal of Pharmaceutics and Biopharmaceutics 2019;139:1–22. https://doi.org/10.1016/j.ejpb.2019.03.010.

[121] Gao C, Zhang L, Wang J, Jin M, Tang Q, Chen Z, et al. Electrospun Nanofibers Promote Wound Healing: Theories, Techniques, and Perspectives. J Mater Chem B 2021;9:3106–30. https://doi.org/10.1039/d1tb00067e.

[122] Haider S, Al-Masry WA, Bukhari N, Javid M. Preparation of The Chitosan containing Nanofibers by Electrospinning Chitosan-Gelatin Complexes. Polym Eng Sci 2010;50:1887–93. https://doi.org/10.1002/pen.21721.

[123] Huang Z-M, Zhang YZ, Ramakrishna S, Lim CT. Electrospinning and Mechanical Characterization of Gelatin Nanofibers. Polymer (Guildf) 2004;45:5361–8. https://doi.org/10.1016/j.polymer.2004.04.005.

[124] Zhan J, Morsi Y, Ei-Hamshary H, Al-Deyab SS, Mo X. In Vitro Evaluation of Electrospun Gelatin–Glutaraldehyde Nanofibers. Front Mater Sci 2016;10:90–100. https://doi.org/10.1007/s11706-016-0329-9.

[125] Juncos Bombin AD, Dunne NJ, McCarthy HO. Electrospinning of Natural Polymers for The Production of Nanofibres for Wound Healing Applications. Materials Science and Engineering C 2020;114:110994. https://doi.org/10.1016/j.msec.2020.110994.

[126] Parham S, Kharazi AZ, Bakhsheshi-Rad HR, Kharaziha M, Ismail AF, Sharif S, et al. Antimicrobial Synthetic and Natural Polymeric Nanofibers as Wound Dressing: A Review. Adv Eng Mater 2022;24:1–22. https://doi.org/10.1002/adem.202101460.

[127] Yusuf Aliyu A, Adeleke OA. Nanofibrous Scaffolds for Diabetic Wound Healing. Pharmaceutics 2023;15. https://doi.org/10.3390/pharmaceutics15030986.

[128] Behere I, Ingavle G. In Vitro and In Vivo Advancement of Multifunctional Electrospun Nanofiber Scaffolds in Wound Healing Applications: Innovative Nanofiber Designs, Stem Cell Approaches, and Future Perspectives. J Biomed Mater Res A 2022;110:443–61. https://doi.org/10.1002/jbm.a.37290.

[129] Liu X, Xu H, Zhang M, Yu DG. Electrospun Medicated Nanofibers for Wound Healing: Review. Membranes (Basel) 2021;11. https://doi.org/10.3390/membranes11100770.

[130] Gizaw M, Thompson J, Faglie A, Lee SY, Neuenschwander P, Chou SF. Electrospun Fibers as a Dressing Material for Drug and Biological Agent Delivery in Wound Healing Applications. Bioengineering 2018;5:1–28. https://doi.org/10.3390/bioengineering5010009.

[131] Merzougui C, Miao F, Liao Z, Wang L, Wei Y, Huang D. Electrospun Nanofibers with Antibacterial Properties for Wound Dressings. J Biomater Sci Polym Ed 2022;33:2165–83. https://doi.org/10.1080/09205063.2022.2099662.

[132] Liu Y, Li C, Feng Z, Han B, Yu DG, Wang K. Advances in the Preparation of Nanofiber Dressings by Electrospinning for Promoting Diabetic Wound Healing. Biomolecules 2022;12. https://doi.org/10.3390/biom12121727.

[133] Valachová K, El Meligy MA, Šoltés L. Hyaluronic Acid and Chitosan-Based Electrospun Wound Dressings: Problems and Solutions. Int J Biol Macromol 2022;206:74–91. https://doi.org/10.1016/j.ijbiomac.2022.02.117.

[134] Walmsley GG, Maan ZN, Wong VW, Duscher D, Hu MS, Zielins ER, et al. Scarless Wound Healing: Chasing The Holy Grail. Plast Reconstr Surg 2015;135:907–17. https://doi.org/10.1097/PRS.0000000000000972.

[135] Croitoru AM, Ficai D, Ficai A, Mihailescu N, Andronescu E, Turculet CF. Nanostructured Fibers Containing Natural or Synthetic Bioactive Compounds in Wound Dressing Applications. Materials 2020;13. https://doi.org/10.3390/ma13102407.

[136] Leena M, Barade A, Rana D, Dhand C, Ramakrishna S, Ramalingam M. Nanofiber Composites in Biomolecular Delivery. Nanofiber Composites for Biomedical Applications, Elsevier Ltd; 2017, p. 225–52. https://doi.org/10.1016/B978-0-08-100173-8.00009-0.

[137] Kennedy KM, Bhaw-Luximon A, Jhurry D. Skin Tissue Engineering: Biological Performance of Electrospun Polymer Scaffolds and Translational Challenges. Regen Eng Transl Med 2017;3:201–14. https://doi.org/10.1007/s40883-017-0035-x.

[138] Lee SM, Park IK, Kim YS, Kim HJ, Moon H, Mueller S, et al. Physical, Morphological, and Wound Healing Properties of a Polyurethane Foam-Film Dressing. Biomater Res 2016;20:15. https://doi.org/10.1186/s40824-016-0063-5.

[139] Hasatsri S, Pitiratanaworanat A, Swangwit S, Boochakul C, Tragoonsupachai C. Comparison of the Morphological and Physical Properties of Different Absorbent Wound Dressings. Dermatol Res Pract 2018;2018:1–6. https://doi.org/10.1155/2018/9367034.

[140] Junker JPE, Caterson EJ, Eriksson E. The Microenvironment of Wound Healing. Journal of Craniofacial Surgery 2013;24:12–6. https://doi.org/10.1097/SCS.0b013e31827104fb.

[141] Zhang K, Bai X, Yuan Z, Cao X, Jiao X, Li Y, et al. Layered Nanofiber Sponge with an Improved Capacity for Promoting Blood Coagulation and Wound Healing. Biomaterials 2019;204:70–9. https://doi.org/10.1016/j.biomaterials.2019.03.008.

[142] MacEwan MR, MacEwan S, Kovacs TR, Batts J. What Makes the Optimal Wound Healing Material? A Review of Current Science and Introduction of a Synthetic Nanofabricated Wound Care Scaffold. Cureus 2017;9. https://doi.org/10.7759/cureus.1736.

[143] Hassiba AJ, El Zowalaty ME, Nasrallah GK, Webster TJ, Luyt AS, Abdullah AM, et al. Review of Recent Research on Biomedical Applications of Electrospun Polymer Nanofibers for Improved Wound Healing. Nanomedicine 2016;11:715–37. https://doi.org/10.2217/nnm.15.211.

[144] Haifei S, Xingang W, Shoucheng W, Zhengwei M, Chuangang Y, Chunmao H. The Effect of Collagen-Chitosan Porous Scaffold Thickness on Dermal Regeneration in a One-Stage Grafting Procedure. J Mech Behav Biomed Mater 2014;29:114–25. https://doi.org/10.1016/j.jmbbm.2013.08.031.

[145] Xiao Y, Ahadian S, Radisic M. Biochemical and Biophysical Cues in Matrix Design for Chronic and Diabetic Wound Treatment. Tissue Eng Part B Rev 2017;23:9–26. https://doi.org/10.1089/ten.teb.2016.0200.

[146] Lamke L-O, Nilsson GE, Reithner HL. The Evaporative Water Loss from Burns and The Water-Vapour Permeability of Grafts and Artificial Membranes Used in The Treatment of Burns. Burns 1977;3:159–65. https://doi.org/10.1016/0305-4179(77)90004-3.

[147] Nawalakhe R, Shi Q, Vitchuli N, Bourham MA, Zhang X, Mccord MG. Novel Atmospheric Plasma Enhanced Silk Fibroin Nanofiber/Gauze Composite Wound Dressings. Journal of Fiber Bioengineering and Informatics 2012;5:227–42. https://doi.org/10.3993/jfbi09201201.

[148] Biji Balakrishnan, M. Mohanty, P.R. Umashankar, A. Jayakrishnan. Evaluation of an In Situ Forming Hydrogel Wound Dressing Based on Oxidized Alginate and Gelatin. Biomaterials 2005;26:6335–42. https://doi.org/10.1016/j.biomaterials.2005.04.012.

[149] Jiang J, Chen S, Wang H, Carlson MA, Gombart AF, Xie J. CO2-Expanded Nanofiber Scaffolds Maintain Activity of Encapsulated Bioactive Materials and Promote Cellular Infiltration and Positive Host Response. Acta Biomater 2018;68:237–48. https://doi.org/10.1016/j.actbio.2017.12.018.

[150] Jiang J, Carlson MA, Teusink MJ, Wang H, MacEwan MR, Xie J. Expanding Two-Dimensional Electrospun Nanofiber Membranes in the Third Dimension by a Modified Gas-Foaming Technique. ACS Biomater Sci Eng 2015;1:991–1001. https://doi.org/10.1021/acsbiomaterials.5b00238.

[151] Langwald SV, Ehrmann A, Sabantina L. Measuring Physical Properties of Electrospun Nanofiber Mats for Different Biomedical Applications. Membranes (Basel) 2023;13:488. https://doi.org/10.3390/membranes13050488.

[152] Ryu H Il, Koo MS, Kim S, Kim S, Park Y-A, Park SM. Uniform-Thickness Electrospun Nanofiber Mat Production System Based on Real-Time Thickness Measurement. Sci Rep 2020;10:20847. https://doi.org/10.1038/s41598-020-77985-0.

[153] Xie B, Zhu W, Ding P, Chen M, Li J, Lei L, et al. Nanofiber Scaffolds Attenuate Collagen Synthesis of Human Dermal Fibroblasts through TGF- β 1/TSG-6 Pathway. Journal of Physics: Materials 2019;2:044001. https://doi.org/10.1088/2515-7639/ab2563.

[154] Ferreira AM, Mattu C, Ranzato E, Ciardelli G. Bioinspired Porous Membranes Containing Polymer Nanoparticles for Wound Healing. J Biomed Mater Res A 2014:n/a-n/a. https://doi.org/10.1002/jbm.a.35121.

[155] Ren X, Han Y, Wang J, Jiang Y, Yi Z, Xu H, et al. An Aligned Porous Electrospun Fibrous Membrane with Controlled Drug Delivery – An Efficient Strategy to Accelerate Diabetic Wound Healing with Improved Angiogenesis. Acta Biomater 2018;70:140–53. https://doi.org/10.1016/j.actbio.2018.02.010.

[156] Jiang J, Li Z, Wang H, Wang Y, Carlson MA, Teusink MJ, et al. Expanded 3D Nanofiber Scaffolds: Cell Penetration, Neovascularization, and Host Response. Adv Healthc Mater 2016;5:2993–3003. https://doi.org/10.1002/adhm.201600808.

[157] Yu H, Chen X, Cai J, Ye D, Wu Y, Fan L, et al. Novel Porous Three-Dimensional Nanofibrous Scaffolds for Accelerating Wound Healing. Chemical Engineering Journal 2019;369:253–62. https://doi.org/10.1016/j.cej.2019.03.091.

[158] Nelson MT, Keith JP, Li B-B, Stocum DL, Li J. Electrospun Composite Polycaprolactone Scaffolds for Optimized Tissue Regeneration. Proceedings of the Institution of Mechanical Engineers, Part N: Journal of Nanoengineering and Nanosystems 2012;226:111–21. https://doi.org/10.1177/1740349912450828.

[159] Hashem MH, Wehbe M, Damacet P, El Habbal RK, Ghaddar N, Ghali K, et al. Electrospun Metal–Organic Framework-Fabric Nanocomposites as Efficient Bactericides. Langmuir 2023;39:9503–13. https://doi.org/10.1021/acs.langmuir.3c01039.

[160] Krysiak ZJ, Knapczyk-Korczak J, Maniak G, Stachewicz U. Moisturizing Effect of Skin Patches with Hydrophobic and Hydrophilic Electrospun Fibers for Atopic Dermatitis. Colloids Surf B Biointerfaces 2021;199:111554. https://doi.org/10.1016/j.colsurfb.2020.111554.

[161] Lin N, Zuo B. Silk Sericin/Fibroin Electrospinning Dressings: A Method for Preparing a Dressing Material with High Moisture Vapor Transmission Rate. J Biomater Sci Polym Ed 2021;32:1983–97. https://doi.org/10.1080/09205063.2021.1952383.

[162] Falde EJ, Yohe ST, Colson YL, Grinstaff MW. Superhydrophobic Materials for Biomedical Applications. Biomaterials 2016;104:87–103. https://doi.org/10.1016/j.biomaterials.2016.06.050.

[163] Yu B, He C, Wang W, Ren Y, Yang J, Guo S, et al. Asymmetric Wettable Composite Wound Dressing Prepared by Electrospinning with Bioinspired Micropatterning Enhances Diabetic Wound Healing. ACS Appl Bio Mater 2020;3:5383–94. https://doi.org/10.1021/acsabm.0c00695.

[164] Kim HN, Hong Y, Kim MS, Kim SM, Suh KY. Effect of Orientation and Density of Nanotopography in Dermal Wound Healing. Biomaterials 2012;33:8782–92. https://doi.org/10.1016/j.biomaterials.2012.08.038.

[165] Rezvani Ghomi E, Khosravi F, Neisiany RE, Shakiba M, Zare M, Lakshminarayanan R, et al. Advances in Electrospinning of Aligned Nanofiber Scaffolds Used for Wound Dressings. Curr Opin Biomed Eng 2022;22:100393. https://doi.org/10.1016/j.cobme.2022.100393.

[166] Sun L, Gao W, Fu X, Shi M, Xie W, Zhang W, et al. Enhanced Wound Healing in Diabetic Rats by Nanofibrous Scaffolds Mimicking The Basketweave Pattern of Collagen Fibrils in Native Skin. Biomater Sci 2018;6:340–9. https://doi.org/10.1039/c7bm00545h.

[167] Wang Y, Chen L. Cellulose Nanowhiskers and Fiber Alignment Greatly Improve Mechanical Properties of Electrospun Prolamin Protein Fibers. ACS Appl Mater Interfaces 2014;6:1709–18. https://doi.org/10.1021/am404624z.

[168] Nauman S, Lubineau G, Alharbi HF. Post Processing Strategies for The Enhancement of Mechanical Properties of Enms (Electrospun Nanofibrous Membranes): A Review. Membranes (Basel) 2021;11:1–38. https://doi.org/10.3390/membranes11010039.

[169] Xia D, Liu Y, Cao W, Gao J, Wang D, Lin M, et al. Dual-Functional Nanofibrous Patches for Accelerating Wound Healing. Int J Mol Sci 2022;23:10983. https://doi.org/10.3390/ijms231810983.

[170] A K, A L. Mechanical Behaviour of Skin: A Review. Journal of Material Science & Engineering 2016;5. https://doi.org/10.4172/2169-0022.1000254.

[171] Shariatzadeh FJ, Nour S, Sadeghi D, Solouk A. Evaluation of Physical Properties of Semi-Thickness Skin, Acellular Dermis and Fascia as Biologic Skin Substitutes. 2016 23rd

Iranian Conference on Biomedical Engineering and 2016 1st International Iranian Conference on Biomedical Engineering (ICBME), IEEE; 2016, p. 1–6. https://doi.org/10.1109/ICBME.2016.7890919.

[172] Xi Y, Ge J, Guo Y, Lei B, Ma PX. Biomimetic Elastomeric Polypeptide-Based Nanofibrous Matrix for Overcoming Multidrug-Resistant Bacteria and Enhancing Full-Thickness Wound Healing/Skin Regeneration. ACS Nano 2018;12:10772–84. https://doi.org/10.1021/acsnano.8b01152.

[173] Donya H, Darwesh R, Ahmed MK. Morphological Features and Mechanical Properties of Nanofibers Scaffolds of Polylactic Acid Modified with Hydroxyapatite/CdSe for Wound Healing Applications. Int J Biol Macromol 2021;186:897–908. https://doi.org/10.1016/j.ijbiomac.2021.07.073.

[174] Minsart M, Van Vlierberghe S, Dubruel P, Mignon A. Commercial Wound Dressings for The Treatment of Exuding Wounds: An In-Depth Physico-Chemical Comparative Study. Burns Trauma 2022;10. https://doi.org/10.1093/burnst/tkac024.

[175] Kennedy KM, Bhaw-Luximon A, Jhurry D. Cell-Matrix Mechanical Interaction in Electrospun Polymeric Scaffolds for Tissue Engineering: Implications for Scaffold Design and Performance. Acta Biomater 2017;50:41–55. https://doi.org/10.1016/j.actbio.2016.12.034.

[176] Gao C, Zhang L, Wang J, Jin M, Tang Q, Chen Z, et al. Electrospun Nanofibers Promote Wound Healing: Theories, Techniques, and Perspectives. J Mater Chem B 2021;9:3106–30. https://doi.org/10.1039/D1TB00067E.

[177] Jiang S, Li SC, Huang C, Chan BP, Du Y. Physical Properties of Implanted Porous Bioscaffolds Regulate Skin Repair: Focusing on Mechanical and Structural Features. Adv Healthc Mater 2018;7. https://doi.org/10.1002/adhm.201700894.

[178] Hinz B. The myofibroblast: Paradigm for a mechanically active cell. J Biomech 2010;43:146–55. https://doi.org/10.1016/j.jbiomech.2009.09.020.

[179] Jerrell RJ, Leih MJ, Parekh A. The Altered Mechanical Phenotype of Fetal Fibroblasts Hinders Myofibroblast Differentiation. Wound Repair and Regeneration 2019;27:29–38. https://doi.org/10.1111/wrr.12677.

[180] Yang L, Fitié CFC, van der Werf KO, Bennink ML, Dijkstra PJ, Feijen J. Mechanical Properties of Single Electrospun Collagen Type I Fibers. Biomaterials 2008;29:955–62. https://doi.org/10.1016/j.biomaterials.2007.10.058.

[181] Dodero A, Scarfi S, Mirata S, Sionkowska A, Vicini S, Alloisio M, et al. Effect of Crosslinking Type on The Physical-Chemical Properties and Biocompatibility of Chitosan-Based Electrospun Membranes. Polymers (Basel) 2021;13. https://doi.org/10.3390/polym13050831.

[182] Dubský M, Kubinová Š, Širc J, Voska L, Zajíček R, Zajícová A, et al. Nanofibers Prepared by Needleless Electrospinning Technology as Scaffolds for Wound Healing. J Mater Sci Mater Med 2012;23:931–41. https://doi.org/10.1007/s10856-012-4577-7.

[183] Chantre CO, Campbell PH, Golecki HM, Buganza AT, Capulli AK, Deravi LF, et al. Production-scale fibronectin nanofibers promote wound closure and tissue repair in a dermal mouse model. Biomaterials 2018;166:96–108. https://doi.org/10.1016/j.biomaterials.2018.03.006.

[184] Ju HW, Lee OJ, Lee JM, Moon BM, Park HJ, Park YR, et al. Wound Healing Effect of Electrospun Silk Fibroin Nanomatrix in Burn-Model. Int J Biol Macromol 2016;85:29–39. https://doi.org/10.1016/j.ijbiomac.2015.12.055.

[185] Zhou T, Wang N, Xue Y, Ding T, Liu X, Mo X, et al. Electrospun tilapia collagen nanofibers accelerating wound healing via inducing keratinocytes proliferation and differentiation. Colloids Surf B Biointerfaces 2016;143:415–22. https://doi.org/10.1016/j.colsurfb.2016.03.052.

[186] Su K, Jeong L, Lee G, Seo B, Jeong Y, Hong S, et al. Electrospinning of Collagen Nanofibers: Effects on The Behavior of Normal Human Keratinocytes and Early-Stage Wound Healing 2006;27:1452–61. https://doi.org/10.1016/j.biomaterials.2005.08.004.

[187] Hsu FY, Hung YS, Liou HM, Shen CH. Electrospun hyaluronate-collagen nanofibrous matrix and the effects of varying the concentration of hyaluronate on the characteristics of foreskin fibroblast cells. Acta Biomater 2010;6:2140–7. https://doi.org/10.1016/j.actbio.2009.12.023.

[188] Chen JP, Chang GY, Chen JK. Electrospun Collagen/Chitosan Nanofibrous Membrane as Wound Dressing. Colloids Surf A Physicochem Eng Asp 2008;313–314:183–8. https://doi.org/10.1016/j.colsurfa.2007.04.129.

[189] Yuan Z, Zhao J, Chen Y, Yang Z, Cui W, Zheng Q. Regulating inflammation using acid-responsive electrospun fibrous scaffolds for skin scarless healing. Mediators Inflamm 2014;2014. https://doi.org/10.1155/2014/858045.

[190] Mohiti-Asli M, Saha S, Murphy S V., Gracz H, Pourdeyhimi B, Atala A, et al. Ibuprofen loaded PLA nanofibrous scaffolds increase proliferation of human skin cells in vitro and

promote healing of full thickness incision wounds in vivo. J Biomed Mater Res B Appl Biomater 2017;105:327–39. https://doi.org/10.1002/jbm.b.33520.

[191] Liu X, Lin T, Gao Y, Xu Z, Huang C, Yao G, et al. Antimicrobial electrospun nanofibers of cellulose acetate and polyester urethane composite for wound dressing. J Biomed Mater Res B Appl Biomater 2012;100 B:1556–65. https://doi.org/10.1002/jbm.b.32724.

[192] Poormasjedi-Meibod MS, Salimi Elizei S, Leung V, Baradar Jalili R, Ko F, Ghahary A. Kynurenine Modulates MMP-1 and Type-I Collagen Expression Via Aryl Hydrocarbon Receptor Activation in Dermal Fibroblasts. J Cell Physiol 2016;231:2749–60. https://doi.org/10.1002/jcp.25383.

[193] Vargas EAT, do Vale Baracho NC, de Brito J, de Queiroz AAA. Hyperbranched polyglycerol electrospun nanofibers for wound dressing applications. Acta Biomater 2010;6:1069–78. https://doi.org/10.1016/j.actbio.2009.09.018.

[194] Jung SM, Min SK, Lee HC, Kwon YS, Jung MH, Shin HS. Spirulina -PCL Nanofiber Wound Dressing to Improve Cutaneous Wound Healing by Enhancing Antioxidative Mechanism. J Nanomater 2016;2016. https://doi.org/10.1155/2016/6135727.

[195] Mohammadi MR, Rabbani S, Bahrami SH, Joghataei MT, Moayer F. Antibacterial performance and in vivo diabetic wound healing of curcumin loaded gum tragacanth/poly(ε-caprolactone) electrospun nanofibers. Materials Science and Engineering C 2016;69:1183–91. https://doi.org/10.1016/j.msec.2016.08.032.

[196] Mohammadi Z, Sharif Zak M, Majdi H, Mostafavi E, Barati M, Lotfimehr H, et al. The effect of Chrysin–Curcumin-Loaded Nanofibres on The Wound-Healing Process in Male Rats. Artif Cells Nanomed Biotechnol 2019;47:1642–52. https://doi.org/10.1080/21691401.2019.1594855.

[197] Yao CH, Chen KY, Chen YS, Li SJ, Huang CH. Lithospermi Radix Extract-Containing Bilayer Nanofiber Scaffold for Promoting Wound Healing in a Rrat Model. Materials Science and Engineering C 2019;96:850–8. https://doi.org/10.1016/j.msec.2018.11.053.

[198] Ahn S, Ardoña HAM, Campbell PH, Gonzalez GM, Parker KK. Alfalfa Nanofibers for Dermal Wound Healing. ACS Appl Mater Interfaces 2019. https://doi.org/10.1021/acsami.9b07626.

[199] Chaudhuri O, Cooper-White J, Janmey PA, Mooney DJ, Shenoy VB. Effects of Extracellular Matrix Viscoelasticity on Cellular Behaviour. Nature 2020;584:535–46. https://doi.org/10.1038/s41586-020-2612-2.

[200] Tracy LE, Minasian RA, Caterson EJ. Extracellular Matrix and Dermal Fibroblast Function in the Healing Wound. Adv Wound Care (New Rochelle) 2016;5:119–36. https://doi.org/10.1089/wound.2014.0561.

[201] Mathew-Steiner SS, Roy S, Sen CK. Collagen in Wound Healing. Bioengineering 2021;8:63. https://doi.org/10.3390/bioengineering8050063.

[202] Cruz MA, Araujo TA, Avanzi IR, Parisi JR, de Andrade ALM, Rennó ACM. Collagen from Marine Sources and Skin Wound Healing in Animal Experimental Studies: a Systematic Review. Marine Biotechnology 2021;23:1–11. https://doi.org/10.1007/s10126-020-10011-6.

[203] Silva T, Moreira-Silva J, Marques A, Domingues A, Bayon Y, Reis R. Marine Origin Collagens and Its Potential Applications. Mar Drugs 2014;12:5881–901. https://doi.org/10.3390/md12125881.

[204] Subhan F, Ikram M, Shehzad A, Ghafoor A. Marine Collagen: An Emerging Player in Biomedical applications. J Food Sci Technol 2015;52:4703–7. https://doi.org/10.1007/s13197-014-1652-8.

[205] Deng A, Yang Y, Du S, Yang S. Electrospinning of In Situ Crosslinked Recombinant Human Collagen Peptide/Chitosan Nanofibers for Wound Healing. Biomater Sci 2018;6:2197–208. https://doi.org/10.1039/C8BM00492G.

[206] Pal P, Dadhich P, Srivas PK, Das B, Maulik D, Dhara S. Bilayered Nanofibrous 3D Hierarchy as Skin Rudiment by Emulsion Electrospinning for Burn Wound Management. Biomater Sci 2017;5:1786–99. https://doi.org/10.1039/C7BM00174F.

[207] Naomi R, Bahari H, Ridzuan PM, Othman F. Natural-based biomaterial for skin wound healing (Gelatin vs. collagen): Expert review. Polymers (Basel) 2021;13. https://doi.org/10.3390/polym13142319.

[208] Ghodbane SA, Dunn MG. Physical and mechanical properties of cross-linked type I collagen scaffolds derived from bovine, porcine, and ovine tendons. J Biomed Mater Res A 2016;104:2685–92. https://doi.org/10.1002/jbm.a.35813.

[209] Liu S, Kau Y, Chou C, Chen J, Wu R, Yeh W. Electrospun PLGA /Collagen Nanofibrous Membrane as Early-Stage Wound Dressing. J Memb Sci 2010;355:53–9. https://doi.org/10.1016/j.memsci.2010.03.012.

[210] Gautam S, Chou C-F, Dinda AK, Potdar PD, Mishra NC. Surface Modification of Nanofibrous Polycaprolactone/Gelatin Composite Scaffold by Collagen Type I Grafting for Skin Tissue Engineering. Materials Science and Engineering: C 2014;34:402–9. https://doi.org/10.1016/j.msec.2013.09.043.

[211] Krithica N, Natarajan V, Madhan B, Sehgal PK, Mandal AB. Type I Collagen Immobilized Poly(caprolactone) Nanofibers: Characterization of Surface Modification and Growth of Fibroblasts. Adv Eng Mater 2012;14:B149–54. https://doi.org/10.1002/adem.201180035.

[212] Tracy LE, Minasian RA, Caterson EJ. Extracellular Matrix and Dermal Fibroblast Function in the Healing Wound. Adv Wound Care (New Rochelle) 2016;5:119–36. https://doi.org/10.1089/wound.2014.0561.

[213] Messadi D V, Bertolamit CN, Ofdentistty S, Crippled SH. CD44 and Hyaluronan Expression in Human Cutaneous Scar Fibroblasts From the Section of Oral and Maxillofacial Surgery* UCLA. vol. 142. 1993.

[214] Larson BJ, Longaker MT, Lorenz HP. Scarless Fetal Wound Healing: A Basic Science Review. Plast Reconstr Surg 2010;126:1172–80. https://doi.org/10.1097/PRS.0b013e3181eae781.

[215] Lovvorn HN, Cass DL, Sylvester KG, Yang EY, Crombleholme TM, Adzick NS, et al. Hyaluronan Receptor Expression Increases in Fetal Excisional Skin Wounds and Correlates With Fibroplasia. n.d.

[216] David-Raoudi M, Tranchepain F, Deschrevel B, Vincent J, Bogdanowicz P, Boumediene K, et al. Differential effects of hyaluronan and its fragments on fibroblasts: Relation to wound healing. Wound Repair and Regeneration 2008;16:274–87. https://doi.org/10.1111/j.1524-475X.2007.00342.x.

[217] Kellar RS, Diller RB, Tabor AJ, Dominguez DD, Audet G, Bardsley TA, et al. Improved Wound Closure Rates and Mechanical Properties Resembling Native Skin in Murine

Diabetic Wounds Treated with a Tropoelastin and Collagen Wound Healing Device. J Diabetes Clin Res 2020;2:10–5. https://doi.org/10.33696/diabetes.1.024.

[218] Baxter RM, Dai T, Kimball J, Wang E, Hamblin MR, Wiesmann WP, et al. Chitosan Dressing Promotes Healing in Third Degree Burns in Mice: Gene Expression Analysis Shows Biphasic Effects for Rapid Tissue Regeneration and Decreased Fibrotic Signaling. J Biomed Mater Res A 2013;101 A:340–8. https://doi.org/10.1002/jbm.a.34328.

[219] Beanes SR, Dang C, Soo C, Ting K. Skin Repair and Scar Formation: The Central Role of TGF-β. Expert Rev Mol Med 2003;5:1–11. https://doi.org/10.1017/S1462399403005817.

[220] Dalton CJ, Lemmon CA. Fibronectin: Molecular Structure, Fibrillar Structure and Mechanochemical Signaling. Cells 2021;10:2443. https://doi.org/10.3390/cells10092443.

[221] Pal P, Dadhich P, Srivas PK, Das B, Maulik D, Dhara S. Bilayered Nanofibrous 3D Hierarchy as Skin Rudiment by Emulsion Electrospinning for Burn Wound Management. Biomater Sci 2017;5:1786–99. https://doi.org/10.1039/C7BM00174F.

[222] Ratner BD, Hoffman AS, Schoen FJ, Lemons JE. Biomaterials Science: An Introduction to Materials in Medicine. MRS Bull 2013;31:59.

[223] Masson-Meyers DS, Andrade TAM, Caetano GF, Guimaraes FR, Leite MN, Leite SN, et al. Experimental Models and Methods for Cutaneous Wound Healing Assessment. Int J Exp Pathol 2020;101:21–37. https://doi.org/10.1111/iep.12346.

[224] Shrivastav A, Mishra AK, Ali SS, Ahmad A, Abuzinadah MF, Khan NA. In Vivo Models for Assessment of Wound Healing Potential: A Systematic Review. Wound Medicine 2018;20:43–53. https://doi.org/10.1016/j.wndm.2018.01.003.

[225] Cribbs RK, Luquette MH, Besner GE. Acceleration of Partial-Thickness Burn Wound Healing with Topical Application of Heparin-Binding EGF-Like Growth Factor (HB-

EGF). Journal of Burn Care & Rehabilitation 1998;19:95–101. https://doi.org/10.1097/00004630-199803000-00002.

[226] Han C, Cheng B, Wu P. Clinical Guideline on Topical Growth Factors for Skin Wounds. Burns Trauma 2020;8. https://doi.org/10.1093/burnst/tkaa035.

[227] Sanchez MC, Lancel S, Boulanger E, Neviere R. Targeting Oxidative Stress and Mitochondrial Dysfunction in The Treatment of Impaired Wound Healing: A Systematic Review. Antioxidants 2018;7:1–14. https://doi.org/10.3390/antiox7080098.

[228] Zhao R, Liang H, Clarke E, Jackson C, Xue M. Inflammation in Chronic Wounds. Int J Mol Sci 2016;17:1–14. https://doi.org/10.3390/ijms17122085.

[229] Martin P, Nunan R. Cellular and Molecular Mechanisms of Repair in Acute and Chronic Wound Healing. British Journal of Dermatology 2015;173:370–8. https://doi.org/10.1111/bjd.13954.

[230] Yan S, Qian Y, Haghayegh M, Xia Y, Yang S, Cao R, et al. Electrospun Organic/Inorganic Hybrid Nanofibers for Accelerating Wound Healing: A Review. J Mater Chem B 2024;12:3171–90. https://doi.org/10.1039/D4TB00149D.

[231] Ding L, Wang S, Yao B, Li F, Li Y, Zhao G, et al. Synergistic Antibacterial and Anti-Inflammatory Effects of a Drug-Loaded Self-Standing Porphyrin-COF Membrane for Efficient Skin Wound Healing. Adv Healthc Mater 2021;10. https://doi.org/10.1002/adhm.202001821.

[232] Krischak GD, Augat P, Claes L, Kinzl L, Beck A. The Effects of Non-Steroidal Anti-Inflammatory Drug Application on Incisional Wound Healing in Rats. J Wound Care 2007;16:76–8. https://doi.org/10.12968/jowc.2007.16.2.27001.

[233] Velasco M, Guaitero E. A Comparative Study of Some Anti-Inflammatory Drugs in Wound Healing of The Rat. Experientia 1973;29:1250–1. https://doi.org/10.1007/BF01935101.

[234] Ferreira H, Matamá T, Silva R, Silva C, Gomes AC, Cavaco-Paulo A. Functionalization of Gauzes with Liposomes Entrapping an Anti-Inflammatory Drug: A Strategy to Improve Wound Healing. React Funct Polym 2013;73:1328–34. https://doi.org/10.1016/j.reactfunctpolym.2013.05.012.

[235] Shukla SK, Sharma AK, Gupta V, Yashavarddhan MH. Pharmacological Control of Inflammation in Wound Healing. J Tissue Viability 2019;28:218–22. https://doi.org/10.1016/j.jtv.2019.09.002.

[236] Su W-H, Cheng M-H, Lee W-L, Tsou T-S, Chang W-H, Chen C-S, et al. Nonsteroidal Anti-Inflammatory Drugs for Wounds: Pain Relief or Excessive Scar Formation? Mediators Inflamm 2010;2010:1–8. https://doi.org/10.1155/2010/413238.

[237] Shedoeva A, Leavesley D, Upton Z, Fan C. Wound Healing and the Use of Medicinal Plants. Evidence-Based Complementary and Alternative Medicine 2019;2019:1–30. https://doi.org/10.1155/2019/2684108.

[238] Criollo-Mendoza MS, Contreras-Angulo LA, Leyva-López N, Gutiérrez-Grijalva EP, Jiménez-Ortega LA, Heredia JB. Wound Healing Properties of Natural Products: Mechanisms of Action. Molecules 2023;28:598. https://doi.org/10.3390/molecules28020598.

[239] Liu R, Qin S, Li W. Phycocyanin: Anti-Inflammatory Effect and Mechanism. Biomedicine & Pharmacotherapy 2022;153:113362. https://doi.org/10.1016/j.biopha.2022.113362.

[240] Namazi MR, Fallahzadeh MK, Schwartz RA. Strategies for Prevention of Scars: What Can We Learn from Fetal Skin? Int J Dermatol 2011;50:85–93. https://doi.org/10.1111/j.1365-4632.2010.04678.x.

[241] Xiao Z, Guo Z. Cell-Laden Electrospinning and Its Biomedical Applications. J Phys Conf Ser 2023;2610:012068. https://doi.org/10.1088/1742-6596/2610/1/012068.

[242] Ranjbar-Mohammadi M, Rabbani S, Bahrami SH, Joghataei MT, Moayer F. Antibacterial Performance and In Vivo Diabetic Wound Healing of Curcumin Loaded Gum Tragacanth/Poly(E-Caprolactone) Electrospun Nanofibers. Materials Science and Engineering: C 2016;69:1183–91. https://doi.org/10.1016/j.msec.2016.08.032.

[243] Warriner R, Burrell R. Infection and The Chronic Wound: A Focus on Silver. Adv Skin Wound Care 2005;18 Suppl 1:2–12. https://doi.org/10.1097/00129334-200510001-00001.

[244] Leaper D, Assadian O, Edmiston CE. Approach to Chronic Wound Infections. British Journal of Dermatology 2015;173:351–8. https://doi.org/10.1111/bjd.13677.

[245] Ersanli C, Voidarou C, Tzora A, Fotou K, Zeugolis DI, Skoufos I. Electrospun Scaffolds as Antimicrobial Herbal Extract Delivery Vehicles for Wound Healing. J Funct Biomater 2023;14. https://doi.org/10.3390/jfb14090481.

[246] Mouro C, Gouveia IC. Electrospun Wound Dressings with Antibacterial Function: A Critical Review of Plant Extract and Essential Oil Incorporation. Crit Rev Biotechnol 2023. https://doi.org/10.1080/07388551.2023.2193859.

[247] Zare MR, Khorram M, Barzegar S, Asadian F, Zareshahrabadi Z, Saharkhiz MJ, et al. Antimicrobial Core–Shell Electrospun Nanofibers Containing Ajwain Essential Oil for Accelerating Infected Wound Healing. Int J Pharm 2021;603:120698. https://doi.org/10.1016/j.ijpharm.2021.120698.

[248] Ross JA, Allan N, Olson M, Schatz C, Nation PN, Gawaziuk JP, et al. Comparison of The Efficacy of Silver-Based Antimicrobial Burn Dressings in a Porcine Model of Burn Wounds. Burns 2020;46:1632–40. https://doi.org/10.1016/j.burns.2020.04.004.

[249] Rath G, Hussain T, Chauhan G, Garg T, Goyal AK. Collagen Nanofiber Containing Silver Nanoparticles for Improved Wound-Healing Applications. J Drug Target 2016;24:520–9. https://doi.org/10.3109/1061186X.2015.1095922.

[250] Xiu ZM, Zhang QB, Puppala HL, Colvin VL, Alvarez PJJ. Negligible particle-specific antibacterial activity of silver nanoparticles. Nano Lett 2012;12:4271–5. https://doi.org/10.1021/nl301934w.

[251] Hadisi Z, Nourmohammadi J, Nassiri SM. The Antibacterial and Anti-Inflammatory Investigation of Lawsonia Inermis-Gelatin-Starch Nano-Fibrous Dressing in Burn Wound. Int J Biol Macromol 2018;107:2008–19. https://doi.org/10.1016/j.ijbiomac.2017.10.061.

[252] Suryamathi M, Viswanathamurthi P, Seedevi P. Herbal Plant Leaf Extracts Immobilized PCL Nanofibrous Mats as Skin-Inspired Anti-infection Wound Healing Material. Regen Eng Transl Med 2022;8:94–105. https://doi.org/10.1007/s40883-020-00193-9.

[253] Liu X, Lin T, Gao Y, Xu Z, Huang C, Yao G, et al. Antimicrobial Electrospun Nanofibers of Cellulose Acetate and Polyester Urethane Composite for Wound Dressing 2012:1556–65. https://doi.org/10.1002/jbm.b.32724.

[254] Branski LK, Pereira CT, Herndon DN, Jeschke MG. Gene Therapy in Wound Healing: Present Status and Future Directions. Gene Ther 2007;14:1–10. https://doi.org/10.1038/sj.gt.3302837.

[255] Ashcroft GS, Mills SJ, Lei K, Gibbons L, Jeong M-J, Taniguchi M, et al. Estrogen Modulates Cutaneous Wound Healing by Downregulating Macrophage Migration Inhibitory Factor. Journal of Clinical Investigation 2003;111:1309–18. https://doi.org/10.1172/JCI16288.

[256] Xie Y, Wang L, Sun H, Wang Y, Yang Z, Zhang G, et al. Polysaccharide from Alfalfa Activates RAW 264.7 Macrophages through MAPK and NF-κB Signaling Pathways. Int J Biol Macromol 2019;126:960–8. https://doi.org/10.1016/j.ijbiomac.2018.12.227.

[257] Patisaul HB, Jefferson W. The Pros and Cons of Phytoestrogens. Front Neuroendocrinol 2010;31:400–19. https://doi.org/10.1016/j.yfrne.2010.03.003.

[258] Haensel D, Dai X. Epithelial-to-Mesenchymal Transition in Cutaneous Wound Healing: Where We are and Where We are Heading. Developmental Dynamics 2018;247:473–80. https://doi.org/10.1002/dvdy.24561.

[259] Yin S-Y, Peng A-P, Huang L-T, Wang Y-T, Lan C-W, Yang N-S. The Phytochemical Shikonin Stimulates Epithelial-Mesenchymal Transition (EMT) in Skin Wound Healing. Evidence-Based Complementary and Alternative Medicine 2013;2013:1–13. https://doi.org/10.1155/2013/262796.

[260] Hsiao C-Y, Tsai T-H, Chak K-F. The Molecular Basis of Wound Healing Processes Induced by Lithospermi Radix: A Proteomics and Biochemical Analysis. Evidence-Based Complementary and Alternative Medicine 2012;2012:1–15. https://doi.org/10.1155/2012/508972.

[261] Li Y, Tredget EE, Ghaffari A, Lin X, Kilani RT, Ghahary A. Local Expression of Indoleamine 2,3-Dioxygenase Protects Engraftment of Xenogeneic Skin Substitute.

Journal of Investigative Dermatology 2006;126:128–36. https://doi.org/10.1038/sj.jid.5700022.

[262] Li Y, Kilani RT, Rahmani-Neishaboor E, Jalili RB, Ghahary A. Kynurenine Increases Matrix Metalloproteinase-1 and -3 Expression in Cultured Dermal Fibroblasts and Improves Scarring In Vivo. Journal of Investigative Dermatology 2014;134:643–50. https://doi.org/10.1038/jid.2013.303.

[263] Poormasjedi-Meibod MS, Hartwell R, Kilani RT, Ghahary A. Anti-Scarring Properties of Different Tryptophan Derivatives. PLoS One 2014;9. https://doi.org/10.1371/journal.pone.0091955.

[264] Matysik-Woźniak A, Paduch R, Turski WA, Maciejewski R, Jünemann AG, Rejdak R. Effects of Tryptophan, Kynurenine and Kynurenic Acid Exerted on Human Reconstructed Corneal Epithelium In Vitro. Pharmacological Reports 2017;69:722–9. https://doi.org/10.1016/j.pharep.2017.02.020.

[265] Papp A, Hartwell R, Evans M, Ghahary A. The Safety and Tolerability of Topically Delivered Kynurenic Acid in Humans. A Phase 1 Randomized Double-Blind Clinical Trial. J Pharm Sci 2018;107:1572–6. https://doi.org/10.1016/j.xphs.2018.01.023.

[266] Nazarnezhad S, Baino F, Kim H-W, Webster TJ, Kargozar S. Electrospun Nanofibers for Improved Angiogenesis: Promises for Tissue Engineering Applications. Nanomaterials 2020;10:1609. https://doi.org/10.3390/nano10081609.

[267] Kumar P, Kumar S, Udupa EP, Kumar U, Rao P, Honnegowda T. Role of Angiogenesis and Angiogenic Factors in Acute and Chronic Wound Healing. Plast Aesthet Res 2015;2:243. https://doi.org/10.4103/2347-9264.165438.

[268] Guo Y, Huang J, Fang Y, Huang H, Wu J. 1D, 2D, and 3D Scaffolds Promoting Angiogenesis for Enhanced Wound Healing. Chemical Engineering Journal 2022;437:134690. https://doi.org/10.1016/j.cej.2022.134690.

[269] Nazarnezhad S, Baino F, Kim H-W, Webster TJ, Kargozar S. Electrospun Nanofibers for Improved Angiogenesis: Promises for Tissue Engineering Applications. Nanomaterials 2020;10:1609. https://doi.org/10.3390/nano10081609.

[270] Dipietro LA. Angiogenesis and Scar Formation in Healing Wounds. Curr Opin Rheumatol 2013;25:87–91. https://doi.org/10.1097/BOR.0b013e32835b13b6.

[271] Demidova-Rice TN, Durham JT, Herman IM. Wound Healing Angiogenesis: Innovations and Challenges in Acute and Chronic Wound Healing. Adv Wound Care (New Rochelle) 2012;1:17–22. https://doi.org/10.1089/wound.2011.0308.

[272] Zhu Z, Liu Y, Xue Y, Cheng X, Zhao W, Wang J, et al. Tazarotene Released from Aligned Electrospun Membrane Facilitates Cutaneous Wound Healing by Promoting Angiogenesis. ACS Appl Mater Interfaces 2019;11:36141–53. https://doi.org/10.1021/acsami.9b13271.

[273] Shan Y-H, Peng L-H, Liu X, Chen X, Xiong J, Gao J-Q. Silk Fibroin/Gelatin Electrospun Nanofibrous Dressing Functionalized with Astragaloside IV Induces Healing and Anti-Scar Effects on Burn Wound. Int J Pharm 2015;479:291–301. https://doi.org/10.1016/j.ijpharm.2014.12.067.

[274] Satish A, Korrapati PS. Nanofiber-Mediated Sustained Delivery of Triiodothyronine: Role in Angiogenesis. AAPS PharmSciTech 2019;20:110. https://doi.org/10.1208/s12249-019-1326-y.

[275] Gasowska K, Naumnik B, Klejna K, Myśliwiec M. The Influence of Uunfractionated and Low-Molecular Weight Heparins on The Properties of Human Umbilical Vein Endothelial Cells (HUVEC). Folia Histochem Cytobiol 2009;47. https://doi.org/10.2478/v10042-009-0008-0.

[276] Tavakoli M, Mirhaj M, Salehi S, Varshosaz J, Labbaf S, Golshirazi A, et al. Coaxial Electrospun Angiogenic Nanofiber Wound Dressing Containing Advanced Platelet Rich-Fibrin. Int J Biol Macromol 2022;222:1605–18. https://doi.org/10.1016/j.ijbiomac.2022.09.109.

[277] Zehra M, Zubairi W, Hasan A, Butt H, Ramzan A, Azam M, et al. Oxygen Generating Polymeric Nano Fibers That Stimulate Angiogenesis and Show Efficient Wound Healing in a Diabetic Wound Model. Int J Nanomedicine 2020;Volume 15:3511–22. https://doi.org/10.2147/IJN.S248911.

[278] Mohammadian F, Eatemadi A. Drug Loading and Delivery Using Nanofibers Scaffolds. Artif Cells Nanomed Biotechnol 2017;45:881–8. https://doi.org/10.1080/21691401.2016.1185726.

[279] Zamani M, Prabhakaran MP, Ramakrishna S. Advances in Drug Delivery via Electrospun and Electrosprayed Nanomaterials. Int J Nanomedicine 2013;8:2997–3017. https://doi.org/10.2147/IJN.S43575.

[280] Son YJ, Kim WJ, Yoo HS. Therapeutic Applications of Electrospun Nanofibers for Drug Delivery Systems. Arch Pharm Res 2014;37:69–78. https://doi.org/10.1007/s12272-013-0284-2.

[281] Liu M, Duan XP, Li YM, Yang DP, Long YZ. Electrospun Nanofibers for Wound Healing. Materials Science and Engineering C 2017;76:1413–23. https://doi.org/10.1016/j.msec.2017.03.034.

[282] Ji W, Yang F, Van Den Beucken JJJP, Bian Z, Fan M, Chen Z, et al. Fibrous scaffolds loaded with protein prepared by blend or coaxial electrospinning. Acta Biomater 2010;6:4199–207. https://doi.org/10.1016/j.actbio.2010.05.025.

[283] Aavani F, Khorshidi S, Karkhaneh A. A Concise Review on Drug-Loaded Electrospun Nanofibres as Promising Wound Dressings. J Med Eng Technol 2019;43:38–47. https://doi.org/10.1080/03091902.2019.1606950.

[284] Zahedi P, Karami Z, Rezaeian I, Jafari S-H, Mahdaviani P, Abdolghaffari AH, et al. Preparation and Performance Evaluation of Tetracycline Hydrochloride Loaded Wound Dressing Mats Based on Electrospun Nanofibrous Poly(Lactic acid)/Poly(ϵ-Caprolactone) Blends. J Appl Polym Sci 2012;124:4174–83. https://doi.org/10.1002/app.35372.

[285] Kim K, Luu YK, Chang C, Fang D, Hsiao BS, Chu B, et al. Incorporation and Controlled Release of a Hydrophilic Antibiotic Using Poly(Lactide-co-Glycolide)-Based Electrospun Nanofibrous Scaffolds. Journal of Controlled Release 2004;98:47–56. https://doi.org/10.1016/j.jconrel.2004.04.009.

[286] Chen L, Bromberg L, Hatton TA, Rutledge GC. Electrospun Cellulose Acetate Fibers Containing Chlorhexidine as a Bactericide. Polymer (Guildf) 2008;49:1266–75. https://doi.org/10.1016/j.polymer.2008.01.003.

[287] Gliścińska E, Gutarowska B, Brycki B, Krucińska I. Electrospun Polyacrylonitrile Nanofibers Modified by Quaternary Ammonium Salts. J Appl Polym Sci 2013;128:767–75. https://doi.org/10.1002/app.38210.

[288] Calamak S, Aksoy EA, Ertas N, Erdogdu C, Sagıroglu M, Ulubayram K. Ag/Silk Fibroin Nanofibers: Effect of Fibroin Morphology on Ag+ Release and Antibacterial Activity. Eur Polym J 2015;67:99–112. https://doi.org/10.1016/j.eurpolymj.2015.03.068.

[289] Hwang S, Jeong S. Electrospun Nano Composites of Poly(vinyl pyrrolidone)/Nano-Silver for Antibacterial Materials. J Nanosci Nanotechnol 2011;11:610–3. https://doi.org/10.1166/jnn.2011.3243.

[290] Lee K, Lee S. Multifunctionality of Poly(Vinyl Alcohol) Nanofiber Webs Containing Titanium Dioxide. J Appl Polym Sci 2012;124:4038–46. https://doi.org/10.1002/app.34929.

[291] Kalinov K, Ignatova M, Maximova V, Rashkov I, Manolova N. Modification of Electrospun Poly(ε-Caprolactone) Mats by Formation of a Polyelectrolyte Complex between Poly(Acrylic Acid) and Quaternized Chitosan for Tuning of Their Antibacterial Properties. Eur Polym J 2014;50:18–29. https://doi.org/10.1016/j.eurpolymj.2013.10.016.

[292] Kangwansupamonkon W, Tiewtrakoonwat W, Supaphol P, Kiatkamjornwong S. Surface Modification of Electrospun Chitosan Nanofibrous Mats for Antibacterial Activity. J Appl Polym Sci 2014;131. https://doi.org/10.1002/app.40981.

[293] Sarhan WA, Azzazy HME. High Concentration Honey Chitosan Electrospun Nanofibers: Biocompatibility and Antibacterial Effects. Carbohydr Polym 2015;122:135–43. https://doi.org/10.1016/j.carbpol.2014.12.051.

[294] Kim HS, Yoo HS. MMPs-Responsive Release of DNA from Electrospun Nanofibrous Matrix for Local Gene Therapy: In vitro and In vivo Evaluation. Journal of Controlled Release 2010;145:264–71. https://doi.org/10.1016/j.jconrel.2010.03.006.

[295] Yoo HS, Kim TG, Park TG. Surface-Functionalized Electrospun Nanofibers for Tissue Engineering and Drug Delivery. Adv Drug Deliv Rev 2009;61:1033–42. https://doi.org/10.1016/j.addr.2009.07.007.

[296] Park CH, Kim K-H, Lee J-C, Lee J. In-situ Nanofabrication via Electrohydrodynamic Jetting of Countercharged Nozzles. Polymer Bulletin 2008;61:521–8. https://doi.org/10.1007/s00289-008-0976-9.

[297] Wei Q, Xu F, Xu X, Geng X, Ye L, Zhang A, et al. The Multifunctional Wound Dressing with Core–Shell Structured Fibers Prepared by Coaxial Electrospinning. Front Mater Sci 2016;10:113–21. https://doi.org/10.1007/s11706-016-0339-7.

[298] Yang Y, Li X, Qi M, Zhou S, Weng J. Release Pattern and Structural Integrity of Lysozyme Encapsulated in Core–Sheath Structured Poly(dl-Lactide) Ultrafine Fibers Prepared by Emulsion Electrospinning. European Journal of Pharmaceutics and Biopharmaceutics 2008;69:106–16. https://doi.org/10.1016/j.ejpb.2007.10.016.

[299] Wang Z, Qian Y, Li L, Pan L, Njunge LW, Dong L, et al. Evaluation of Emulsion Electrospun Polycaprolactone/Hyaluronan/Epidermal Growth Factor Nanofibrous Scaffolds for Wound Healing. J Biomater Appl 2016;30:686–98. https://doi.org/10.1177/0885328215586907.

[300] Song W, Tang Y, Qian C, Kim BJ, Liao Y, Yu DG. Electrospinning spinneret: A bridge between the visible world and the invisible nanostructures. Innovation 2023;4. https://doi.org/10.1016/j.xinn.2023.100381.

[301] Zhang X, Yu N, Ren Q, Niu S, Zhu L, Hong L, et al. Janus Nanofiber Membranes with Photothermal-Enhanced Biofluid Drainage and Sterilization for Diabetic Wounds. Adv Funct Mater 2024;34. https://doi.org/10.1002/adfm.202315020.

[302] Zhao P, Zhou K, Xia Y, Qian C, Yu DG, Xie Y, et al. Electrospun Trilayer Eccentric Janus Nanofibers for a Combined Treatment of Periodontitis. Advanced Fiber Materials 2024. https://doi.org/10.1007/s42765-024-00397-6.

[303] Wang M, Hou J, Yu DG, Li S, Zhu J, Chen Z. Electrospun tri-layer nanodepots for sustained release of acyclovir. J Alloys Compd 2020;846. https://doi.org/10.1016/j.jallcom.2020.156471.

[304] Sun Y, Zhou J, Zhang Z, Yu DG, Bligh SWA. Integrated Janus nanofibers enabled by a co-shell solvent for enhancing icariin delivery efficiency. Int J Pharm 2024;658. https://doi.org/10.1016/j.ijpharm.2024.124180.

[305] Wang ML, Yu DG, Bligh SWA. Progress in preparing electrospun Janus fibers and their applications. Appl Mater Today 2023;31. https://doi.org/10.1016/j.apmt.2023.101766.

[306] Zhou J, Yi T, Zhang Z, Yu DG, Liu P, Wang L, et al. Electrospun Janus core (ethyl cellulose//polyethylene oxide) @ shell (hydroxypropyl methyl cellulose acetate succinate) hybrids for an enhanced colon-targeted prolonged drug absorbance. Adv Compos Hybrid Mater 2023;6. https://doi.org/10.1007/s42114-023-00766-6.

[307] Mao H, Zhou J, Yan L, Zhang S, Yu D-G. Hybrid films loaded with 5-fluorouracil and Reglan for synergistic treatment of colon cancer via asynchronous dual-drug delivery. Front Bioeng Biotechnol 2024;12. https://doi.org/10.3389/fbioe.2024.1398730.

[308] Yu DG, Gong W, Zhou J, Liu Y, Zhu Y, Lu X. Engineered shapes using electrohydrodynamic atomization for an improved drug delivery. Wiley Interdiscip Rev Nanomed Nanobiotechnol 2024;16. https://doi.org/10.1002/wnan.1964.

[309] Gong W, Yang W, Zhou J, Zhang S, Yu DG, Liu P. Engineered beads-on-a-string nanocomposites for an improved drug fast-sustained bi-stage release. Nanocomposites 2024;10:240–53. https://doi.org/10.1080/20550324.2024.2362477.

[310] Sun L, Zhou J, Chen Y, Yu DG, Liu P. A combined electrohydrodynamic atomization method for preparing nanofiber/microparticle hybrid medicines. Front Bioeng Biotechnol 2023;11. https://doi.org/10.3389/fbioe.2023.1308004.

[311] Xu S-C, Qin C-C, Yu M, Dong R-H, Yan X, Zhao H, et al. A Battery-Operated Portable Handheld Electrospinning Apparatus. Nanoscale 2015;7:12351–5. https://doi.org/10.1039/C5NR02922H.

[312] Kamali A, Shamloo A. Fabrication and Evaluation of a Bilayer Hydrogel-Electrospinning Scaffold Prepared by The Freeze-Gelation Method. J Biomech 2020;98:109466. https://doi.org/10.1016/j.jbiomech.2019.109466.

[313] Nakipoglu M, Özkabadayı Y, Karahan S, Tezcaner A. Bilayer Wound Dressing Composed of Asymmetric Polycaprolactone Membrane and Chitosan-Carrageenan Hydrogel Incorporating Storax Balsam. Int J Biol Macromol 2024;254:128020. https://doi.org/10.1016/j.ijbiomac.2023.128020.

[314] Song Y, Hu Q, Liu S, Wang Y, Zhang H, Chen J, et al. Electrospinning/3D Printing Drug-Loaded Antibacterial Polycaprolactone Nanofiber/Sodium Alginate-Gelatin Hydrogel Bilayer Scaffold for Skin Wound Repair. Int J Biol Macromol 2024:129705. https://doi.org/10.1016/j.ijbiomac.2024.129705.

[315] Asadi N, Mehdipour A, Ghorbani M, Mesgari-Abbasi M, Akbarzadeh A, Davaran S. A Novel Multifunctional Bilayer Scaffold Based on Chitosan Nanofiber/Alginate-Gelatin

Methacrylate Hydrogel for Full-Thickness Wound Healing. Int J Biol Macromol 2021;193:734–47. https://doi.org/10.1016/j.ijbiomac.2021.10.180.

[316] Kim JW, Kim MJ, Ki CS, Kim HJ, Park YH. Fabrication of Bi-Layer Scaffold of Keratin Nanofiber and Gelatin-Methacrylate Hydrogel: Implications for Skin Graft. Int J Biol Macromol 2017;105:541–8. https://doi.org/10.1016/j.ijbiomac.2017.07.067.

[317] Franco RA, Nguyen TH, Lee B-T. Preparation and Characterization of Electrospun PCL/PLGA Membranes and Chitosan/gelatin Hydrogels for Skin Bioengineering Applications. J Mater Sci Mater Med 2011;22:2207–18. https://doi.org/10.1007/s10856-011-4402-8.

[318] Jonidi Shariatzadeh F, Logsetty S, Liu S. Ultrasensitive Nanofiber Biosensor: Rapid In Situ Chromatic Detection of Bacteria for Healthcare Innovation. ACS Appl Bio Mater 2024;7:2378–88. https://doi.org/10.1021/acsabm.4c00038.

[319] Gwynne L, Williams GT, Yan KC, Patenall BL, Gardiner JE, He XP, et al. TCF-ALP: A fluorescent probe for the selective detection of: Staphylococcus bacteria and application in “smart” wound dressings. Biomater Sci 2021;9:4433–9. https://doi.org/10.1039/d0bm01918f.

[320] Landa G, Miranda-Calderon LG, Sebastian V, Irusta S, Mendoza G, Arruebo M. Selective point-of-care detection of pathogenic bacteria using sialic acid functionalized gold nanoparticles. Talanta 2021;234:122644. https://doi.org/10.1016/j.talanta.2021.122644.

[321] Thet NT, Mercer-Chalmers J, Greenwood RJ, Young AER, Coy K, Booth S, et al. SPaCE Swab: Point-of-Care Sensor for Simple and Rapid Detection of Acute Wound Infection. ACS Sens 2020;5:2652–7. https://doi.org/10.1021/acssensors.0c01265.

[322] Marston W. Venous Ulcers. Atlas of Endovascular Venous Surgery, Elsevier; 2019, p. 547–65. https://doi.org/10.1016/B978-0-323-51139-1.00020-6.

[323] Malone M. The Microbiome of Diabetic Foot Ulcers and the Role of Biofilms. The Microbiology of Skin, Soft Tissue, Bone and Joint Infections, Elsevier; 2017, p. 41–56. https://doi.org/10.1016/B978-0-12-811079-9.00003-3.

[324] Gao X, Li M, Zhao M, Wang X, Wang S, Liu Y. Metabolism-Triggered Colorimetric Sensor Array for Fingerprinting and Antibiotic Susceptibility Testing of Bacteria. Anal Chem 2021. https://doi.org/10.1021/acs.analchem.1c05006.

[325] Gwynne L, Williams GT, Yan KC, Gardiner JE, Hilton KLF, Patenall BL, et al. The Evaluation of Ester Functionalised TCF-Based Fluorescent Probes for the Detection of Bacterial Species. Isr J Chem 2021;61:234–8. https://doi.org/10.1002/ijch.202000105.

[326] Dong M, Sun X, Li L, He K, Wang J, Zhang H, et al. A bacteria-triggered wearable colorimetric band-aid for real-time monitoring and treating of wound healing. J Colloid Interface Sci 2022;610:913–22. https://doi.org/10.1016/j.jcis.2021.11.146.

[327] Gao Y, Chen Y, Li M, Jia L, Zhang L, Zhu J. Gelatin-based photonic hydrogels for visual detection of pathogenic Pseudomonas aeruginosa. Sens Actuators B Chem 2021;329:129137. https://doi.org/10.1016/j.snb.2020.129137.

[328] Kiti K, Thanomsilp C, Suwantong O. The potential use of colorimetric pH sensor from Clitoria ternatea flower for indicating bacterial infection in wound dressing application. Microchemical Journal 2022;177:107277. https://doi.org/10.1016/j.microc.2022.107277.

[329] Kuo SH, Shen CJ, Shen CF, Cheng CM. Role of pH value in clinically relevant diagnosis. Diagnostics 2020;10:1–17. https://doi.org/10.3390/diagnostics10020107.

[330] Bennison LR, Miller CN, Summers RJ, Minnis AMB, Sussman G, McGuiness W. The pH of wounds during healing and infection: a descriptive literature review. Wound Practice & Research: Journal of the Australian Wound Management Association 2017;25:63–9.

[331] Kruse CR, Singh M, Targosinski S, Sinha I, Sørensen JA, Eriksson E, et al. The effect of pH on cell viability, cell migration, cell proliferation, wound closure, and wound reepithelialization: In vitro and in vivo study. Wound Repair and Regeneration 2017;25:260–9. https://doi.org/10.1111/wrr.12526.

[332] Schneider LA, Korber A, Grabbe S, Dissemond J. Influence of pH on wound-healing: A new perspective for wound-therapy? Arch Dermatol Res 2007;298:413–20. https://doi.org/10.1007/s00403-006-0713-x.

[333] Fu T, Stupnitskaia P, Matoori S. Next-Generation Diagnostic Wound Dressings for Diabetic Wounds. ACS Measurement Science Au 2022. https://doi.org/10.1021/acsmeasuresciau.2c00023.

[334] Bender J, Flieger A. Lipases as Pathogenicity Factors of Bacterial Pathogens of Humans. Handbook of Hydrocarbon and Lipid Microbiology, Berlin, Heidelberg: Springer Berlin Heidelberg; 2010, p. 3241–58. https://doi.org/10.1007/978-3-540-77587-4_246.

[335] Jaeger KE, Ransac S, Dijkstra BW, Colson C, van Heuvel M, Misset O. Bacterial lipases. FEMS Microbiol Rev 1994;15:29–63. https://doi.org/10.1016/0168-6445(94)90025-6.

[336] Stehr F, Kretschmar M, Kröger C, Hube B, Schäfer W. Microbial lipases as virulence factors. J Mol Catal B Enzym 2003;22:347–55. https://doi.org/10.1016/S1381-1177(03)00049-3.

[337] Ghadimi D, Fölster-Holst R, Ebsen M, Röcken C, Dörfer C, Uchiyama J, et al. Exploring the Interplay between Nutrients, Bacteriophages, and Bacterial Lipases in Host- and

Bacteria-mediated Pathogenesis. Endocr Metab Immune Disord Drug Targets 2023;24. https://doi.org/10.2174/0118715303257321231024094904.

[338] Gardner SE, Frantz RA. Wound Bioburden and Infection-Related Complications in Diabetic Foot Ulcers. Biol Res Nurs 2008;10:44–53. https://doi.org/10.1177/1099800408319056.

[339] Hampton S. Bacteria and wound healing. Journal of Community Nursing 2007;21:32–40. https://doi.org/10.1097/01.qco.0000124361.27345.d4.

[340] Tang H, Yi B, Wang X, Shen Y, Zhang Y. Understanding the cellular responses based on low-density electrospun fiber networks. Materials Science and Engineering: C 2021;119:111470. https://doi.org/10.1016/j.msec.2020.111470.

[341] Leclech C, Barakat AI. Is there a universal mechanism of cell alignment in response to substrate topography? Cytoskeleton 2021;78:284–92. https://doi.org/10.1002/cm.21661.

[342] Wang Y. Effect of Aligned Nanoscale Surface Structures on Microbial Adhesion. 2019.

[343] Yao W, Liu K, Liu H, Jiang Y, Wang R, Wang W, et al. A Valuable Product of Microbial Cell Factories: Microbial Lipase. Front Microbiol 2021;12:1–16. https://doi.org/10.3389/fmicb.2021.743377.

[344] Liu YY, Xu JH, Hu Y. Enhancing effect of Tween-80 on lipase performance in enantioselective hydrolysis of ketoprofen ester. J Mol Catal B Enzym 2000;10:523–9. https://doi.org/10.1016/S1381-1177(00)00093-X.

[345] Kurpanik R, Lechowska-Liszka A, Mastalska-Popławska J, Nocuń M, Rapacz-Kmita A, Ścisłowska-Czarnecka A, et al. Effect of Ionic and Non-Ionic Surfactant on Bovine Serum Albumin Encapsulation and Biological Properties of Emulsion-Electrospun Fibers. Molecules 2022;27:3232. https://doi.org/10.3390/molecules27103232.

[346] Boonpratum C, Naemchanthara P, Limsuwan P, Naemchanthara K. Effects of chitosan and Tween 80 addition on the properties of nanofiber mat through the electrospinning. E-Polymers 2022;22:234–48. https://doi.org/10.1515/epoly-2022-0029.

[347] Carter JL, Kelly CA, Marshall JE, Jenkins MJ. Effect of thickness on the electrical properties of PEDOT:PSS/Tween 80 films. Polym J 2023. https://doi.org/10.1038/s41428-023-00854-w.

[348] Mala JGS, Takeuchi S. Understanding structural features of microbial lipases - An overview. Anal Chem Insights 2008;2008:9–19. https://doi.org/10.4137/aci.s551.

[349] Khan FI, Lan D, Durrani R, Huan W, Zhao Z, Wang Y. The lid domain in lipases: Structural and functional determinant of enzymatic properties. Front Bioeng Biotechnol 2017;5:1–13. https://doi.org/10.3389/fbioe.2017.00016.

[350] Carrasco-López C, Godoy C, de las Rivas B, Fernández-Lorente G, Palomo JM, Guisán JM, et al. Activation of bacterial thermo alkalophilic lipases is spurred by dramatic structural rearrangements. Journal of Biological Chemistry 2009;284:4365–72. https://doi.org/10.1074/jbc.M808268200.

[351] Abaházi E, Boros Z, Poppe L. Additives enhancing the catalytic properties of lipase from burkholderia cepacia immobilized on mixed-function-grafted mesoporous silica gel. Molecules 2014;19:9818–37. https://doi.org/10.3390/molecules19079818.

[352] Kim A, Kim HS, Park SO. Measuring of the perceptibility and acceptability in various color quality measures. J Opt Soc Korea 2011;15:310–7. https://doi.org/10.3807/JOSK.2011.15.3.310.

[353] Gangakhedkar NS. Colour measurement methods for textiles. Colour Measurement, Elsevier; 2010, p. 221–52. https://doi.org/10.1533/9780857090195.2.221.

[354] Carney BC, Chen JH, Kent RA, Rummani M, Alkhalil A, Moffatt LT, et al. Reactive Oxygen Species Scavenging Potential Contributes to Hypertrophic Scar Formation. Journal of Surgical Research 2019;244:312–23. https://doi.org/10.1016/j.jss.2019.06.006.

[355] van der Veer WM, Bloemen MCT, Ulrich MMW, Molema G, van Zuijlen PP, Middelkoop E, et al. Potential cellular and molecular causes of hypertrophic scar formation. Burns 2009;35:15–29. https://doi.org/10.1016/j.burns.2008.06.020.

[356] Butzelaar L, Ulrich MMW, Mink Van Der Molen AB, Niessen FB, Beelen RHJ. Currently known risk factors for hypertrophic skin scarring: A review. Journal of Plastic, Reconstructive and Aesthetic Surgery 2016;69:163–9. https://doi.org/10.1016/j.bjps.2015.11.015.

[357] Abebe A, Birhanu A. Methicillin Resistant Staphylococcus aureus: Molecular Mechanisms Underlying Drug Resistance Development and Novel Strategies to Combat. Infect Drug Resist 2023;Volume 16:7641–62. https://doi.org/10.2147/IDR.S428103.

[358] de Kraker MEA, Stewardson AJ, Harbarth S. Will 10 Million People Die a Year due to Antimicrobial Resistance by 2050? PLoS Med 2016;13:e1002184. https://doi.org/10.1371/journal.pmed.1002184.

[359] Sarah Pabst. Antimicrobial resistance. 2023.

[360] Shyam Bishen. What is antimicrobial resistance and how can we tackle it? 2024.

[361] Prestinaci F, Pezzotti P, Pantosti A. Antimicrobial resistance: a global multifaceted phenomenon. Pathog Glob Health 2015;109:309–18. https://doi.org/10.1179/2047773215Y.0000000030.

[362] Yang J, He Y, Li Z, Yang X, Gao Y, Chen M, et al. Intelligent wound dressing for simultaneous in situ detection and elimination of pathogenic bacteria. Acta Biomater 2024;174:177–90. https://doi.org/10.1016/j.actbio.2023.11.045.

[363] Pang Q, Yang F, Jiang Z, Wu K, Hou R, Zhu Y. Smart wound dressing for advanced wound management: Real-time monitoring and on-demand treatment. Mater Des 2023;229:111917. https://doi.org/10.1016/j.matdes.2023.111917.

[364] Rani Raju N, Silina E, Stupin V, Manturova N, Chidambaram SB, Achar RR. Multifunctional and Smart Wound Dressings—A Review on Recent Research Advancements in Skin Regenerative Medicine. Pharmaceutics 2022;14:1574. https://doi.org/10.3390/pharmaceutics14081574.

[365] Yang C, Yang C, Chen Y, Liu J, Liu Z, Chen H-J. The trends in wound management: Sensing, therapeutic treatment, and “theranostics.” Journal of Science: Advanced Materials and Devices 2023;8:100619. https://doi.org/10.1016/j.jsamd.2023.100619.

[366] Joorabloo A, Liu T. Smart theranostics for wound monitoring and therapy. Adv Colloid Interface Sci 2024;330:103207. https://doi.org/10.1016/j.cis.2024.103207.

[367] Ran P, Xia T, Zheng H, Lei F, Zhang Z, Wei J, et al. Light-triggered theranostic hydrogels for real-time imaging and on-demand photodynamic therapy of skin abscesses. Acta Biomater 2023;155:292–303. https://doi.org/10.1016/j.actbio.2022.11.039.

[368] Yang J, He Y, Li Z, Yang X, Gao Y, Chen M, et al. Intelligent wound dressing for simultaneous in situ detection and elimination of pathogenic bacteria. Acta Biomater 2024;174:177–90. https://doi.org/10.1016/j.actbio.2023.11.045.

[369] Pang Q, Lou D, Li S, Wang G, Qiao B, Dong S, et al. Smart Flexible Electronics-Integrated Wound Dressing for Real-Time Monitoring and On-Demand Treatment of Infected Wounds. Advanced Science 2020;7. https://doi.org/10.1002/advs.201902673.

[370] Halliwell B, Clement MV, Long LH. Hydrogen peroxide in the human body. FEBS Lett 2000;486:10–3. https://doi.org/10.1016/S0014-5793(00)02197-9.

[371] Kumar D, Singh V, Behal S, Maniar K, Chawdhary S, Bhattacharyya R, et al. Plasma Hydrogen Peroxide: A Myth or Reality? Indian Journal of Clinical Biochemistry 2019;34:118–9. https://doi.org/10.1007/s12291-018-0746-x.

[372] Chen G, Deng H, Song X, Lu M, Zhao L, Xia S, et al. Reactive oxygen species-responsive polymeric nanoparticles for alleviating sepsis-induced acute liver injury in mice. Biomaterials 2017;144:30–41. https://doi.org/10.1016/j.biomaterials.2017.08.008.

[373] Swebocki T. Minimum Inhibitory Concentration (MIC) and Minimum Bactericidal Concentration (MBC) Assays Using Broth Microdilution Method v1 2023. https://doi.org/10.17504/protocols.io.5qpvo3x6dv4o/v1.

[374] Mohamed Salleh NA binte, Tanaka Y, Sutarlie L, Su X. Detecting bacterial infections in wounds: a review of biosensors and wearable sensors in comparison with conventional laboratory methods. Analyst 2022;147:1756–76. https://doi.org/10.1039/D2AN00157H.

[375] Fu L, Deng S, Luo Y, Fu Q, Fan Y, Jia L. An ultrasensitive colorimetric biosensor for the detection of Gram-positive bacteria by integrating paper-based enrichment and carbon dot-based selective recognition. Talanta 2023;265:124920. https://doi.org/10.1016/j.talanta.2023.124920.

[376] Qureshi A, Niazi JH. Biosensors for detecting viral and bacterial infections using host biomarkers: a review. Analyst 2020;145:7825–48. https://doi.org/10.1039/D0AN00896F.

[377] Slavnova TD, Chibisov AK, Görner H. Kinetics of Salt-Induced J-aggregation of Cyanine Dyes. J Phys Chem A 2005;109:4758–65. https://doi.org/10.1021/jp058014k.

[378] Eisfeld A, Briggs JS. The J- and H-bands of organic dye aggregates. Chem Phys 2006;324:376–84. https://doi.org/10.1016/j.chemphys.2005.11.015.

[379] Hestand NJ, Spano FC. Expanded Theory of H- and J-Molecular Aggregates: The Effects of Vibronic Coupling and Intermolecular Charge Transfer. Chem Rev 2018;118:7069–163. https://doi.org/10.1021/acs.chemrev.7b00581.

[380] Cerritelli S, O'Neil CP, Velluto D, Fontana A, Adrian M, Dubochet J, et al. Aggregation Behavior of Poly(ethylene glycol- *bl* -propylene sulfide) Di- and Triblock Copolymers in Aqueous Solution. Langmuir 2009;25:11328–35. https://doi.org/10.1021/la900649m.

[381] Yi S, Allen SD, Liu Y-G, Ouyang BZ, Li X, Augsornworawat P, et al. Tailoring Nanostructure Morphology for Enhanced Targeting of Dendritic Cells in Atherosclerosis. ACS Nano 2016;10:11290–303. https://doi.org/10.1021/acsnano.6b06451.

[382] Tao W, He Z. ROS-responsive drug delivery systems for biomedical applications. Asian J Pharm Sci 2018;13:101–12. https://doi.org/10.1016/j.ajps.2017.11.002.

[383] Liang J, Liu B. ROS-responsive drug delivery systems. Bioeng Transl Med 2016;1:239–51. https://doi.org/10.1002/btm2.10014.

[384] Magnusson S, Logsetty S. Burn Outcomes. Burn Care and Treatment, Cham: Springer International Publishing; 2021, p. 165–71. https://doi.org/10.1007/978-3-030-39193-5_12.

[385] Tai Y, Woods EL, Dally J, Kong D, Steadman R, Moseley R, et al. Myofibroblasts: Function, Formation, and Scope of Molecular Therapies for Skin Fibrosis. Biomolecules 2021;11:1095. https://doi.org/10.3390/biom11081095.

[386] Zhu Z, Hou Q, Li M, Fu X. Molecular Mechanism of Myofibroblast Formation and Strategies for Clinical Drugs Treatments in Hypertrophic Scars. J Cell Physiol 2020;235:4109–19. https://doi.org/10.1002/jcp.29302.

[387] Verhaegen PDHM, Van Zuijlen PPM, Pennings NM, Van Marle J, Niessen FB, Van Der Horst CMAM, et al. Differences in collagen architecture between keloid, hypertrophic scar, normotrophic scar, and normal skin: An objective histopathological analysis. Wound Repair and Regeneration 2009;17:649–56. https://doi.org/10.1111/j.1524-475X.2009.00533.x.

[388] Kandhwal M, Behl T, Singh S, Sharma N, Arora S, Bhatia S, et al. Role of Matrix Metalloproteinase in Wound Healing. Am J Transl Res 2022;14:4391–405.

[389] Tripathi S, Soni K, Agrawal P, Gour V, Mondal R, Soni V. Hypertrophic scars and keloids: a review and current treatment modalities. Biomedical Dermatology 2020;4. https://doi.org/10.1186/s41702-020-00063-8.

[390] Frasson DN, Valange M, Almeras I, Izquierdo M, Ster G. Textbook on Scar Management. Cham: Springer International Publishing; 2020. https://doi.org/10.1007/978-3-030-44766-3.

[391] Ding JY, Sun L, Zhu ZH, Wu XC, Xu XL, Xiang YW. Nano drug delivery systems: a promising approach to scar prevention and treatment. J Nanobiotechnology 2023;21:1–14. https://doi.org/10.1186/s12951-023-02037-4.

[392] Nabai L, Ghahary A, Jackson J. Localized Controlled Release of Kynurenic Acid Encapsulated in Synthetic Polymer Reduces Implant—Induced Dermal Fibrosis. Pharmaceutics 2022;14. https://doi.org/10.3390/pharmaceutics14081546.

[393] Li Y, Kilani RT, Rahmani-Neishaboor E, Jalili RB, Ghahary A. Kynurenine increases matrix metalloproteinase-1 and -3 expression in cultured dermal fibroblasts and improves scarring in vivo. Journal of Investigative Dermatology 2014;134:643–50. https://doi.org/10.1038/jid.2013.303.

[394] Zhuang Z, Wang Y, Feng Z, Lin X, Wang Z, Zhong X, et al. Targeting Diverse Wounds and Scars: Recent Innovative Bio-design of Microneedle Patch for Comprehensive Management. Small 2023. https://doi.org/10.1002/smll.202306565.

[395] Beaven E, Kumar R, Bhatt HN, Esquivel S V., Nurunnabi M. Myofibroblast specific targeting approaches to improve fibrosis treatment. Chemical Communications 2022;58:13556–71. https://doi.org/10.1039/d2cc04825f.

[396] Zheng M, Wiraja C, Yeo DC, Chang H, Lio DCS, Shi W, et al. Oligonucleotide Molecular Sprinkler for Intracellular Detection and Spontaneous Regulation of mRNA for Theranostics of Scar Fibroblasts. Small 2018;14. https://doi.org/10.1002/smll.201802546.

[397] Nabai L, Pourghadiri A, Ghahary A. Hypertrophic Scarring: Current Knowledge of Predisposing Factors, Cellular and Molecular Mechanisms. Journal of Burn Care & Research 2020;41:48–56. https://doi.org/10.1093/jbcr/irz158.

[398] Fu M, Peng D, Lan T, Wei Y, Wei X. Multifunctional Regulatory Protein Connective Tissue Growth Factor (CTGF): A Potential Therapeutic Target for Diverse Diseases. Acta Pharm Sin B 2022;12:1740–60. https://doi.org/10.1016/j.apsb.2022.01.007.

[399] Chen Z, Zhang N, Chu HY, Yu Y, Zhang ZK, Zhang G, et al. Connective Tissue Growth Factor: From Molecular Understandings to Drug Discovery. Front Cell Dev Biol 2020;8:1–17. https://doi.org/10.3389/fcell.2020.593269.

[400] Lali F V., Martin YH, Metcalfe AD. Advances in Biopharmaceutical Agents and Growth Factors for Wound Healing and Scarring. Skin Tissue Engineering and Regenerative Medicine, Elsevier; 2016, p. 337–55. https://doi.org/10.1016/B978-0-12-801654-1.00017-6.

[401] Yazdani S, Bansal R, Prakash J. Drug targeting to myofibroblasts: Implications for fibrosis and cancer. Adv Drug Deliv Rev 2017;121:101–16. https://doi.org/10.1016/j.addr.2017.07.010.

[402] Rayego-Mateos S, Rodrigues-Díez R, Morgado-Pascual JL, Rodrigues Díez RR, Mas S, Lavoz C, et al. Connective tissue growth factor is a new ligand of epidermal growth factor receptor. J Mol Cell Biol 2013;5:323–35. https://doi.org/10.1093/jmcb/mjt030.

[403] Pink DL, Loruthai O, Ziolek RM, Wasutrasawat P, Terry AE, Lawrence MJ, et al. On the Structure of Solid Lipid Nanoparticles. Small 2019;15. https://doi.org/10.1002/smll.201903156.

[404] Rigon RB, Gonçalez ML, Severino P, Alves DA, Santana MHA, Souto EB, et al. Solid lipid nanoparticles optimized by 22 factorial design for skin administration: Cytotoxicity in NIH3T3 fibroblasts. Colloids Surf B Biointerfaces 2018;171:501–5. https://doi.org/10.1016/j.colsurfb.2018.07.065.

[405] Roces CB, Lou G, Jain N, Abraham S, Thomas A, Halbert GW, et al. Manufacturing considerations for the development of lipid nanoparticles using microfluidics. Pharmaceutics 2020;12:1–19. https://doi.org/10.3390/pharmaceutics12111095.

[406] Akbari J, Saeedi M, Ahmadi F, Hashemi SMH, Babaei A, Yaddollahi S, et al. Solid Lipid Nanoparticles and Nanostructured Lipid Carriers: A Review of The Methods of

Manufacture andRoutes of Administration. Pharm Dev Technol 2022;27:525–44. https://doi.org/10.1080/10837450.2022.2084554.

[407] Li J, Sun L, Liu Y, Yao H, Jiang S, YunzhuPu, et al. To reduce premature drug release while ensuring burst intracellular drug release of solid lipid nanoparticle-based drug delivery system with clathrin modification. Nanomedicine 2019;15:108–18. https://doi.org/10.1016/j.nano.2018.05.014.

[408] Xie D, Nakachi K, Wang H, Elashoff R, Koeffler HP. Elevated Levels of Connective Tissue Growth Factor, WISP-1, and CYR61 in Primary Breast Cancers Associated with More Advanced Features 1. Cancer Res 2001;61:8917–23.

[409] Hellinger JW, Schömel F, Buse J V., Lenz C, Bauerschmitz G, Emons G, et al. Identification of Drivers of Breast Cancer Invasion by Secretome Analysis:Insight into CTGF Signaling. Sci Rep 2020;10:17889. https://doi.org/10.1038/s41598-020-74838-8.

[410] Farmoudeh A, enayatifard R, Saeedi M, Talavaki F, Ghasemi M, Akbari J, et al. Methylene blue loaded solid lipid nanoparticles: Preparation, optimization, and in-vivo burn healing assessment. J Drug Deliv Sci Technol 2022;70:103209. https://doi.org/10.1016/j.jddst.2022.103209.

[411] Tiwari N, Osorio-Blanco ER, Sonzogni A, Esporrín-Ubieto D, Wang H, Calderón M. Nanocarriers for Skin Applications: Where Do We Stand? Angewandte Chemie International Edition 2022;61. https://doi.org/10.1002/anie.202107960.

[412] Jain SK, Chaurasiya A, Gupta Y, Jain A, Dagur P, Joshi B, et al. Development and characterization of 5-FU bearing ferritin appended solid lipid nanoparticles for tumour targeting. J Microencapsul 2008;25:289–97. https://doi.org/10.1080/02652040701799598.

[413] Silva AC, González-Mira E, García ML, Egea MA, Fonseca J, Silva R, et al. Preparation, characterization and biocompatibility studies on risperidone-loaded solid lipid nanoparticles (SLN): High pressure homogenization versus ultrasound. Colloids Surf B Biointerfaces 2011;86:158–65. https://doi.org/10.1016/j.colsurfb.2011.03.035.

[414] Vivek K, Reddy H, Murthy RSR. Investigations of the effect of the lipid matrix on drug entrapment, in vitro release, and physical stability of olanzapine-loaded solid lipid nanoparticles. AAPS PharmSciTech 2007;8:16–24. https://doi.org/10.1208/pt0804083.

[415] Keen JH, Willingham MC, Pastan IH. Clathrin-coated vesicles: Isolation, dissociation and factor-dependent reassociation of clathrin baskets. Cell 1979;16:303–12. https://doi.org/10.1016/0092-8674(79)90007-2.

[416] Matsui W, Kirchhausen T. Stabilization of clathrin coats by the core of the clathrin-associated protein complex AP-2. Biochemistry 1990;29:10791–8. https://doi.org/10.1021/bi00500a011.

[417] Nabai L, Ghahary A, Jackson J. Localized Controlled Release of Kynurenic Acid Encapsulated in Synthetic Polymer Reduces Implant—Induced Dermal Fibrosis. Pharmaceutics 2022;14. https://doi.org/10.3390/pharmaceutics14081546.

[418] Poormasjedi-Meibod MS, Hartwell R, Kilani RT, Ghahary A. Anti-Scarring Properties of Different Tryptophan Derivatives. PLoS One 2014;9. https://doi.org/10.1371/journal.pone.0091955.

[419] Poormasjedi-Meibod MS, Pakyari M, Jackson JK, Salimi Elizei S, Ghahary A. Development of a nanofibrous wound dressing with an antifibrogenic properties in vitro and in vivo model. J Biomed Mater Res A 2016;104:2334–44. https://doi.org/10.1002/jbm.a.35770.

[420] Chen P-S, Wang M-Y, Wu S-N, Su J-L, Hong C-C, Chuang S-E, et al. CTGF enhances the motility of breast cancer cells via an integrin-αvβ3–ERK1/2-dependent S100A4-upregulated pathway. J Cell Sci 2007;120:2053–65. https://doi.org/10.1242/jcs.03460.

[421] Kim H-S, Nagalla SR, Oh Y, Wilson E, Roberts CT, Rosenfeld RG. Identification of a family of low-affinity insulin-like growth factor binding proteins (IGFBPs): Characterization of connective tissue growth factor as a member of the IGFBP superfamily (peptide hormonesserum inducible factorstransforming growth factor). Cell Biology Communicated by Melvin M Grumbach 1997;94:12981–6.

[422] Shah RM, Rajasekaran D, Ludford-Menting M, Eldridge DS, Palombo EA, Harding IH. Transport of stearic acid-based solid lipid nanoparticles (SLNs) into human epithelial cells. Colloids Surf B Biointerfaces 2016;140:204–12. https://doi.org/10.1016/j.colsurfb.2015.12.029.

[423] Matthaeus C, Taraska JW. Energy and Dynamics of Caveolae Trafficking. Front Cell Dev Biol 2021;8. https://doi.org/10.3389/fcell.2020.614472.

[424] Martins S, Costa-Lima S, Carneiro T, Cordeiro-Da-Silva A, Souto EB, Ferreira DC. Solid lipid nanoparticles as intracellular drug transporters: An investigation of the uptake mechanism and pathway. Int J Pharm 2012;430:216–27. https://doi.org/10.1016/j.ijpharm.2012.03.032.

[425] Granja A, Nunes C, Sousa CT, Reis S. Folate receptor-mediated delivery of mitoxantrone-loaded solid lipid nanoparticles to breast cancer cells. Biomedicine and Pharmacotherapy 2022;154. https://doi.org/10.1016/j.biopha.2022.113525.

[426] Gupta AK, Berry C, Gupta M, Curtis A. Receptor-mediated Targeting of Magnetic Nanoparticles Using Insulin as a Surface Ligand to Prevent Endocytosis. IEEE Trans Nanobioscience 2003;2:255–61. https://doi.org/10.1109/TNB.2003.820279.

[427] Morcavallo A, Stefanello M, Iozzo R V., Belfiore A, Morrione A. Ligand-Mediated Endocytosis and Trafficking of the Insulin-Like Growth Factor Receptor I and Insulin Receptor Modulate Receptor Function. Front Endocrinol (Lausanne) 2014;5. https://doi.org/10.3389/fendo.2014.00220.

[428] Shi-Wen X, Leask A, Abraham D. Regulation and function of connective tissue growth factor/CCN2 in tissue repair, scarring and fibrosis. Cytokine Growth Factor Rev 2008;19:133–44. https://doi.org/10.1016/j.cytogfr.2008.01.002.

[429] Chen Y, Segarini P, Raoufi F, Bradham D, Leask A. Connective Tissue Growth Factor is Secreted through The Golgi and is Degraded in The Endosome. Exp Cell Res 2001;271:109–17. https://doi.org/10.1006/excr.2001.5364.

[430] Leask A, Denton CP, Abraham DJ. Insights into the Molecular Mechanism of Chronic Fibrosis: The Role of Connective Tissue Growth Factor in Scleroderma. Journal of Investigative Dermatology 2004;122:1–6. https://doi.org/10.1046/j.0022-202X.2003.22133.x.

[431] Blom IE, Goldschmeding R, Leask A. Gene Regulation of Connective Tissue Growth Factor: New Targets for Antifibrotic Therapy? vol. 21. 2002.

[432] Jain A, Singhai P, Gurnany E, Updhayay S, Mody N. Transferrin-tailored solid lipid nanoparticles as vectors for site-specific delivery of temozolomide to brain. Journal of Nanoparticle Research 2013;15. https://doi.org/10.1007/s11051-013-1518-4.

[433] Ak G, Ünal A, Karakayalı T, Özel B, Selvi Günel N, Hamarat Şanlıer Ş. Brain-targeted, drug-loaded solid lipid nanoparticles against glioblastoma cells in culture. Colloids Surf B Biointerfaces 2021;206:111946. https://doi.org/10.1016/j.colsurfb.2021.111946.

[434] Ma C, Wu M, Ye W, Huang Z, Ma X, Wang W, et al. Inhalable solid lipid nanoparticles for intracellular tuberculosis infection therapy: macrophage-targeting and pH-sensitive properties. Drug Deliv Transl Res 2021;11:1218–35. https://doi.org/10.1007/s13346-020-00849-7.

[435] van der Veer WM, Bloemen MCT, Ulrich MMW, Molema G, van Zuijlen PP, Middelkoop E, et al. Potential cellular and molecular causes of hypertrophic scar formation. Burns 2009;35:15–29. https://doi.org/10.1016/j.burns.2008.06.020.

[436] Lin X, Lai Y. Scarring Skin: Mechanisms and Therapies. Int J Mol Sci 2024;25:1458. https://doi.org/10.3390/ijms25031458.

[437] Ma Y, Liu Z, Miao L, Jiang X, Ruan H, Xuan R, et al. Mechanisms underlying pathological scarring by fibroblasts during wound healing. Int Wound J 2023;20:2190–206. https://doi.org/10.1111/iwj.14097.

[438] Butzelaar L, Ulrich MMW, Mink van der Molen AB, Niessen FB, Beelen RHJ. Currently known risk factors for hypertrophic skin scarring: A review. Journal of Plastic, Reconstructive & Aesthetic Surgery 2016;69:163–9. https://doi.org/10.1016/j.bjps.2015.11.015.

[439] Rahim K, Saleha S, Zhu X, Huo L, Basit A, Franco OL. Bacterial Contribution in Chronicity of Wounds. Microb Ecol 2017;73:710–21. https://doi.org/10.1007/s00248-016-0867-9.

[440] Scalise A, Bianchi A, Tartaglione C, Bolletta E, Pierangeli M, Torresetti M, et al. Microenvironment and microbiology of skin wounds: the role of bacterial biofilms and related factors. Semin Vasc Surg 2015;28:151–9. https://doi.org/10.1053/j.semvascsurg.2016.01.003.

[441] Qian L, Fourcaudot AB, Yamane K, You T, Chan RK, Leung KP. Exacerbated and prolonged inflammation impairs wound healing and increases scarring. Wound Repair and Regeneration 2016;24:26–34. https://doi.org/10.1111/wrr.12381.

[442] Holzer-Geissler JCJ, Schwingenschuh S, Zacharias M, Einsiedler J, Kainz S, Reisenegger P, et al. The Impact of Prolonged Inflammation on Wound Healing. Biomedicines 2022;10:856. https://doi.org/10.3390/biomedicines10040856.

[443] Landén NX, Li D, Ståhle M. Transition from inflammation to proliferation: a critical step during wound healing. Cellular and Molecular Life Sciences 2016;73:3861–85. https://doi.org/10.1007/s00018-016-2268-0.

[444] van der Veer WM, Bloemen MCT, Ulrich MMW, Molema G, van Zuijlen PP, Middelkoop E, et al. Potential cellular and molecular causes of hypertrophic scar formation. Burns 2009;35:15–29. https://doi.org/10.1016/j.burns.2008.06.020.

[445] Asatiani N, Valtera J, Lisnenko M, Havlickova K, Kovacicin J, Lukas D, et al. Evaluation of Fiber Orientation of Ac and Dc Electrospun Plcl Nanofibrous Layers. NANOCON Conference Proceedings - International Conference on Nanomaterials 2021:240–5. https://doi.org/10.37904/nanocon.2021.4353.

[446] Astuti NH, Wibowo NA, Ayub MRSSN. The Porosity Calculation of Various Types of Paper Using Image Analysis. Jurnal Pendidikan Fisika Indonesia 2018;14:46–51. https://doi.org/10.15294/jpfi.v14i1.9878.

[447] Bessa LJ, Fazii P, Di Giulio M, Cellini L. Bacterial isolates from infected wounds and their antibiotic susceptibility pattern: some remarks about wound infection. Int Wound J 2015;12:47–52. https://doi.org/10.1111/iwj.12049.

[448] Bowler PG, Duerden BI, Armstrong DG. Wound Microbiology and Associated Approaches to Wound Management. Clin Microbiol Rev 2001;14:244–69. https://doi.org/10.1128/CMR.14.2.244-269.2001.

[449] Petkovšek Z, Eleršič K, Gubina M, Žgur-Bertok D, Starčič Erjavec M. Virulence Potential of Escherichia coli Isolates from Skin and Soft Tissue Infections. J Clin Microbiol 2009;47:1811–7. https://doi.org/10.1128/JCM.01421-08.

[450] Liu Y, Gu J, Zhang J, Yu F, Wang J, Nie N, et al. LiFePO4 nanoparticles growth with preferential (010) face modulated by Tween-80. RSC Adv 2015;5:9745–51. https://doi.org/10.1039/c4ra14791j.

[451] Huan S, Liu G, Han G, Cheng W, Fu Z, Wu Q, et al. Effect of Experimental Parameters on Morphological, Mechanical and Hydrophobic Properties of Electrospun Polystyrene Fibers. Materials 2015;8:2718–34. https://doi.org/10.3390/ma8052718.

[452] Szymczyk K, Taraba A, Szaniawska M. Interactions of Tween 20, 60 and 80 with dye molecules: Spectroscopic analysis. J Mol Liq 2019;290:111227. https://doi.org/10.1016/j.molliq.2019.111227.

[453] Kurpanik R, Lechowska-Liszka A, Mastalska-Popławska J, Nocuń M, Rapacz-Kmita A, Ścisłowska-Czarnecka A, et al. Effect of Ionic and Non-Ionic Surfactant on Bovine Serum Albumin Encapsulation and Biological Properties of Emulsion-Electrospun Fibers. Molecules 2022;27:3232. https://doi.org/10.3390/molecules27103232.

[454] Mahmood ME, Al-koofee D a F. Effect of Temperature Changes on Critical Micelle Concentration for Tween Series Surfactant. Global Journal of Science Frontier Research Chemistry 2013;13:1–7.

[455] Prajapati K, Patel S. Micellization of Surfactants in Mixed Solvent of Different Polarity. Arch Appl Sci Res 2012;4:662–8.

[456] Santhanalakshmi J, Maya SI. Solvent effects on reverse micellisation of Tween 80 and Span 80 in pure and mixed organic solvents. Proceedings of the Indian Academy of Sciences: Chemical Sciences 1997;109:27–38. https://doi.org/10.1007/bf02871358.

[457] Joachim D. Wound cleansing: benefits of hypochlorous acid. J Wound Care 2020;29:S4–8. https://doi.org/10.12968/jowc.2020.29.Sup10a.S4.

[458] Robson MC, Payne WG, Ko F, Mentis M, Donati G, Shafii SM, et al. Hypochlorous Acid as a Potential Wound Care Agent: Part II. Stabilized Hypochlorous Acid: Its Role in Decreasing Tissue Bacterial Bioburden and Overcoming the Inhibition of Infection on Wound Healing. J Burns Wounds 2007;6:e6.

[459] Li J, Sun L, Liu Y, Yao H, Jiang S, YunzhuPu, et al. To reduce premature drug release while ensuring burst intracellular drug release of solid lipid nanoparticle-based drug delivery system with clathrin modification. Nanomedicine 2019;15:108–18. https://doi.org/10.1016/j.nano.2018.05.014.

[460] Deák Á, Csapó E, Juhász Á, Dékány I, Janovák L. Anti-ulcerant kynurenic acid molecules intercalated Mg/Al-layered double hydroxide and its release study. Appl Clay Sci 2018;156:28–35. https://doi.org/10.1016/j.clay.2018.01.024.

[461] Zhao X, Shi C, Zhou X, Lin T, Gong Y, Yin M, et al. Preparation of a nanoscale dihydromyricetin-phospholipid complex to improve the bioavailability: in vitro and in

vivo evaluations. European Journal of Pharmaceutical Sciences 2019;138:104994. https://doi.org/10.1016/j.ejps.2019.104994.

[462] Asikin-Mijan N, Lee H V., Juan JC, Noorsaadah AR, Taufiq-Yap YH. Catalytic deoxygenation of triglycerides to green diesel over modified CaO-based catalysts. RSC Adv 2017;7:46445–60. https://doi.org/10.1039/c7ra08061a.

[463] Gupta U, Singh VivekK, Kumar V, Khajuria Y. Spectroscopic Studies of Cholesterol: Fourier Transform Infra-Red and Vibrational Frequency Analysis. Materials Focus 2014;3:211–7. https://doi.org/10.1166/mat.2014.1161.

[464] Tunsirikongkon A, Pyo YC, Kim DH, Lee SE, Park JS. Optimization of polyarginine-conjugated PEG lipid grafted proliposome formulation for enhanced cellular association of a protein drug. Pharmaceutics 2019;11. https://doi.org/10.3390/pharmaceutics11060272.

[465] Chantaburanan T, Teeranachaideekul V, Chantasart D, Jintapattanakit A, Junyaprasert VB. Effect of binary solid lipid matrix of wax and triglyceride on lipid crystallinity, drug-lipid interaction and drug release of ibuprofen-loaded solid lipid nanoparticles (SLN) for dermal delivery. J Colloid Interface Sci 2017;504:247–56. https://doi.org/10.1016/j.jcis.2017.05.038.